

**Proceedings of the
VDE/IEEE
Power and Energy Student Summit 2018
2th - 4th July 2018
University of Kaiserslautern**



Supported by:



innogy



In cooperation with:



PESS 2018 Conference-Team

Conference Chair

- Prof. Dr.-Ing. Wolfram H. Wellßow



Organization-Team

- Dagmar Häßel
- Daniel Henschel
- Karin Schweikert
- Marco Weisenstein



Contact Team

pess@rhrk.uni-kl.de

Review-Team

- Robert Brandalik, University of Kaiserslautern
- Prof. Dr.-Ing. Michael Braun, Karlsruhe Institut of Technology
- Prof. Dr.-Ing. Wolfgang Gawlik, Vienna University of Technology
- Prof. Dr.-Ing. Karsten Glöser, University of Applied Science Kaiserslautern
- Prof. Dr.-Ing. Jutta Hanson, Technical University of Darmstadt
- Prof. Dr.-Ing. Marc Klemm, HTW Saarbrücken, University of Applied Science
- Athanasios Krontiris, ABB AG
- Prof. Dr.-Ing. Michael Kurrat, Technical University of Braunschweig
- Haiyan Ma, University of Kaiserslautern
- Prof. Dr.-Ing. Michael Mann, University of Applied Sciences Aschaffenburg
- Dr.-Ing. Gert Mehlmann, Friedrich-Alexander University of Erlangen-Nürnberg
- Prof. Dr.-Ing. Albert Moser, RWTH Aachen University
- Johannis Porst, Friedrich-Alexander University of Erlangen-Nürnberg
- Simon Resch, Friedrich-Alexander University of Erlangen-Nürnberg
- Prof. Dr.-Ing. Krzysztof Rudion, University of Stuttgart
- Prof. Dr.-Ing. Peter Schegner, Technical University of Dresden
- Jakob Schindler, Friedrich-Alexander-University of Erlangen-Nürnberg
- Prof. Dr.-Ing. Detlef Schulz, Helmut Schmidt University of Hamburg
- Prof. Dr.-Ing. Stefan Tenbohlen, University of Stuttgart
- Kishan Veerashekar, Friedrich-Alexander University of Erlangen-Nürnberg
- Marco Weisenstein, University of Kaiserslautern
- Prof. Dr.-Ing. Wolfram Wellßow, University of Kaiserslautern
- Prof. Dr.-Ing. Dirk Westermann, University of Ilmenau
- Prof. Dr.-Ing. Martin Wolter, Otto von Guericke University of Magdeburg
- Prof. Dr.-Ing. Markus Zdrallek, University of Wuppertal

Contents

Grid Specific Control Parameter for Voltage Regulated Distribution Transformers With Active Power Dependent Setpoint Setting Sebastian Becker, University of Kaiserslautern	p. 1-6
Method to Coordinate Optimal and Individual Charging for Aggregators of Electric Vehicles Flavio Gromann, Andreas Raab and Kai Strunz, Technical University of Berlin	p. 7-11
Evaluation of Data Preprocessing Techniques for Battery Management Systems Nuttapong Sansuk, Dominik Jöst, Dirk Sauer and Nisai Fuengwarodsakul, RWTH Aachen	p. 12-17
Consideration of Maintenance Aspect for Conversion of Transposed AC Lines to Hybrid AC/DC Lines Pavel Tikhonov, Alexander Novitskiy and Dirk Westermann, University of Ilmenau	p. 18-23
AC Fault Analysis of DRU-VSC Hybrid HVDC Topology for Offshore Wind Farm Integration Melanie Hoffmann, Nasser Hemdan, Michael Kurrat, Christian Rathke and Andreas Menze, Technical University of Braunschweig	p. 24-29
Model Reduction of a Low Voltage Grid by Current Source to Investigate Small-Signal Stability Jan Kircheis, Teng Jiang, Julian Willkomm, Steffen Schlegel and Dirk Westermann, University of Ilmenau	p. 30-35
Impact of Increasing Renewable Generation on Power System Stability Aiko Schinke and István Erlich (†), University of Duisburg-Essen	p. 36-41
Comparison and Evaluation of Voltage Stability Indices for OPF application Johannes Kayser, Florian Sass and Dirk Westermann, University of Ilmenau	p. 42-47
Protection Security Assessment System in the Context of Power System Restoration Tobias Hanika, Michael Jaworski and Johann Jäger, University of Erlangen-Nürnberg	p. 48-53
Influence of Measurement Error on a New Voltage-less Distance Protection Method Linjie Li, Martin Biller and Johann Jäger, University of Erlangen-Nürnberg	p. 54-58
Investigation on Membership Function Design for Fuzzy Logic based Fault Classification Nicholas Mohnlein and Jakob Schindler, University of Erlangen-Nürnberg	p. 59-64
Influence of Meteorological Conditions on European Electricity Markets Samuel Kyei Dankwah, Levin Skiba and Wijarn Wangdee, RWTH Aachen	p. 65-70
Power Plant Dispatch Considering Heat Cogeneration Lucas Bernhard Temmen, Timo Breithaupt and Lutz Hofmann, University of Hannover	p. 71-76
Security-constrained optimization of power plant dispatch in interconnected networks with several market areas and price zones Nicola Gast, Andre Richter and Martin Wolter, Otto von Guericke University of Magdeburg	p. 77-82
Evaluation of a Transition Path to a Future Scenario of Lower Saxony's Energy Supply under Variation of Storage Capacity and Power Thomas Wolgast, Christoph Blaufuß and Lutz Hofmann, University of Hannover	p. 83-88
Detection and Localization of Power Plant Outages using Machine Learning Algorithms Bharathwajanprabu Ravisankar and Stefan Dalhues, Technical of Dortmund	p. 89-94

Contribution to Distribution System State Estimation with Hachtel's Augmented Matrix Approach Annika Brüggemann, Tobias Hoffmann, Florian Rewald and Christian Rehtanz, University of Dortmund	p. 95-99
Impact Analysis of Decentralized Energy Devices Participating in Load Frequency Control Xinya Song, Teng Jiang, Steffen Schlegel and Dirk Westermann, University of Ilmenau	p. 100-104
Application of a pseudo value generation tool for loads in low voltage state estimation Patrick Gassler, University of Kaiserslautern	p. 105-109
Investigations of real-time Performance Using OPAL-RT and acceleration methods based on different power converter models Yuelin Zeng, Hui Cai, Teng Jiang, Steffen Schlegel and Dirk Westermann, University of Ilmenau	p. 110-114
Concept of an Adaptable Protection Device for Low Voltage Networks Kevin Alexander Egle, Florian Grumm, Marc Florian Meyer, Maik Plenz and Detlef Schulz, Helmut Schmidt University of Hamburg	p. 115-119
Demand Side Integration Architecture for low voltage smart grids Sara Mohammadi, University of Kaiserslautern	p. 120-125
Practical Approach of Realizing Co-simulation by Using eMEGASIM and ePHASORSIM based on Inverter Dominated Grid Xinya Song, Teng Jiang, Steffen Schlegel and Dirk Westermann, University of Ilmenau	p. 126-131
Coupling Low Voltage Grids as Cost-Efficient Solution for Higher Share of Electric Vehicle Christoph Baumann, University of Kaiserslautern	p. 132-137
Highly Renewable Energy Integrated Grid Stability by Microgrid Vishal Undre, Alberto Dolara and Sonia Leva, Politecnico di Milano	p. 138-141

Grid Specific Control Parameters for Voltage Regulated Distribution Transformers With Active Power Dependent Setpoint Setting

Sebastian Becker, B. Sc.

Lehrstuhl für Energiesysteme und Energiemanagement
Technische Universität Kaiserslautern (TUK)
Kaiserslautern, Germany

Abstract— Due to the steadily increasing load and installed capacity of photovoltaic systems in low voltage grids, new challenges for the voltage stability arise. The use of a voltage regulated distribution transformer with active power dependent setpoint setting allows to react to the current load and feed-in situation in the grid by observing the power at the transformer. To ensure safe operation, it is important to determine suited parameters that define the required power-voltage characteristic. The presented determination rule uses several load and feed-in scenarios to determine the active power in the breakpoints of the power-voltage characteristic. Safe operation shall be ensured due to the use of worst-case assumptions for developing the scenarios. Validation through potential and time series analyses reveals some weak spots of this determination rule. However, it shows also the importance of grid specific parameters. The analysis of the performed simulations results in proposals for further improvements of the determination rule. Altogether, this paper contributes to strengthen the acceptance of voltage regulated distribution transformers with active power dependent setpoint setting by a better understanding of the importance of right parameter setting and thus, to a more cost-efficient grid reinforcement.

Keywords—component; on-load tap changer; low voltage; distributed generation; grid specific parameters

I. INTRODUCTION

A. Motivation

The German energy transition with the two central aims of massive CO₂-reduction and phase-out of all nuclear power plants, leads to fundamental changes in the German electric power supply system [1]. The subsidies to support the power generation out of renewable energies caused a boom in the solar industry: From 2010 up to 2013 the installed capacity P_{inst} of photovoltaic (PV) systems has tripled (see Fig. 1). These are mainly installed in low voltage (LV) grids [2:25-26]. However, the growth has slowed down in the past few years. But regarding the continuously improvement of PV system efficiencies, it can be assumed that retrofitting will increase P_{inst} again rapidly.

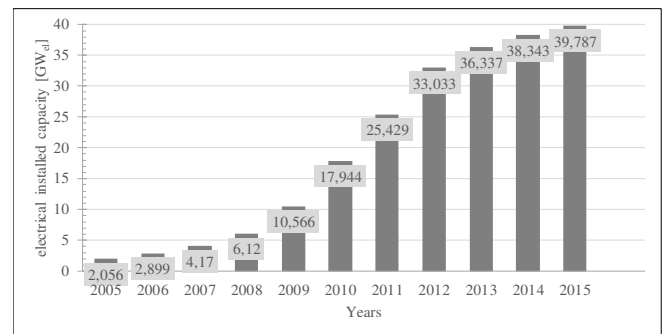


Figure 1. Installed capacity of PV systems in Germany from 2005 to 2015. Data from [3].

In LV grids with a high installed capacity it is possible that the generation of energy is higher than the consumption. The resulting bidirectional power flow lead to a voltage rise, that affects the voltage quality. The grid operator is committed to regulate the voltage level according to DIN EN 50160 in between a range of $\pm 10\%$ of the nominal voltage U_n (0.4 kV in Germany). Hence, according to VDE-AR-N 4105 [4:33], PV systems can already disconnect at $+9\%$ U_n . To avoid violations of this voltage band the grid operators have to adopt voltage stability measures. Besides the classic grid expansion several other measures and new components exist, like the voltage regulated distribution transformer (RDT). RDT can be used instead of common transformers and provide the ability to step on load between different transmission ratios. By changing the transmission ratio, the RDT adjusts the voltage at the LV busbar (BB) and, as a consequence, affects the voltage in the whole LV grid. In the standard control concept, the control target is the BB voltage. A stepping is initiated after the voltage leaves a tolerance band (TB) which is around the setpoint, e.g. the nominal voltage. An advanced control concept extends the standard concept by an active power dependent setpoint setting (APS). This makes it possible to react more sensitively to the generation and load situation in the LV grid.

$\pm 50\%$ of the power at the transformer P_T to be rather on the safe side avoiding violations of the legitimate voltage band and to make it easier to integrate new PV systems. [8] use an easy rule to determine the parameters. However, the determination rule is only partial grid specific and not generalizable.

The aim of [9] is to investigate the effects of RDT in an area of connected grids. They use a reference scenario without a RDT to determine the parameters for APS. The P-U characteristic must be determined so that the voltage violations of the lower and upper voltage limit in the reference scenario are eradicated applying APS. The breakpoints of the characteristic are at $\pm 80\% P_T$. With this high power at the breakpoints it can be assumed that violations of the voltage band still occur during operation. Although this determination rule requires the simulation of a reference scenario, it's simple to apply. Nonetheless it's not generalizable, thus it's not suitable for planning principles.

The analysis of former papers shows that approaches exist to frame planning principles including voltage stability with RDT. The use of SP allows an easy and fast implementation. However, this may lead to untapped potential. To exploit the potential as full as possible, it is necessary to determine GP. The biggest disadvantages of the regarded approaches are the huge effort and the deep understanding for the determination or the non-generalizability of the rules. Therefore, these approaches are not suited for planning principles. For this reason, this paper has the following goal: Develop a determination rule, that is practicable and easy to apply on the one hand. On the other hand, it yields individual and GP for voltage control by RDT with APS.

III. DEVELOPMENT OF THE DETERMINATION RULE

A. Conception and development of the scenarios

The presented determination rule requires the simulation of several load and feed-in scenarios. Fig. 3 shows the several scenarios, which are used in the determination rule. Different colors denote the several scenarios.

Simulations of the assumed worst-case-scenarios of the feed-in case ('green scenario') and the load case ('red scenario') yield the highest and lowest values of active power at the transformer and voltage in the LV grid. These values can be used to scale the required RDT. Hence, the worst-case voltage rise and drop is known.

To present the minimum voltage band between $u_{BB,LV}$ and the upper and lower voltage limit, the voltage $u_{BB,LV}$ is set to setpoint, raised by half the TB, for feed-in scenarios. For load scenarios it's set to setpoint, reduced by half the TB. In both cases the voltage at the BB lies exactly on the TB. A small voltage rise, respectively drop, would cause the RDT to initiate a stepping.

To simulate the highest possible voltage drop in the 'red scenario', all loads consume the maximum load assumption P_{BA} according to applied planning criteria and there is no power feed-in of any PV system in the LV grid. Thus, the

'red scenario' determines the maximum P_T and the lowest possible voltages that can occur applying this determination rule. Notice, the load in real operation may differ significantly. However, the 'red scenario' is according to usual planning principles a worst-case load scenario [10:2./2-2./3]. Analogous to the 'red scenario', all PV systems in the 'green scenario' feed in $100\% P_{inst}$ and there is no load in the LV grid. In the following, lines with voltages above the upper voltage limit in the 'green scenario' are declared as critical lines, as well as lines with voltages below the lower voltage limit in the 'red scenario'. Given the chance to eliminate one or more critical lines, without risking violation of the other voltage limit, the setpoint can be slightly adjusted.

The 'purple scenario' and the 'orange scenario' restrict the area for $p_{b,1}$ in a comprehensible way. Both are based on the 'green scenario' and examine the power flow situation in the LV grid, if the voltage in a single critical line is right at the upper limit. Therefore, these scenarios must be simulated for each critical line of the 'green scenario'. In the 'purple scenario' are no loads in the LV grid and each PV system feeds in its maximum P_{inst} . The power feed-in in the regarded critical line must be reduced till the voltage in this line is right at the upper voltage limit. In the 'orange scenario' each PV system also feeds in $100\% P_{inst}$. Whereas all loads consume the maximum P_{BA} . In the regarded critical line is no load and the power feed-in should be adjusted, so that the highest voltage in this line is at the upper voltage limit.

The simulations of the 'purple-' and the 'orange scenario' yield the values $p_{purple,j}$ and $p_{orange,j}$ for the critical lines S_j . The parameter $p_{b,1}$ should be between the most positive $p_{orange,j}$ and the most negative $p_{purple,j}$. The power flow $p_{purple,j}$ is the most negative power flow at the RDT in the case of a voltage band violation in S_j . The smallest power flow at the transformer in the case of a voltage band violation in S_j is given with $p_{orange,j}$. For the control concept with APS, the 'orange scenario' is the most difficult situation to identify the voltage band violation by only observing the power flow at the RDT. Especially for a positive p_{orange} , that indicates a load case. Out of this reason, the 'grey scenario' is designated to determine $p_{b,1}$, based on the 'orange scenario'. In the regarded critical line, there is still no load and the power feed-in should be set so that the voltage in this line is at the upper voltage limit. All other loads consume the maximum P_{BA} . The modification of the 'orange scenario' is that in other lines the feed-in of all PV systems is set to $40\% P_{inst}$ (see B). This simultaneity factor models the limited extent of LV grids, so that in the case of maximum power feed-in of PV systems in the critical line, there is very likely also a power feed-in of PV systems in other lines.

- | | |
|---|--|
| ✱ | 100 % power feed-in of PV systems, no load |
| ✱ | 100 % power feed-in of all PV systems, no load, reduce power feed-in of PV systems in the critical line till the highest voltage is at the upper limit |
| ✱ | In the critical line is no load and power feed-in of PV systems is so high so that the highest voltage is at the upper limit, max. load and 0 % power feed-in of PV systems in other lines |
| ✱ | Power feed-in of PV systems in the critical line is so high so that the highest voltage is at the upper limit, max. load and 40% power feed-in of all PV systems in other lines |
| ✱ | Max. load, no power feed-in |
| ✱ | Max. load, reduce load in the critical line till the lowest voltage is at the lower limit |

Figure 3. Overview of the several load and feed-in scenarios.

The ‘pink scenario’ is designated to determine $p_{b,2}$, the breakpoint of the P-U characteristic in the load case. Therefore, it is based on the ‘red scenario’. In the whole LV grid is full load and no power feed-in. The load in the critical line is reduced, so that the lowest voltage is right at the lower voltage limit.

The ‘grey scenario’ and the ‘pink scenario’ set the power in the breakpoints of the P-U characteristic. To define these scenarios, it must come to a compromise. The slope of the characteristic should not be too high on the one hand. On the other hand, the determined parameters should guarantee a secure operation of the RDT, also in sensible worst-case situations.

B. Simultaneity factor of PV systems

In some of the presented scenarios, the power feed-in in the critical line is 100 % P_{inst} , whereas it is 0 % P_{inst} in all other lines. Because of the limited extent of LV grids, these worst-case-scenarios are very unlikely. The distribution of the power flow is more pessimistic than it would be in a worst-case situation in real operation. To handle this, a simultaneity factor is introduced in the ‘grey scenario’ to determine the parameter $p_{b,1}$. The simultaneity factor G is the percentage of P_{inst} in non-critical lines that can be assumed as current power feed-in in these lines, if there is maximum power feed-in in the critical line. The current power feed-in in non-critical lines n can be calculated with (1):

$$P_{EA,n} = P_{EA,\text{inst},n} \cdot G, \forall n. \quad (1)$$

Using the simultaneity factor only in the ‘grey scenario’ allows to keep the determination rule simpler. This eschewal minimizes the additional effort. Hence, only the ‘grey scenario’ has direct influence on the parameter determination. It’s satisfying to have precise, but not unsafe, results only for the ‘grey scenario’.

The investigations of [11], [12] and [13] show a big range in determining a simultaneity factor for PV systems in LV grids. Depending on the situation, the factor can be between 30 % and 80 %. To define the ‘grey scenario’ as worst-case-scenario, that is also as realistic as possible, the simultaneity factor is set to 40 % in the presented determination rule.

C. Determination of the additional voltage

The determination of $u_{\text{add,max}}$ and $u_{\text{add,min}}$ depends on the maximum voltage rise or drop Δu , in the LV grid, that occurs in both worst-case-scenarios. With

$$\Delta u = |u_{\text{min}} - u_{\text{BB,LV}}| \quad (2)$$

shows (3) the formula to determine $u_{\text{add,min}}$:

$$u_{\text{add,min}} = \begin{cases} -u_{\text{Stufe}}, & \text{if } \Delta u - u_{\text{Stufe}} + \frac{u_{\text{TB}}}{2} < 10 \% \\ -u_{\text{TB}}, & \text{else} \end{cases} \quad (3)$$

The lowest possible voltage at the BB is $u_{\text{TB}}/2$ below the setpoint. Hence, the highest possible voltage drop is the voltage drop in the LV grid Δu plus the $u_{\text{TB}}/2$ voltage drop at

the BB due to the MV level. Assuming an extreme load case in the LV grid, it’s very likely that the surrounding grids are also in a load case. This means, the MV level, thereby $u_{\text{BB,LV}}$ as well, is below 100 % U_n . The addition of $u_{\text{add,min}} = -u_{\text{step}}$ is sufficient to initiate a stepping. If the upper condition of (3) is valid, one single stepping is enough to avoid a violation of the voltage band. Otherwise, a more negative additional voltage is necessary to initiate at least two steppings. Equation (5) determines $u_{\text{add,max}}$ using

$$\Delta u = u_{\text{max}} - u_{\text{BB,LV}} \quad (4)$$

and underlays the analogous consideration:

$$u_{\text{add,max}} = \begin{cases} u_{\text{step}}, & \text{if } \Delta u - u_{\text{step}} + \frac{u_{\text{TB}}}{2} < 9 \% \\ u_{\text{TB}}, & \text{else} \end{cases} \quad (5)$$

D. Procedure of the parameter determination

The procedure to determine the parameters has three stages. The scenarios of chapter III.A. must be simulated on the first stage. With the result that maximum values of power and voltage in the grid are known and the parameters $p_{b,1}$ and $p_{b,2}$ are determined. On stage two, the parameters of the additional voltage $u_{\text{add,max}}$ and $u_{\text{add,min}}$ are determined, using the results of the scenario simulations according to formulas described in III.C. Finally, the parameters p_0 and u_0 are determined on stage three.

The procedure to determine $p_{b,1}$ and $p_{b,2}$ is shown in Fig. 4. It can be divided into three phases. Worst-case scenarios ‘green’ and ‘red’ are simulated in the first phase. Depending on the maximum voltage in the grid, there exist two possibilities to determine $p_{b,1}$ in phase 2 and $p_{b,2}$ in phase 3. Basically, both parameters are determined by the ‘green-’ and ‘red scenario’, if there occurs no violation of the voltage band. Otherwise the ‘purple-’, ‘orange-’ and ‘grey scenario’ are needed to determine $p_{b,1}$ and the ‘pink scenario’ is needed to determine $p_{b,2}$.

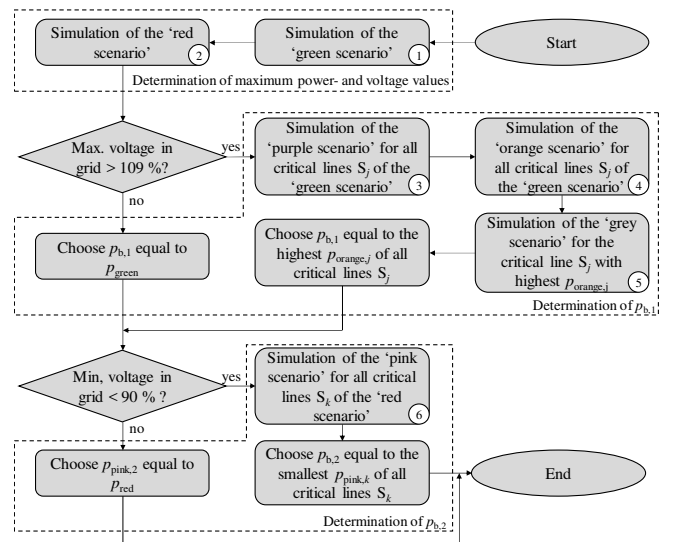


Figure 4. Procedure to determine the parameters $p_{b,1}$ and $p_{b,2}$.

IV. VALIDATION

A. Applying the determination rule

To validate the determination rule, GP for 5 real grids in Rhineland-Palatine are determined. These grids are denoted as ‘Weisenheim’, ‘Heuchelheim’, ‘Forst’, ‘Essingen’ and ‘Birkenheide’. The results of a PA and TSA using GP are compared to the results with SP (see Fig. 7a for the P-U characteristic of SP) [6]. The observed grids were altered to create a future scenario for 2030. A peak load of 30 kW is assumed to consider the increasing number of e-mobility. Also, the scenario includes a PV penetration of 50 % with an assumed average of 9.2 kW installed power per household.

To visualize the determination, the simulation results of the several scenarios can be plotted into a P-U diagram (see Fig. 5 as example for a P-U diagram). The diagram shows p_{RDT} on the x-axis against u_i on the y-axis. For each scenario and each line, always the highest voltage (for the feed-in scenarios ‘green’, ‘purple’, ‘orange’ and ‘grey’) or the lowest voltage (for the load scenarios ‘red’ and ‘pink’) as well as the active power at the transformer are plotted.

Fig. 5 shows the P-U diagram for the parameter determination of ‘Weisenheim’. For the simulation of the ‘green scenario’, the maximum voltages in S_4 and S_5 are above the upper limit, so these are the critical lines. The simulation of the ‘purple-’ and ‘orange scenario’ for these two lines span the range of $p_{b,1}$ (orange rectangle in Fig. 5). To be as safe as possible in avoiding over-voltages the ‘grey scenario’ is simulated for S_4 . Due to much load in S_5 , $p_{b,1}$ is located in the area of a load case. Consequently, S_5 is the critical line in the ‘red scenario’ and therefore, $p_{b,2}$ is determined by the simulation of the ‘pink scenario’ for S_5 . The resulting P-U characteristic (see Fig. 7 b) is very sharp, since both breakpoints are close together. Due to the high $u_{add,min}$, according to (3), the slope increases further.

B. Simulation and results

1) Potential analysis

In Fig. 6, the comparison is made between the results of the PA using SP and GP. It shows the potential for integration of load and installed capacity of PV systems into the LV grids.

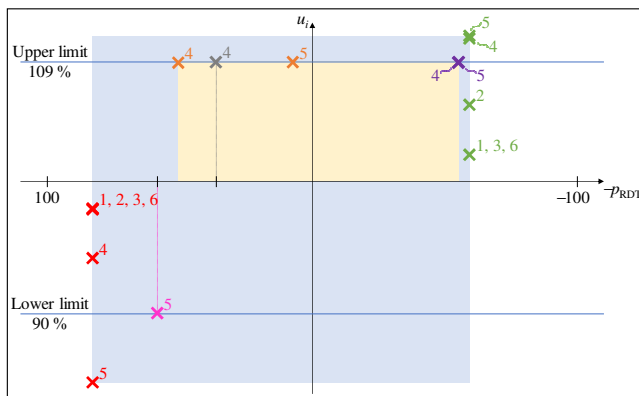


Figure 5. P-U diagram for the parameter determination of ‘Weisenheim’.

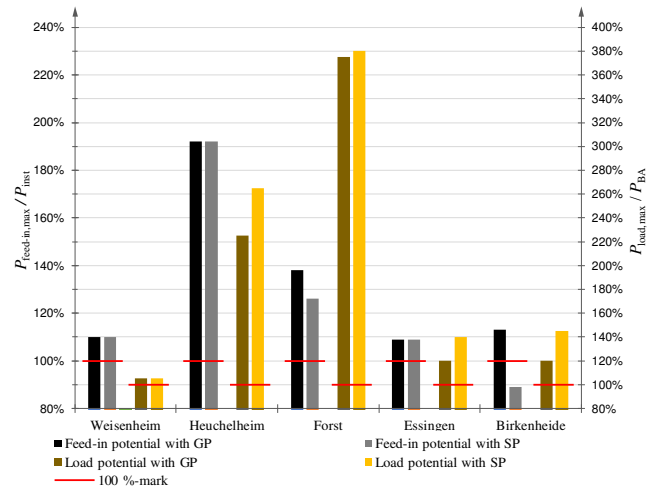


Figure 6. Potential for integration of additional PV capacity and loads.

The result shows a positive integration potential (above 100 %) for all grids, except the feed-in integration potential using SP in ‘Birkenheide’. The integration potential in ‘Weisenheim’, ‘Essingen’ and ‘Birkenheide’ for feed-in as well as load is in between a range of 105 % and 145 %. Against this, the integration potential in ‘Heuchelheim’ and ‘Forst’ is much higher.

The comparison between GP and SP shows that the use of SP results in a higher load integration potential in four of five grids. However, using GP results in higher feed-in integration potential in two grids. Indeed in ‘Birkenheide’, the use of GP provides a potential to integrate 113 % P_{inst} . While using SP, violations of the voltage band start to occur with a power feed-in of 89 % P_{inst} .

2) Time series analysis

TSA examines the behavior of the RDT over one year. To get results that are as realistic as possible, individual load profiles are used instead of standard load profiles. Load and feed-in time series are created by a Matlab tool that is described in [14]. In the scenario year 2030, time series with datapoints every 15 minutes are examined, which correspond to 35040 datapoints overall. In this examination, the TSA is performed for the grids ‘Weisenheim’, ‘Heuchelheim’ and ‘Forst’.

In Table I, the main results of the TSA are presented. The use of SP and GP can avoid any violation of the voltage band in ‘Heuchelheim’ and ‘Forst’. Thereby, the number of steppings is a bit lower using GP. In ‘Weisenheim’, 23 violations of the voltage band occurred using SP. While using GP, 1119 violations can be observed. However, only one violation of the upper voltage limit occurred in each analysis, at the same datapoint. At this datapoint, u_{add} equals $u_{add,max}$ using both parameters. Therefore, this violation could only be avoided with a higher $u_{add,max}$. Using GP, the additional voltage equals $u_{add,max}$ at all datapoints indeed. Since the highest observed p_{RDT} is 28.67 %, the point of changing u_{add} is never reached (see Fig. 7). So, the higher $u_{add,min}$, compared to SP, has no effect on avoiding violations of the lower voltage limit.

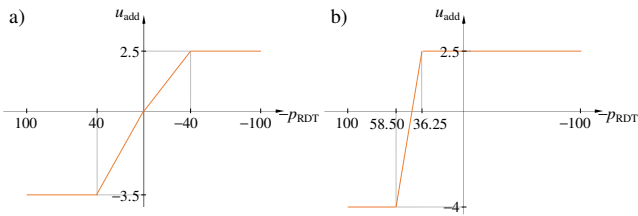


Figure 7. P-U characteristic of a) SP and b) GP for ‘Weisenheim’.

To the contrary, the permanent addition of $u_{add,max}$ leads to further problems of under-voltages in the grid. The use of SP provides a $u_{add,min}$ of -3.5% . Since the minimum observed u_{add} in TSA is about -2.5% , the height of $u_{add,min}$ has also no effects. More precisely, a more grid specific positioned $p_{b,2}$ could help to avoid more violations of the lower voltage limit.

C. Findings

PA shows that it isn’t possible to feed in 100% P_{inst} in ‘Birkenheide’ using SP. For this worst-case situation, the use of SP can’t avoid a violation of the legitimate voltage band. Apart from that, the use of both GP and SP provide an additional potential for the integration of further load and feed-in. Nevertheless, employing PA is, besides the TSA, only one part of the validation. The failure of the SP in ‘Birkenheide’ is no disqualifier.

Validation through TSA shows many violations of the voltage band in ‘Weisenheim’. The use of GP cannot avoid the occurrence of 1118 violations of the lower voltage limit. Because of the very positive $p_{b,1}$, the characteristic of GP is very sharp. Hence, in the TSA using GP p_{RDT} never reached $p_{b,1}$. In the ‘grey scenario’, full load is assumed in every line, except the critical line. Instead of the very good predictable worst-case power feed-in of PV systems, prediction of the worst-case load is much harder. Therefore, it’s difficult to estimate the load in worst-case scenarios for the parameter estimation. Due to the fact, that $p_{b,1}$ is very positive according to the presented determination rule, the assumed load in the ‘grey scenario’ is apparently too pessimistic.

The comparison shows that both parameters are very good in avoiding violations of the upper voltage limit, although $p_{b,1}$ of the SP is far in the negative area. This proves the conclusion, that the assumptions to determine the grid specific $p_{b,1}$ with the ‘grey scenario’ are unnecessarily pessimistic. A flatter characteristic of GP would lead to a better situation-dependent u_{add} . An adjustment of the feed-in scenarios may unlock a big potential of improvement.

TABLE I. NUMBER OF VOLTAGE BAND VIOLATIONS AND NUMBER OF STEPPINGS AS RESULT OF THE TSA.

	Number of voltage band violations		Number of steppings	
	GP	SP	GP	SP
Weisenheim	1119	23	397	1389
Heuchelheim	0	0	1205	1459
Forst	0	0	1087	1357

V. OUTLOOK

The simulations presented in this paper show the advantages of RDT with APS and their contribution to the voltage control in LV grids. Furthermore, the importance of suited parameters for APS could be demonstrated. Nevertheless, the validation of the presented determination rule revealed some weak spots. Some points to improve the determination rule could be identified as well. Further examinations to adjust the underlying worst-case scenarios may result in considerable improvements for the performance of APS with grid specific parameters.

It’s very difficult to consider all worst-case scenarios using the APS concept in grids with a quite asymmetrical distribution of loads and PV systems. For these grids, it could be still necessary to use another control concept, like remote voltage metering, or to implement further components, like an additional line voltage regulator. At some point, it should be even considered to abandon the use of a RDT and adopt other measures proposed by state of the art guidelines [5].

REFERENCES

- [1] Federal Ministry for Economic Affairs and Energy, “Energiekonzept: für eine umweltschonende, zuverlässige und bezahlbare Energieversorgung”, 2010.
- [2] Federal Ministry for Economic Affairs and Energy, “Moderne Verteilernetze für Deutschland: Verteilernetzstudie”, 2014.
- [3] AGEE-stat, “Zeitreihen zur Entwicklung der erneuerbaren Energien in Deutschland”, 2016.
- [4] VDE-AR-N-4105, Erzeugungsanlagen am Niederspannungsnetz, Berlin: VDE-Verlag, 2011.
- [5] P. Hauße et al., “Leitfaden zur Integration spannungsstabilisierender Applikationen in Niederspannungsnetze”, 2nd version, 2018.
- [6] P. Hauße, C. Wendel, M. Arnold, W. H. Wellßow, “Entwicklung von Planungsgrundsätzen für die Niederspannungsnetze der Pflanzwerke AG”, proceedings of the VDE-congress in Frankfurt/Main, 2014.
- [7] O. Brückl, Informationsportal regelbare Ortsnetztransformatoren. [Online] Available: <http://ront.info>. Accessed on: Apr. 30 2018.
- [8] S. Eilenberger et al., “Probabilistische Netzsimulation zur Bewertung von regelbaren Transformatoren: Energieversorgung auf dem Weg nach 2050”, proceedings of the international ETG-congress in Berlin, 2013.
- [9] F. Portratz et al., “Erkenntnisse neuer Netzplanungsansätze für das Verteilnetz unter Berücksichtigung regelbarer Ortsnetztransformatoren (RONT): Zur zukünftigen Wechselwirkung von elektrischem Netz und Energiemarktaktivitäten”, proceedings of the ETG-symposium in Kassel, 2015.
- [10] W. Kaufmann, “Planung öffentlicher Elektrizitätsverteilungssysteme“, 1st ed. Berlin: VDE-Verl., 1995.
- [11] T. Stetz et al., “Stochastische Analyse von Smart-Meter Messdaten: Intelligente Energieversorgung der Zukunft“, proceedings of the VDE-Congress in Stuttgart, 2012.
- [12] M. Mohrmann, B. Lehde, A. Hengelbrock, and L. Hofmann, “Untersuchung der Veränderung von Haushaltslasten anhand von Messzeitreihen aus einem Forschungsprojekt“, proceedings of the NEIS-conference in Hamburg, 2013.
- [13] J. Weniger et al., “Einfluss verschiedener Betriebsstrategien auf die Netzeinspeisung räumlich verteilter PV-Speichersysteme“, proceedings of the PV-symposium in Bad Steffelstein, 2015.
- [14] N. Nicolas, “Synthesis of domestic load curves for low voltage grid simulations“, proceedings of the PESS in Nürnberg, 2017.

Method to Coordinate Optimal and Individual Charging for Aggregators of Electric Vehicles

Flavio Gromann, Andreas F. Raab and Kai Strunz

I. INTRODUCTION

Abstract—The restructuring of the transport sector towards the massive usage of electrified vehicles requires dedicated solutions for the market and system integration. For that purpose, aggregation entities are introduced to establish the integration process of electric vehicle (EV) fleets in the energy market. This process is detailed by specifying the sequences for day-ahead operations. The proposed method realizes optimal energy procurements for day-ahead charging of EV fleets without dictating the user's driving behavior. Optimization techniques are applied to calculate optimal charging schedules for the entire fleet. These schedules are then used as indirect control signals to coordinate the individual EV charging process. The integrative market solution is verified through modeling and a sound set of simulations. The results confirm the added value and applicability of using the developed charging methodology.

Keywords—Aggregation concepts, charging optimization, individual charging, electric vehicles, power scheduling.

NOMENCLATURE

Indexes:

i	index of electric vehicles
k	time step counter
n	number of electric vehicles users

Sets:

H_{ts}	set of time steps
----------	-------------------

Variables:

c^{da}	cost per amount of energy per time interval τ at the, e.g. day-ahead market
Γ_i^{ev}	grid connection per time interval τ for electric vehicle i
$E_i^{d,ev}$	driving energy demand per interval τ for, e.g. electric vehicle i
$E_i^{r,ev}$	battery capacity per, e.g. electric vehicle i
P_i^{ev}	charging power of, e.g. electric vehicle i
SoE_i^{ev}	state of energy of, e.g. electric vehicle i
τ	time interval
η	charging efficiency

THE electrification of the transportation sector can contribute to achieving the objective of reducing greenhouse gas emissions [1]. In the literature, different concepts for energy management and supply of electrified vehicles are proposed [2]–[4].

With regard to charging strategies for EVs, the usage of aggregation concepts to realize the market participation for individual users of EVs is discussed in [5]. In this context, several optimization techniques for smart charging strategies are proposed [6]–[10] to reduce the overall energy cost and offering ancillary services for the power system.

The optimization techniques in [11] deal with aggregated EV variables, e.g. pooled driving energy demands for the upcoming day, to calculate the charging schedules. A comparison of aggregated with individual optimization approaches to assesses the deviations of resulting charging schedules is mentioned in [12]. The optimization approach in [13] considers risk aversion to find the optimal charging schedules at the vehicle level under uncertain price and mobility conditions. To avoid mobility uncertainties, the users in [14], [15] have to submit their driving profiles for the upcoming day.

The novel charging methodology presented here, can be used by Electric Vehicle Supplier/Aggregators (EVS/A) to estimate the required driving energy demands, optimize the charging schedules, and coordinate the individual EV charging processes without information of the user's driving behaviors.

The organizational framework is presented in Section II. In Section III the optimization approach used for day-ahead market operation is detailed. The extensive simulation and results are provided in Section IV. Finally, Section V contains the concluding remarks.

II. MODELING ARCHITECTURE FOR THE EV SUPPLIER/AGGREGATOR

In the following, the Electric Vehicle Supplier/Aggregator (EVS/A) is introduced to establish the day-ahead market access for EVs. The EVS/A bundles the EVs to fleets, procures the required charging energy, and supports the individual EV charging. Based on the temporal price signal of the day-ahead market, the EVS/A defines the charging strategy and calculates the charging schedules for the energy procurements. The charging schedules are then used to coordinate the individual EV charging process.

A. Structure

In the proposed structure, the EVS/A has the responsibility of managing the energy demand of EVs and purchase electricity [16] on the day-ahead market. The EVS/A sell charging services, offering access and metering services to the owner of EVs. A possible structure to organize the energy procurements in the day-ahead market operations is shown in

Flavio Gromann (e-mail: flavio.gromann@tu-berlin.de), Andreas F. Raab and Kai Strunz are with the School of Electrical Engineering and Computer Science, TU Berlin, Germany.

This work was supported by the Federal Ministry for Economic Affairs and Energy (Germany) through the research project *Netzintegration mobiler Energiespeicher: Testbasierte Evaluierung, technische Potentiale und Bereitschaft von Fahrzeughaltern* (NET INES), under Contract 03ET4005C.

Manuscript submitted on MARCH 9, 2018.

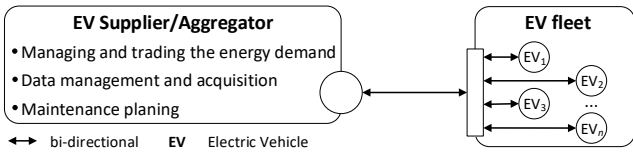


Fig. 1. Service-centric function of EVS/A in the aggregation structure for electric vehicles.

Fig. 1. For each EV fleet, the EVS/A combines the functions of managing and satisfying the energy demands, including data management, maintenance planning, and operating data acquisition. In this context, the following explanations detail the overall model architecture for the energy procurement and scheduling processes.

B. Processes for Day-Ahead Operations

The methodology for day-ahead operations of EV fleets distinguishes the optimization and application process as shown in the sequences of Fig. 2. In the optimization process, the EVS/A scheduler generates driving energy demand profiles as described in Section II-C in more detail preliminary. Each of these profiles represents the predicted temporally resolved daily driving energy demand without geo-data information. There is no direct correlation between an individual driving energy demand profile and the respectively user. The amount of driving energy demand profiles is as many as participating users. The resulting predicted driving energy demand profiles are then forwarded to the EVS/A optimizer. In parallel, the EVS/A optimizer formulates the objective function and define the constraints for the charging optimization process as detailed further in Section III. For the charging optimization,

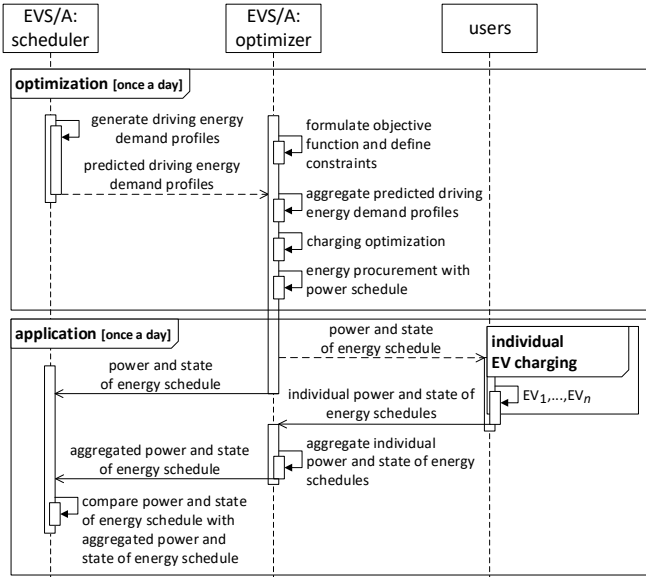


Fig. 2. Day-ahead charging optimization and application.

the predicted driving energy demand profiles are aggregated by the EVS/A optimizer. Based on the resulting predicted driving energy demand profile and the before mentioned objective function and constraints, the power and state of energy schedule for the fleet are calculated for the upcoming day. With the power schedule, the EVS/A optimizer procures the required charging energy in the day-ahead market.

Finally, in the application process, the power and state of energy schedule are forwarded to each EV at the beginning of the upcoming day. For evaluation purpose, the schedules are also forwarded to the EVS/A scheduler.

Based on the power and state of energy schedule, the individual charging of each EV is coordinated by the individual EV charging method as detailed in Section III. At the end of the upcoming day, the resulting individual power and state of energy schedules are forwarded to the EVS/A optimizer. The EVS/A optimizer aggregate these schedules and forward it to the EVS/A scheduler. For evaluation purpose, the EVS/A scheduler compares the aggregated power and state of energy schedules of the application process with the power and state of energy schedule of the optimization process.

C. Driving Energy Demand Generation and Evaluation

The driving energy demand profiles are modeled by using a Monte Carlo approach [13], [17]. These profiles are calculated under consideration of statistic data of the MiD-Study [18]. Each of these profiles represents the temporally resolved daily driving energy demand of the private user. The assumed time interval τ of these profiles is 0.25 h. One element of the driving energy demand profiles is represented by the driving energy demand $E_i^{ev,d}$ of EV i at time step k .

For evaluation purpose, the driving energy demand profiles are aggregated and the equivalent driving power demand profiles are calculated. The aggregated driving power demand profiles for EV fleets with different number of users are shown in Fig. 3.

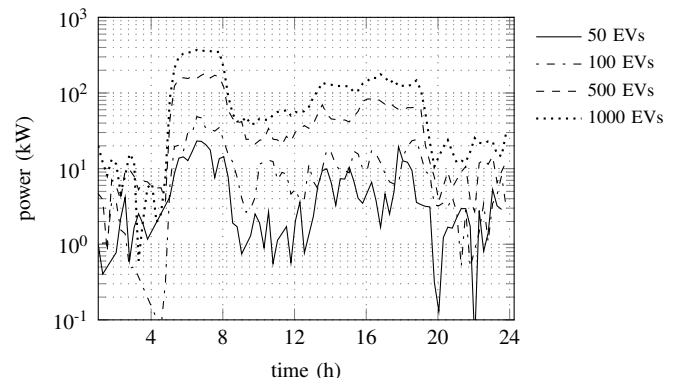


Fig. 3. Aggregated driving power demands for private electric vehicle users.

It can be observed that the variability of individual driving power demand profiles is decreasing with higher numbers of considered EVs within the fleet. The results show that the individual and stochastic driving behaviors are mutually compensated.

III. CHARGING OPTIMIZATION AND APPLICATION FOR EV FLEETS

In this Section, the charging optimization and the individual EV charging method are detailed, as shown in the sequences of Fig. 2. First, optimal charging schedules are calculated within the charging optimization method. Then, the resulting schedules are applied by the individual EV charging method to coordinate the charging process of each EV.

A. Charging Optimization

The optimization is a constrained linear programming problem with the aim to minimize the total charging costs in day-ahead market operations. Regarding the trading period of the day-ahead market, the optimization horizon is one day and denoted by the set of time steps H_{ts} . The time interval τ is 0.25 h so that the set of time steps is $H_{ts} = \{1, 2, \dots, 96\}$ respectively. The objective function is formulated with the day-ahead market price per amount of energy c^{da} , the charging power of the EV fleet P^{fleet} and charging efficiency η for every time step k by:

$$\min \sum_{k \in H_{ts}} P^{\text{fleet}}(k) \cdot \eta \cdot \tau \cdot c^{da}(k) \quad (1)$$

The minimization is subject to constraints (2) and (4). The first constraint limit the charging power by cumulating the maximal possible charging power P_i^{max} of each individual EV i with:

$$P^{\text{fleet}}(k) \leq \sum_{i \in H_{\text{fleet}}} P_i^{\text{max}} \quad (2)$$

The state of energy SoE^{fleet} of the fleet depends on the aggregated battery capacity $E^{r,\text{fleet}}$, the charging power, the driving energy demand, and the number of EV users n as follows:

$$SoE^{\text{fleet}}(k) = \sum_{i \in H_{\text{fleet}}} \frac{SoE_i^{\text{ini}}}{n} + \sum_{k \in H_{ts}} \left(\frac{P^{\text{fleet}}(k) \cdot \tau}{E^{r,\text{fleet}}} \cdot \sum_{i \in H_{\text{fleet}}} \frac{\Gamma_i^{\text{ev}}(k)}{n} - \sum_{i \in H_{\text{fleet}}} \frac{E_i^{\text{d,ev}}(k)}{E_i^{\text{r,ev}}} \right) \quad (3)$$

The aggregated battery capacity is the accumulation of the battery capacities $E_i^{\text{r,ev}}$ of each individual EV i of the considered fleet. The constraint (4) is introduced to remain the state of energy SoE^{fleet} of the fleet between the minimal SoE^{min} and maximal SoE^{max} .

$$SoE^{\text{min}} \leq SoE^{\text{fleet}}(k) \leq SoE^{\text{max}} \quad (4)$$

Additionally, this constraint secures sufficient energy for driving within the fleet.

B. Individual EV Charging

Each EV i is initialized with the power and the state of energy schedule as shown in the sequences of Fig. 2 and calculated in Section III-A. The schedules are used as indirect control signals to coordinate the individual EV charging with the power $P^{\text{fleet}}(k)$ and state of energy $SoE^{\text{fleet}}(k)$ of the fleet at time step k . Considering a variable charging power P_i^{ev} , the state of energy SoE_i^{ev} for each individual EV i is then calculated by:

$$SoE_i^{\text{ev}}(k) = SoE_i^{\text{ini}} + \sum_{k \in H_{ts}} \left(\frac{P_i^{\text{ev}}(k) \cdot \tau}{E_{r,i}^{\text{ev}}} \cdot \Gamma_i(k) - \frac{E_{d,i,k}^{\text{ev}}}{E_{r,i}^{\text{ev}}} \right) \quad (5)$$

The adjustment of P_i^{ev} is calculated by the proportion of the state of energy SoE_i^{ev} of EV i at time step $k-1$, with the driving energy demand and the state of energy of the fleet by:

$$P_i^{\text{ev}}(k) = \frac{SoE^{\text{fleet}}(k)}{SoE_i^{\text{ev}}(k-1) - \frac{E_i^{\text{d,ev}}(k)}{E_{r,i}^{\text{ev}}}} \cdot \frac{P^{\text{fleet}}(k)}{n} \quad (6)$$

The determination of the charging power of each EV i at time step k is subject to the constraint (7) to limit the maximal charging power P^{max} .

$$P_i^{\text{ev}}(k) \leq P^{\text{max}} \quad (7)$$

The value of the maximal charging power depends on the charging infrastructure.

IV. STUDY CASES

In this Section, two different cases are studied. In the first case, the proposed day-ahead charging optimization and application approach is validated for different fleet sizes. The power and state of energy schedule (PsEop) of the optimization process are compared to the aggregated power and state of energy schedule (PsEap) of the application process. With the second case, the application of the PsEop for the individual EV charging process are explained.

A. Day-ahead charging operations for Different Fleet Sizes

For the day-ahead charging optimization and application as shown in the sequences of Fig. 2, the EVS/A uses the objective function (1) to minimize the total charging costs. The applied day-ahead price signal is shown in Fig. 4 and is taken from historical data of the European Energy Exchange. The objective function is subjected to the constraints (4) and (2). The maximal charging power is 3.7 kW. Further it is assumed that the initial SoE^{ini} and final state of energy SoE^{fin} are set to 0.8 pu, the minimum state of energy SoE^{min} is 0.1 pu and the maximum state of energy SoE^{max} is 1.0 pu.

For validation purpose, the day-ahead charging optimization and application is applied to a fleet with 50 and 1,000 EV users. The resulting charging schedules for the fleet with 50 EVs is shown in Fig. 5. It can be observed that the PsEop deviates from the PsEap. This is caused by the varying driving power demands as shown in Fig. 4. The observed driving power demand is less than the predicted. Consequently, the final state of energy of the optimization process is 0.9 pu and 0.1 pu higher as the final state of energy of the application process.

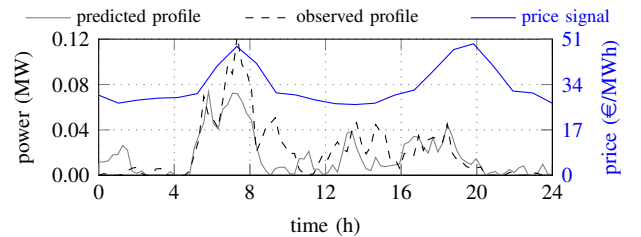


Fig. 4. Driving power demand of 50 EVs and day-ahead price signal.

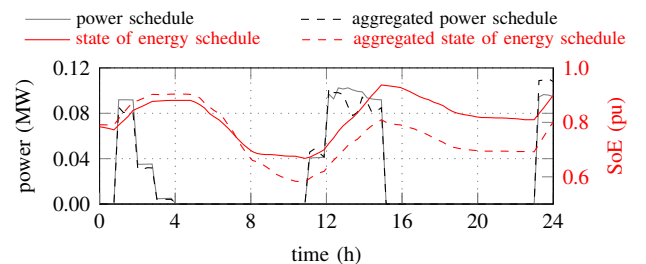


Fig. 5. Power and state of energy schedules for 50 EVs.

The variation of the PsEop to the PsEap can be reduced with increasing number of EV users. The power and state of energy schedules for the fleet with 1,000 EV users are shown in Fig. 7. Both, the PsEop as well as the PsEap indicate matching behaviors.

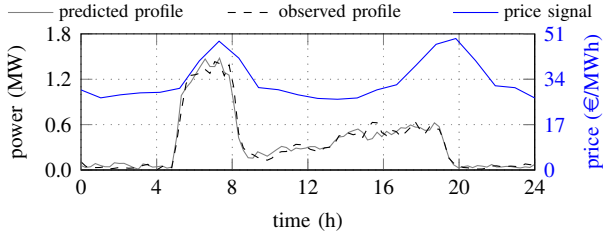


Fig. 6. Driving power demand of 1,000 EVs and day-ahead price signal.

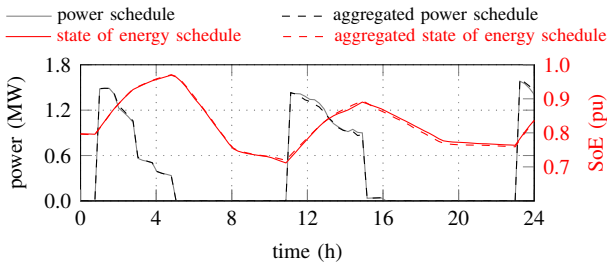


Fig. 7. Power and state of energy schedules for 1,000 EVs.

This is due to the more accurate prediction of the driving energy demand. With higher numbers of EV users the divergences of the driving power demands, as shown in Fig. 6 and evaluated in Section II-C, are mutually compensated. The simulation results indicate that the accuracy of the conducted day-ahead charging optimization and application can be improved with higher numbers of aggregated EV users within the fleet.

B. Analysis of the Individual EV charging

Once the EVS/A has obtained the power and state of energy schedule of the charging optimization process, the results are forwarded to procure the energy on the day-ahead market. The same schedules are used as indirect control signals for individual EV charging process. The charging power of connected EVs is proportionally determined as described in Section III-B. Fig. 8, Fig. 9 and Fig. 10 represent a selection of three EV users with different driving behaviors to show the effects caused by applying the proposed individual EV charging process. The grey areas indicate the time of con-

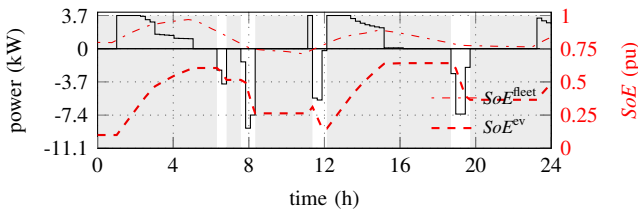


Fig. 8. Charging schedules of EV 1 with initial SoE of 0.1.

nection. Negative power values refer to the power demand for driving while positive values show the observed charging profile. As can be seen, the selected EVs have a different state

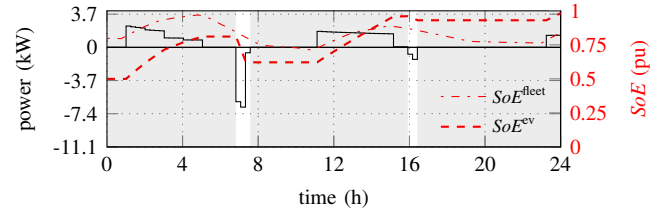


Fig. 9. Charging schedules of EV 2 with initial SoE of 0.5.

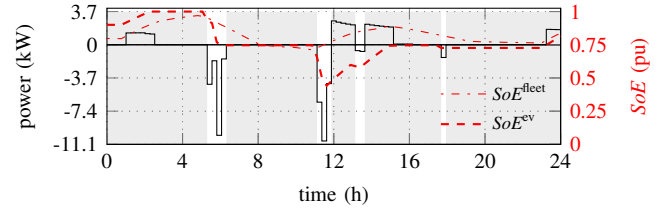


Fig. 10. Charging schedules of EV 3 with initial SoE of 0.9.

of energy conditions at the start of the individual charging process. This influences the individual charging power through the individual EV charging described by (6). For example, the SoE^{ev} of EV 1 is 0.1 pu at 0:00 h while the SoE^{fleet} of the EV fleet is 0.75 pu. This leads to a high proportion factor and the maximal charging power of 3.7 kW is utilized. In contrast, the proportional factor is decreasing when SoE^{ev} is equal or greater than SoE^{fleet} . An example for that is given in Fig. 9 and Fig. 10, respectively. The charging power and the charging activity are lowered, which is particularly shown by the charging profile of EV 3.

V. CONCLUSION

In this paper, a methodology was presented to realize optimized energy procurements for day-ahead charging operations of EV fleets without dictating the users driving behavior. An optimization for EV fleets for day-ahead operation was developed to take advantage of the predictive energy demand profiles and determine optimized charging schedules. Thanks to the developed individual EV charging process, the optimized charging schedules can be applied to coordinate the individual charging process. For further research, the approach can be combined with controllable loads, thermal storage systems and fluctuating renewable energy source to facilitate the large-scale integration of EVs and efficiently deal with market and power system integration.

REFERENCES

- [1] European Climate Foundation, "Roadmap 2050," *Policy*, no. April, pp. 1–9.
- [2] J. A. Peças Lopes, F. J. Soares, and P. M. R. Almeida, "Integration of Electric Vehicles in the Electric Power System," *Proceedings of the IEEE*, vol. 99, no. 1, pp. 168–183, 2011.
- [3] D. Papadaskalopoulos and G. Strbac, "Decentralized participation of electric vehicles in network-constrained market operation," in *Innovative Smart Grid Technologies (ISGT Europe), 2012 3rd IEEE PES International Conference and Exhibition on*, Oct 2012, pp. 1–8.
- [4] A. O'Connell, D. Flynn, and A. Keane, "Rolling Multi-Period Optimization to Control Electric Vehicle Charging in Distribution Networks," *Power Systems, IEEE Transactions on*, vol. 29, no. 1, pp. 340–348, Jan. 2014.
- [5] R. J. Bessa and M. A. Matos, "Economic and technical management of

an aggregation agent for electric vehicles: A literature survey,” *European Transactions on Electrical Power*, vol. 22, pp. 334–350, 2012.

- [6] J. Zhao, C. Wan, Z. Xu, and J. Wang, “Risk-based day-ahead scheduling of electric vehicle aggregator using information gap decision theory,” *IEEE Transactions on Smart Grid*, vol. 8, no. 4, pp. 1609–1618, July 2017.
- [7] J. Zheng, X. Wang, K. Men, C. Zhu, and S. Zhu, “Aggregation model-based optimization for electric vehicle charging strategy,” *IEEE Transactions on Smart Grid*, vol. 4, pp. 1058–1066, 2013.
- [8] Z. Liu, D. Wang, H. Jia, N. Djilali, and W. Zhang, “Aggregation and bidirectional charging power control of plug-in hybrid electric vehicles: Generation system adequacy analysis,” *Sustainable Energy, IEEE Transactions on*, vol. 6, no. 2, pp. 325–335, April 2015.
- [9] D. Koraki and K. Strunz, “Wind and solar power integration in electricity markets and distribution networks through service-centric virtual power plants,” vol. PP, pp. 1–1, 06 2017.
- [10] D. Koraki, J. Keukert, and K. Strunz, “Congestion management through coordination of distribution system operator and a virtual power plant,” in *2017 IEEE Manchester PowerTech*, June 2017, pp. 1–6.
- [11] T. Sousa, H. Morais, J. a. Soares, and Z. Vale, “Day-ahead resource scheduling in smart grids considering Vehicle-to-Grid and network constraints,” *Applied Energy, Journal on*, vol. 96, pp. 183–193, 2012.
- [12] R. Bessa and M. Matos, “Global against divided optimization for the participation of an EV aggregator in the day-ahead electricity market. Part II: Numerical analysis,” *Electric Power Systems Research, Journal on*, vol. 95, pp. 319–329, Feb. 2013.
- [13] I. Momber, A. Siddiqui, T. G. S. Román, and L. Söder, “Risk averse scheduling by a pev aggregator under uncertainty,” *IEEE Transactions on Power Systems*, vol. 30, no. 2, pp. 882–891, March 2015.
- [14] C. Shao, X. Wang, X. Wang, C. Du, and B. Wang, “Hierarchical charge control of large populations of evs,” *IEEE Transactions on Smart Grid*, vol. 7, no. 2, pp. 1147–1155, March 2016.
- [15] W. Wei, F. Liu, and S. Mei, “Charging strategies of ev aggregator under renewable generation and congestion: A normalized nash equilibrium approach,” *IEEE Transactions on Smart Grid*, vol. 7, no. 3, pp. 1630–1641, May 2016.
- [16] M. A. Ortega-Vazquez, F. Bouffard, and V. Silva, “Electric Vehicle Aggregator/System Operator Coordination for Charging Scheduling and Services Procurement,” *Power Systems, IEEE Transactions on*, vol. 28, no. 2, pp. 1806–1815, 2013.
- [17] F. Soares, J. A. Lopes, P. Almeida, C. Moreira, and L. Seca, “A stochastic model to simulate electric vehicles motion and quantify the energy required from the grid,” in *Power Systems Computation Conference (PSCC), Stockholm, Sweden*, 08 2011.
- [18] R. Follmer, B. Lenz, B. Jesske, and S. Quandt, “Mobilität in Deutschland 2008 Ergebnisbericht,” Deutsches Zentrum für Luft- und Raumfahrt e.V. Institut für Verkehrsforschung, Berlin, Tech. Rep.

BIOGRAPHIES

Flavio Gromann received his master in Industrial and Electrical Engineering at Technische Universität Berlin (TUB) Berlin, Germany. Currently, he is working at the TU Berlin, School of Electrical Engineering and Computer Science at the SENSE Chair. His main research topics are the grid integration of electric vehicles fleets by using aggregation concepts, optimization techniques and control algorithm. He also considers combined systems of thermal and electric units.

Andreas F. Raab received his diploma in Industrial Engineering and Management in 2010 from the Technische Universität Berlin (TUB), Germany. He is currently working there towards his Ph.D. degree at the faculty Electrical Engineering and Computer Science. His research interests are the integration of distributed and renewable energy sources in power systems, realizations of Microgrids and Virtual Power Plants with focus on power system impacts, interoperability and economic potentials to participate in energy markets.

Kai Strunz received the Dipl.-Ing. and Dr.-Ing. degrees (summa cum laude) from the Saarland University, Saarbrücken, Germany, in 1996 and 2001, respectively. He was with Brunel University, London, U.K., from 1995 to 1997. From 1997 to 2002, he was with the Division Recherche et Développement of Electricité de France, Paris, France. From 2002 to 2007, he was an Assistant Professor of electrical engineering with the University of Washington, Seattle, WA, USA. Since 2007, he has been Professor for SENSE at TU Berlin, Germany. Dr. Strunz was the Chairman of the Conference IEEE PES Innovative Smart Grid Technologies, TU Berlin, in 2012. He is a Chairman of the IEEE Power and Energy Society Subcommittee on Distributed Generation and Energy Storage and Vice Chairman of the Subcommittee on Research in Education. On behalf of the Intergovernmental Panel on Climate Change, he acted as a Review Editor for the Special Report on Renewable Energy Sources and Climate Change Mitigation.

Evaluation of Data Preprocessing Techniques for Battery Management Systems

Nuttapong Sansuk¹, Dominik Jöst², Nisai H. Fuengwarodsakul¹, Dirk Uwe Sauer²

¹King Mongkut's University of Technology North Bangkok, The Sirindhorn International Thai-German Graduate School of Engineering, Department of Electrical Power Engineering, 10800 Bangkok, Thailand

²RWTH Aachen University, Chair for Electrochemical Energy Conversion and Storage Systems, Institute for Power Electronics and Electrical Drives (ISEA), D-52056 Aachen, Germany

Abstract—The Battery Management System (BMS) is employed to assure the safety of electric vehicles equipped with a lithium-ion battery storage. As almost every modern system employs sophisticated algorithms determining battery state and accomplishing control strategy, the development of data processing techniques inside such a complex BMS is a big opportunity and challenge for engineers.

As the data quality is important for battery diagnostics, this study aims to implement and evaluate the proposed data preprocessing technique focusing on data cleaning and fault detection. The simulation outcomes testify improvement of data in term of precision and reliability after being processed by the data preprocessing strategy.

Keywords—battery; electric vehicle; outlier detection; data preprocessing; noisy sensors; Bayesian theory; battery management system

I. INTRODUCTION

The battery system is considered as one of the most important parts in Electric vehicles (EVs), which have been widely become a profound breakthrough tackling against problems concerning environmental pollution and energy deficiency [1]. On account of high energy and power density, fast reaction time, low self-discharge rate and high cycle and calendar lifetime, lithium-ion batteries (LIBs) have recently been the most preferable alternative for EVs [2]. However, a great number of researchers are still targeting to increase both energy density and lifetime of LIBs for automotive industries. Hence modern BMS systems have been developed into greater complexity and increasing integration of estimation algorithms [3].

As all techniques require reliable data in terms of voltage, temperature and current to achieve their estimation accuracy per se, the measured data from sensors nevertheless contain noises. Many researchers put effort into this issue by trying to get rid of the estimation error. Particularly for State-of-Charge (SoC) estimation which is an essential information for a battery pack. The Open-Circuit Voltage (OCV) based estimation is efficiently used for LIBs in Electrical Vehicles (EVs). Moreover, the algorithm yields a highly accurate estimation when the prediction of the battery “pure” OCV, without all overvoltages, is applied. Nonetheless, the optimal result is difficult to derive

due to sensor noises and quantization of the measured battery voltage in practical battery systems [4]. Therefore, it’s worth proposing a new approach to diminish the error caused by the noises occurring in battery systems.

This study introduces a data preprocessing technique to improve the data quality including noise reduction and fault detection. In data centric view, noises and faults can be interpreted as outliers with different level of abnormalities. Accordingly, the true value of corrupt data can be estimated by detecting those outliers. Outlier detection techniques had been earlier employed in several researches regarding to battery systems such as cell-balancing, charging demand prediction and fault diagnosis using either distance- or density-based techniques, which are sufficient only for low-dimensional data [5] - [7]. A high dimensional approach based on angular distribution (ABOD) also provenly provided an accurate State-of-Health (SoH) estimation [8]. Plus, its computational complexity has been shown and revised [9].

As a consequence, the high-dimensional data outlier detection based on angular distribution is utilized as the basis of the proposed data preprocessing strategy. Detecting divorced data points is not exclusively used for fault risk detection, it can also be used to reduce the impact of noises in the data stream by identifying impure elements and applying an uncertainty-reducing approach (e.g., Bayes’s theorem) before passing on to diagnostic algorithms.

The purpose of this study is to implement and integrate the data processing technique in a diagnostic system of a developed battery system in MATLAB/Simulink platform. Its performance and evidence of improvement in data quality are shown in the simulation results.

II. OUTLIER DETECTION

A battery system is prone to generate some odd data points caused by the measurement noise. Not only more precise diagnostic estimation but also better fault detection can be achieved if the anomalies can be detected.

Some relevant definitions of the outlier detection’s parameters are presented in this section. Furthermore, the application of the ABOD concept to find the abnormality is described.

The outlier detection algorithms are mainly divided into statistics-based, depth-based, distance-based, density-based and high-dimensional approaches [10]. All outlier algorithms aforementioned beside the high-dimensional approach are inadequate for high-dimensional data [8], [9]. Thus, the high-dimensional data outlier detection algorithm is adopted in this article in order to accomplish more efficient outlier detection in massive data stream.

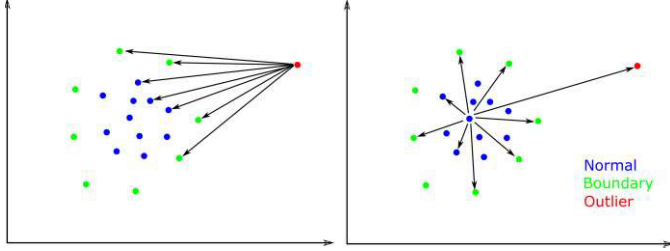


Fig. 1 Two-dimensional data set distribution

As demonstrated in Fig. 1, the angle distributions among vectors from the center point and isolated point to the other points of data set are apparently different. Considering a point inside of the data set, the angle fluctuation variously spreads following the directions to other points. In contrast, the angles from an outlying point to other different points are slightly different from another. Thereby, its fluctuation is relatively small. Accordingly, it could be concluded that the smaller the variance of angle distribution is, the more potential the point has to be an outlier [9].

The variance of angles (VOA) is used as an outlier factor in order to evaluate the stage of abnormality for each point in the data set, as follows: [11].

Definition 1, given a point set $S \subseteq R^d$, $|S| = n$ and a point $p \in S$. For a random pair of different points $a, b \in S \setminus \{p\}$, let Θ_{apb} denote the angle between the different vectors $a - p$ and $b - p$. The angle-based outlier factor $VOA(p)$ is the variance of Θ_{apb}

$$VOA(p) = Var[\Theta_{apb}] = MOA_2 - (MOA_1(p))^2 \quad (1)$$

where MOA_2 and MOA_1 are defined as follows:

$$MOA_1(p) = \frac{\sum_{a,b \in S \setminus \{p\}} \Theta_{apb}}{(\frac{1}{2})(n-1)(n-2)} \quad (2)$$

$$MOA_2(p) = \frac{\sum_{a,b \in S \setminus \{p\}} \Theta_{apb}^2}{(\frac{1}{2})(n-1)(n-2)} \quad (3)$$

Now that the variance of angle distribution and the degree of anomaly for each points of data set can be identified, the data set

can be segregated into fair, tainted with noises and massively uncommon which is considered likely to be a fault.

III. DATA CLEANING

Recovering correct values of the corrupt data is difficult on account of unpredictable white noise in measurement. Nevertheless, the effect of noises can be reduced if the true reading can be estimated and the characteristics of noises can be derived. As shown in Fig. 2, three inputs of the cleaning module are the noisy observations, the noise expression, the distribution of the true reading [12].

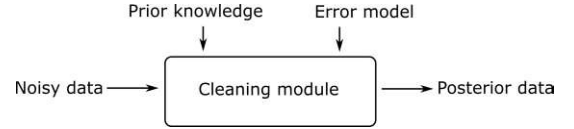


Fig. 2 Data cleaning framework

The prior knowledge represents a distribution of the true sensor reading. In this study, the characteristics of normal data set after being preprocessed is used. Whereas, the distribution of whole data set is used as the error model variance with zero mean.

The uncertainty-reducing approach is performed by applying Bayes's theorem for an observed value o . The Gaussian distribution of random error has zero mean and a known standard deviation $\sim N(0, \delta^2)$. The true value t is normally distributed as $p(o|t) \sim N(\mu_s, \sigma_s^2)$. A more accurate uncertainty model can be derived by adopting the Bayes's theorem as follows:

$$p(t|o) = \frac{p(o|t)p(t)}{p(o)} \quad (3)$$

The posterior distribution also follows a Gaussian distribution as $p(t|o) \sim N(\mu_t, \sigma_t^2)$ which can be computed from the equations below

$$\mu_t = \frac{\delta^2}{\sigma_s^2 + \delta^2} \mu_s + \frac{\sigma_s^2}{\sigma_s^2 + \delta^2} o \quad (4)$$

$$\sigma_t^2 = \frac{\sigma_s^2 \delta^2}{\sigma_s^2 + \delta^2} \quad (5)$$

As clean data must be an exact single value, the expectation value is used as the approach to find the most decent output of the probability distribution as $E(t) = \int_{-\infty}^{\infty} tp_s(t)dt$ [12].

IV. DATA PREPROCESSING ALGORITHM

The fundamental concept of the data preprocessing strategy introduced in this article could be outlined as follows:

- i. The developed data preprocessing technique is merged with the diagnostic estimation algorithm in the master system to classify the incoming data points as normal,

tainted or unusual points in order to detect faults and reduce the estimation error due to sensor noises.

- ii. The considered battery system including a battery string, slave and master module is employed for the simulation in MATLAB/Simulink platform.
- iii. All data sets are continuously preprocessed with a class index for every data points. The corrupt data points are detected and cleaned by the bayesian approach to weaken the effect of sensor noises before being used in the diagnostic process. Additionally, a boolean parameter is created and used as the indicator of fault risk if any outlier is detected.

The description and flow chart of the preprocessing algorithm are given in the next section for a better understanding of the detailed processes.

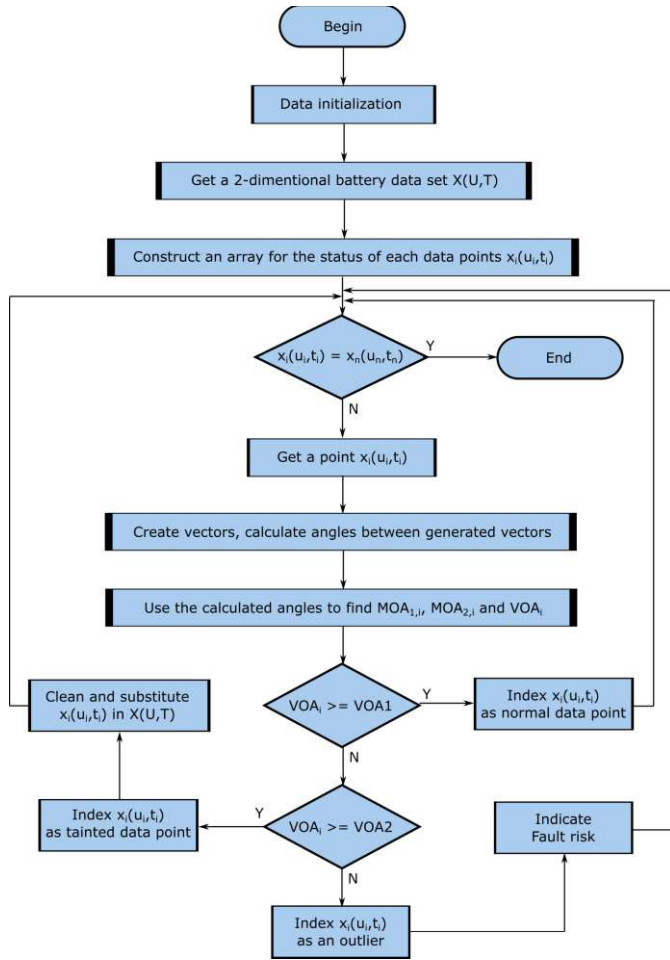


Fig. 3 Flow diagram of data preprocessing

As demonstrated in Fig. 3, the algorithm processes are described as follows:

Input: The multi-dimensional battery data set including cell voltages and temperatures $X(U,T)$.

Output: Clean data set $X'(U',T')$, data class set, enable flag

- i. The incoming data set $X(U,T)$ with its elements is obtained.
- ii. A data set array is created with the length according to the number of battery cells (n) in order to store the grade index of each data points.
- iii. Choose an element in the data set $x_i(u_i,t_i)$.
- iv. By constructing vectors between the selected element to other data points in multi-dimensional plane, the angles between each vectors can be calculated.
- v. Using the calculated angles to find VOA of the selected data point by adopting the formulas (1), (2) and (3).
- vi. Applying the pre-set thresholds VOA1 and VOA2 to determine the grade index of $x_i(u_i,t_i)$ and store it in the data class array.
- vii. After being classified, the action will be taken unless the data point is normal. If the data is categorized as corrupted, the data element will be substituted to the previous value $x_i(u_i,t_i)$ in its set $X(U,T)$ by expectation value of the posterior clean data. On the other hand, if the data is considered as an outlier, the enable flag will be set to indicate the fault risk.
- viii. Get a new element $x_{i+1}(u_{i+1},t_{i+1})$ and repeat step iv. to vii. until the processed data reach the last element of data set $x_n(u_n,t_n)$

V. BATTERY SYSTEM AND SIMULATION MODEL

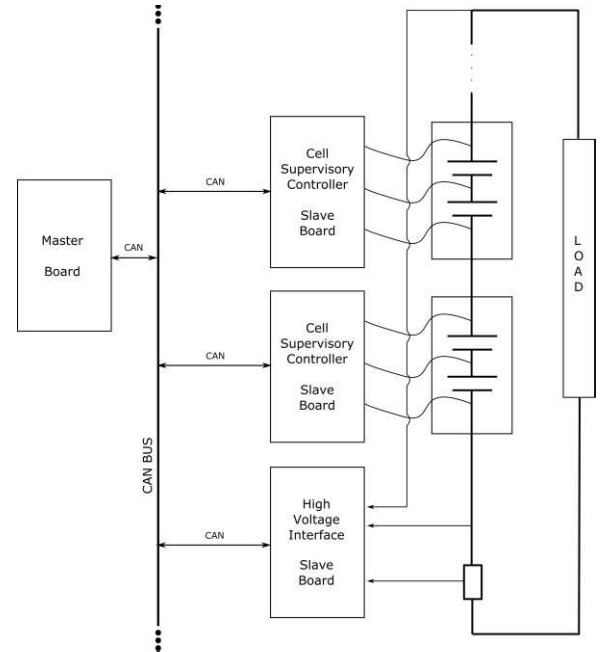


Fig. 4 Simple distributed master-slave BMS module

Since safety and reliability play the major roles in the development of BMS design, the distributed modular master-slave architecture has been widely used. Its structure is highly flexible and reliable [13].

As shown in Fig. 4, the BMS system consists of a master module and slave modules. Cell voltages and temperatures are sensed through the Cell Supervisory Controller, whereas pack current and voltage are taken from the High Voltage Interface.

All the data is transmitted to the master system via a CAN bus which is a commonly used communication protocol in industry and vehicle systems.

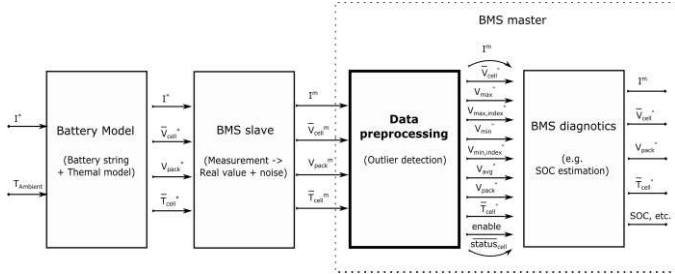


Fig. 5 Diagram of the battery system model

The simulation design is based on the concept illustrated in Fig. 5. The scheme mainly includes a battery model, a BMS master module and its slave modules, as the major focus goes toward the improvement of data processing in the master system.

A. Battery Model

At the first stage, the battery model is designed as a simple 12-cell Li-ion battery string illustrated in Fig. 6. The battery cells are formed based on the simplified impedance model by Buller utilizing ISEA battery framework [14]. Each of the elements in the battery string contains an Open-Circuit Voltage source (U_{oc}), an inductance (L), an ohmic resistance (R_i), a ZARC element (Z_{zarc}), a Warburg impedance (Z_w) and a parallel RC, representing charge transfer resistance (R_{ct}) and double layer capacitance (C_{dl}). The output quantities of the model are cell voltage and temperature (u_i, t_i) where the input requirements are current ($I_{\text{charge/discharge}}$) and ambient temperature (T_{ambient}).

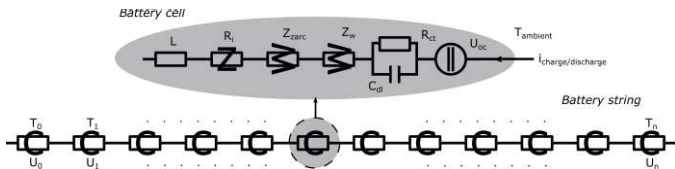


Fig. 6 Battery string module

B. BMS Slave

Considering the actual BMS system, the data from measurement modules must be converted from analog to digital. Therefore, the Analog to Digital Converter (ADC) is modeled in every slave module. Moreover, white noise and outlier fault are also generated in the ADC models to represent actual behaviors of the real measurement.

C. BMS Master

To obtain diagnostic values such as SoC, SoH, Open-Circuit Voltage, Capacity, Impedance, Resistance, etc., all algorithms must be individually applied in the master system. Apart from the diagnostic algorithms, the data quality is significantly concerned as well in this study. Consequently, the main sections

designed in the master model are data preprocessing and diagnostics.

- Data preprocessing

After having been transmitted to the master board through a CAN channel, the data from the slave board is at first refined in the preprocessing section by applying the strategy proposed in this research. Not only the clean data, but also the classes of each data points, whether they are normal, tainted or unusual, are provided by the data preprocessing.

- BMS diagnostics

Calculation or estimation of parameters, such as battery SoC, SoH, Capacity, Resistance and Impedance, are executed using the measured data. With the better data quality, these estimations are benefited from the data preprocessing. As a results, the state of battery pack can be accurately determined.

VI. SYSTEM ASSUMPTIONS AND SIMULATION RESULTS

TABLE I. MODEL PARAMETERS OF LIBS (25°C T_{AMBIENT})

Parameter	Value
C_{max}	12.9282 to 13.1119 Ah
T_{initial}	24.9781 to 25.0141 °C
$\text{SOC}_{\text{initial}}$	49.9064 to 50.0766 %

In this section, the simulation verification is presented to show the performance of proposed data preprocessing strategy. Firstly, the simulation model initiation and assumptions are stated. Secondly, the outlier detection and correction technique is simulated to verify noise reduction and fault detection.

A. Battery Model set-up

The 12-cell KOKAM battery string, with individual 13 Ah cells, is modeled to be employed in a simulation framework developed by ISEA. The battery framework has a capability to perform coupled electrical-thermal simulations of storage systems in real time [15]. The elements in the equivalent circuit model vary following their SOC and thermal state. OCV curves of the battery cells are almost identical for different ambient temperatures between the SOC range of 0-100%. The range of initial parameters of battery cells are listed in TABLE I.

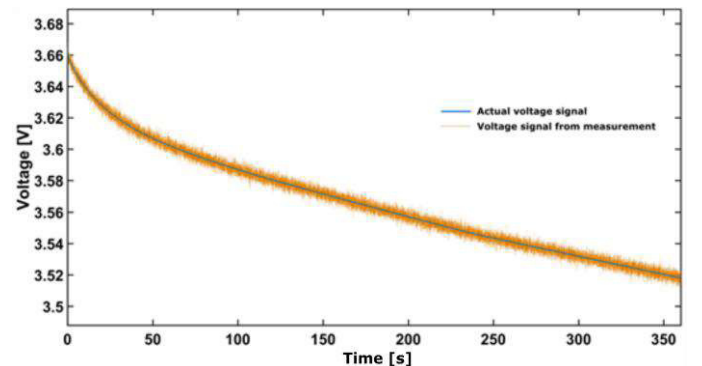


Fig. 7 Actual and measured voltage signal of a battery cell and noise generated from simulation ($\sigma_v = 2.5$ mV)

B. Data preprocessing simulation

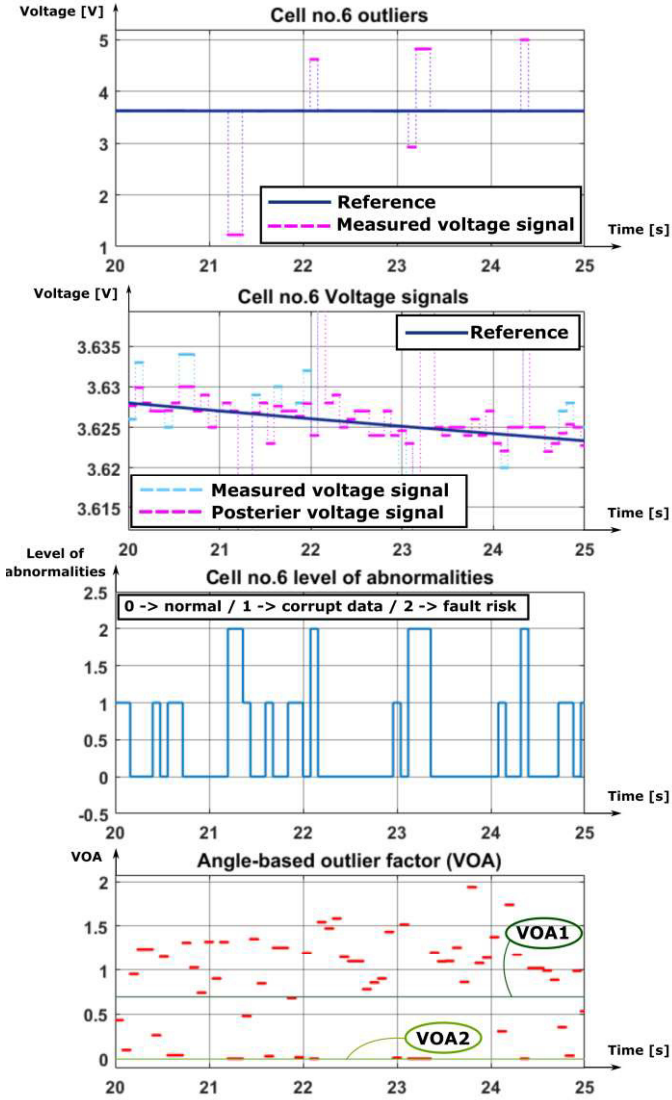


Fig. 8 Results of the data preprocessing under noise and outliers generated from the simulation ($\sigma_V = 2.5 \text{ mV}$) and preset outlier factors ($\text{VOA1} = 0.7$, $\text{VOA2} = 0.01$)

The test scenario is done by applying a constant discharging current of 20 A for 360 seconds. As a result, the final SOC range of the cells in battery pack is reduced to 34.436 to 34.7728% from the initial values. White noises are generated in the measurement module with standard deviation $\sigma_V, \sigma_I = 2.5 \text{ mV}$ or all current and cell voltages sensors. Besides, an ADC model with 1 mV quantization step is also added to each sensor. With the sensor and quantization noise feature, output voltage signals of the slave module are noisy as shown in Fig. 7. The difference between the maximum and minimum actual voltage among the battery cells is 3.516 mV. While, the bandwidth of noises generated in the simulation can be calculated as $2.355\sigma_V = 5.888 \text{ mV}$ which is more than the range of actual voltage among battery cells. Accordingly, the aforementioned figures imply a good illustration of the cheap sensor network which is the main assumption in the test case.

The results in Fig. 8 demonstrate the verification of the data preprocessing technique. Additional outliers from a cell in the battery pack are detected and indicated as fault risk owing to their profoundly small angle distribution with the calculated VOA less than VOA2 which is set to 0.01 in this test scenario. On the other hand, the data points with the VOA more than the abnormality threshold, $\text{VOA1} = 0.7$, are defined to be normal. Whereas, the noise-contaminated data, with the VOA between VOA1 and VOA2 , is cleaned by the algorithm so that the inaccuracy of data is reduced. The posterior signal is clearly seen to yield the higher accuracy than the original signal comparing to the reference. The high improvement is evident especially at high noise-contamination

VII. CONCLUSION

A data preprocessing strategy for BMS is introduced in this paper. By adopting an outlier detection algorithm based on angle distribution, the data quality for diagnostic algorithms can be improved, as the effect of sensor noises in the measurement is greatly reduced. Furthermore, the random outliers can be detected and notified the risk of faults in the battery system.

For future work, the uncertainty-reducing algorithm will be improved by deriving a more precise prior knowledge. In addition, the influence of data preprocessing on diagnostic algorithms shall be investigated.

REFERENCES

- [1] J. B. Zhang, L. G. Lu, and Z. Li. "Key technologies and fundamental academic issues for traction battery systems," *Journal of Automotive Safety and Energy*, vol. 2, no. 003, 2012.
- [2] B. Scrosati and J. Garche, "Lithium batteries: Status, prospects and future," *J. Power Sources*, vol. 195, no. 9, pp. 2419–2430, May 2010.
- [3] J. Timmermans, A. Nikolian, J. De Hoog, R. Gopalakrishnan, S. Goutam, N. Omar, T. Coosemans, J. Van Mierlo, A. Warnecke, D. U. Sauer, M. Swierczynski, D. Stroe, E. Martinez-Laserna, E. Sarasketa-Zabala, J. Gastelurrutia, and N. Nieto, "Batteries 2020 – Lithium-ion battery first and second life ageing, validated battery models, lifetime modelling and ageing assessment of thermal parameters,".
- [4] W. Waag, "Adaptive algorithms for monitoring of lithium-ion batteries in electric vehicles," Ph.D dissertation, RWTH Aachen University, Aachen, 2014.
- [5] C. Piao, Z. Wang, J. Cao, W. Zhang, and S. Lu, "Lithium-Ion Battery Cell-Balancing Algorithm for Battery Management System Based on Real-Time Outlier Detection," *Mathematical Problems in Engineering*, 2015.
- [6] M. B. Arias and S. Bae, "Electric vehicle charging demand forecasting model based on big data technologies," *Appl. Energy*, vol. 183, pp. 327–339, Dec. 2016.
- [7] Y. Zhao, P. Liu, Z. Wang, L. Zhang, and J. Hong, "Fault and defect diagnosis of battery for electric vehicles based on big data analysis methods," *Appl. Energy*, vol. 207, pp. 354–362, Dec. 2017.
- [8] C. Piao, Z. Hu, L. Su, and J. Zhao, "A Novel Battery State of Health Estimation Method Based on Outlier Detection Algorithm," *Journal of Electrical Engineering & Technology*, vol. 11, no. 6, pp. 1802–1811, 2016.
- [9] C. Piao, Z. Huang, L. Su, and S. Lu, "Research on Outlier Detection Algorithm for Evaluation of Battery System Safety," *Adv. Mech. Eng.*, vol. 6, p. 830402, Jan. 2014.
- [10] H. P. Kriegl, P. Kröger, and A. Zimek, "Outlier detection techniques," *Tutorial at KDD*, vol. 10, 2010.
- [11] N. Pham and R. Pagh, "A Near-linear Time Approximation Algorithm for Angle-based Outlier Detection in High-dimensional Data," *in*

Proceedings of the 18th ACM SIGKDD International Conference on Knowledge Discovery and Data Mining, pp. 877–885, 2012.

- [12] E. Elnahrawy and B. Nath, “Cleaning and Querying Noisy Sensors,” in *Proceedings of the International Workshop on Wireless Sensor Networks and Applications (WSNA)*, 2003.
- [13] H. L. Zhu, Z. B. Wu, D. L. Wang, and J. Y. Sun, “Design and Implementation of Distributed Battery Management System,” *Adv. Mater. Res.*, vol. 608–609, pp. 1039–1042, 2013.
- [14] S. Buller, “Impedance based simulation models for energy storage devices in advanced automotive power systems,” Ph.D dissertation, RWTH Aachen University, Aachen, 2002.
- [15] F. Hust *et al.*, ‘ISEA-Framework’, 2017. [Online]. Available: <https://github.com/FHust/ISEAFramework>. [Accessed: 13- Apr- 2018].

Consideration of Maintenance Aspect for Conversion of Transposed AC Lines to Hybrid AC/DC Lines

Pavel Tikhonov, Alexander Novitskiy, Dirk Westermann

Department of Power Systems
Technische Universität Ilmenau
Ilmenau, Germany

Abstract—One of the possibilities to increase the transfer capacity of a EHV AC double-circuit overhead line is to convert the AC transmission line to hybrid AC/DC line. In this case one circuit remains EHV AC line and other circuit will be operated as HVDC line. Long distance AC transmission lines are usually transposed. HVDC lines do not require a transposition, but in case of a hybrid AC/DC line the DC power circuit is affected by the transposed AC power circuit. The AC line transposition reduces AC currents induced in the DC power circuit, but can cause the increase of induced line-to-ground voltages in the DC power circuit switched off and grounded for the maintenance. It can cause the violation of the permissible values of the touch voltages. The influence of conventional transposition schemas on the touch voltages is considered in the paper.

Keywords— HVDC transmission; electromagnetic coupling; transmission lines; touch voltage; maintenance

I. INTRODUCTION

The use of HVDC technique for the power transmission becomes more and more popular in last years. One of the options is the conversion of existing AC lines to DC operation [1]. Double- or multi-circuit overhead transmission lines can be converted to hybrid AC/DC power lines containing AC and DC power circuit on the same tower [2] – [5]. In this case AC and DC power circuits can be operated independently of each other.

Long distance AC transmission lines are usually transposed. HVDC lines do not require a transposition, but in case of a hybrid AC/DC line the DC power circuit is affected by the transposed AC power circuit. The AC line transposition reduces AC currents induced in the DC power circuit, but can cause the increase of induced line-to-ground voltages in the DC power circuit switched off and grounded for the maintenance.

The increase of the induced voltages in the switched off and grounded AC line near to the transposition towers of the influencing line was shown in [6, 7] for parallel HVAC transmission lines located close to each other in the right-of-way.

The case of a multi-circuit hybrid AC/DC transmission line was studied in [8]. In [8] was noted that the maximal values of the induced voltages caused by transposed AC

influencing line can be significantly higher than the maximal values of the induced voltages caused by non-transposed influencing line.

It can cause the violation of the permissible values of the touch voltages during the maintenance of the switched off and grounded power circuit of the hybrid AC/DC transmission line and therefore can be dangerous for the working person.

A transposed double-circuit EHV AC power line which can be converted to a hybrid AC/DC transmission line is considered below. The goal of the paper is to analyze the influence of different transposition schemas of the transposed double-circuit transmission line on the touch voltages induced in the switched off and grounded power circuit.

II. METHODOLOGY OF THE STUDY

The pylon of the double-circuit AC overhead power line which can be converted to a hybrid AC/DC transmission line is shown schematically in Fig. 1. The power circuits I and II can be operated independently of each other.

Fig. 2 illustrates the case of the maintenance of one power circuit. The power circuit II is switched off and grounded at both ends, the working person is protected by an additional protective grounding PG, the power circuit I remains in operation. The power is transferred from station A to station B.

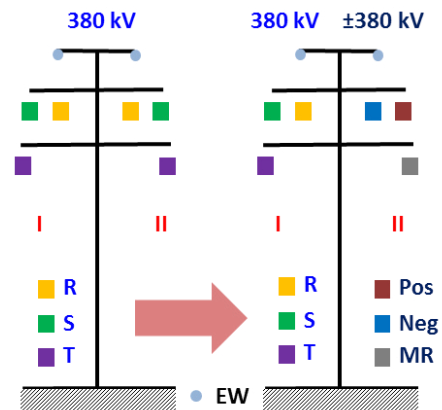


Fig. 1. Conversion of double-circuit AC line to hybrid AC/DC line (R, S, T – AC phase conductors, Pos., Neg. – DC positive and negative conductors, MR – metallic return conductor, EW – earth wires)

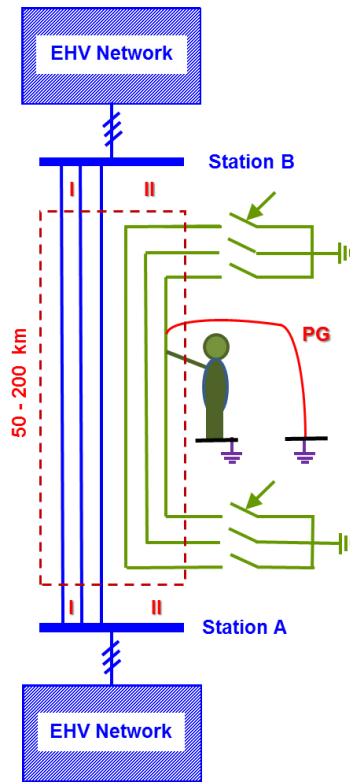


Fig. 2. Touching the wire by the working person in the presence of the protective grounding (PG)

The analysis of the influence of transposition schemas of the transmission line on the touch voltages induced in the switched off and grounded power circuit was carried out using MATLAB / Simulink software package. The mathematical model was created and the working conditions of the person were simulated. The position of the working place was sequentially moved from one line end to other.

Fig. 3 shows the simulation of the touching the wire by the maintenance person in the MATLAB / Simulink model.

It must be noted that the protective grounding is not always physically earthed directly at the working place. In case of so-called "bracket" or "bracketed grounding" grounds are installed within a section or two from the work site (for example, at the next pole or tower), allowing workers to be "working between grounds" or "bracketed by grounds" [9, 10]. The protective grounding earthed at a distance from the working person is shown in Fig. 3.

The double-circuit overhead line (OHL) was simulated as a multi-wire transmission line taking into account the line and conductor geometry, the electromagnetic coupling between conductors, skin effect in the wires and the ground return. The line lengths of 50 km and 200 km were simulated. The line was modelled as a row of sequential connected segments (OHL_i , OHL_{i+1} , etc.). Each segment contains one or several spans. Pylon ground impedances were represented as equivalent resistances R_{earth} for each modelled segment as it is shown in Fig. 3. Touch voltage U_{touch} was measured using voltmeter connected parallel to the worker's equivalent resistance R_{worker} .

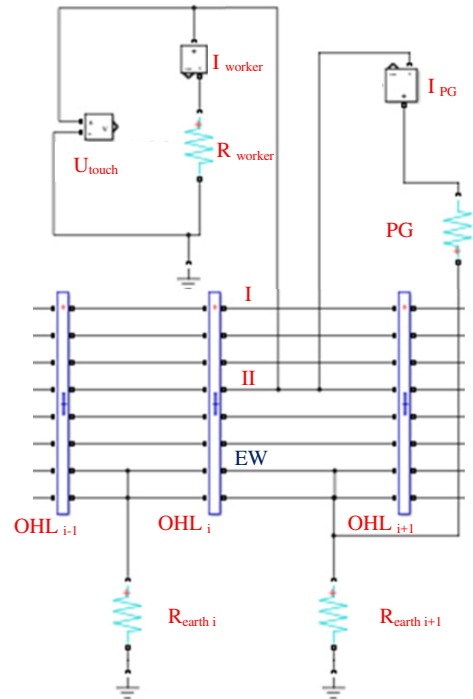


Fig. 3. Simulation of the touching the wire by the working person in the MATLAB / Simulink model. Circuit II is under maintenance.

The least possible amount of the segments was simulated: segments near the substations and segments between the transposition towers. The circuit representing the touching the wire by the working person was connected between the segments. In order to set the position of measurement across the power line, the parameters of the segments such as the length and equivalent resistance of the segment were changing step by step. The main difficulty of this simulation is the strong dependence between the topology of the model and the results of the measurement. In particular, the blocks of pylon's impedances can be placed on the right or on the left side of the line's segment. These two variants lead to different results of the measurement of touch voltages etc. In order to avoid such a difference, two opposite situations (variants A and B) were simulated. They are shown in Fig. 4. Touch voltage at each simulated working place was determined as the mean value of the measurement results for both variants of the simulation.

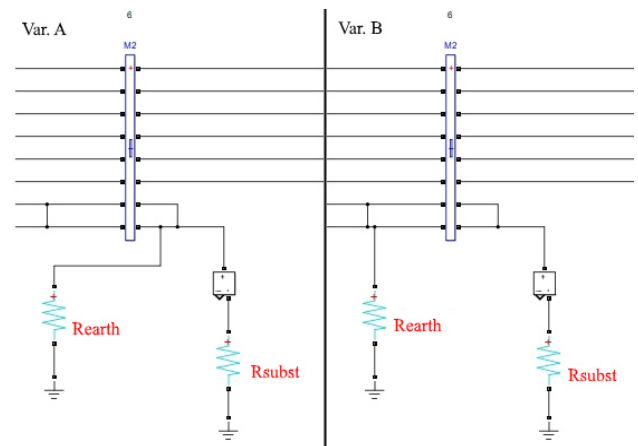


Fig. 4. Two variants of the model's geometry (R_{subst} - substation earthing)

The equivalent resistance of a working person was assumed $R_{\text{worker}} = 1000 \text{ Ohm}$ and was implemented in the model as it is shown in Fig. 3.

The continuous line currents of 1800 A and 3600 A (maximal permissible continuous current value for the simulated conductor bundle) were simulated in the circuit I under normal operation conditions. The touch voltages were measured in the switched off and grounded circuit II.

III. INVESTIGATION RESULTS

Simulation results for the cases of non-transposed circuits and the influencing line currents of 1800 A and 3600 A are presented in Fig. 5 and 6. The lengths of the power line of 50 km and 200 km were considered in the simulations.

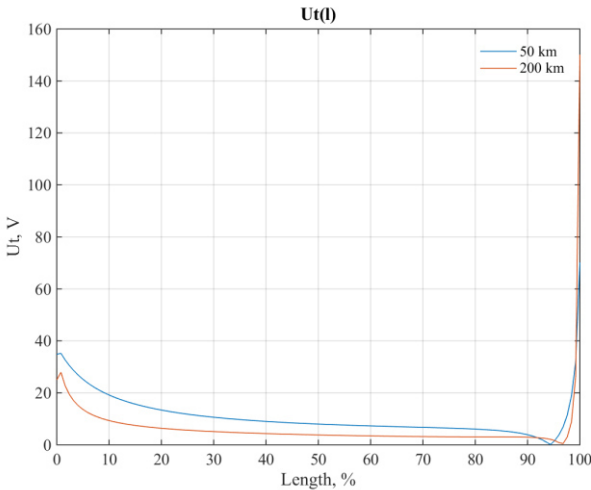


Fig. 5. Touch voltage in the switched off and grounded circuit II. Both circuits are non-transposed. The lengths of the line are 50 km and 200 km. Continuous line current 1800 A.

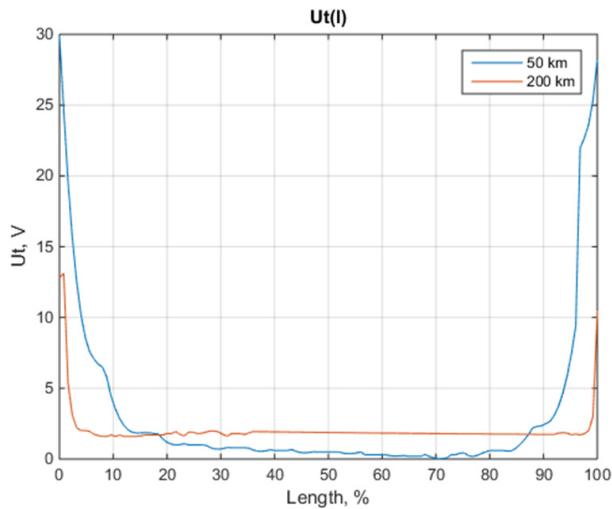


Fig. 6. Touch voltage in the switched off and grounded circuit II. Both circuits are non-transposed. The lengths of the line are 50 km and 200 km. Continuous line current 3600 A.

In addition to normal operating conditions of the power transfer from station A to station B, a situation of a no-load line operation under the full operating voltage was also simulated. The influencing power line was switched off at the receiving end. The simulations were carried out for the cases of transposed and non-transposed lines. The results of the touch voltage measurements for one case of the transposition are presented in Fig. 7 as an example.

From Fig. 5 can be seen that the touch voltage in the switched off and grounded circuit II of non-transposed double-circuit line does not exceed the value 30 V in case of the line operation under the continuous current of 1800 A. Taking into account the permissible touch voltage values in Germany of 50 V AC [13] it can be concluded that the maintenance of the switched off and grounded circuit of non-transposed double-circuit overhead line in the presented case of 1800 A can be carry out without additional constraints. Fig. 6 shows, that if the value of the line current is 3600 A, the values of the touch voltage can exceed the permissible value of 50 V near to the receiving end of the line. In that case it is necessary to use additional constraints during the work.

From Fig. 7 can be seen, that the values of the touch voltages of no-load operating state of the power line are significantly less than 50 V and don't consist any danger for the working personal in both considered cases of 50 and 200 km power line length. However it can be seen, that the values of the touch voltages in that case have an increase on the both ends of the power line.

Fig. 8 – 15 represent different cases of line transposition schemas taken into consideration according to [11, 12].

Fig. 8 – 11 characterize the cases with the line current of 1800 A, Fig. 12 – 15 characterize the case of 3600 A.

Fig. 10, 11, 14, 15 characterize the same schema of double-circuit line transposition, but different positions of the line under maintenance (circuit II is switched off and grounded).

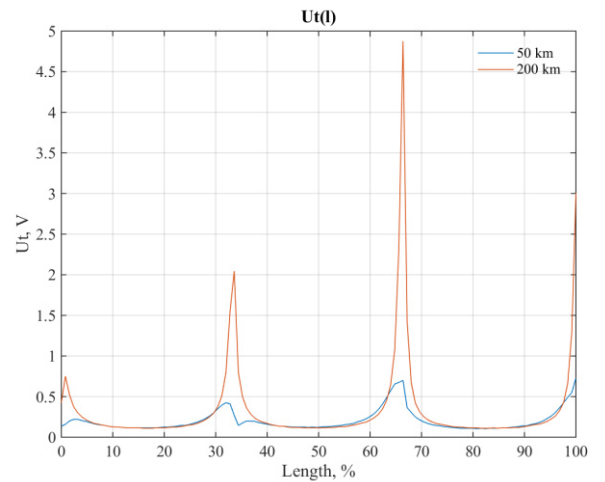


Fig. 7. Touch voltage in the no-load simulation. Both circuits are transposed corresponding to the variant 1 (see Fig. 8a)). Circuit I switched off at the receiving end. The lengths of the line are 50 km and 200 km.

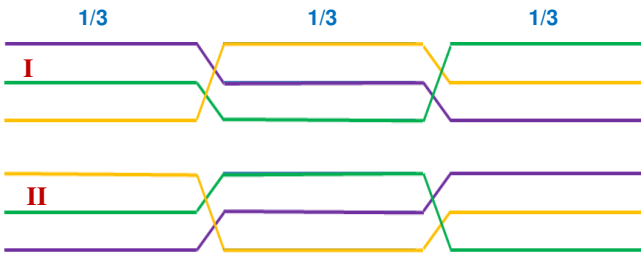


Fig. 8 a). Double-circuit line transposition, Variant 1

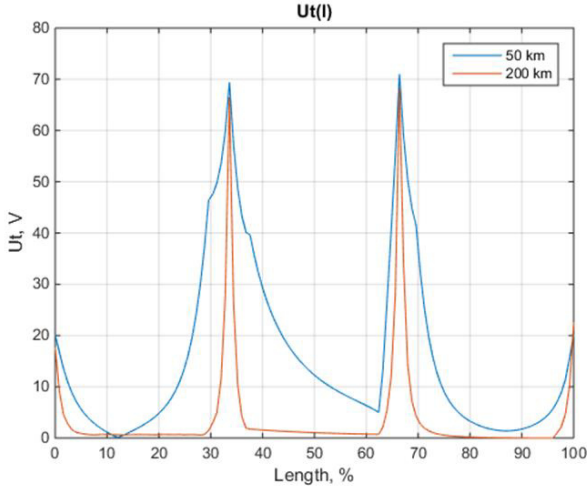


Fig. 8 b). Touch voltage in the circuit II, circuit I is in operation, continuous line current 1800 A, Variant 1

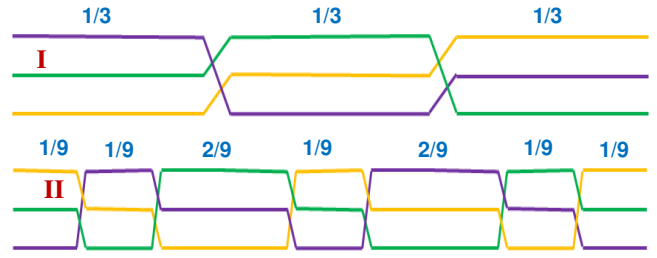


Fig. 10 a). Double-circuit line transposition, Variant 3

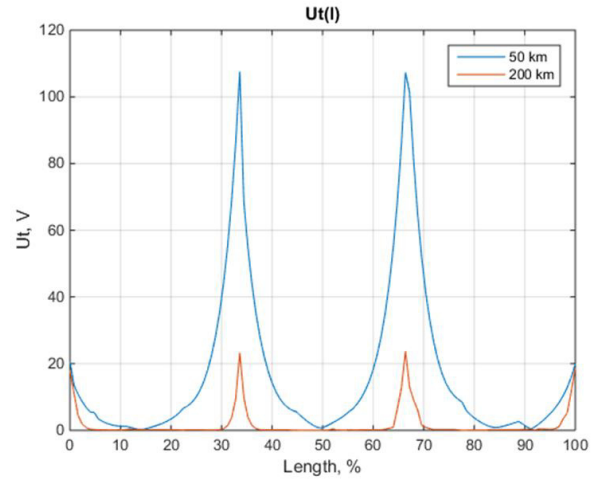


Fig. 10 b). Touch voltage in the circuit II, circuit I is in operation, continuous line current 1800 A, Variant 3

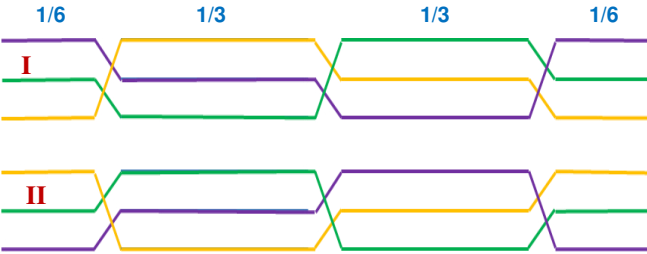


Fig. 9 a). Double-circuit line transposition, Variant 2

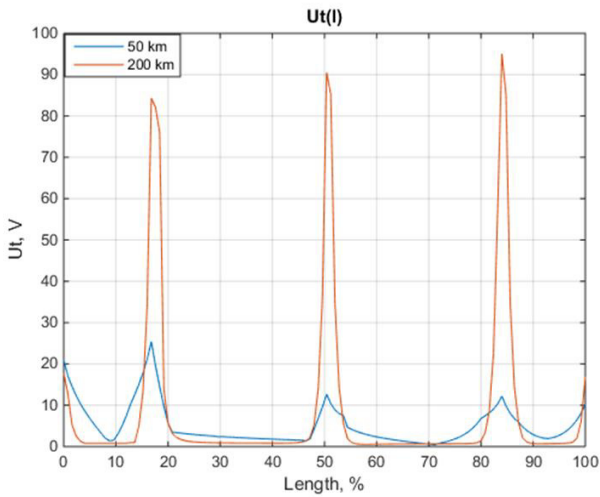


Fig. 9 b). Touch voltage in the circuit II, circuit I is in operation, continuous line current 1800 A, Variant 2

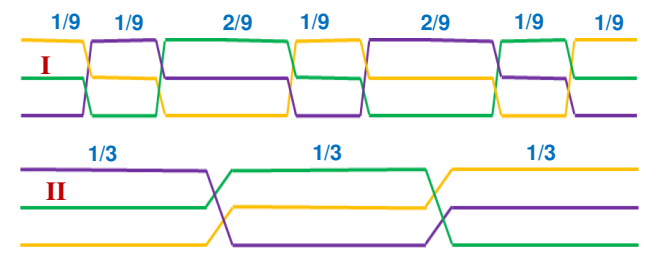


Fig. 11 a). Double-circuit line transposition, Variant 4

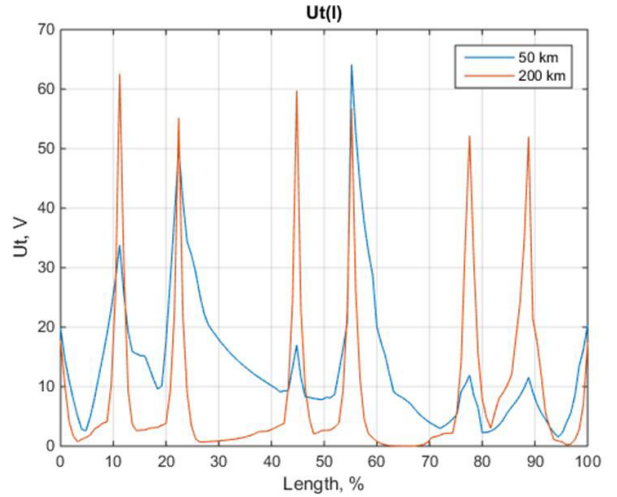


Fig. 11 b). Touch voltage in the circuit II, circuit I is in operation, continuous line current 1800 A, Variant 4

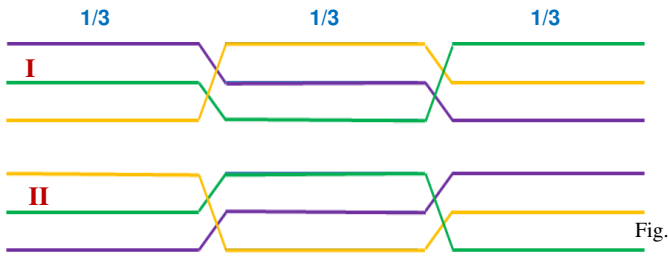


Fig. 12 a). Double-circuit line transposition, Variant 1

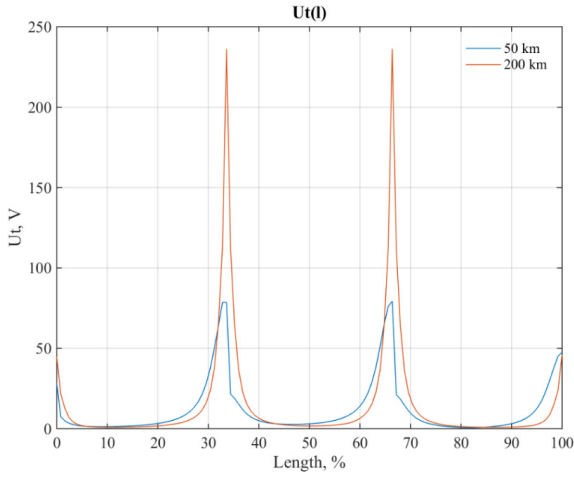


Fig. 12 b). Touch voltage in the circuit II, circuit I is in operation, continuous line current 3600 A, Variant 1

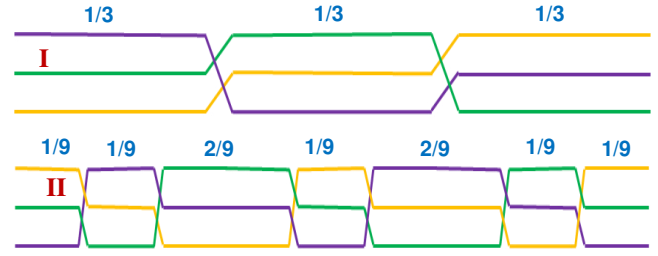


Fig. 14 a). Double-circuit line transposition, Variant 3

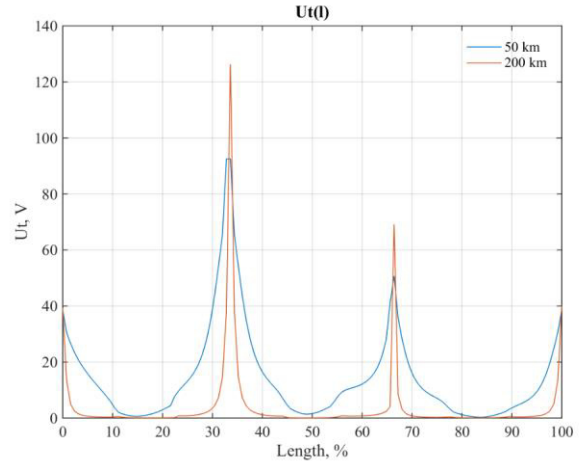


Fig. 14 b). Touch voltage in the circuit II, circuit I is in operation, continuous line current 3600 A, Variant 3

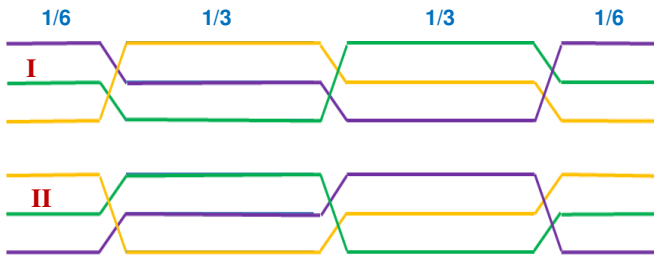


Fig. 13 a). Double-circuit line transposition, Variant 2

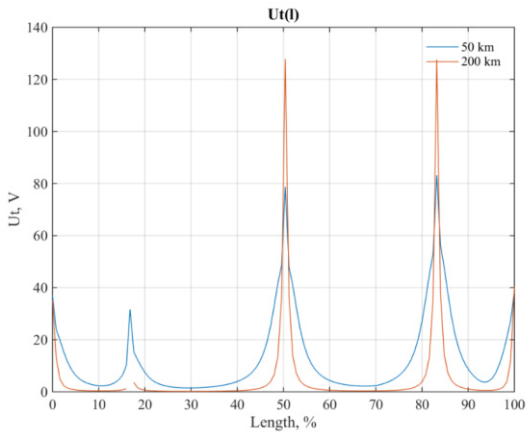


Fig. 13 b). Touch voltage in the circuit II, circuit I is in operation, continuous line current 3600 A, Variant 2

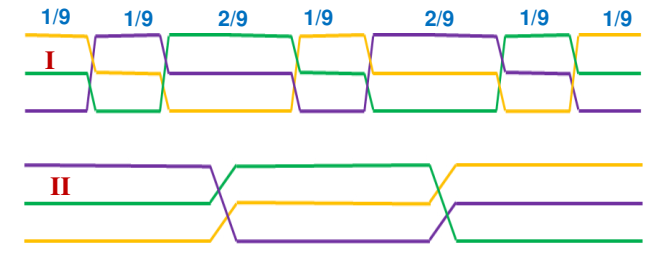


Fig. 15 a). Double-circuit line transposition, Variant 4

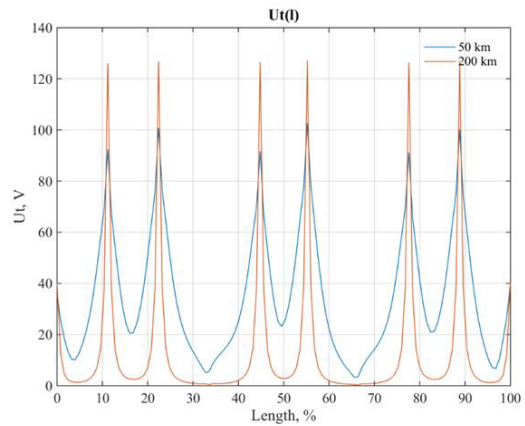


Fig. 15 b). Touch voltage in the circuit II, circuit I is in operation, continuous line current 3600 A, Variant 4

Simulation results for all four considered variants of the double-circuit line transposition demonstrate the increase of the touch voltage values in the switched off and grounded circuit of transposed double-circuit line near to transposition towers of the influencing circuit. It can be seen in Fig. 8 – 15.

Locations of the transposition towers of the switched off and grounded circuit of double-circuit overhead transmission line have no significant effect regarding the touch voltage increase. It means that the non-uniformity of the influenced circuit under maintenance is secondary in comparison with the non-uniformity of the influencing power circuit with respect to the touch voltage changes. It can be seen from Fig. 10, 11 and Fig. 14, 15.

From Fig. 8 – 15 it can be clearly seen that the simulation results for all four considered variants of the double-circuit line transposition contain the cases characterized by the touch voltage values which violate the limit of 50 V.

In comparison to the Fig. 8 – 11, Fig. 12 – 15 show, that the value of the current in the working power line affects the peak values of the touch voltages in the points of transposition and on the sides of the line near the substations. The values of the touch voltages are directly dependent on the values of the influencing line current and achieve their maximum values in the case of maximal continuous influencing line current of 3600 A.

It means that the maintenance of the switched off and grounded circuit of transposed double-circuit overhead line requires additional protective measures in the cases of transposition characterized by the expected values of the touch voltages higher than the allowed limit of 50 V AC.

Mathematical simulations can be recommended for the analysis of expected values of the touch voltages.

IV. SUMMARY

Maintenance conditions of the switched off and grounded DC power circuit of transposed double-circuit hybrid AC/DC transmission line with respect to the expected touch voltage values caused by the operating AC power circuit are considered in the paper.

The influence of conventional transposition schemas on the expected touch voltage values was analyzed. It was shown that line transposition can cause the violation of the allowed touch voltage limit in the switched off and grounded power circuit near to the transposition towers of the influencing power circuit under normal operating conditions.

Investigation results are valid both for hybrid AC/DC and for AC/AC double-circuit transposed overhead line.

It is recommended to use mathematical simulations for the determination of expected values of the touch voltages at the stage of planning and design of hybrid AC/DC overhead lines converted from EHV AC transmission lines.

REFERENCES

- [1] 583 WG B2.41 - Guide to the Conversion of Existing AC Lines to DC Operation, CIGRE, May 2014
- [2] B. Sander, J. Lundquist, I. Gutman, C. Neumann, B. Rusek, K.-H. Weck, "Conversion of AC multi-circuit lines to AC-DC hybrid lines with respect to the environmental impact," Cigre Science & Engineering, N°1, Feb. 2015, pp-36-47
- [3] J. Lundkvist, I. Gutman, L. Weimers, "Feasibility study for converting 380 kV AC lines to hybrid AC/DC lines," EPRI HVDC & FACTS Conf., 5 – 6 Nov. 2009, Westminster, USA
- [4] M. Kizilcay, A. Agdemir, M. Lösing, "Interaction of a HVDC System with 400-kV AC Systems on the Same Tower," in Proc. of the conf. IPST 2009, 2 – 6 June 2009, Kyoto, Japan
- [5] A. Novitskiy, D. Westermann, "Some Aspects of Steady State Simulations of AC/DC Hybrid Transmission Lines," in Proc. of the conf. IEEEIC 2017, 6 – 9 June 2017, Milan, Italy
- [6] Efimov B. V., Fastiy G. P., Yakubovich M. V., "Induced voltages on aerial lines by non-uniform adjacent routes," Electric Power Plants, N 8, 2002, pp. 32-38 (in Russian)
Ефимов Б. В., Фастий Г. П., Якубович М. В., «Наведенные напряжения на воздушных линиях при неоднородных трассах сближения,» Электрические станции, № 8, 2002, стр. 32-38.
- [7] O. Zalesova, V. Selivanov. Calculation of induced voltage in disconnected transmission lines 110 kV. Transactions of Kola Science Centre RAN, № 10 (28) / 2015 (in Russian)
О.Залесова, В.Селиванов. Расчет наведенного напряжения на отключенных линиях электропередачи 110 кВ. Труды Кольского научного центра РАН, № 10 (28) / 2015
- [8] I. Konotop, A. Novitskiy, D. Westermann, "Influence of 380 kV AC Systems on the Maintenance Conditions of the HVDC System in a Hybrid AC/DC Overhead Line," in Proc. of 10th Electric Power Quality and Supply Reliability Conference, 29 – 31 Aug. 2016, Tallinn, Estonia
- [9] "Protective Grounding and Bonding." Occupational Safety and Health Administration, United States Department of Labor. Internet Publication https://www.osha.gov/SLTC/etools/electric_power/hazardous_energy_control_protective_ground.html
- [10] M. El-Sharkawi, Electric Safety, Practice and standards, CRC Press, 2014
- [11] TGL 6928 Bl. 1. Starkstrom –Freileitungen. Verdrillungen. Dez. 1969
- [12] G. Herold, Elektrische Energieversorgung II, Schlembach Fachverlag, 2010
- [13] DGUV Vorschrift 3 Elektrische Anlagen und Betriebsmittel Unfallverhütungsvorschrift. BGW Berufsgenossenschaft für Gesundheitsdienst und Wohlfahrtspflege. 2014

AC Fault Analysis of DRU-VSC Hybrid HVDC Topology for Offshore Wind Farm Integration

Melanie Hoffmann, Nasser G.A. Hemdan, and
Michael Kurrat

Institute of High Voltage Technology and Electric Power
Systems (elenia), Technische Universität Braunschweig
Braunschweig, Germany

Christian Rathke, and Andreas Menze

TenneT Offshore GmbH
Lehrte, Germany

Abstract—High Voltage Direct Current (HVDC) is a beneficial technology for the transmission of large offshore wind power over long cables to the shore. However, the main drawback is the high converter cost. In this paper, a proposed hybrid topology based on diode rectifier units (DRU) and voltage source converters (VSC) is introduced with a potential for cost reduction. The focus of the current research is fault analysis of parallel DRU-VSC as a hybrid integration topology. A test system was built in PSCAD based on a real offshore wind farm connection. Two control strategies for the power flow were developed and tested regarding their performance during different AC faults. The results show that the VSC is the main source of the fault current.

Index Terms—HVDC Transmission, Diode Rectifier Unit, Voltage Source Converter, Offshore Wind Power

INTRODUCTION

It is advised to connect Offshore Wind Farms (OWF) which are far away from the shore, such as those in the German North Sea, via HVDC transmission systems to the shore based on economic and technical reasons. However, such HVDC connections are challenging because wind farms represent weak AC systems that need to be efficiently controlled through the HVDC converters. VSC-based HVDC transmission is already used by TenneT based on its advantage of independent active and reactive power control and supporting the system for OWF integration. However, VSC-based HVDC technology is very expensive. To ensure a cost-efficient energy transmission system and an affordable electricity price for the consumers, even with more offshore wind farms being connected in the future, it is important to identify possibilities to reduce the integration cost for OWFs.

Siemens has introduced a so-called diode-rectifier unit (DRU) that could reduce the total grid connection costs for OWFs by 30 % [1]. However, the pure solution with DRUs has some disadvantages because the DRUs are passive elements that can neither be controlled nor provide auxiliary power for the wind turbines and OWF substation. Hybrid topologies which combine for example DRU and VSC converters can be used in order to reduce the integration cost of OWF and improve the system performance [2], [3].

The literature review has shown that many studies analyzed the state of the art OWF integration concept which is only based on VSCs [4–7]. In addition, different hybrid topologies have been introduced and studied [8]–[9]. For example a proposed hybrid solution based on a wind farm side VSC and a line commutated converter (LCC) on the onshore side [8]. However, the operating principles of both converter topologies are different; the VSC controls the DC voltage and the LCC the DC current. Consequently, a commutation failure can occur in case of a voltage dip at the LCC. It is therefore difficult to realize this topology in practice because a VSC needs an almost constant DC voltage for a reliable and stable operation. Additionally, the series connection of DRU and VSC was studied in [10] and [11]. This concept consists of multiple converters that are connected via one HVDC cable to shore. If this cable is damaged a large amount of power can suddenly not be transmitted anymore. This paper introduces a hybrid topology which is characterized by the parallel operation of DRU and VSC both connected to separate HVDC cables to shore. The literature research has also shown that the VSC HVDC grid connection topology for OWFs has been studied regarding its fault behavior in detail [12], [13]. However, a fault analysis of hybrid topologies especially for the parallel operation of DRU and VSC has not been investigated in the literature. The current paper introduces a fault analysis of a DRU-VSC topology for the integration of OWFs based on a real network.

This paper is structured as follows: first, the DRU as well as different hybrid transmission system concepts are introduced. Second, the implementation of the parallel operation of DRU and VSC in PSCAD/EMTDC including the control strategies are described. Third, the fault analysis results and the conclusion including future work are presented.

HIGH VOLTAGE DIRECT CURRENT (HVDC) CONVERTER TECHNOLOGIES

When connecting offshore wind farms or two AC grids using HVDC, three converter technologies can be utilized: VSC, LCC and DRU. VSC and LCC are able to act as an inverter or a rectifier, whereas, a DRU is only able to convert

AC to DC. It is important to know that only VSCs offer voltage and frequency control for the OWF, controllability of reactive power and black start capability. This paper will focus on the DRU.

Siemens has proposed a so-called DRU to connect offshore wind farms to shore in a more cost-effective way [14]. The DRU solution could reduce the space, weight, operating expenditure as well as capital expenditure compared to current VSC-HVDC converter solutions [15], [16]. According to Siemens, the total expenditure will be decreased by 30 % and transmission losses will be decreased by 20 % when the DRU is used [15], [1]. The reason for lower losses are lower switching and conducting losses of diodes compared to IGBTs due to a lower on state voltage and switching frequency. According to Siemens, the DRU is able to transmit 1.2 GW of power from OWFs that are located more than 160 km away from shore. The setup would look as follows: the offshore conversion from AC to DC would be done by diode rectifiers and the onshore conversion to AC would be performed by VSCs. For connecting and operating an existing wind farm with an HVDC link that uses DRUs, it is according to Siemens important to be able to switch to an existing AC link as a backup which would be possible within 2.2 seconds (see Fig. 1) [14], [16].

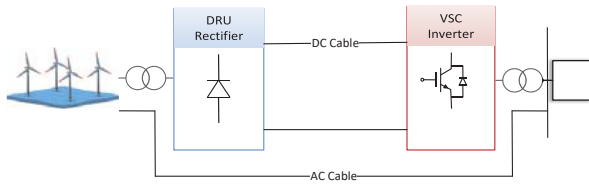


Figure 1: HVDC transmission concept based on DRU and VSC

OFFSHORE WIND FARM CONNECTION CONCEPTS

To ensure the controllability, power reversal and black start capability for the offshore wind farm grid, the combination of DRUs and VSCs was introduced. Three different topologies that combine both converter types are proposed in this section with a focus on the parallel operation of DRU and VSC.

A. Parallel Operation of DRU and VSC

One possibility of a hybrid DRU-VSC concept is the parallel operation of a DRU and a VSC as shown in Fig. 2. Each offshore converter is connected to an onshore VSC via separate HVDC cables.

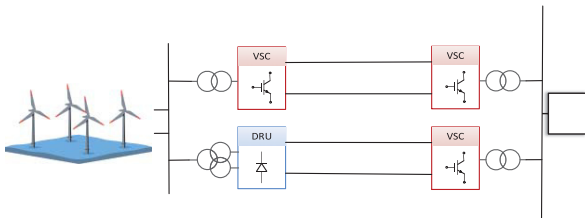


Figure 2: Parallel operation of DRU and VSC

1) Advantages

The parallel operation of DRU and VSC has the following advantages:

- Voltage and frequency controllability on the offshore AC side as well as the black start capability can still be handled by the VSC [17].
- Increasing the transmission capacity from OWFs to shore can be achieved with lower investment costs compared with the state of the art technology.
- Combining a DRU with a VSC is especially beneficial if a VSC is already built. More precisely, a modular extension of the connection capacity is possible.

2) Disadvantage

The following disadvantages need to be taken into consideration when implementing the parallel operation of DRU and VSC in the real world:

- The existence of two cable systems increases the overall cost.

B. Parallel Connection of DRU and VSC

Instead of having separate HVDC systems connected to each offshore converter, it might also be possible to connect a DRU and a VSC in parallel to one onshore VSC (see Fig. 3). This would decrease the cable costs but at the same time reduce the redundancy compared to the parallel operation topology. More details about this topology are given in [2].

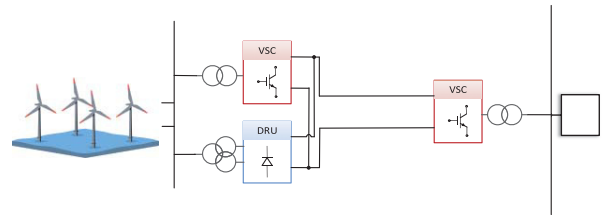


Figure 3: Parallel connection of DRU and VSC

C. DRU connected in series with VSC

The idea behind this topology is illustrated in Fig. 4. In this topology all offshore converters are connected in series and only two cables transmit the power produced by the OWF to shore. This topology has been studied in detail in [10] and [11].

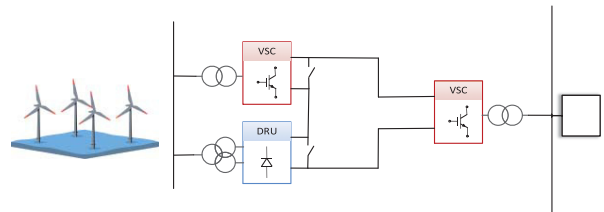


Figure 4: DRU connected in series with VSC

SYSTEM MODELLING AND CONTROL SCHEMES

Figure 5 provides the basic components and structure of the test system which have been built in PSCAD. The left-hand side of the graphic represents the OWF which consists of two 600 MW wind farms. Therefore, a total of 1200 MW can be supplied to the HVDC transmission system via two 10 km AC cables, modelled as a Pipe-Type cable in PSCAD. The wind turbines are of type 4 which means that they are full converter based generators. For this study only the DC to AC converter

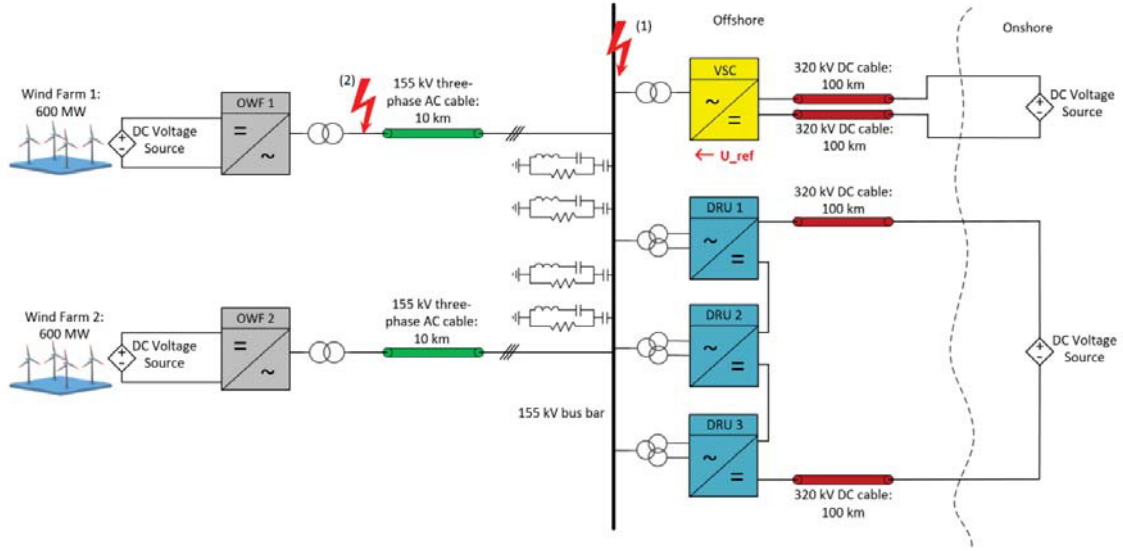


Figure 5: Overall model of the parallel connection of DRU and VSC

from the wind turbine was modelled. This converter was then scaled to a 600 MW converter to represent the behavior of a wind farm. Each of these two converters consists of a two-level VSC which is connected to a DC voltage source.

The right-hand side of Fig. 5 shows the 600 MW VSC converter in yellow and three 24-pulse DRUs that can together transmit 1200 MW of power to shore, illustrated in blue. The VSC represents a MMC, modelled as an average value model [18].

Each DRU was modelled as two in series connected 12-pulse diode rectifiers including capacitors to reduce ripples. The three DRUs and the VSC are connected to a 100 km long HVDC cable each which is based on the coaxial cable model from PSCAD. The model also includes harmonic filters that are tuned to mitigate the 5th, 7th, 11th and 13th harmonics.

The focus of this study was on the offshore side of a HVDC transmission system for OWFs. Therefore, as a first step, the HVDC cables were connected to DC voltage sources with a constant voltage level.

PROPOSED POWER FLOW CONTROL SCHEMES

The amount of active power transmitted via the DRU and the VSC needs to be controlled. This can be done by identifying an appropriate parameter to be controlled. It has been found that by controlling the AC voltage of the 155 kV busbar through the VSC, the power flow distribution through the VSC and DRUs can be efficiently controlled. Two control schemes were developed, implemented and tested in PSCAD for this purpose. One control strategy is based on a PI controller and the other on the characteristic curve of the DRU. These are described in the following subsections.

A. PI controller

The implementation of the PI controller (PI) in PSCAD is illustrated in Fig. 6. P_{ref} is the reference active power that should be transmitted via the VSC.

The reference active power can be given as follows:

1. A fixed value
2. A percentage value of the total supplied power from the wind generators (e.g. 50%)

P_{VSC} is measured at the 155 kV side of the transformer connecting the VSC. Depending on the difference between both values, the AC voltage magnitude U_{ref} will be adjusted with the PI controller. U_{ref} is then used by the VSC to control the voltage at the 155 kV busbar and therefore the power flow via the cable resistance to the DC voltage source.

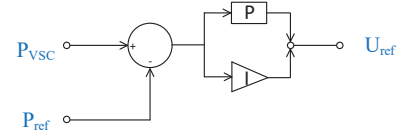


Figure 6: PSCAD implementation of PI control scheme

B. Characteristic curve

The power transmitted via the DRU can be adjusted by controlling the AC voltage on the 155 kV busbar. More precisely, the higher the AC voltage, the more power can be transmitted via the DRU. This functionality forms the basis for the characteristic curves (CCs) which are illustrated in Fig. 7. The slopes of the CCs vary depending on the number of DRUs in service. For example needs the voltage be higher when only one DRU has to transmit 300 MW compared to the case where three DRUs are in service so that each one only needs to transmit 100 MW. Fig. 8 shows the implementation of the CC in PSCAD. It can be seen that the power supplied by the OWF is the input parameter and that U_{ref} is the PI controller, the output variable.

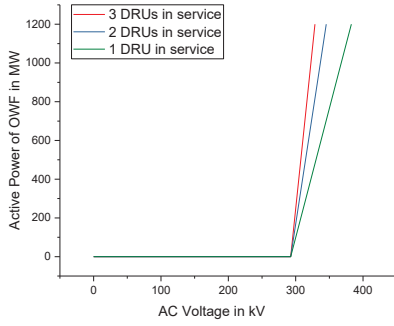


Figure 7: Characteristic curves of the DRU

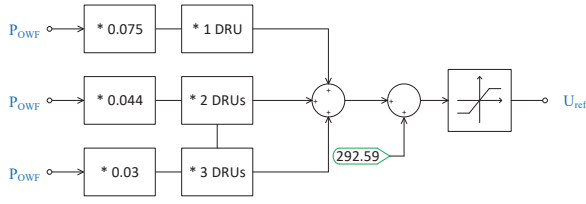


Figure 8: PSCAD implementation of the characteristic curve control scheme

FAULT ANALYSIS

To evaluate the behavior of the parallel operation of DRU and VSC in case of AC faults, different fault scenarios were investigated. The influence of faults when the OWF supplies the maximum power of 1200 MW have been tested as the worst case. The fault location was selected on the 155 kV busbar (fault location (1) in Fig. 5) and on the substation of OWF 1 (fault location (2) in Fig. 5). Based on the offshore grid connection rules [19], the fault duration was set to 150 ms. Different fault resistances were investigated. However, only the cases with the fault resistances of 0.01Ω are presented here. The following fault types were studied:

- Single Line to Ground Fault (SLG)
- Three Phase to Ground Fault (TPG)
- Line to Line Fault (LL)

In addition, the scenario where a fault occurs in two DRUs (F2DRU) was investigated. In this case, the faulted DRU was short circuited on the DC side and a switch on the AC side disconnected them from the AC busbar simultaneously.

A. Influence of Faults on the HVDC Transmission System

Fig. 9 illustrates the AC rms voltage at the 155 kV busbar in case of SLG, LL and TPG faults at fault location 1. It can be seen that the voltage collapses to zero for a TPG fault. The LL and SLG faults disturb the system similarly but not as much as the TPG fault. The voltage recovers to its initial value after 250 ms (SLG, LL) or 300 ms (TPG). The plots in Fig. 9 were derived when the power was controlled with the CC. It was seen that the behavior of the AC rms voltage was similar when the PI controller was utilized.

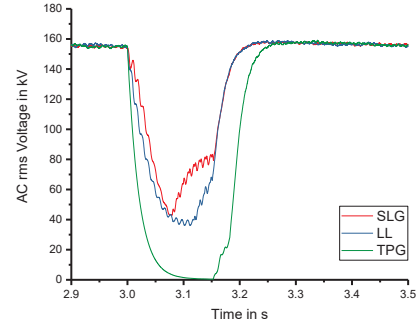


Figure 9: AC rms Voltage at 155 kV busbar (based on CC control)

Fig. 10 shows the maximum fault current in case of a SLG fault. The fault current distribution among the components in case of LL or TPG faults was similar. Therefore, only one diagram is given here which represents the general fault current in different parts of the OWF connection system for all faults that were tested in this study. The AC rms current was measured at each OWF, the VSC and at each DRU. It can be seen that the current at the VSC is the highest, whereas, the lowest values occur at each DRU. It is important that the fault current is limited by the OWF and the VSC to ensure a safe operation. The fault current can be limited by adjusting the controller parameters of the OWF converters.

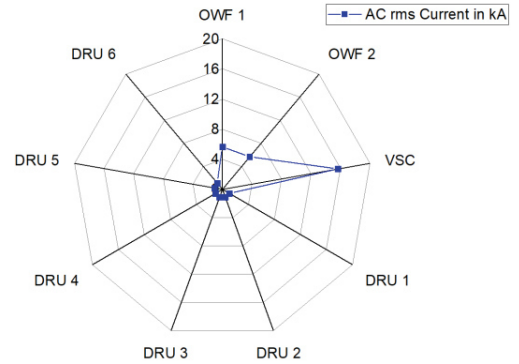


Figure 10: AC rms fault current for SLG fault (based on CC control)

Fig. 11 shows the DC voltage measured at the DRU.

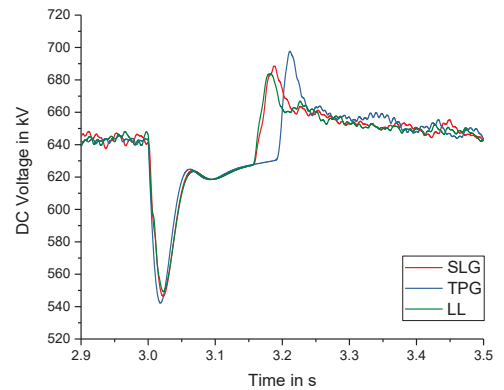


Figure 11: DC Voltage at DRU (based on CC control)

It can be seen that the DC voltage decreases to a minimum of 540 kV. This is a deviation of about 15% from the nominal

voltage of 640 kV. The DC voltage recovers in case of all faults to 640 kV after approximately 215 ms (SLG, LL) or 255 ms (TPG). The percentage of the ripples is equal to 2%.

The DC voltage at the VSC is illustrated in Fig. 12 for the case that the power is controlled with the CC. The DC voltage looks similar when the PI controller is used. The effect of all faults is similar. The duration of the disturbance is about 300 ms and the fluctuations are equal to about 40 %. Comparing the DC voltage at the DRU (Fig. 11) and at the VSC (Fig. 12) shows that less DC voltage fluctuation is present in the HVDC cable connected to the DRU compared to the one connected to the VSC. This can be explained with the switching characteristics of the VSC. In addition, it can be derived from Fig. 12 that the fluctuation of the DC voltage is the highest in case of the TPG fault.

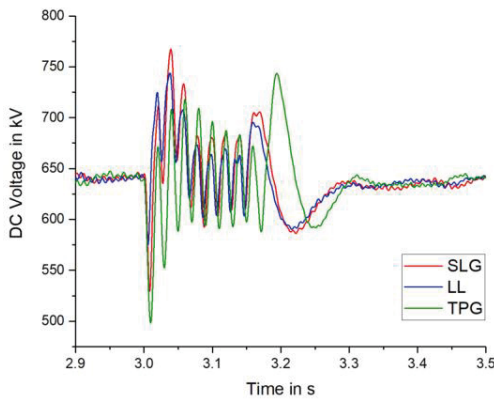


Figure 12: DC Voltage at VSC (based on CC control)

The DC currents shown in Fig. 13 were measured at the DRU when the CC was utilized to control the power flow. The results are similar when the power flow control was done by the PI controller. Fig. 13 illustrates that the DC current dropped to a slightly negative value directly when the fault occurred and then stayed around zero for about 150 ms (SLG and LL) or 190 ms (TPG). The negative current can be explained with the discharging of the capacitors at the DRUs. When the DC current is zero, no power can be transmitted to shore.

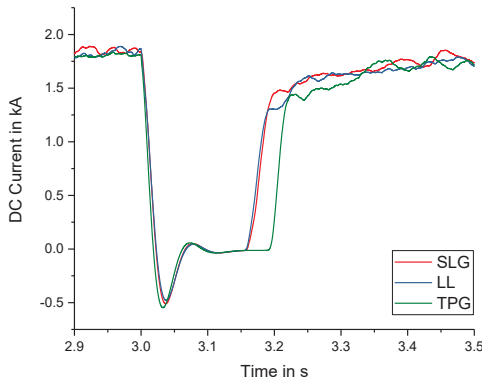


Figure 13: DC Current at DRU (based on CC control)

B. Fault on the OWF substation

Fig. 14 and 15 show the influence of a SLG fault at the substation of OWF 1 (Fault location (2) in Fig. 5) on the AC

voltage and current, respectively. The results for both control schemes, PI and CC, are presented. Fig. 14 and 15 show that the impact on OWF 1 is, as expected, bigger than for OWF 2.

It can be seen from Fig. 14 that the AC rms voltage drops to a lower value when the CC is used. This shows that the AC voltage drop can be limited with the PI controller parameters.

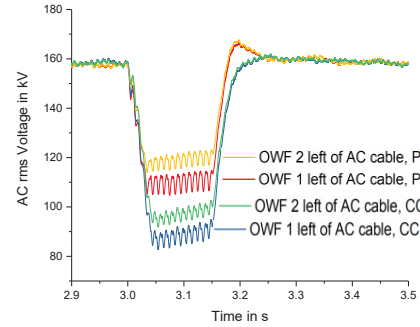


Figure 14: AC rms Voltage for fault at OWF 1

Fig. 15 illustrates that the difference between the control schemes is relatively small for the AC rms current. It can also be seen that the current in the OWF farm is limited and does not exceed 7 kA. This can also be seen from Fig. 10.

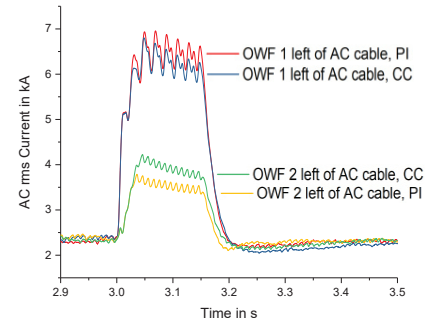


Figure 15: AC rms Current for fault at OWF 1

C. Fault in DRUs

Fig. 16 illustrates the AC voltage at the 155 kV busbar when two of the three 24-pulse DRUs are out of service for example because of faults in the DRUs and therefore, disconnected from the HVDC transmission system. The results shown in Fig. 16 were derived when the power flow is controlled with the CC. The results are similar when the PI controller is used. Fig. 16 shows that the AC rms voltage drops to a minimum of 20 kV for about 100 ms before it recovers to its nominal voltage. A voltage drop to such a low voltage level is critical for the stability of the system.

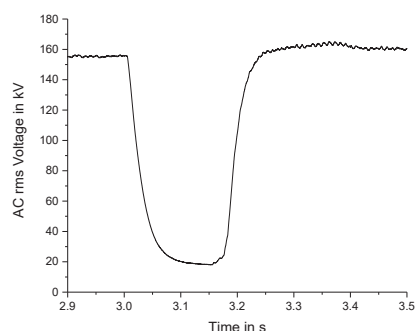


Figure 16: AC Voltage at 155 kV busbar for F2DRU case (based on CC control)

Fig. 17 illustrates the change of the DC voltage in the HVDC cable connecting the DRUs to shore when two of the three 24 pulse DRUs need to be disconnected due to faults. It can be seen that the voltage dropped to a minimum value of 55 kV for a short duration before it recovers to about 213 kV. It shows that one DRU can only achieve one third of the nominal voltage of 640 kV (± 320 kV). Consequently, 400 MW instead of the maximum 1200 MW can be transmitted to shore with one remaining DRU.

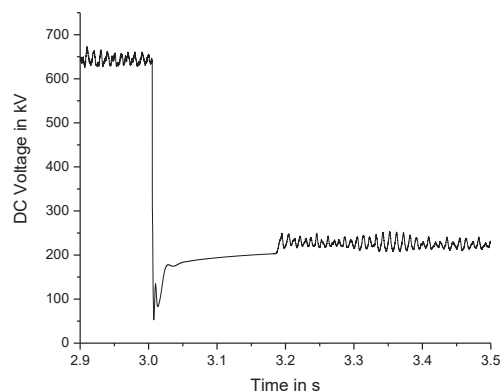


Figure 17: DC Voltage at DRUs for F2DRU case and power control with CC

CONCLUSION AND FUTURE WORK

In this paper, the AC fault behavior of the parallel operation of DRU and VSC was presented. It could be seen that the HVDC transmission system recovers to its initial stable operating point after the occurrence of SLG, TPG and LL faults. In addition, the case where two DRUs are out of service and disconnected from the remaining transmission system showed that one third of the maximum power of 1200 MW can still be transmitted to shore via the remaining DRU. No major difference between the two control schemes, PI and CC, for controlling the power flow was found for this study.

The following open points can be identified:

- It is necessary to study DC faults and their influence on the HVDC transmission system including the DRU.
- It would also be beneficial to work on fault detection methodologies that allow an early detection and isolation of AC as well as DC faults.

REFERENCES

- [1] Siemens AG, "Siemens revolutioniert Netzanschluss von Offshore-Windkraftwerken," Neunte Nationale Maritime Konferenz 2015.
- [2] Melanie Hoffmann, "Innovative Offshore Wind Farm Connection Concepts Using Different HVDC Converter Technologies," TU Braunschweig, 2018.
- [3] Melanie Hoffmann, Christian Rathke, Andreas Menze, Nasser G. A. Hemdan, and Michael Kurrat, *Parallel Operation of HVDC DRU and VSC Converters for Offshore Wind Farm Connection: Technical-Economic Feasibility*.
- [4] P. Bresesti, W. L. Kling, R. L. Hendriks, and R. Vailati, "HVDC Connection of Offshore Wind Farms to the Transmission System," *IEEE Trans. On Energy Conversion*, vol. 22, no. 1, pp. 37–43, 2007.
- [5] H. Ahmad, S. Coppens, and B. Uzunoglu, "Connection of an Offshore Wind Park to HVDC Converter Platform without Using Offshore AC Collector Platforms," in *2013 IEEE Green Technologies Conference (GreenTech 2013)*, Denver, CO, pp. 400–406.
- [6] Thomas Ackermann, "Transmission Systems for Offshore Wind Farms," *IEEE Power Engineering Review*, pp. 23–27, 2002.
- [7] J. Wu, Z.-X. Wang, L. Xu, and G.-Q. Wang, "Key Technologies of VSC-HVDC and its Application on Offshore Wind Farm in China," *Renewable and Sustainable Energy Reviews*, vol. 36, pp. 247–255, 2014.
- [8] R. E. Torres-Olguin, M. Molinas, and T. Undeland, "Offshore Wind Farm Grid Integration by VSC Technology With LCC-Based HVDC Transmission," *IEEE Trans. Sustain. Energy*, vol. 3, no. 4, pp. 899–907, 2012.
- [9] R. Zeng, L. Xu, L. Yao, S. J. Finney, and Y. Wang, "Hybrid HVDC for Integrating Wind Farms With Special Consideration on Commutation Failure," *IEEE Trans. Power Delivery*, vol. 31, no. 2, pp. 789–797, 2016.
- [10] T. H. Nguyen, D.-C. Lee, and C.-K. Kim, "A Series-Connected Topology of a Diode Rectifier and a Voltage-Source Converter for an HVDC Transmission System," *IEEE Trans. Power Electron.*, vol. 29, no. 4, pp. 1579–1584, 2014.
- [11] I. Haukaas, "Hybrid HVDC Transmission for Large-Scale Offshore Wind Integration," Norwegian University of Science and Technology 2017.
- [12] R. G.-V. Bardo Rios, "Dynamic modelling of VSC-HVDC for connection of offshore wind farms," in *9th IET International Conference 2010*, pp. P22-P22.
- [13] M. Mohammadi, M. Avendano-Mora, M. Barnes, J. Y. Chan, *A Study on Fault Ride-Through of VSC-Connected Offshore Wind Farms: 21–25 July 2013, Vancouver, BC, Canada*. Piscataway, NJ, Piscataway, NJ: IEEE, 2013.
- [14] Slavomir Seman, Ngoc Tuan Trinh, Rainer Zurowski, Sarina Kreplin, "Modelling of the Diode-Rectifier Based HVDC Transmission Solution for Large Offshore Wind Power Plants Grid Access," International Workshop on Large-Scale Integration of Wind Power into Power Systems as well as on Transmission Networks for Offshore Wind Power Plants 2015.
- [15] Peter Menke, "New Grid Access Solutions for offshore wind farms," EWEA Offshore 2015.
- [16] Thomas Hammer, Slavomir Seman, Peter Menke, Felix Hacker, Bert Szangolies, Jochen Meth, Jörg Dorn, Karsten Loppach, Rainer Zurowski, "Diode-Rectifier HVDC link to onshore power systems: Dynamic Performance of Wind Turbine Generators and Reliability of liquid immersed HVDC Diode Rectifier Units," CIGRE B4-121, 2016.
- [17] Jakob Glasdam, Jesper Hjerrild, Lukasz Hubert Kocewiak, Claus Leth Bak, *Review on Multi-Level Voltage Source Converter Based HVDC Technologies for Grid Connection of Large Offshore Wind Farms*, 2012 IEEE International Conference on Power System Technology.
- [18] J. Peralta, H. Saad, S. Denneriere, J. Mahseredjian, and S. Nguefeu, "Detailed and Averaged Models for a 401-Level MMC-HVDC System," *IEEE Trans. Power Delivery*, vol. 27, no. 3, pp. 1501–1508, 2012.
- [19] TenneT TSO GmbH, "Offshore-Netzanschlussregeln - O-NAR," 2017.

Model Reduction of a Low Voltage Grid by Current Source to Investigate Small-Signal Stability

J. Kircheis, T. Jiang, J. Willkomm, S. Schlegel, D. Westermann

Power Systems Group
Technische Universität Ilmenau
Ilmenau, Germany

Abstract- Over the last decades, model reduction has been an essential tool in analyzing bulk power systems. With the increasing penetration levels of power converters in distribution grids, the complexity of these grids is increased. Nevertheless, the stability analysis of these grids becomes more important, due to the increasing power generation in these grids. To achieve a computationally efficient grid model, this paper presents a new model reduction technique for inverter-dominated grids. By retaining the grids input-output characteristics, the reduced grid model is suitable for the small-signal stability analysis. The method is based on the principle of aggregation, where the aggregated grid is expressed by a controlled current source. The proposed method is applied on a Cigré reference grid and validated through simulations. Their results show a better computational efficiency, with the dynamic behavior being well approximated. With the new method, it is possible to simulate more grid levels, which is important for the stability analysis in future grids.

Keywords-distribution grids; model reduction; inverter-dominated grids; small-signal stability

I. INTRODUCTION

The environmental awareness of citizens in Germany has been rising continuously over the last decade. For many citizens, the need to live in an intact and healthy environment is a basic requirement for a healthy life [1]. Current environmental issues like the climate change or the air pollution in cities expose the urgency of developing and improving concepts to ensure a healthy environment in the future. One of these concepts is the in the late 1980s initiated “Energiewende” in Germany. With the aim of creating a sustainable energy supply, the Energiewende leads to a transformation of the power system in Germany. A crucial feature of the Energiewende is the Energy Concept 2050. In 2050, the share of renewable energy needs to be 80 % of the total electrical energy consumption in Germany [2]. This leads to shutdowns of conventional power plants while the generation of electrical energy based on renewable energy is growing. Renewable energies are predominantly implemented in low voltage grids, more precisely in distribution grids. For a successful integration of renewable energies, the conversion system plays an important role. Conversion systems are usually built up of a bridge circuit of semiconductor elements and a controller, which form a power converter. The state of the art is the use of self-commutated, pulse-width modulated power converters in power systems, especially in distribution systems [3].

To investigate the small-signal stability of grids with power converters, an appropriate approach of modeling these grids is necessary. An essential part of modeling inverter-dominated grids is the modeling of power converters [4]. Various modeling concepts and techniques for simulating power converters already exist, which differ in complexity and considered electrical phenomena [5]. Due to the increasing number of inverters connected to the grid, it is not possible to model each inverter detailed. The model complexity should be reduced to keep the simulation time in an acceptable period. Even by choosing a reduced inverter model (e.g., phasor model) the simulation time can exceed acceptable limits, and numerical problems can occur [6], [7]. This paper presents a model reduction technique to analyze the small-signal stability of distribution grids. This method allows faster simulation time while avoiding numerical problems. By using a controlled current source for model reduction, the number of simulated inverters can be increased significantly. The current source is controlled by an estimated transfer function, which represents the dynamic behavior of a specific grid. Using a Cigré reference grid, this method is validated. Furthermore, this paper specifies the common model reduction techniques used in modeling of power systems.

This paper will be arranged as follows: firstly, an overview of conventional model reduction techniques will be given in Section II. Secondly, the proposed model reduction technique will be described in Section III. In Section IV a test grid will be presented to validate this method. In Section V the results of the validation will be outlined. Finally, in Section VI a conclusion is provided.

II. POWER SYSTEM MODEL REDUCTION

Generally, model reduction is used to replace a given mathematical model by a smaller one, which still describes the system or a relevant part of it with adequate accuracy. The primary challenge in model reduction is to find a trade-off between the model order and the model accuracy [8]. Model reduction does not only reduce the computational complexity of mathematical models, but it is also suitable for finding a model with the lowest number of variables [9].

An important part of model reduction is the classification of the power system into two areas: internal area (or study area) and external area. The internal area is usually modeled in detail, while the model of the external area is reduced [10]. Based on this practice two main strategies of model reduction are applied in power systems. On the one hand, power systems can be reduced based on similar physical properties of its components like power lines, load, and machines [11]. This strategy mainly focuses on reducing the number of modeled generators. Another approach is the use of mathematical methods used in control theory to reduce the size of a model. Model reduction is a wide area; the following overview only presents a selection of methods.

A. Physical strategy

Historically, the physical strategy and the corresponding methods formed the first attempt of reducing models in power systems [12]. Regarding the reduction of transmission grid models, the physical strategy is well established [13]. This approach can be divided up into two processes: identify coherency and aggregate coherent components.

1) Coherency

Coherency denotes the phenomenon that the rotor angle of some electrical machines swing in the same way after a disturbance occurred. Since generators tend to swing together in groups, it is usually possible to find coherent generators [8], [10]. Identifying coherent groups of generators is not a straightforward task, during the last decades several methods were developed to find coherent groups [14], [15]. After finding a coherent group of machines, the group needs to be aggregated by an equivalent model.

2) Aggregation

Each coherent group is replaced by an equivalent model. This equivalent model represents a single generator that exhibits the same swing of rotor angle after a disturbance like the coherent group. The equivalent model is usually described by a voltage source and the swing equation, while the control devices of the group generators are aggregated [8].

B. Mathematical strategy

The use of model reduction techniques used in control theory is a pretty new approach in the modeling of power systems [11]. Due to the increasing penetration of renewable energy sources in electrical grids, model reduction techniques based on the physical approach may not be sufficient anymore [6], [12]. Therefore, the use of highly theoretical and general algorithms seems to be a practical solution to extend model reduction also to inverter-dominated grids [12].

1) Krylov subspace approach

The Krylov subspace is given by:

$$K_k(A, b) = \text{span}\{b, Ab, \dots, A^{k-1}b\}, \quad (1)$$

where $A \in R^{n \times n}$ and $b \in R^{n \times 1}$. For the Krylov subspace approach the system needs to be described in a linear form [10]. The linear form can be obtained by linearization of the nonlinear model [16]. Simplified, a linear single-input single-output system

(SISO) is assumed. The general structure of a time-invariant SISO system can be described as follows:

$$\dot{x}(t) = Ax(t) + bu(t), \quad y(t) = c^T x(t) + du(t), \quad (2)$$

where $x \in R^n$ is the vector of the state variables, $A \in R^{n \times n}$ is the dynamic matrix, $b \in R^{n \times 1}$ the input vector, $c^T \in R^{1 \times n}$ is the output vector, and $d \in R$ is the scalar feed-through term. A reduced-order approximation can be expressed as follows:

$$\dot{\tilde{x}}(t) = \tilde{A}\tilde{x}(t) + \tilde{b}u(t), \quad \tilde{y}(t) = \tilde{c}^T \tilde{x}(t) + \tilde{d}u(t), \quad (3)$$

where $\tilde{x} \in R^{m \times 1}$, $\tilde{A} \in R^{m \times m}$, $\tilde{b} \in R^{m \times 1}$, $\tilde{c}^T \in R^{1 \times m}$, $\tilde{d} \in R$ is a scalar and $m < n$. The transfer function is generally given by:

$$G(s) = c^T (sI - A)^{-1} b, \quad (4)$$

where s denotes the complex frequency and I is the identity matrix [11]. The feed-through term d is assumed to be zero. The transfer function can be expressed by a Taylor series with the interpolation point σ :

$$G(s) = \sum_{j=1}^{\infty} c^T \cdot [(\sigma I - A)^{-1}]^j \cdot b \cdot (s - \sigma)^{j-1}, \quad (5)$$

where

$$c^T \cdot [(\sigma I - A)^{-1}]^j \cdot b, \quad (6)$$

are called moments of the transfer function [10], [17]. The moments describe the derivatives of the transfer function. The systems transfer function can be approximated if only a specific number of moments are considered [17]. To approximate the transfer function around different interpolation points σ^k the following Krylov subspaces are applied:

$$V = \text{span} \bigcup_{k=1}^K K_{j_{bk}} \left\{ (\sigma^k I - A)^{-1}, (\sigma^k I - A)^{-1} b \right\}, \quad (7)$$

$$Z = \text{span} \bigcup_{k=1}^K K_{j_{ck}} \left\{ (\sigma^k I - A^T)^{-1}, (\sigma^k I - A^T)^{-1} c^T \right\}. \quad (8)$$

With Z and V , the system expressed by (2) can be reduced as follows:

$$\begin{aligned} \dot{\tilde{x}}(t) &= (Z^T V)^{-1} Z^T A V \tilde{x}(t) + (Z^T V)^{-1} Z^T b u(t), \\ y(t) &= c^T V \tilde{x}(t). \end{aligned} \quad (9)$$

2) Balanced Truncation Method

Another mathematical strategy of model reduction is the balanced truncation method. This method delivers reduced-order models by retaining controllability and observability [10]. The system expressed by (2) is rewritten with multiple inputs and multiple outputs:

$$\dot{x}(t) = Ax(t) + Bu(t), \quad y(t) = Cx(t) + Du(t), \quad (10)$$

where $x \in R^n$ is the vector of the state variables, $A \in R^{n \times n}$ is the dynamic matrix, $B \in R^{n \times r}$ the input matrix, $C \in R^{q \times n}$ is the output matrix, and $D \in R^{q \times r}$ is the scalar feed-through matrix. The balanced truncation method uses two important quantities of linear time-invariant (LTI) systems, the observability gramian and the controllability gramian [10]. The observability gramian W_o and the controllability gramian W_c are solutions of the Lyapunov equations [10], [16]:

$$AW_c + W_c A^T = -BB^T, \quad A^T W_o + W_o A = -C^T C. \quad (11)$$

The projection matrices T_L and T_R , where $T_L, T_R \in R^{n \times m}$ and $m \ll n$ transform the system into a reduced one [16]. The matrices of the reduced system can be obtained as follows:

$$\tilde{A} = T_L^T A T_R, \quad \tilde{B} = T_L^T B, \quad \tilde{C} = C T_R, \quad \tilde{D} = D. \quad (12)$$

To obtain the projection matrices, various methods exist [10], [16]. In this paper the use of Cholesky decomposition and singular value decomposition is described to obtain these matrices.

First, the Cholesky decomposition of the controllability gramian and the observability gramian must be computed [16]. The Cholesky decomposition factorizes a matrix into a product of a lower triangular matrix and its conjugate transpose. The decompositions of both gramians are denoted as follows:

$$W_c = L_c \cdot L_c^T, \quad W_o = L_o \cdot L_o^T. \quad (13)$$

The singular value decomposition of the product $L_o \cdot L_c^T$ is computed:

$$L_o \cdot L_c^T = U \Sigma V^T, \quad (14)$$

where U and V are column orthogonal matrices and Σ is a diagonal matrix with the diagonal elements $\sigma_1, \sigma_2 \dots \sigma_n$, which are the singular values of the product [16]. The projection matrices can be obtained using:

$$T_L^T = \Sigma_m^{-1/2} V_m^T L_o^T, \quad T_R = L_c U_m \Sigma_m^{-1/2}, \quad (15)$$

where U_m and V_m are the leading m columns of U and V and $\Sigma_m^{-1/2}$ is a diagonal matrix containing the diagonal elements $1/\sqrt{\sigma_1}, 1/\sqrt{\sigma_2} \dots 1/\sqrt{\sigma_m}$ [16].

III. MODEL REDUCTION BY CONTROLLED CURRENT SOURCE

The method of model reduction presented in this paper is based on the principle of aggregation. Instead of aggregating coherent generators, a distribution grid is substituted by a three-phase controlled current source, which approximates the dynamic behavior of the distribution grid. This method focuses on retaining the input-output characteristics of the distribution grid, and it is suitable to reduce distribution grids modeled by the phasor model. To approximate the input-output characteristic a mathematical model is created, which calculates the value of the output quantity as a function of the input quantity. The calculated values are the reference values for the controlled current source. Fig. 1 shows the general structure of a distribution grid with loads and inverters fed from a medium

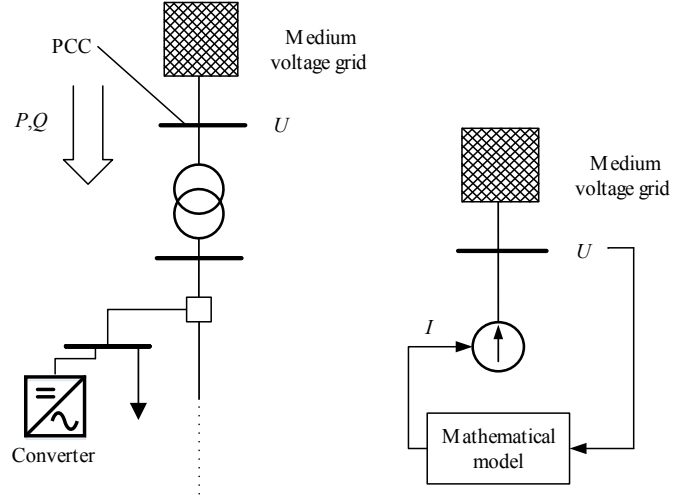


Figure 1. Distribution grid

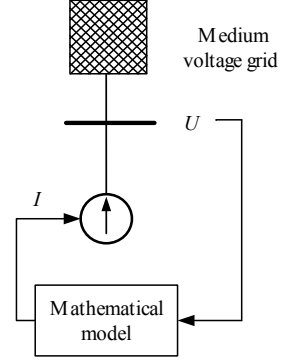


Figure 2. Reduced grid

voltage side. In this paper, the input quantity is the feeding voltage U of the grid, and the output quantity is the active power P and reactive power Q of the grid. These quantities are appropriate to assess the small-signal stability of a distribution grid, by applying a voltage step on the medium voltage side and analyzing the active and reactive power of the distribution grid [18]. Fig. 2 illustrates the reduced grid. The proposed method can be divided up into four steps:

A. Mathematical model

At first, a mathematical model must be developed, which describes the input-output characteristic of the respective quantities. The voltage U at PCC is chosen as input quantity and the active power P and the reactive power Q , both measured at PCC, are chosen as output quantities. The mathematical model is expressed by:

$$P(U) = P_{\text{load}} + P_{\text{dyn}}, \quad Q(U) = Q_{\text{load}} + Q_{\text{dyn}}, \quad (16)$$

where the active power $P(U)$ and the reactive power $Q(U)$ are separated into a dynamic term ($P_{\text{dyn}}, Q_{\text{dyn}}$) and into a steady term ($P_{\text{load}}, Q_{\text{load}}$). The dynamic term represents the change of power due to the inverter interactions, and the steady term represents the change of power due to the loads. As already mentioned, $P(U)$ and $Q(U)$ are the reference values for the controlled current source. In the following two sections, the mathematical description of the loads and of the inverter dynamics will be given.

B. Aggregation of loads

The loads in the distribution grid are aggregated by summing up the active and reactive power of each load, which leads to the aggregated load with P_{load} and Q_{load} . The loads are treated as constant impedance loads, to simplify their respective mathematical model. The power demand of the aggregated load only depends on the feeding voltage U :

$$P_{\text{load}} = U^2/Rn^2, \quad Q_{\text{load}} = U^2/Xn^2, \quad (17)$$

where R is the aggregated resistance, X is the aggregated reactance and n represents the turns ratio of the MV/LV transformer. Assuming that P_{ref} and Q_{ref} are the active and reactive power of the aggregated load at a reference voltage U_{ref} , the actual active and reactive power of the aggregated load P_{load} and Q_{load} can be calculated as follows:

$$P_{\text{load}} = P_{\text{ref}} \frac{U^2}{U_{\text{ref}}^2} - P_{\text{inv}}, \quad Q_{\text{load}} = Q_{\text{ref}} \frac{U^2}{U_{\text{ref}}^2} - Q_{\text{inv}}, \quad (18)$$

where U is the actual feeding voltage and P_{inv} and Q_{inv} are the injected active and reactive power of all inverters. With (18) and a controlled current source it is possible to approximate the grid in steady-state, whereas the inverter dynamics P_{dyn} and Q_{dyn} are zero.

C. Aggregation of inverter dynamics

With the use of system identification, two transfer functions are estimated: $G_p(s)$ characterizes the transfer behavior between the input ΔU and the output P_{dyn} and $G_q(s)$ express the transfer behavior between the input ΔU and the output Q_{dyn} , where ΔU is equal to $U - U_{\text{ref}}$. The transfer functions are estimated based on measured data ($u(t) = \Delta U$ and $y(t) = P_{\text{dyn}}/Q_{\text{dyn}}$) of the original grid. A voltage step ΔU from the medium voltage side is applied, and P and Q are measured at PCC, whereby the measured data is reduced by the offsets of P and Q to obtain the values of P_{dyn} and Q_{dyn} . The estimated transfer functions only describe the dynamic behavior of the grids input-output characteristic caused by the inverter interactions. Assuming a stable system, the dynamic behavior converges to zero. Consequently, the DC gains of the estimated transfer functions should be approximately zero.

The distribution grid with inverters is a highly nonlinear system [19]. Therefore, an estimation of a transfer function corresponds to a linearization around an equilibrium point. By analyzing small-signal stability, linearization around an equilibrium is often used. Nevertheless, the linearization is only valid when small disturbances are applied [20], [21]. For the addressed purpose the input ΔU should be limited to $\pm 10\%$ [18].

D. Controlled Current Source

The values calculated by (16) are the reference values for the controlled current source. To calculate the corresponding currents, different solutions are possible. In this paper, the calculation of the current is based on the dq -frame [22].

IV. TEST GRID

To validate the proposed method, the Cigré reference grid for the European low voltage distribution network benchmark is used [23]. The grid is extended by five inverters, representing distributed energy resources (DER) connected to the grid. Fig. 3 illustrates the structure of this grid. The loads are modeled as constant impedance loads, and the load parameters can be found in Table I. The inverters are controlled by an inner current controller, which tracks the reference values of the external P- and Q-controller. The reference value for the injected active power is $P_{\text{inv}} = 4$ kW and $Q_{\text{inv}} = 1.32$ kvar for the reactive

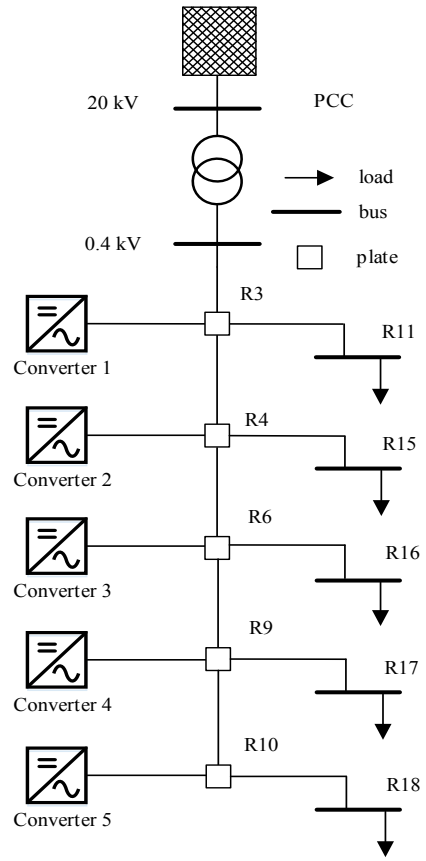


Figure 3. Test grid

power (capacitive), where every inverter has the same reference value. Further information on the grid parameters can be found in [23].

TABLE I. LOAD PARAMETERS

Load	Active Power, P (kW)	Inductive Reactive Power, Q (kvar)
R11	14.55	9.0
R15	145.35	90.09
R16	63.75	39.51
R17	14.55	9.0
R18	63.75	39.51

V. RESULTS

The presented model reduction technique is applied on the test grid described in the prior section. Following, the reduced model of the test grid will be compared to the original model concerning the small-signal stability and the simulation speed. The simulations were performed in the simulation environment MATLAB Simulink.

A. Model reduction of the test grid

The aggregation of the loads is based on (18), the determined parameters can be found in Table II. The parameters of the estimated transfer functions can be found in Table III, where the transfer functions are expressed in the polynomial form: $G(s) = N(s) / D(s)$.

TABLE II. PARAMETERS AGGREGATED LOAD

Quantity	Value
P_{ref}	301.95 kW
Q_{ref}	187.11 kvar
U_{ref}	1 pu
P_{inv}	20 kW
Q_{inv}	6.6 kvar

TABLE III. PARAMETERS ESTIMATED TRANSFER FUNCTIONS

Coefficient	Transfer function	
	$G_p(s)$	$G_q(s)$
D_0	3.98e09	8.016e12
D_1	4.486e07	2.408e11
D_2	2.266e05	2.036e08
D_3	338.3	1.285e06
D_4	1	1
N_0	1.043e08	2.763e13
N_1	7.076e08	-1.837e14
N_2	6.301e08	1.327e13
N_3	7.046e06	4.98e10

B. Comparison of small-signal stability

To compare the small-signal stability of the reduced model with the original model, a voltage step ΔU on the PCC is applied, and P and Q are compared. The scenario is described in Table IV.

TABLE IV. SIMULATION SCENARIO

Feeding voltage, U		
From	To	Value (pu)
0 s	0.5 s	1
0.5 s	0.75 s	1.1

Fig. 4 presents the dynamic response of P of both the original and the reduced model. Striking is the offset between the original grid and the reduced grid, due to the neglect of line impedances and transformer impedances. Fig. 5 illustrates the dynamic response of Q , again for both models. Consequently, an offset can be detected here as well.

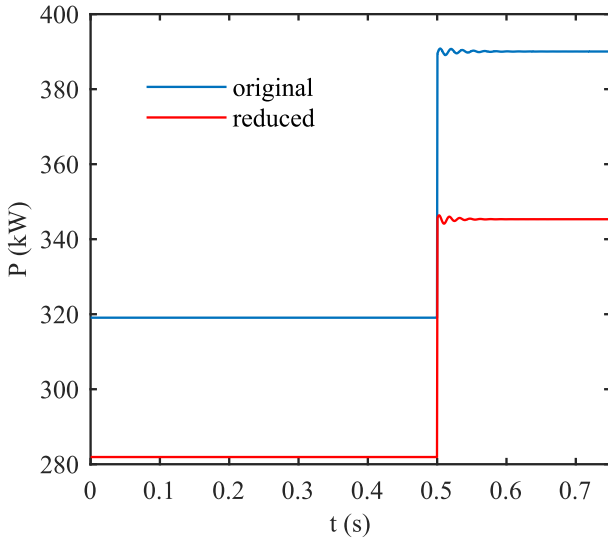


Figure 4. Simulation results of active power at PCC

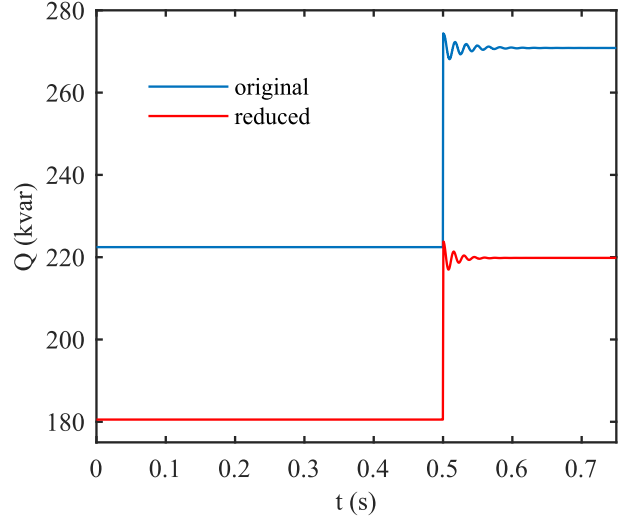


Figure 5. Simulations results of reactive power at PCC

To assess the small-signal stability, the dynamic behavior of P respectively Q is significant. For that purpose, the oscillation behavior of P of the original grid and of the reduced grid is directly compared by removing the offset, see Fig. 6. The reduced grid shows approximately the same oscillation behavior of P compared to the original grid. Nevertheless, a time delay between the two oscillations exist. For better comparability, the characteristics of the oscillations are illustrated in Table V. It can be detected that the power oscillation of the reduced grid shows a higher peak, by a lower peak time. However, the oscillation of the reduced grid is more damped than the oscillation of the original grid, which can be proved due to the smaller settling time of 0.5790 s. Moreover, the frequency of the oscillation of the reduced grid is higher (66.4 s^{-1}) than the oscillation of the original grid (61.8 s^{-1}).

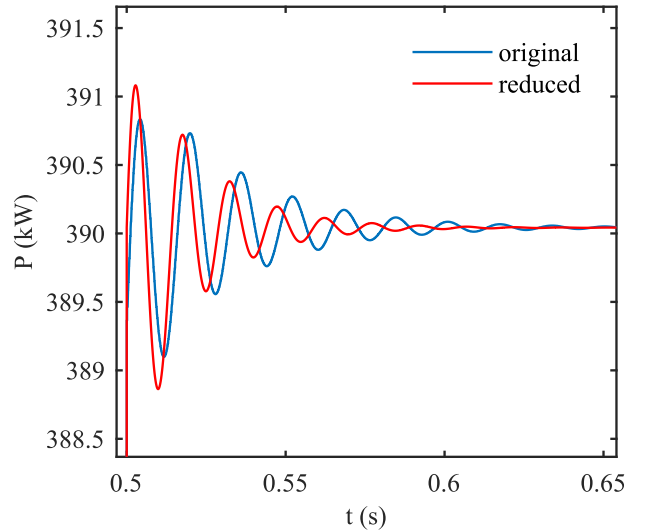


Figure 6. Simulation results of active power at PCC (oscillation behavior)

Despite the existing deviations, the dynamic behavior of P is well approximated by the reduced grid. Using the reduced grid to assess the small-signal stability will result in similar findings.

TABLE V. OSCILLATION CHARACTERISTICS

Quantity	Model	
	Reduced	Original
Peak	391.08 kW	390.83 kW
Peak time	0.5028 s	0.5039 s
Overshoot	26.65 %	20.28%
Settling time	0.5790 s	0.6191 s
Frequency	66.4 s ⁻¹	61.8 s ⁻¹

C. Comparison of simulation speed

Based on the scenario described in Table IV, the simulation speed of the reduced model and the original model were compared. The simulation of the reduced model is 30 % faster than the simulation of the original model. The used hardware and the solver settings are described in Table VI.

TABLE VI. SIMULATION SPEED COMPARISON

Model	Computing Time	Benefit
Reduced	417 s	30 %
Original	595 s	
Used hardware	CPU: i5-4300U 1.9 GHZ, RAM: 4 GB	
Solver settings	ODE 8, time step: 2.5e-6 s	

VI. CONCLUSION

With the increasing amount of power converters connected to the grid, the need for efficient modeling inverter-dominated grids arises. In this paper, a new model reduction method was introduced, which allows efficient model reduction of inverter-dominated grids while retaining input-output-characteristics to assess small-signal stability. This model reduction technique leads to faster simulation times, whereby numerical problems can be avoided. To validate this method a Cigré reference grid was modeled and reduced by applying the new technique. The reduced grid and the original grid were compared in simulations, concerning the small-signal stability and the simulation speed. The simulations reveal that the reduced grid approximates the dynamic behavior well, while the simulation speed is improved significantly. Regarding the steady behavior, the reduced model shows a constant deviation. In further scientific work, the deviation should be analyzed and removed to obtain a reduced model which also approximates the original model in the steady state.

REFERENCES

- [1] Umweltbundesamt, "Umweltbewusstsein in Deutschland 2016: Ergebnisse einer repräsentativen Bevölkerungsumfrage," pp. 16-17 [Online] Available: https://www.bmub.bund.de/fileadmin/Daten_BMU/Pool/Broschueren/umweltbewusstsein_deutschland_2016_bf.pdf. Accessed on: 19.03.2018.
- [2] Bundesregierung, "Das Energiekonzept 2050," pp. 1-4 [Online] Available: https://www.bundesregierung.de/Content/DE/HTML/Breg/Anlagen/info-grafik-energie-textversion.pdf?__blob=publicationFile. Accessed on: 19.03.2018.
- [3] J. Hanson, Hillberg, H. Claes, G. Linhofer, P.K. Steimer, "Power Electronics Building Blocks-Bausteine leistungselektronischer Systeme in elektrischen Netzen," ETG-Fachbericht, no. 98, 2005.
- [4] Z. Liu, T. Jiang, S. Schlegel, D. Westermann, "Simulation and Comparison of Inverter Models in Inverter-dominated Power Distribution Grid," in PESS 2017.
- [5] V. J. Thottuvelil, D. Chin, and G. C. Verghese, "Hierarchical approaches to modeling high-power-factor AC-DC converters," IEEE Trans. Power Electron., vol. 6, no. 2, pp. 179–187, 1991.
- [6] L. Luo and S. V. Dhople, "Spatiotemporal Model Reduction of Inverter-Based Islanded Microgrids," IEEE Trans. Energy Convers., vol. 29, no. 4, pp. 823–832, 2014.
- [7] R. P. Burgos, F. F. Zapata, E. P. Wiechman, and L. D. Salazar, "Power converter analysis and design using Matlab: a transfer function approach," in ISIE'98: Proceedings : IEEE International Symposium on Industrial Electronics : Pretoria, South Africa, University of Pretoria, 7-10 July, 1998, Piscataway, N.J.: IEEE, 1998, pp. 552–557.
- [8] S. Djukic and A. Saric, "Dynamic model reduction: An overview of available techniques with application to power systems," Serb J Electr Eng, vol. 9, no. 2, pp. 131–169, 2012.
- [9] K. Willcox, J. Peraire, "Balanced Model Reduction via the Proper Orthogonal Decomposition," AIAA Journal, Vol. 40, No. 11, Nov. 2002, pp. 2323 – 2330.
- [10] J. H. Chow, Ed., "Power System Coherency and Model Reduction," London: Springer, 2013.
- [11] G. Scarcioiti, "Low Computational Complexity Model Reduction of Power Systems With Preservation of Physical Characteristics," IEEE Trans. Power Syst., vol. 32, no. 1, pp. 743–752, 2017.
- [12] C. Sturk, L. Vanfretti, F. Milano, and H. Sandberg, "Structured model reduction of power systems," in American Control Conference (ACC), 2012: 27 - 29 June 2012, Montreal, QC, Canada, Piscataway, NJ: IEEE, 2012, pp. 2276–2282.
- [13] J. H. Chow, R. Galarza, P. Accari, and W. W. Price, "Inertial and slow coherency aggregation algorithms for power system dynamic model reduction," IEEE Trans. Power Syst., vol. 10, no. 2, pp. 680–685, 1995.
- [14] A. Fathy, "Identification of Coherent Generators for Large-Scale Power Systems Using Fuzzy Algorithm," WSEAS Transactions on Systems and Control, vol. 6, 2011.
- [15] M. H. Haque, "Identification of coherent generators for power system dynamic equivalents using unstable equilibrium point," IEEE Proc. C Gener. Transm. Distrib. UK, vol. 138, no. 6, p. 546, 1991.
- [16] Z. Zhu, G. Geng, and Q. Jiang, "Power System Dynamic Model Reduction Based on Extended Krylov Subspace Method," IEEE Trans. Power Syst., vol. 31, no. 6, pp. 4483–4494, 2016.
- [17] E. Rudy, H. Panzer, and B. Lohmann, "How to choose a single expansion point in Krylov-based model reduction?," Lehrstuhl für Regelungstechnik-TU München, 2009.
- [18] M. Schärferberg, "Untersuchung der Wechselwirkungen zwischen leistungselektronisch integrierten Netzelementen im Verteilernetz," Masterarbeit, TU Ilmenau, Ilmenau, 2017.
- [19] M. Rasheduzzaman, J. A. Mueller, and J. W. Kimball, "Reduced-Order Small-Signal Model of Microgrid Systems," IEEE Trans. Sustain. Energy, vol. 6, no. 4, pp. 1292–1305, 2015.
- [20] X.-F. Wang, M. Irving, and Y. Song, Eds., "Modern Power Systems Analysis," Boston, MA: Springer-Verlag US, 2008.
- [21] P. Kundur, N. J. Balu, and M. G. Lauby, "Power system stability and control," New York: McGraw-Hill, 1994.
- [22] A. Yazdani and R. Iravani, "Voltage-sourced converters in power systems: Modeling, control, and applications," Hoboken, New Jersey, Piscataway, New Jersey: IEEE Press Wiley; IEEE Xplore, 2010.
- [23] K. Strunz et al, "Benchmark systems for network integration of renewable and distributed energy resources," [Paris] (21 rue d'Artois, 75008): CIGRÉ, 2010.

Impact of Increasing Renewable Generation on Power System Stability

Aiko Schinke

Institute of Electrical Power Systems
University of Duisburg-Essen
Duisburg, Germany

István Erlich

Institute of Electrical Power Systems
University of Duisburg-Essen
Duisburg, Germany

Abstract—Renewables like photovoltaic and wind generation have shown a large-scale development in Germany with a total capacity of 99.7 GW in 2016. This paper deals with the quantitative assessment of the impact of a high penetration of converter-based PV and wind generation including HVDC connected offshore wind farms on the overall stability of the larger interconnected transmission system. In particular, the effect of the various requirements regarding voltage control, frequency control and active power control during contingency situations is analyzed. Therefore, a new fully-integrated EMT-type model representing multiple PV power plants in the distribution system is introduced. Simulations on a representative benchmark test network are used to assess and quantify the overall impact and to identify appropriate measures to overall stability of the power system. Finally, the proposed improvements are evaluated considering the present developments in Germany.

Index Terms—Photovoltaic, distribution system, wind generation, HVDC, transmission system, EMT-type model.

I. INTRODUCTION

Over the last decades renewable energy sources (RES) have shown an unexpected development in Germany by providing 33.3 % of the total electricity generation in 2017 [1]. Especially wind turbines (WTs) and photovoltaic (PV) units are driving this development and constituted an installed capacity of 90.3 GW in 2016 [1]. In contrast to other RES, WTs and PV units are converter-based technologies, hence, leading to a lack of rotating mass in the power system. Additionally, the behavior of these units is characterized by the volatility of the primary energy source and a governmental guaranteed feed-in priority towards non-renewable energy sources. Besides the power demand in Germany typically varies between 35 GW and 85 GW during off-peak and peak periods, respectively [2]. Hence the significance of converter-based RES with respect to power system dynamics is clear.

Resulting from the role of RES in the generation mix, the performance requirements vis-à-vis the network are laid-down by law and in various standards. In terms of high and extra-high voltage levels the TransmissionCode 2007 is applicable [3], meanwhile for medium voltage (MV) levels the technical guideline of the BDEW applies [4]. On the other hand generating units in low voltage (LV) networks are facing completely different standards for connection and parallel

operation defined by the VDE [5], hence introduced separately hereinafter. For instance, reactive power supply in steady-state operation is specified according to a fixed $\cos\varphi - P$ characteristic, typically without explicit requirement to contribute to steady state voltage control. Also, there is no requirement regarding dynamic voltage support during large voltage drops. Hence there are no requirements concerning high and low voltage ride through in low voltage networks. Instead small generation units are required to disconnect in cases of voltage or frequency limit violations. Since more than 23.6 GW of the installed capacity of RESs is constituted by LV connected PV units [1], the impact of these units on the power system dynamics is not negligible anymore. With the increasing number of WTs and PV units powered by the policy aims of the German government, it is inevitable to analyse their effect on the dynamic behavior of the superordinate network. In addition, solutions to improve the overall stability shall be developed and benchmarked with the present situation.

For this reason, a new fully-integrated PV model for EMT-type simulations will be introduced, representing the distributed characteristics of multiple PV power plants and taking the corresponding LV and MV requirements into consideration. This model also includes the distribution system (DS) to which the PV units are connected. Besides, common models of Type 3 and 4 WTs are used in wind farms (WFs) representing the average behavior of today's wind generation. In addition, an offshore wind farm (OWF) using HVDC are implemented. For the quantitative assessment of the impact of converter-based RES on the overall stability of power systems, the benchmark test network PST16 presented in [6] will be used. Multiple WFs and PV units are connected to selected bus bars in parallel to the loads. When comparing the installed capacity of converter-based RES with the peak power demand in Germany it is obviously that high shares in the instantaneous electricity generation are constituting a realistic scenario. Hence, an exemplary share of converter-based RES comprising approx. 55 % of the total generation is selected. Based on the simulation results appropriate measures for improvement will be introduced, analyzed and discussed.

II. REQUIREMENTS IN LOW VOLTAGE NETWORKS

The technical requirements for the connection and operation in LV networks are specified in the German standard VDE-AR-

N4105 [5]. This standard contains specifications regarding active and reactive power control, protective functions during grid disturbances and the corresponding quality of those services under certain conditions. In this paper the relevant aspects of the requirements are introduced, which differ from the Transmission Code 2007 and need to be implemented in LV connected units.

A. Active Power Control

Since 2011 the technical requirements in low voltage networks with regard to active power control do not differ from those in (TransmissionCode, 2007). Hence a continuous active power reduction with $\Delta p = 0.4$ p.u./Hz for frequencies between 50.2 and 51.5 Hz is required. Only at a frequency exceeding 51.5 Hz or falling below 47.5 Hz, disconnection is allowed. Although for some power plants exceptions may be allowed [7], these details will not be considered in this paper.

B. Reactive Power Control

In terms of reactive power, generating units are required to contribute to steady state voltage control only upon the request of the distribution system operator (DSO), meanwhile dynamic voltage control is not required. However, in general a reactive power supply during steady state operation is restricted to a characteristic $\cos\phi - P$ curve or to a constant $\cos\phi$ value, hence, not controlling the voltage directly. Moreover, the reactive power during steady state operation is limited to 0.31 p.u. for units with a nominal power between 3.68 and 13.8 kVA and to 0.48 p.u. for larger units. Smaller units are not required to contribute at all.

C. Protective Functions

Any disconnection of the power plants in low voltage networks resulting from voltage or frequency limit violation has to take place in less than 100 ms. Considering terminal voltages, the upper and lower protection thresholds are 1.15 p.u. and 0.8 p.u., respectively. Regarding grid frequency, upper and lower protection thresholds are typically defined as 51.5 Hz and 47.5 Hz, respectively.

D. Resynchronization after Disconnection

Following a disconnection as described above, the power plant is allowed to reconnect and synchronize with the grid after 60 s if voltage and frequency stay within the limits 1.1 p.u. and 0.85 p.u., and 47.5 Hz and 50.05 Hz, respectively. For a short interruption (SI) of less than 3 s duration, reconnection is already allowed after 5 s. The maximum active power ramp rate is 0.1 p.u./min., with the active power set-point immediately before SI as a base.

III. INTEGRATED PV AND DS MODEL

More than 93 % of the installed capacity of PV generation in 2015 was connected to LV or MV levels, i.e. to the distribution system (DS). The model and control representation of a representative PV unit including a load in parallel and equivalent circuit of the superordinate DS (based upon [8]) is shown in Fig. 1. In this context the values of the DS equivalent are calculated individually for LV and MV connected PV units, respectively. The PV unit itself comprises of a three-phase connected two-level inverter, a PV array and the control system.

Steady state voltage control is performed through transformer tap changers and the system automatics of the DS are neglected.

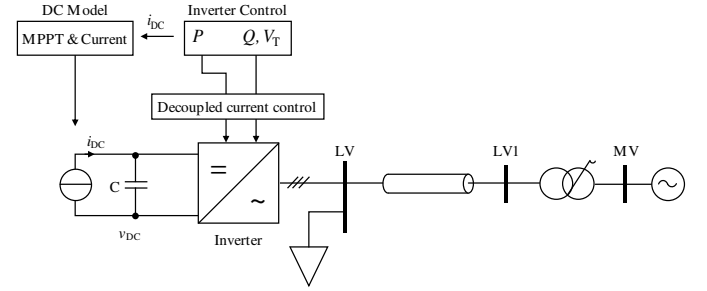


Fig. 1 PV unit model and control representation.

A. PV-Array

To improve computational efficiency, the PV model, shown in Fig. 2 proposed in [9], is implemented.

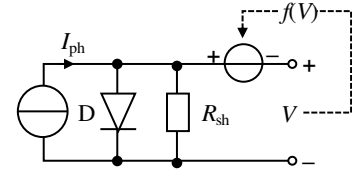


Fig. 2 Equivalent circuit of the implemented PV array model.

The behavior of the $I-V$ characteristic is described by equations (1) and (2):

$$I = I_{ph} - I_s \left[e^{\frac{q f(V)}{N_s k_B T A}} - 1 \right] - \frac{f(V)}{R_{sh}} \quad (1)$$

$$f(V) = \alpha_0 + \alpha_1 V + \alpha_2 V^2 + \alpha_3 V^3 \quad (2)$$

In these equations I_{ph} is the photoelectric current, I_s the reverse saturation current, R_{sh} the shunt resistance and A the ideality factor, where q : elementary charge ($1.60217657 \times 10^{-19}$ C), k_B : Boltzmann constant ($1.3806488 \times 10^{-23}$ J/K), T : module temperature, and N_s : number of cells connected in series. The parameters α_0 , α_1 , α_2 , and α_3 can be derived for a given module type as shown in [9].

B. Three-Phase Two-Level Inverter

The chosen three-phase two-level (3P-2L) inverter is one of the most common topologies for PV inverters and a well-established technology [10]. In addition, the MMPT is carried out centralized and a transformer-less topology is implemented, i.e. the inverter utilizes single-stage conversion [11].

C. Control Schema

The inverter control schema is designed to represent the distributed characteristics of PV power plants in the DS, fulfilling the requirements at the MV and LV level (see [4] and [5]). Therefore, an active power reduction control determines the active power set-point p_{red} depending on the grid frequency. Additionally, for LV connected PV units the set-point p_{red} is set

to zero when exceeding the frequency or voltage limits for more than 100 ms. The PV array model based on equations (1) and (2) uses the current DC voltage v_{DC} as illustrated in Fig. 3 to calculate the PV module current $i_{PV,OP}$ and voltage $v_{PV,OP}$ for the corresponding operating point (OP).

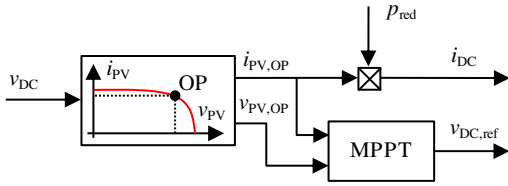


Fig. 3 PV model, MPPT control and DC voltage reference.

The maximum power point tracker (MPPT) uses the OP current and voltage to calculate reference DC voltage $v_{DC,ref}$ based on the incremental conductance algorithm [12]. The DC current source set-point i_{DC} is calculated by multiplying OP current $i_{PV,OP}$ and active power set-point p_{red} in a feed forward connection.

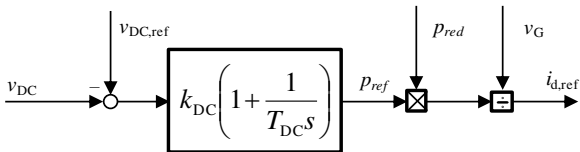


Fig. 4 DC voltage control and active current reference.

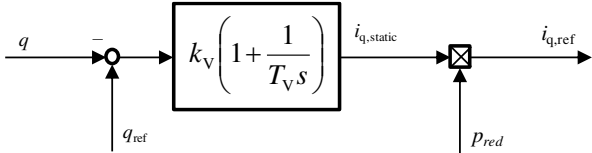


Fig. 5 Reactive power control and current reference.

Fig. 4 and Fig. 5 illustrate commonly used DC voltage and reactive power control schemes as shown in [13], extended by a feed-forward term for the active power set-point. Generic current control, current limitation and reference voltage limitation are implemented without any modifications as described in [14].

IV. INTEGRATED WIND TURBINE MODELS

More than 97 % of the installed capacity of wind generation in 2015 was connected to the MV or HV levels. Additionally, Type 3 and Type 4 WT were constituting 33 % and 52 % of the total installed capacity in Germany in 2015, respectively. Hence a representative wind farm is used in this paper, whereby several Type 3 and 4 WTs are connected in parallel either to the MV or the HV level. Furthermore, an offshore wind farm using HVDC transmission is implemented as introduced hereinafter. In this context 3P-2L converters are used (as introduced for PV).

A. Type 3 Wind Turbine Model

The model and control representation of a Type 3 WT with doubly fed induction generator (DFIG) as introduced in [15] is depicted in Fig. 6. The general structure of the control can be divided into the machine-side converter (MSC) and the grid-side converter (LSC), as well as the speed control. In this context the reduced third-order model DFIG model is used, since it is

suitable to represent the response of common wind power plants, especially in terms of reactive power support during voltage drops due to external faults. However, the model was already introduced by Rueda et al. [15], hence, the specific control schema will not be discussed hereinafter.

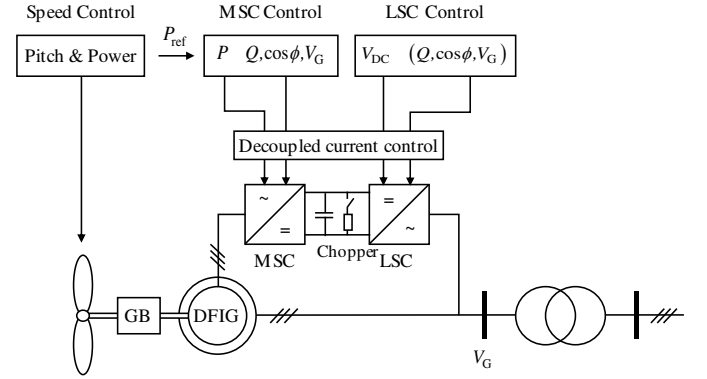


Fig. 6 Type 3 WT model and control representation [15].

B. Type 4 Wind Turbine Model

The general structure of the Type 4 WT control is shown in Fig. 7. In this context the feed-in active power of the synchronous generator and the machine side converter is assumed to be remain constant for the applied time periods of investigation hereinafter. Therefore, a controlled current source is used representing the constant power supply of the generator into the DC link (acc. to [13]). However, the model was already introduced by Neumann et al. [13], hence, the specific control schema will not be discussed hereinafter.

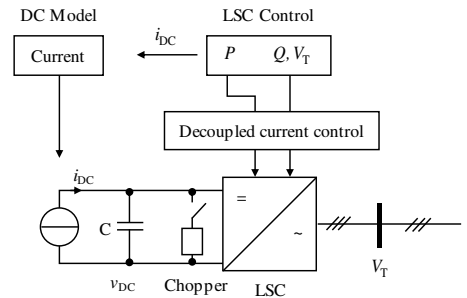


Fig. 7 Type 4 WT model and control representation [13].

C. Offshore Wind Farm & HVDC

In terms of offshore wind farms (OWFs) more than 74 % of the installed capacity in Germany corresponds to interconnection lengths greater than 40 km [16]. Hence, the interconnection between OWF and grid is typically carried out using high voltage direct current (HVDC) transmission [17]. Therefore, voltage-sourced modular multilevel converters (VSC-MMCs) are used for a HVDC transmission link of an OWF as illustrated in Fig. 8. On the offshore side a typical collector and submarine network is used, as shown in [14].

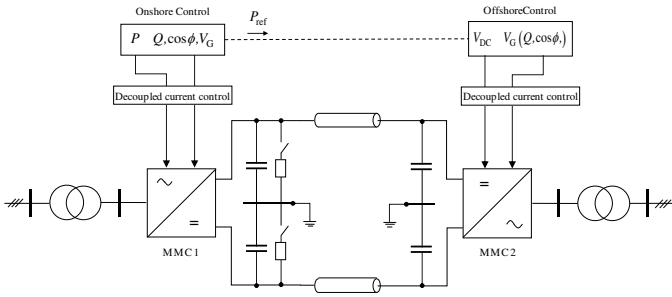


Fig. 8 HVDC transmission link model representation.

The control of the HVDC link is carried out using decoupled current control on both sides. The offshore side converter is controlling the DC voltage and reference active power via pulse width modulation (PWM) as shown in [18]. However, the model was already introduced in an example of PowerFactory [18], hence, the specific control schema will not be discussed hereinafter.

V. BENCHMARK TEST NETWORK & SIMULATIONS

To simulate the impact of distributed renewable generation on the power system the test network PST 16 as depicted in Fig. 9a as well as the previously introduced models are used. The test grid represents a 380/220 kV transmission system with typical line parameters. In prior studies of Teeuwesen [6] the grid was supplied exclusively by thermal and hydro power plants with a total load of 16.8 GW of active power. The PV and DS models have been placed at eight selected connection points supplying 900 MW each, accounting for 39.9% of the total generation. The WFs (including the OWF) have been placed at ten selected

connection points supplying 300 MW each, accounting for 15 % of the total generation. To keep the total power generation unchanged, some of the synchronous generators are removed. A three-phase short circuit of 150 ms duration behind a fault impedance at bus C1 was used to study the impact of different control strategies on dynamic behavior of the test grid.

A. Simulation with Standard Requirements

Following the three-phase short circuit, the terminal voltages of the PV units close to the fault drop below 0.8 p.u. (see Fig. 10). Therefore, the protection relays of the LV connected PV units C1 and C3 are activated since the voltage does not recover within 100 ms. As a result, both PV units are disconnected 150 ms after fault onset leading to a lack of active and reactive power. Meanwhile the synchronous generators accelerate due to the three-phase short circuit during the fault. Hence the frequencies at the terminals of the synchronous generators are increasing as shown in Fig. 11. However, since no system automatic is implemented in the DS to reduce the load in case of violation of the voltage limits, the synchronous generators are not able to stabilize the power system after fault clearing. Therefore, all generators continue accelerating even after fault-clearing (see Fig. 11). Finally, 850 ms after fault clearing the first generators in area A and C close to the fault location go out of step and start operating asynchronously (see Fig. 12). The result reveals that the disconnection of the PV units in the low voltage DS has severely degraded system security, and the whole system runs the risk of losing stability. Post-fault stabilization would require several measures to improve voltage stability (e.g. FACTS) and frequency stability (e.g. additional frequency-responsive spinning reserve).

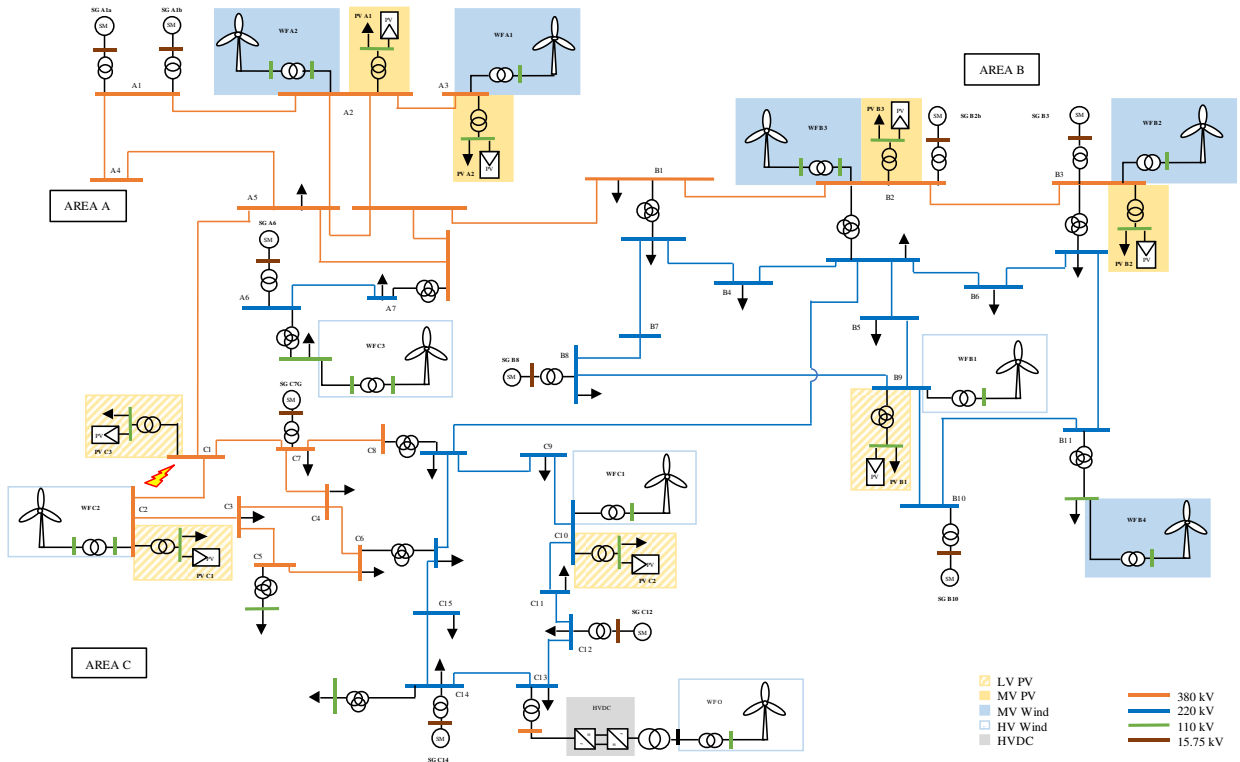


Fig. 9 PST 16 including PV and WTs at different connections and showing fault location at busbar C1.

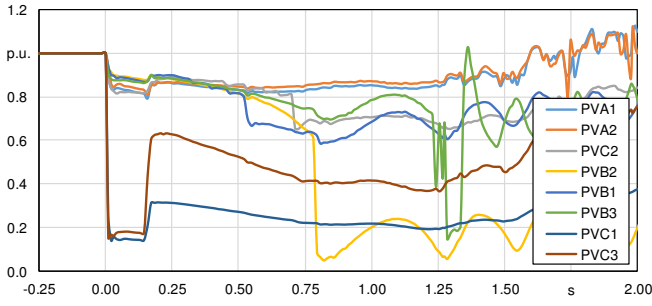


Fig. 10 Terminal voltages of PV units in the test grid.

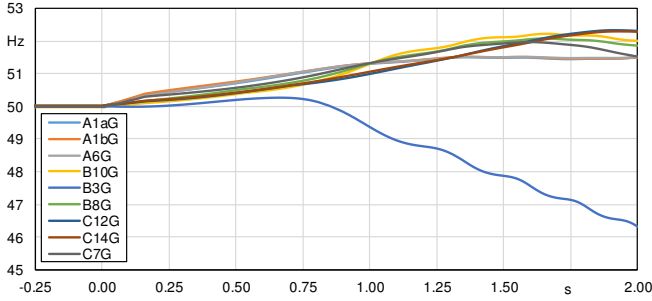


Fig. 11 Grid frequencies at the synchronous generators.

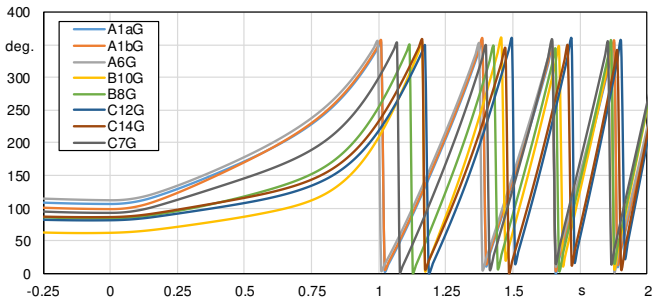


Fig. 12 Rotor angles of the synchronous generators.

B. Simulation with improved Requirements

As already mentioned above the post-fault disconnection of the PV units in the low voltage DS can potentially lead to system instability. As a solution, this paper proposes the modification of the requirements of the TransmissionCode 2007 and the application for all voltage levels, i.e. also for low voltage connected PV units. In this context the implementation of two major requirements (as shown in Fig. 13) has been determined to be of particular importance:

- Low and high voltage ride through (LVRT & HVRT) capability is proposed to prevent power plants connected to the low voltage network from post-fault disconnection
- Dynamic voltage control without any dead band and the application of equation (3) is proposed

$$k = \frac{\Delta i_{q,dyn.}}{\Delta v} \geq 2.0 p.u. \quad (3)$$

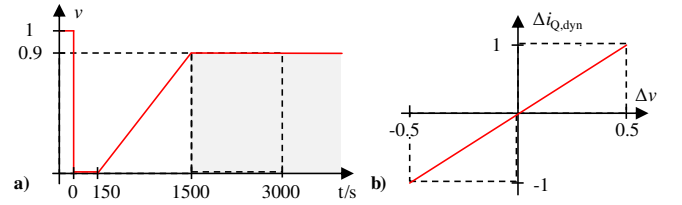


Fig. 13 Proposed improvements for the requirements of generating units.

For the LVRT & HVRT requirements as illustrated in Fig. 13a disconnection is only allowed, if the voltage drops below the red boundary, during the interval from 150 to 1,500 ms after the fault occurrence (i.e. voltage values inside the hatched area). After 1,500 ms the standard voltage limits apply and disconnection is only admissible through system automatics. The proposed dynamic voltage control as shown in Fig. 13 requires a continuous reactive current supply $\Delta i_{Q,dyn.}$ using a proportional constant k (greater than 2 p.u.) in case of voltage deviations Δv according to equation (3). The proposals above are contrasting the present requirements of the TransmissionCode 2007 but participation of all available power plants during disturbances is ensured, even for larger fault distances.

The simulation was re-run by considering the improved requirements and using a proportional constant k of 4 p.u. Fig. 14 depicts the resulting post-fault terminal voltages of the PV units in the low voltage network. Only the terminal voltages of the PV units C1 and C3 close to the fault location drop below 0.85 p.u. during the fault. All the terminal voltages can be stabilized immediately after fault clearing within less than 5 ms.

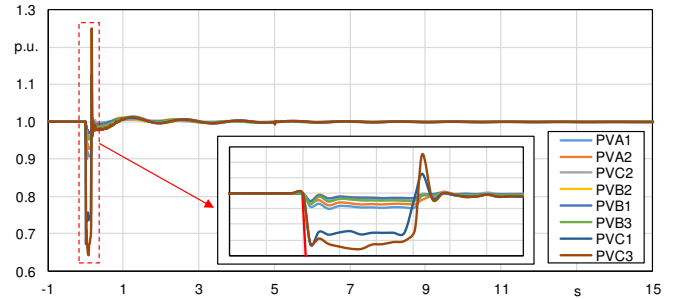


Fig. 14 Terminal voltages of PV units in the test grid with improvements.

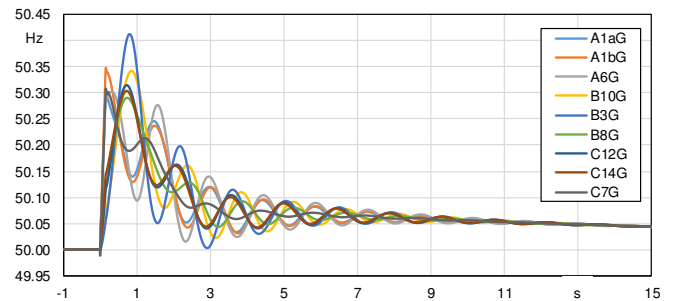


Fig. 15 Grid frequencies at the synchronous generators with improvements.

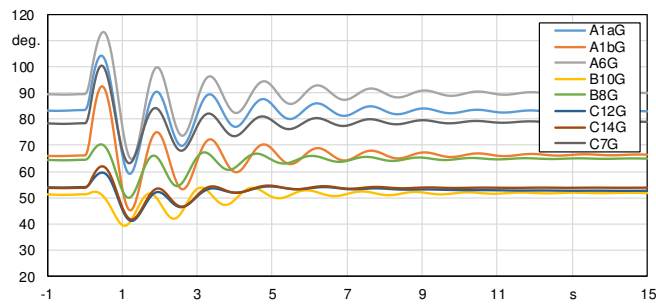


Fig. 16 Rotor angles of the synchronous generators with improvements.

Hence all PV units can fulfill the LVRT & HVRT requirements completely. All synchronous generators remain in stable operation, as illustrated in Fig. 15. Most of the synchronous generators experience initial acceleration due to the three-phase short circuit but settle to values below 50.15 Hz within 3 s after the fault clearing. In addition, rotor angle stability of all synchronous generators is ensured all the time. Therefore, the proposed changes in the requirement additional features ensure voltage, frequency and rotor-angle stability, and the protective voltage thresholds acc. to VDE-AR-N 4105 are exceeded for only two PV units (C1 and C3) for a duration of less than 200 ms. Most of the PV units connected to a low voltage DS therefore implicitly fulfil the present requirements without any necessity for disconnections. Even when thresholds are exceeded safe operation can be still ensured due to the short time duration (below 200 ms) of critical operation.

VI. CONCLUSION

This paper has demonstrated the potential risks of instable operation of the power system that can be caused by the presently applicable requirements on generating units connected to the low voltage DS. Improved requirements have been proposed and it has been shown that with the implementation of the proposed solution the power system remains stable for the same fault conditions. Therefore, it has been shown that the proposed requirements enhance the overall stability of the power system with a high penetration of PV and wind generation appropriately. By applying LVRT & HVRT requirements acc. to all PV units remain connected to the grid during and after the fault. In addition, the present protective voltage thresholds can be largely maintained by applying an improved dynamic voltage control based on. Compared to other measures, e.g. installing new FACTS units at connections between the transmission and distribution system or increasing the frequency-response reserve, this proposal could be realized rather easily by software-updates of the PV inverters. Finally, the proposed improvements can be considered as an economical measure to reduce the grid development costs for the TSOs and DSOs by utilizing already available resources.

REFERENCES

- [1] Bundesnetzagentur, "EEG in Numbers," 2016. [Online]. Available: www.bundesnetzagentur.de. [Accessed May 2018].
- [2] German TSOs, "Auswirkungen reduzierter Schwungmasse auf einen stabilen Netzbetrieb," 2014. [Online]. Available: www.regelleistung.net.
- [3] TransmissionCode 2007, "Network and System Rules of the German Transmission System Operators," Verband der Netzbetreiber - VDN – e.V. beim VDEW, Berlin, 2007.
- [4] BDEW, "Technical directive for generating units connected to medium-voltage networks," Bundesverband der Energie- und Wasserwirtschaft e.V., Berlin, 2008.
- [5] VDE-AR-N4105, "Power generation systems connected to the low-voltage distribution network," VDE, Berlin, 2011.
- [6] S. P. Teeuwesen, *Oscillatory Stability Assessment of Power Systems using Computational Intelligence*, Duisburg: University of Duisburg-Essen, 2005.
- [7] German Federal Directive, "Ordinance for ensuring the technical safety and system stability of the electricity network (Systemstabilitätsverordnung - SysStabV)," BGBl. I S. 1635, 2012.
- [8] M. K. Donnelly et al., "Impact of Distributed Utility on Transmission System Stability," *IEEE Transactions on Power Systems*, vol. 11, no. 2, pp. 741-746, 1996.
- [9] Y. Mahmoud and E. F. El-Saadany, "A Photovoltaic Model with Reduced Computational Time," *IEEE Transactions on Industrial*, vol. 62, pp. 3534-3544, 2014.
- [10] Z. Özkan and A. M. Hava, "Three-Phase Inverter Topologies for Grid-Connected Photovoltaic Systems," *IEEE International Power Electronics Conference, Hiroshima, Japan*, pp. 498-505, 2014.
- [11] W. Xiao, *Photovoltaic power system: modelling, design and control*, Hoboken, NJ (USA): John Wiley & Sons, 2017.
- [12] B. Liu, S. Duan and P. Xu, "Analysis and Improvement of Maximum Power Point Tracking Algorithm Based on Incremental Conductance Method for Photovoltaic Array," *IEEE International Conference on Power Electronics and Drive Systems, Bangkok, Thailand*, p. 637-641, 2007.
- [13] T. Neumann et al., "Novel Direct Voltage Control by Wind Turbines," *IEEE Power and Energy Society General Meeting (PESGM), Boston, MA, USA*, 2016.
- [14] I. Erlich, et al., "New Control of Wind Turbines Ensuring Stable and Secure Operation Following Islanding of Wind Farms," *IEEE Transactions on Energy Conversion*, vol. 32, no. 3, pp. 1263-1271, 2017.
- [15] F. M. Gonzalez-Longatt and J. L. Rueda, *PowerFactory Applications for Power System Analysis*, Cham: Springer, 2014.
- [16] Fraunhofer-Institut für Windenergie und Energiesystemtechnik (IWES), "Windenergie Report Deutschland," Fraunhofer Verlag, Kassel, 2016.
- [17] E. Mircea, *Advanced Solutions in Power Systems : HVDC, FACTS, and Artificial Intelligence*, Somerset: Wiley, IEEE, 2016.
- [18] DIgSILENT PowerFactory, "HVDC Connected Offshore Wind Farm, r1337," DIgSILENT PowerFactory, Gomaringen, Germany.

Comparison and Evaluation of Voltage Stability Indices for OPF application

Johannes Kayser, Florian Sass, Student Member, IEEE, Dirk Westermann, Senior Member, IEEE

Power System Group
Technische Universität Ilmenau
Ilmenau, Germany

Abstract—The vast increase of renewable energy sources causes future challenges for the power system. Therefore, voltage stability became a major concern in order to maintain a reliable power supply. This paper analyses and compares different methods to indicate the voltage stability condition of an operation point in order to forecast an imminent voltage collapse. In distinction to existing comparisons of voltage stability indicators, a new validation criterion has been used to evaluate the applicability and reliability for transmission systems.

Keywords—voltage stability; voltage collapse; indication; index; degree of meshing;

NOMENCLATURE

Indices and sets

i, j	Bus i and j respectively
L	Load
G	Generator

Variables

V	Voltage magnitude
δ	Voltage angle
\underline{S}	Apparent power
P	Active power
Q	Reactive power
\underline{Z}	Branch impedance
θ	Branch impedance angle
R	Branch resistance
X	Branch reactance
Y	Admittance matrix
\underline{I}	Vector of complex currents

I. INTRODUCTION

The Expansion of electrical power systems could not satisfy the vast increase of renewable energy generation in the past [1]. This causes a higher utilization of the existing capacities and weakens the grid regarding faults and disturbances. Therefore, voltage stability became a major concern. In distinction to the operational security limits, voltage stability is defined as the ability of a power system to maintain steady voltages at all buses in the system after being subjected to a disturbance [2], [3].

Stabilizing effects can be reached by using FACTS and VSC-HVDC-systems to provide reactive power. In order to provide an optimal reactive power infeed, it is necessary to be aware of the voltage stability condition of the power system. Originally, the determination of voltage stability conditions requires long term dynamic simulations since the voltage behavior is affected by the nonlinear dynamic performance of the power system [2]. Such complex considerations are hard to integrate into an Optimal Power Flow (OPF) calculation. In order to minimize resources and maintain a high performance for the evaluation of voltage stability condition of a power system, various alternative methods have been developed. These methods can be distinguished by the different approaches, such as modal analysis [1], Jacobian determinant [4], sensitivity analysis [5] and P - V curve based line indices [6]–[8].

With intent to obtain a fast method for future OPF application, chosen methods have been discussed, compared and validated in this paper. In distinction to former comparisons of voltage stability indices (e.g. [7], [9]), a sensitivity analysis method is compared to several line index methods. Furthermore, the reliability and accuracy of these methods have been examined for a meshed system considering the specific amount of connected branches at the stressed bus. The analysis has been made by using a validation algorithm that differs from procedures of existing comparisons of voltage stability indices. The chosen methods are introduced and compared in section II. In section III the validation process is presented and discussed. Subsequently, the numerical case study and conclusions are presented in section IV and V.

II. METHODS TO EVALUATE VOLTAGE STABILITY

In order to evaluate voltage stability of a steady state system, several methods have been proposed. To achieve a high performance for optimization processes several line index methods and a sensitivity analysis have been chosen for further considerations. The choice of the methods is referred to the numerical complexity with intent to obtain a fast method. This section focuses on the formulation and discussion of the chosen voltage stability indices and gives a first comparison of the methods based on their assumptions and formulations.

A. Line Index Methods

The line index methods, such as the Line Stability Index (*LMN*) from [6], the Line Stability Factor (*LQP*) from [7], the Fast Voltage Stability Index (*FVSI*) from [7] and the New Voltage Stability Index (*NVSI*) from [8] have been derived from a two bus system as shown in Figure 1 and were developed to determine the distance to voltage collapse of the power receiving bus.

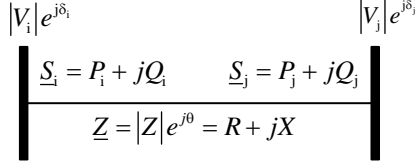


Figure 1. 2-Bus System representation

The theory of the line index methods is based on the P - V curve of a transmission line between two buses. By the usage of the quadratic voltage equation (1) a stability criterion can be formulated.

$$V_j = \sqrt{\frac{V_i^2}{2} - QX} \pm \sqrt{\frac{V_i^4}{4} - X^2 P^2 - XV_i^2 Q} \quad (1)$$

Therefore, the radicand of the quadratic voltage equation must be greater than zero to maintain voltage stability. The range to indicate voltage stability for each line index bears between zero (unloaded) and one (voltage collapse) as shown in Figure 2. Indices greater than one represent the unstable range of the P - V curve.

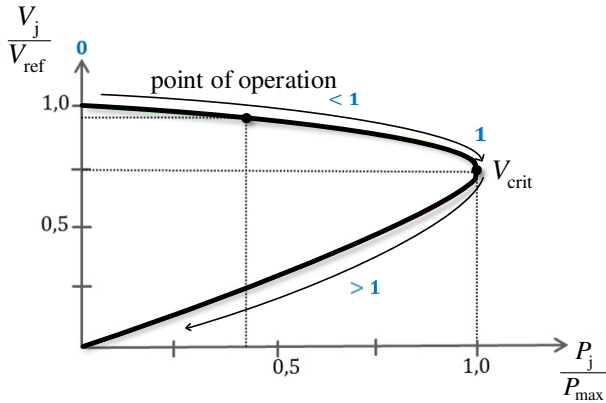


Figure 2. P - V -Curve including index interpretations

The line indices are referred to the respective line in the power system and indicate the voltage stability condition of the power receiving bus as the most stressed bus connected to the respective line.

The derivations of the different line indices are based on different formulations of the power flow between two buses. The *LMN* has been developed on the basis of the power flow formulation as in (2) and (3).

$$S_j = \frac{|V_i||V_j|}{Z} e^{j(\theta-\delta_i+\delta_j)} - \frac{|V_j|^2}{Z} e^{j\theta} \quad (2)$$

$$S_i = \frac{|V_i|^2}{Z} e^{j\theta} - \frac{|V_i||V_j|}{Z} e^{j(\theta+\delta_i-\delta_j)} \quad (3)$$

The authors of the *FVSI*, *LQP*, and *NVSI* referred to a power flow formulation based on the current flow as in (4) and (5).

$$I = \frac{V_i e^{j\delta_i} - V_j e^{j\delta_j}}{|Z| e^{j\theta}} \quad (4)$$

$$I = \left(\frac{S_j}{V_j} \right)^* = \frac{P_j - jQ_j}{V_j e^{j\delta_j}} \quad (5)$$

From this approaches the authors established concerning specific assumptions the quadratic voltage equation. So a lossless power system has been assumed to establish the *LQP* and *NVSI* indices while for the *FVSI* the voltage angles have been neglected since it has been assumed that neighboring buses hold approximately equal voltage angles. The different indices have been derived from the respective resulting stability criterion and are defined as follows.

$$LMN = \frac{4XQ_j}{[V_i \sin(\theta - \delta)]^2} \leq 1 \quad (6)$$

$$FVSI = \frac{4|Z|^2 Q_j}{|V_i|^2 X} \leq 1 \quad (7)$$

$$NVSI = \frac{2X \sqrt{P_j^2 + Q_j^2}}{2Q_j X - V_j^2} \leq 1 \quad (8)$$

$$LQP = 4 \left[\frac{X}{|V_i|^2} \right] \left[\frac{X}{|V_i|^2} P_i^2 + Q_j \right] \leq 1 \quad (9)$$

It can be noticed that in contrast to the *LQP* and *NVSI* there is no direct relation to active power flow. Therefore active power is only be considered by indirect relations like the voltage angle (only *LMN*) and voltage magnitude which may cause a loss of accuracy.

B. L Index Method

The *L*-index method is introduced in [5] and is a sensitivity analysis based on the admittance matrix relation of the power system. In contrast to the line indices the *L*-index points directly to the load buses of a system regarding voltage stability indication. The derivation is based on following relation.

$$\begin{pmatrix} I_L \\ I_G \end{pmatrix} = \mathbf{Y} \cdot \begin{pmatrix} V_L \\ V_G \end{pmatrix} = \begin{pmatrix} Y_{LL} & Y_{LG} \\ Y_{GL} & Y_{GG} \end{pmatrix} \cdot \begin{pmatrix} V_L \\ V_G \end{pmatrix} \quad (10)$$

In order to do sensitivity analysis the equation must be sorted by known and unknown variables. To sort the equation \mathbf{Y} must be converted to a hybrid matrix \mathbf{H} by partial inversion

of the submatrices which yields (11) with its resulting submatrices defined as (12)-(15).

$$\begin{bmatrix} V_L \\ I_G \end{bmatrix} = \mathbf{H} \cdot \begin{bmatrix} I_L \\ V_G \end{bmatrix} = \begin{bmatrix} Z_{LL} & F_{LG} \\ K_{GL} & L_{GG} \end{bmatrix} \cdot \begin{bmatrix} I_L \\ V_G \end{bmatrix} \quad (11)$$

$$Z_{LL} = Y_{LL}^{-1} \quad (12)$$

$$F_{LG} = -Y_{LL}^{-1} Y_{LG} \quad (13)$$

$$K_{GL} = Y_{GL} Y_{LL}^{-1} \quad (14)$$

$$L_{GG} = Y_{GG} - Y_{LG} Y_{GL} Y_{LL}^{-1} \quad (15)$$

To evaluate the voltage stability of a system the top line of the equation is sufficient.

$$|V_L| = |Z_{LL}| \cdot |I_L| + |F_{LG}| \cdot |V_G| \quad (16)$$

Assuming that $|Z_{LL}| \cdot |I_L| \approx |V_L|$ the equation can be converted to the L -index definition (17).

$$L = \left| 1 - \frac{F_{LG} V_G}{V_L} \right| \quad (17)$$

C. Comparison of the Methods

In this section the introduced methods have been compared to each other with respect to defined criteria such as assumptions, required variables and information content. The following table is referred to [9] with the extension by the L -index.

TABLE 1. COMPARISON OF LMN , $FVSI$, LQP , $NVSI$ AND L -INDEX

Comparison of Voltage stability indices	Criteria		
	Assumptions	Variables	Information content
L	$\frac{R}{X} \ll 1$	Y, V	Distance to voltage collapse
LMN	-	Q, X, V, θ, δ	Distance to voltage collapse
$FVSI$	$\delta \approx 0$	Q, V, Z	Distance to voltage collapse
$NVSI$	$R = 0$	Q, P, V, X	Distance to voltage collapse
LQP	$\frac{R}{X} \ll 1$	Q, P, V, X	Distance to voltage collapse

Considering the assumptions from Table 1 it can be noticed that almost every method requires a lossless power system or a power system with a very low R/X relation. Therefore these methods are only suitable for high voltage transmission systems to maintain a high accuracy. Furthermore, the required information for the calculations are similar and regard to the power flow solution of an operating point, the topology and designing data. All these methods yield an index that indicates the distance to the point of voltage collapse.

III. VALIDATION PROCESS

In this chapter, the validation procedure is introduced. In [6]–[9] the authors expected the power system to be voltage instable if the respective index gains the value 1. As defined in [1] voltage instability occurs if the Jacobi-matrix becomes singular. A singularity of the Jacobi-matrix eventuates if the solution of (1) becomes complex. At this point, the convergence can't be achieved and there is no numerical solution of the power flow calculation. To validate the introduced methods, the power system must be increasingly stressed until the Jacobi-matrix becomes singular and no power flow solution exists. In contrast to the validation process from [6]–[9] a reliable and accurate functionality of the methods is verified if the respective index gains the value 1 at the breaking point. The algorithm described in Figure 3 is applied in the introduced validation procedure.

Since most of the considered methods are based on a single line between two buses, it is necessary to determine the functionality of these methods for meshed systems by considering buses with a different amount of connections to

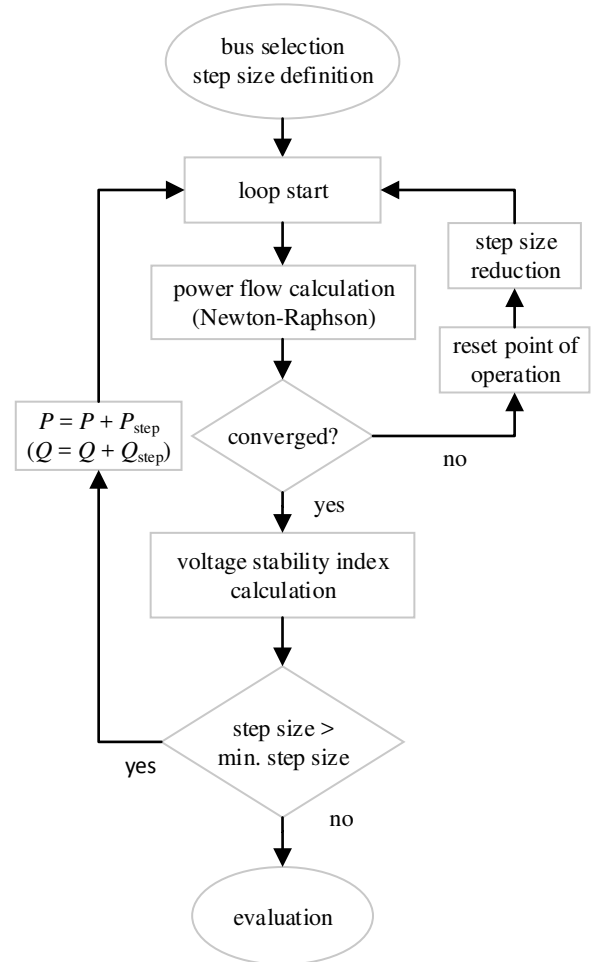


Figure 3. Algorithm for a validation process

further buses. Furthermore, the reliability and accuracy of the methods have been analyzed with respect to the influence of either active or reactive overload.

IV. NUMERICAL CASE STUDY

The introduced methods initially have been verified in a 2-bus system. Since the 2-bus system is the basis of the derivations of the methods, it is a suitable test system to distinguish the respective characteristics of the methods. Subsequently, the analysis of the introduced voltage stability indices has been performed on the IEEE 118-Bus Test System from [10] to validate the methods within a meshed test environment with regard to a general applicability and reliability for transmission systems.

A. 2-Bus Test System

To proof the functionality and to determine the characteristics of the methods regarding increasing stress on a bus voltage the methods have been initially tested in a 2-bus test system as shown in Figure 1. The Test system consists of one slack bus and one load bus connected via a branch. Furthermore the system is defined as a high voltage transmission system with a very low R/X relation.

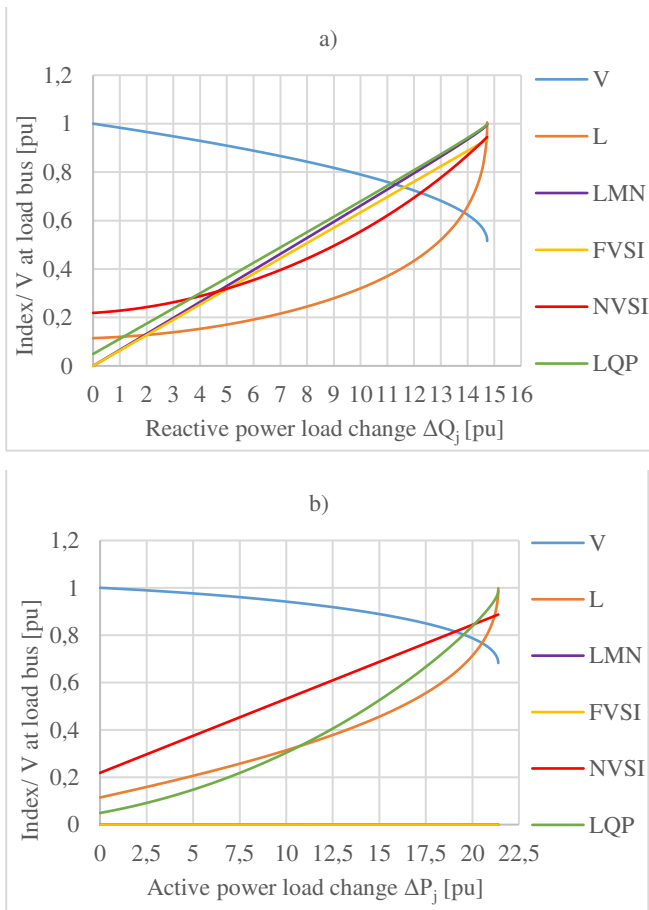


Figure 4. Index progressions for a) reactive and b) active power load increase at load bus

In Figure 4 the reactive and active power load respectively have been increased until the voltage at the load bus collapsed. Regarding the reactive power load increase shown in Figure 4a, it can be noticed that every index method is been suitable

to forecast an imminent voltage collapse. All the indices reached a final value close to one at the point of voltage collapse. While the LMN , $FVSI$ and LQP index have an almost linear slope, the L and $NVSI$ index have a nonlinear slope regarding reactive power load change.

In Figure 4b the active power load has been increased until the voltage at the load bus has collapsed. Unlike to the reactive power load change, in this case, only the L , $NVSI$ and LQP index have been able to indicate an imminent voltage collapse. Thereby the L and LQP index have been more accurate than the $NVSI$ while the LMN and $FVSI$ haven't shown any change of their index value regarding active power load change. The L -index has a nonlinear slope regarding to active power load change while the $NVSI$ index has unlike to the reactive power load change an almost linear slope and the LQP a nonlinear slope.

The analysis in the 2-bus test system has shown that all indices are able to indicate voltage collapse regarding to a reactive power load change while only the LQP , $NVSI$ and L index have been able to indicate the imminent voltage collapse regarding to an active power load change. The LMN and $FVSI$ index haven't been responding to the active power load change which leads to the assumption that these two methods are only sensitive to reactive power changes.

B. IEEE 118-Bus test system

After the verification in an unmeshed system the methods have been analyzed in the IEEE 118-bus test system. The IEEE 118-bus test system is a high voltage transmission system and consists of 54 synchronous machines, 64 load buses and 186 branches. The low R/X relation satisfies the requirement of the methods. Furthermore, the test system includes buses with up to 5 connected branches and is therefore suitable for considerations regarding the impact of the degree of meshing. To analyze the functionality of the methods regarding to the degree of meshing two load buses (Bus 45 and Bus 75) with a different amount of branch connections have been chosen randomly. Bus 45 is connected to three buses while bus 75 has 5 connected buses.

In Figure 5a the reactive power load change has been increased at bus 45. All the index methods have been able to forecast the imminent voltage collapse with high accuracy. Only the deviation of the $NVSI$ index has increased compared to the unmeshed system in Figure 4a.

Figure 5b shows the indices over the increase of active power load at bus 45. In this case, the impact of the degree of meshing on the index results is more clearly. The LQP indicates an imminent voltage collapse much earlier than it occurred while the L and $NVSI$ index have been able to indicate the voltage collapse with high accuracy. It can be noticed that somehow the LMN and $FVSI$ index respond to an active power load change which cannot directly be affiliated with the higher degree of meshing.

Figure 5c shows the different indices over the reactive power load change at bus 75. It can be noticed that all indices excluding the L -index indicated an imminent voltage collapse earlier than it occurred. This can be affiliated with the high

number of connected buses that provide reactive power for the stressed bus. All the line index methods consider only the interaction of two buses which results in a relation between the provided reactive power from bus i and the voltage drop at bus j . The stressed bus is, however, receiving reactive power from other connected buses that contribute to maintain voltage stability. This may cause an early indication of a voltage collapse. The L -index is in opposition to the line index methods based on a sensitivity analysis that is able to consider the effect of every generator unit on the stressed bus.

Figure 5d shows the indices over the increase of active power load change. As with the reactive power load change the line index methods indicated an early voltage collapse. In this case the L -index hasn't been able to indicate the voltage collapse by its final value.

The analysis in a meshed high voltage transmission system has shown that the L -index method is the most reliable index method. However, the L -index method is not reliable for every bus in the considered test system and its accuracy seems to have a dependency on the degree of meshing of the stressed bus. To proof this assumption the calculations have been made for every load bus in the test system. The L -index values at the point of voltage collapse regarding active and reactive power load change respectively are shown in Figure 6.

Considering the connected branches of the respective buses it can be noticed that the reliability of the L -index method decreases with an increasing number of connections. However, the quality of the result is also affected by further impact factors since also buses with only two or three connected branches show unsatisfying indication results. A deeper analysis might be necessary.

V. CONCLUSIONS

In this paper different methods to indicate the point of voltage collapse have been analyzed, compared and validated. The intention was to obtain a reliable and fast method for the usage within an optimization process for reactive power infeed. Therefore the methods have been validated and analyzed under consideration of a procedure that differs from the validation process the authors from [6]–[9] used.

The analysis of the index methods in the 2-bus system has shown that in general there is a higher sensitivity to the reactive power load change than to active power load change. The conclusion that the LMN and $FVSI$ index are not able to indicate voltage stability conditions regarding active power load change has been refuted by the analysis in the IEEE 118-bus test system. It could be observed that the line index

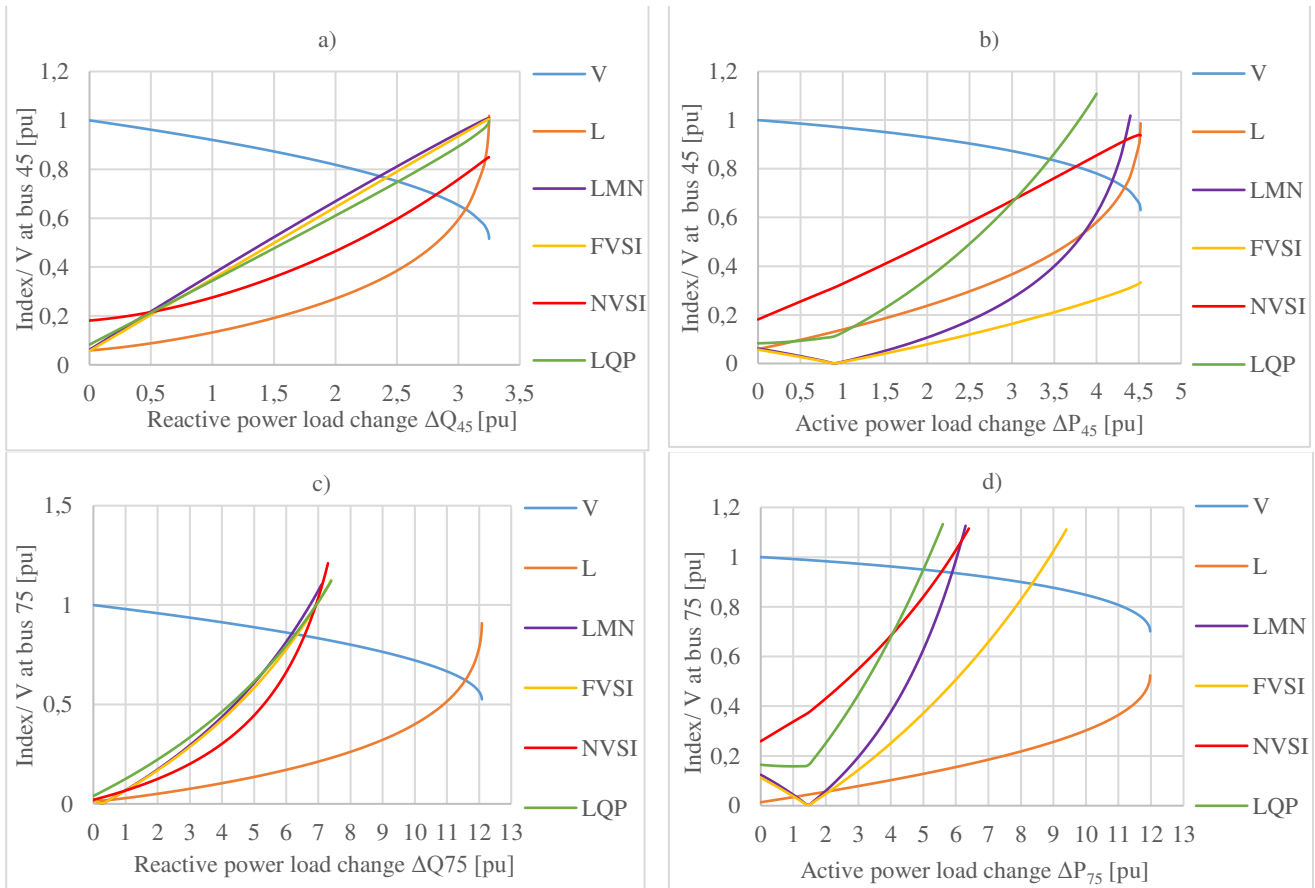


Figure 5. Index progressions for a) reactive b) active power load increase at bus 45 and c) reactive and d) active power load increase at bus 7

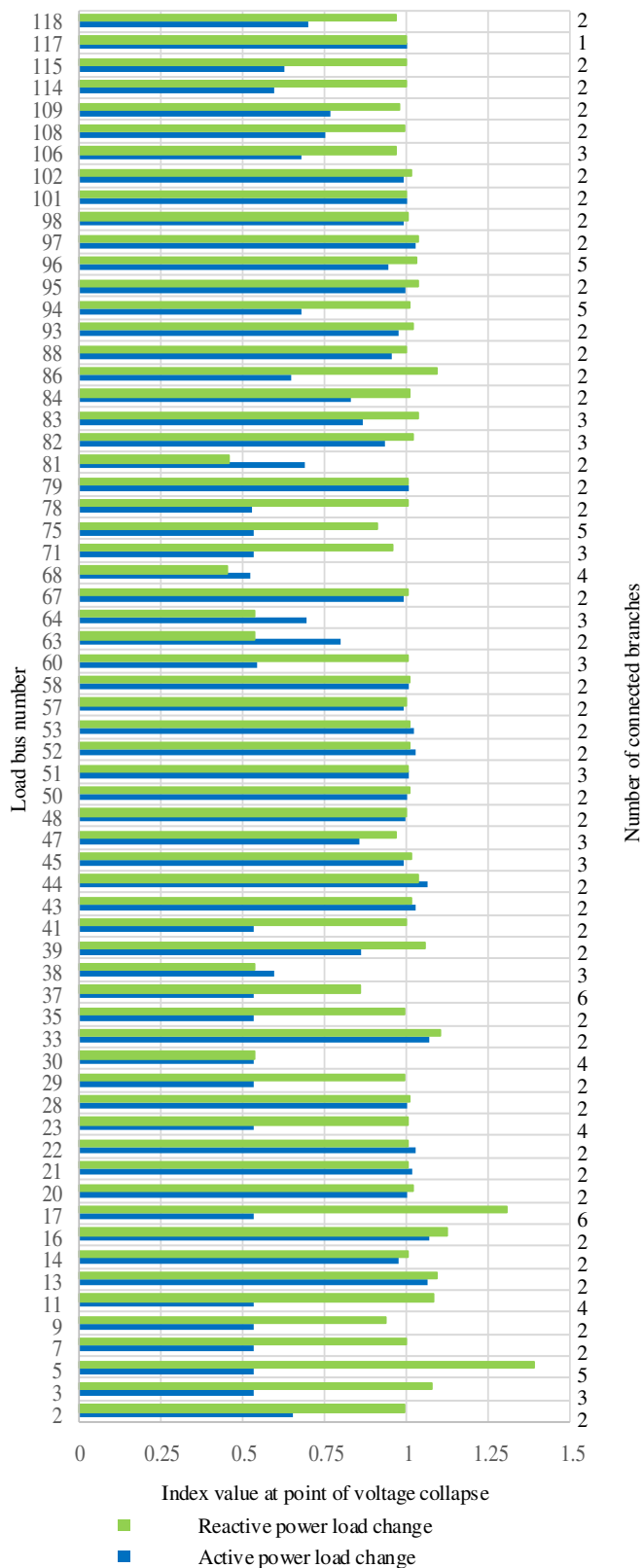


Figure 6. L -index for active/reactive power load increase at all load buses respectively

methods (LMN , $FVSI$, $NVSI$ and LQP) are tending to an early indication of an imminent voltage collapse for an increasing number of connected branches at the stressed bus. The L -index provided the most reliable and accurate results. However also the L -index method could not indicate the critical voltage situation for a bus with a higher degree of meshing regarding to active power load change.

Conclusively the analysis has shown that none of these methods could reliably indicate an imminent voltage collapse within all test conditions. It can be inferred that the L -index method, compared to the line index methods, is the most reliable and most accurate method for a fast evaluation of voltage stability conditions for a point of operation. Nevertheless the L -index result needs to be verified by dynamic simulations before constructive considerations are valid, since the reliability of these method varies for every bus in a system. Furthermore the voltage stability index methods have been effected by other bus specific influences that impact the functionality and reliability of these methods. These influences should be determined and analyzed in further examinations.

REFERENCES

- [1] Y.-H. Hong, C.-T. Pan and W.-W. Lin, "Fast calculation of a voltage stability index of power systems," IEEE Trans. Power Syst, vol. 12, no. 4, pp. 1555–1560, 1997.
- [2] P.S. Kundur and N.J. Balu, Eds, Power system stability and control. New York, NY: McGraw-Hill, 1994.
- [3] "Definition and Classification of Power System Stability IEEE/CIGRE Joint Task Force on Stability Terms and Definitions," IEEE Trans. Power Syst, vol. 19, no. 3, pp. 1387–1401, 2004.
- [4] A. Kazemi, H. A. Shayanfar, A. Rabiee and J. Aghaie, "Power system security improvement using the unified power flow controller (UPFC)," in 2006 IEEE Power India Conference: IEEE, 2006.
- [5] P. Kessel and H. Glavitsch, "Estimating the Voltage Stability of a Power System," IEEE Trans. Power Delivery, vol. 1, no. 3, pp. 346–354, 1986.
- [6] M. Moghavvemi and F. M. Omar, "Technique for contingency monitoring and voltage collapse prediction," IEE Proc. Gener. Transm. Distrib, vol. 145, no. 6, p. 634, 1998.
- [7] I. Musirin and T. K. Abdul Rahman, "Novel fast voltage stability index (FVSI) for voltage stability analysis in power transmission system," in Novel Fast Voltage stability Index (FVSI) for voltage stability analysis in Power transmission system: IEEE, 2002.
- [8] R. Kanimozhi and K. Selvi, "A Novel Line Stability Index for Voltage Stability Analysis and Contingency Ranking in Power System Using Fuzzy Based Load Flow," Journal of Electrical Engineering and Technology, vol. 8, no. 4, pp. 694–703, 2013.
- [9] N. A. M. Ismail, A. A. M. Zin, A. Khairuddin and S. Khokhar, "A comparison of voltage stability indices," in 2014 IEEE 8th International Power Engineering and Optimization Conference (PEOCO2014): IEEE, 2014.
- [10] University of Washington, Power Systems Test Case Archive: 118 Bus Power Flow Test Case. Available: https://www2.ee.washington.edu/research/pstca/pf118/pg_tca118b.us.htm (2018, Mar. 29).

PROTECTION SECURITY ASSESSMENT SYSTEM in the CONTEXT of POWER SYSTEM RESTORATION

Tobias Hanika, Michael Jaworski and Johann Jaeger
 Lehrstuhl fuer Elektrische Energiesysteme
 Friedrich-Alexander-University
 Erlangen-Nuremberg (FAU)
 Germany, 91052 Erlangen

Abstract—In this paper, protection system behaviour during power system restoration is examined. Therefore a network model reflecting the medium to high voltage level is developed. Subsequently it is provided with a protection concept according to literature. To analyse the protection system a Protection Security Assessment system (PSA) is developed. Thereafter this analysis tool is applied on a power system restoration based on the bottom up strategy and problematic network areas during the process are shown. Finally improvements for a secure system restoration are derived and tested on their functionality.

I. INTRODUCTION

The increasing infeed of renewable energies leads to previously unusual power flow directions. This increases the complexity of the protection concept. As a result the electrical energy supply network is becoming more susceptible to protection malfunctions. If a large area collapse of the network occurs, it is essential to restore the system safely, smoothly, deliberately and quickly [1]. In order to ensure the safety during the power system restoration, it is important that the network protection devices react accurately even in this exceptional state. However, since their settings are optimized for normal network operation, this can lead to problems. Because it is too time-consuming to identify these faults in the protection concept manually, it is extremely important to have an automated protection evaluation method. Such a method is presented and applied on a study case in this paper.

II. STUDY CASE

To analyse the protection system during power system restoration a network model with a realistic protection concept is needed.

A. Network model

The developed network model is based on the German electrical energy supply network as described in [2]. Due to the used PowerFactory licence there is a boundary to the model size. Therefore the 220 kV and the 400 V level are not included. In the medium voltage level only one radial and one ring network are represented. Other areas on this level are replaced by equivalent loads. The created network model

is shown in figure 2.

The coupling switch installed in the medium-voltage network is used in further power system restoration strategies.

B. Protection concept

The protection concept is implemented according to literature [3]. Therefore four relay models are applied. Three are manufacturer specific and originate from the company 'SIEMENS'. The first is the time overcurrent relay 7SJ80, the second is the distance protection relay 7SA6 and the third is a differential protection device of the 7UT6 series. The fourth is a specially self-developed generic low voltage right trough relay (LVRT-relay), which is located at all power plants.

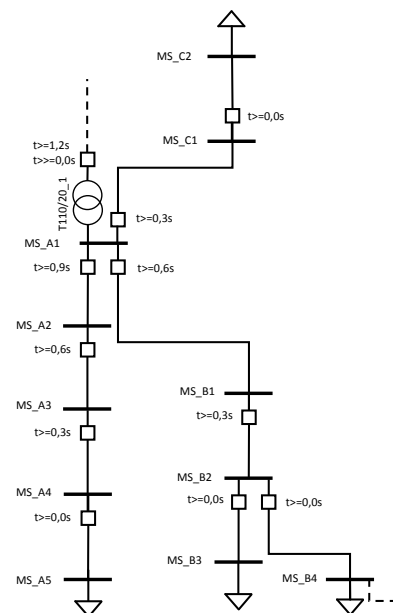


Fig. 1. Protection concept of the radial network

It is responsible for ensuring that the generating units do not disconnect from the grid until the required time has elapsed.

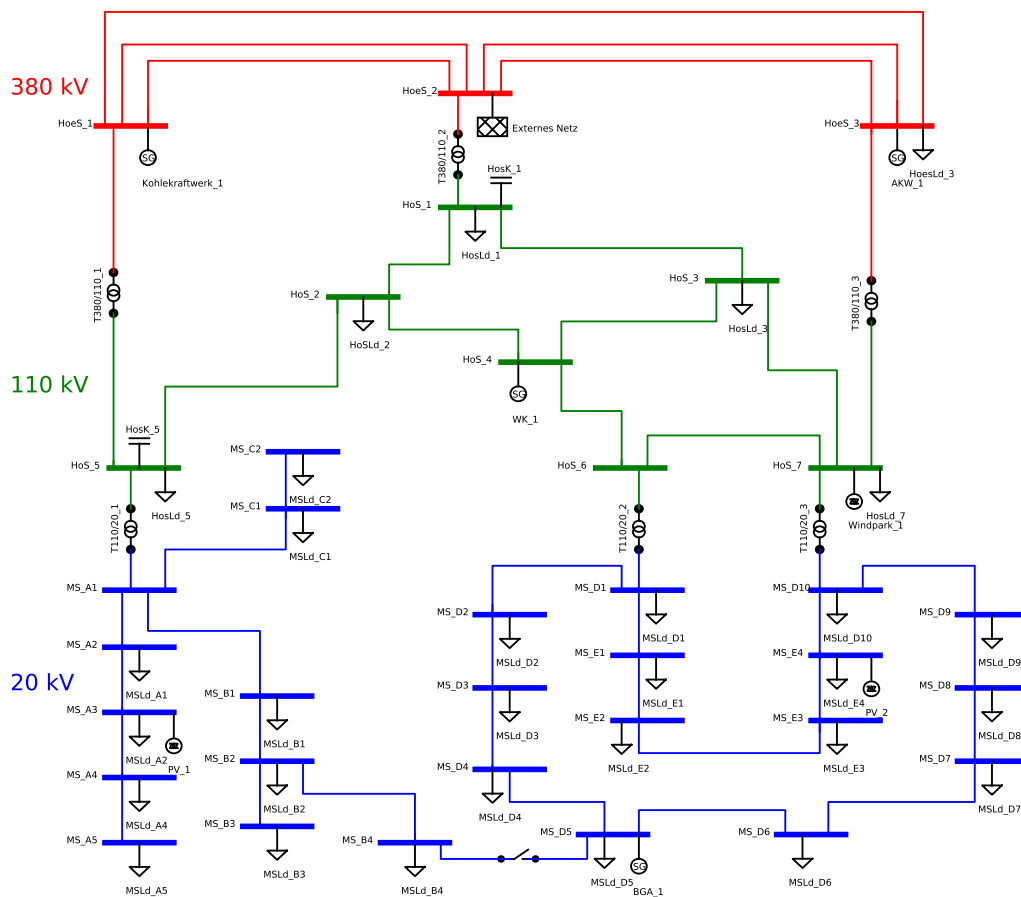


Fig. 2. Developed network model with marked voltage levels

The exact requirements are defined in the Technical Guideline for Generation Plants on the medium-voltage grid of the "Bundesverband der Energie- und Wasserwirtschaft" [4].

Figure 1 shows the protection concept of the radial network by way of example. The boxes represent the overcurrent protection devices. Their time staggering settings are shown next to the boxes.

The lines in the 110 kV and the 380 kV level are protected by distance protection relays. These have three zones with different ranges (85%, 120% and 200% of the main protection zone) and staggering times (0.0 s, 0.3 s and 0.6 s). Furthermore the relay trips at a staggering time of 1.5 s, if its starting conditions are fulfilled.

Every transformer is monitored by a differential protection device and additionally a time overcurrent relay is installed as shown in figure 1.

III. PROTECTION SECURITY ASSESSMENT CONCEPT

To analyse the protection system several Python scripts are developed [5]. There are scripts that collaborate with PowerFactory. Thereby PowerFactory serves as calculation engine for steady state simulations. By incorporating the special

PowerFactory module 'powerfactory.pyd' in the script it is possible to access nearly all parameters in the PowerFactory network. These scripts are responsible for data acquisition. Four further scripts are developed to analyse the data obtained.

A. Data acquisition

To collect data the first script performs stationary stepwise short circuit calculations (short circuit trace) at every bus and on every line, according the procedure shown in figure 3.

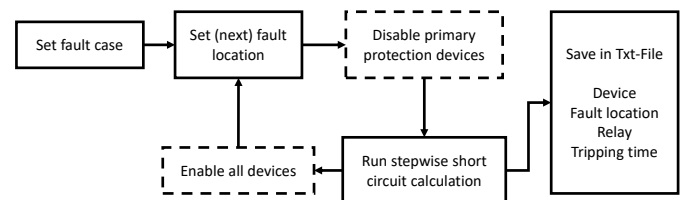


Fig. 3. Procedure of the data acquisition scripts

In the stepwise short circuit calculation the reaction of the protection system is structured in time steps. Each time step is defined via a switching event. For the next time step, the fault currents are recalculated on the basis of the changed grid topology.

To ensure a high resolution based protection screening the lines are divided in 5 % sections and therefore 21 calculations are run through. For the fault case, a distinction can be made between different fault cases with variable fault resistance.

To test the functionality of the secondary protection (back up level) another script performs the same incremental short circuit calculations, with the difference, that ahead of every computation the script disables all primary protection devices except the LVRT-relays. The knowledge about which relay provides which function for which equipment is defined separately in a matrix. It represents the range of the individual protection zones and is determined manually. Starting from the equipment, advancing in radial direction through the network all relevant relays are included. The first relevant protection devices are defined as the primary-, the second as the secondary- and the third as the tertiary protection devices. Thereby the incremental short circuit calculation is carried out until no more protection device is triggered. This is important because cascaded failures may cause further protection trips even after the original fault has been cleared.

Finally the information of the graphical layout is extracted. All acquired data are saved in text files via 'comma-separated values'-style.

B. Data analysis

To evaluate the extracted information four analysis elements, which form the PSA, are developed. These are:

- FT** Fault clearing Time element
- BT** Backup fault clearing Time element
- ST** Selectivity Test element
- GT** Generator Trip analyser element

All evaluation elements show their results in an own graph that reflects the network model, where equipment is differently coloured.

At the **FT**-element the colour refers to the fault clearing time. The function of the **BT**-element is to monitor secondary protection and thus the colour refers to the fault clearing time if primary protection devices are disabled.

The **ST**-element checks if the triggered relays match the relays with primary protection function, given in the matrix. If not, there is a distinction depending on whether the relay has secondary, tertiary or no protection function for the equipment. This serves to evaluate the protection system in terms of its selectivity.

In the **GT**-element each generating unit gets its own colour assigned. Afterwards it is examined if and if so which LVRT relays have tripped for short circuits. According to these results the equipment is coloured in the colour of the largest disconnected generation plant. From this conclusions can be drawn whether a short circuit at this point leads to a collapse of the island.

IV. EXAMINATION OF A NETWORK RESTORATION

For the review of the behaviour of the protection system during power system restoration, a restoration strategy has to

be chosen. Due to the fact that the bottom up strategy is the most challenging approach and no help from neighbouring systems is needed, it is chosen in this paper.

A. Strategy description

In [6], milestones during power system restoration according to the bottom up strategy are defined. These are:

- Building electrical islands
- Synchronisation of these islands
- Establish transmission grid
- Restoration of load
- Connect to neighbouring networks

Criteria that must be kept for a successful construction of recovery islands are named in [7]. These are:

- Each subsystem must have a power plant with black start capability.
- In every recovery island, it should be possible to adapt generation and consumption so that the frequency stays within the specified range.
- Each subsystem should be able to maintain a suitable voltage profile.
- Sufficient monitoring must be possible to ensure internal safety.
- At all tie points where islands should be coupled at least synchro-check relays are necessary.

The implementation of these milestones in the network model is shown in figure 4, taking the island requirements under consideration. There, the stepwise energization process of the network is illustrated.

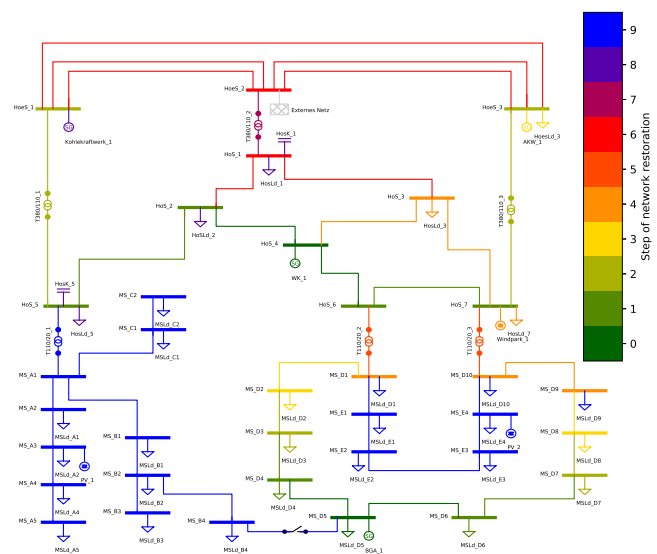


Fig. 4. Steps of network restoration in the bottom up procedure, applied to the network model

In the 110kV level the hydroelectric power plant WK_1 and in the medium-voltage level the biogas plant BGA_1 are

available as power plants with black start capability. Thus they are acting as centres of recovery islands. From the hydroelectric plant, gradually lines, busbars and transformers are connected up to the important power plants AKW_1 and Kohlekraftwerk_1. After connecting the nuclear power plant and the first loads, the high-voltage grid is further energized. Starting from the biogas plant, gradually larger areas of the outer ring are being supplied. Once the active power limit of the system has been reached, only lines and busbars leading to the transformers are supplied with power. In step five, the two islands are merged via the transformers T110/20_2 and T110/20_3. Subsequently, the extra high voltage network is energized. Thereafter, the coal-fired power plant, the compensation facilities and all loads in the 110 kV network are started up or restored. In the final step, the remaining areas of the medium-voltage grid are supplied with energy.

B. Evaluation of protection system behaviour

For the evaluation, all PSA elements are executed for each restoration step. In order to keep this paper short and focussed, only the most critical cases of each evaluation are presented below.

Due to the fact that the proposed method is based on steady state simulations the dynamic transition from one restoration state to another can not be evaluated. To simplify the shown results only three-phase short circuits are considered. The reason for this is that single-phase short circuits would require a detailed description of the network model's grounding concept and the magnitude of two-phase short circuits is only 15 % lower than in a symmetrical fault case (if taken under consideration that the positive and negative sequence of the fault loop are identical).

Figure 5 shows which power plant is shut down for which faults, associated with step four of the power system restoration.

In the medium voltage island, it can be seen that faults close to the biogas plant lead to its disconnection, what leads to a collapse of the island. If the fault is farther away, the protection devices are fast enough to keep the voltage drop at the power plant within the allowed limits. This is because the overcurrent protection in the medium voltage grid relies on using time as its selectivity criterion. Therefore staggering times, which are set starting from the transformer bus bars, reach values up to 1,2 s.

In the high voltage island, it can be seen that faults in zone 1 of the distance protection cause no problems. However, due to the staggering time in zone 2, fault clearing takes longer and the voltage drop reaches inadmissible values and the hydroelectric power station shuts down.

Furthermore, it can be recognized that faults do not affect equipment beyond the transformers into other voltage levels. Accordingly transformers represent barriers in this context due to their high impedance.

The merger of the two islands in step five causes numerous

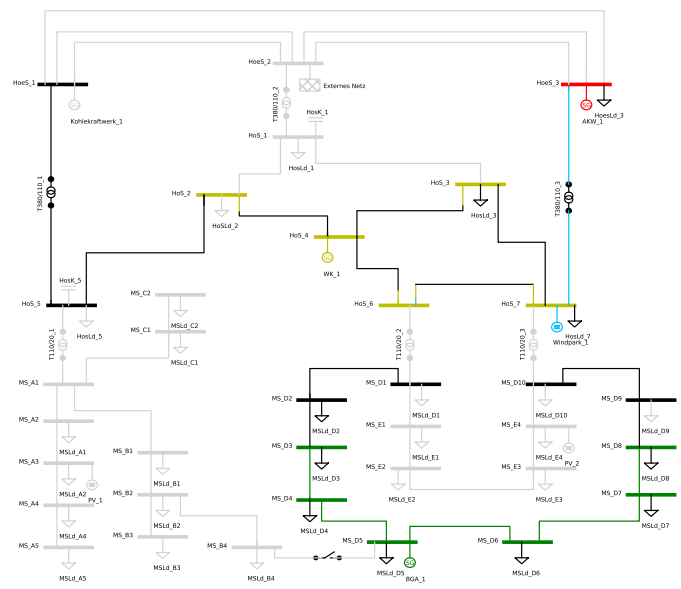


Fig. 5. Result graphic depicting the power plant separation in step four

non selectivities in the high-voltage grid (see figure 6). This is due to fault current flows starting from the biogas plant which trigger relays in the medium voltage level and lead to renewed splitting into two islands.

The non selectivity at bus bar HoeS_1 is attributed to the fact, that the fault current is too low to trigger the time overcurrent relay localized at the transformer. Only the distance protection device on the downstream line clears the fault.

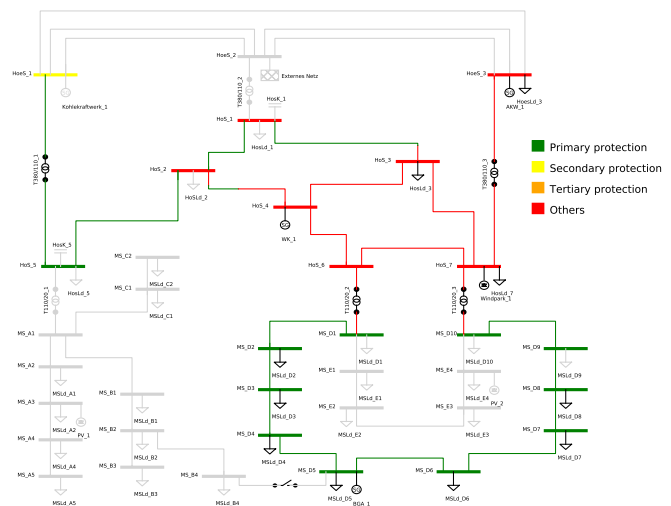


Fig. 6. Result graphic showing the selectivity of the fault clearing in step five

Furthermore there are problems regarding the fault clearing time in terms of the secondary protection, as shown in figure 7. Faults at the bus bars HoS_7 and MS_D10 are not cleared at all, but this is not a specific problem of power system

restoration. Also the problems at MS_D1 and in the area of HoS_5 occur during normal network operation.

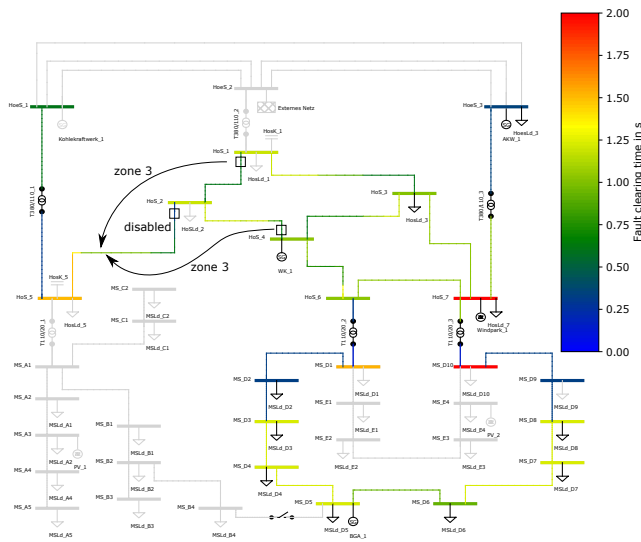


Fig. 7. Result graphic depicting the fault clearing time of secondary protection in step five

The high fault clearing time at the medium voltage bus bar MS_D1 results from the fact, that the transformer protection devices, as primary devices, are disabled and the following distance relays don't register the fault in their area of responsibility. This is due to the high impedance values of the transformer. As a result, the fault is merely cleared after a very high staggering time.

The problems in the area of HoS_5 are due to similar protection behaviour. At the beginning of the line between HoS_2 and HoS_5 faults are cleared in zone 2 of the distance relays with secondary protection function. With increasing distance from bus bar HoS_2, faults are first seen in zone 3 and later not at all in the area of responsibility. This leads to a fault clearing time of 1.5 s.

If protection is working properly and faults are cleared by the primary protection devices fault clearing times remain within acceptable limits, as shown in figure 8.

This applies to all steps of power system restoration concerning the study case.

However, problems may arise if islands are formed with very small generation plants that can provide only low short circuit power. If such an island is utilized to energize equipment in a higher voltage level and a fault occurs there, the short circuit currents will be low due to the high transformer impedance. As a result, they don't exceed the current threshold values set in the time overcurrent protective devices and the fault isn't cleared.

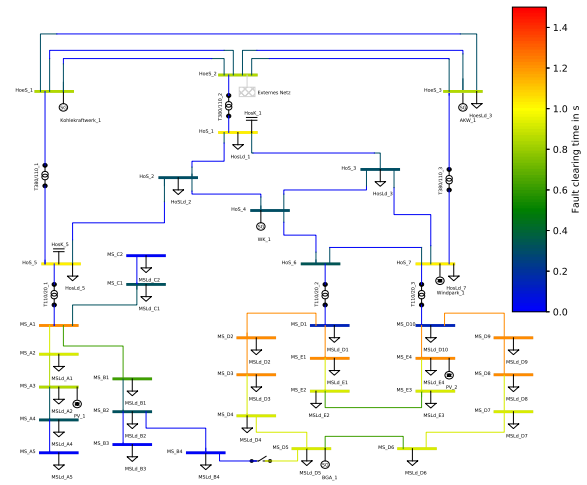


Fig. 8. Result graphic showing fault clearing time in step nine

V. RECOMMENDATIONS

For the problems shown in figure 5 two possible ways of improvement are conceivable. On the one hand another category of protection device settings, anticipating the bidirectional short circuit current flows, could be used in every step. But that would be very time-consuming and therefore not feasible. On the other hand tolerating larger voltage deviations at the generation plants over longer times would endow the protection relays with more time to clear faults. Also in [7] the tolerance of wider than normal voltage variations is demanded.

To solve the problems that occurred in figure 6 the staggering time of the medium voltage protection devices could be increased, but this would lead to inadmissible high fault clearing times concerning faults in their area.

A better solution would be to use distance protection devices at medium voltage level as well. These would not recognize faults in the 110kV level in their area of responsibility and thus the responsible protection devices would clear the fault. Furthermore, this would solve the problems concerning islands in which only a low short-circuit power is available.

To test these recommendations the network model is modified. First, the time overcurrent relays in the ring network are replaced by distance protection devices. Care must be taken to the fact, that if a fault occurs and is cleared on one side of the outer radial network the power infeed of the biogas plant will completely flow through the lines on the faultless side. Thus, up to twice the nominal current flows can occur. Furthermore, the settings of the LVRT relays are changed so that they trigger at the earliest after 0.4 s. As a result, the power plants wait at least until the first staggering time has passed before disconnecting from the grid.

Figure 9 shows the triggering characteristic of the changed low voltage right through relay in detail.

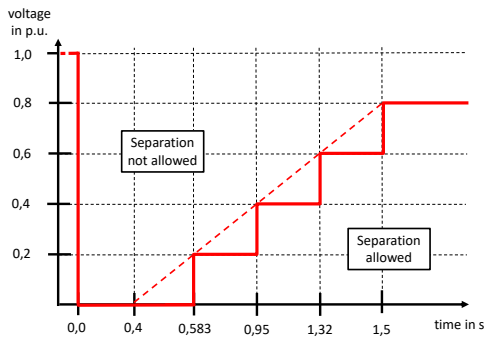


Fig. 9. Characteristic curve of the changed LVRT relay

Due to the toleration of voltage drops over longer times the protection related power plant outages are limited to the busbars to which they are connected (see figure 10).

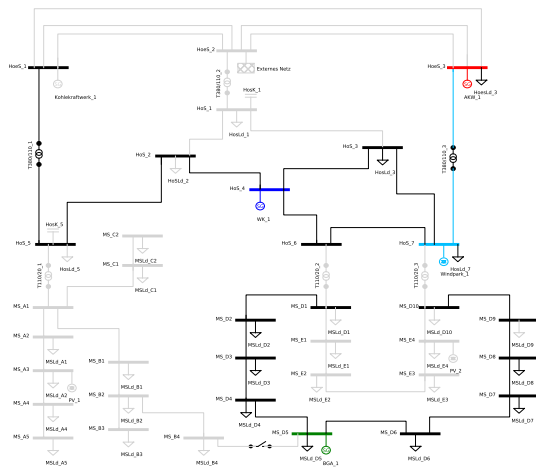


Fig. 10. Result graphic depicting the power plant separation in step four for the improved network

Figure 11 shows, that the change of the protection concept in the ring network averts all nonselectivities on the 110kV level.

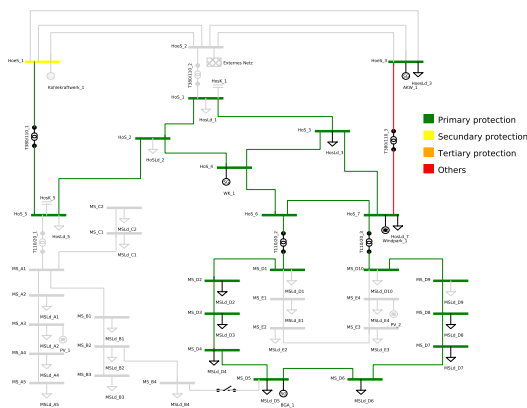


Fig. 11. Result graphic depicting the power plant separation in step five for the improved network

VI. CONCLUSION

In this paper an automated protection system evaluation method according figure 12 is developed. For this purpose, a network model with associated protection concept is set up as a study case. Subsequently a Protection Security Assessment system (PSA) which identifies problematic network areas regarding fault clearing time, backup fault clearing time, selectivity of fault clearing and protection related generator trippings is developed. This PSA system is applied to a power system restoration according bottom up approach.

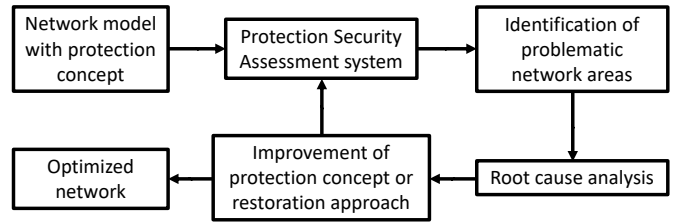


Fig. 12. Procedure of the automated protection system evaluation

An detailed investigation of the resulting problem areas leads to recommendations which would improve the protection system during power system restoration. Implementing these improvements in the network model the PSA system is applied a second time to disclose the effectiveness of these recommendations.

For further recommendations the protection system behaviour should be investigated taking two- and single-phase short circuits under consideration.

REFERENCES

- [1] J. J. Ancona, "A framework for power system restoration following a major power failure," in *IEEE Transactions on Power Systems*, Vol. 10, No. 3. IEEE, August 1995.
- [2] J. Schlabbach and K.-H. Rofalski, *Power System Engineering: Planning, Design, and Operation of Power Systems and Equipment*, 2nd ed. Wiley-VCH Verlag, 2014.
- [3] V. Crastan, *Elektrische Energieversorgung 1: Netzelemente, Modellierung, stationäres Verhalten, Bemessung, Schalt- und Schutztechnik*, 4th ed. Springer Verlag, 2015.
- [4] "Erzeugungsanlagen am mittelspannungsnetz," BDEW Bundesverband der Energie- und Wasserwirtschaft e.V., Technische Richtlinie, Juni 2008.
- [5] <https://www.python.org/>.
- [6] Y. Hou, C.-C. Liu, P. Zhang, and K. Sun, "Construction power system restoration strategies," in *Electrical and Electronics Engineering*. ELECO, 2009.
- [7] M. M. Adibi and L. H. Fink, "Power system restoration planning," in *IEEE Transactions on Power Systems*, Vol. 9, No. 1. IEEE, Februar 1994.

Influence of Measurement Errors on a New Voltage-less Distance Protection Method

Linjie Li, Martin Biller, Johann Jaeger
 FAU University of Erlangen-Nuremberg
 Chair of Electrical Energy Systems
 Erlangen, Germany

Abstract—On the one hand, closed ring operation of medium-voltage distribution networks leads to benefits such as voltage balancing and reduction of transportation losses and thus increases the networks capacity to integrate DERs. On the other hand, some significant problems for conventional distance protection arise. A new distance protection based on negative-sequence currents has been developed in order to determine the distance from the fault location to the relays at the substation for unbalanced faults. The impact of measurement errors from current transformers (CTs) and voltage transformers (VTs) on the accuracy of the new method is a question that remains. Thus, in this paper, an appropriate network model of an excerpt of a distribution grid is investigated. Steady-state fault calculation of unbalanced faults under several system states is executed using MATLAB. The impact of measurement errors from CTs and VTs on the determination of distance is considered. The results show that the distance results of the new method are by far more accurate than for the conventional distance protection method in most of the cases, even under the impact of measurement errors caused by CTs and VTs.

Keywords- closed ring; distance protection; measurement errors

I. NETWORK MODEL

Fig. 1 shows the network model of a closed ring medium-voltage distribution network, which consists of an infeed from the sub-transmission system, a transformer, and 13 nodes in total. DERs are connected to nodes n5, n9 and n11. Every node in the ring, namely n3...n13, supplies a load. The total length of the line in the closed ring is 25.95 km.

Two protection relays, which are supplied with signals from three current transformers and three voltage transformers each are installed at the bus bar (node n2). Phase-to-ground and phase-to-phase faults are applied to every node in the ring from node 3 to node 13 in five different scenarios as shown in table 1. For an additional series of simulations, measurement errors of transformers are taken into consideration for the same five scenarios. All calculations are based on the method of error matrices as described in [1].

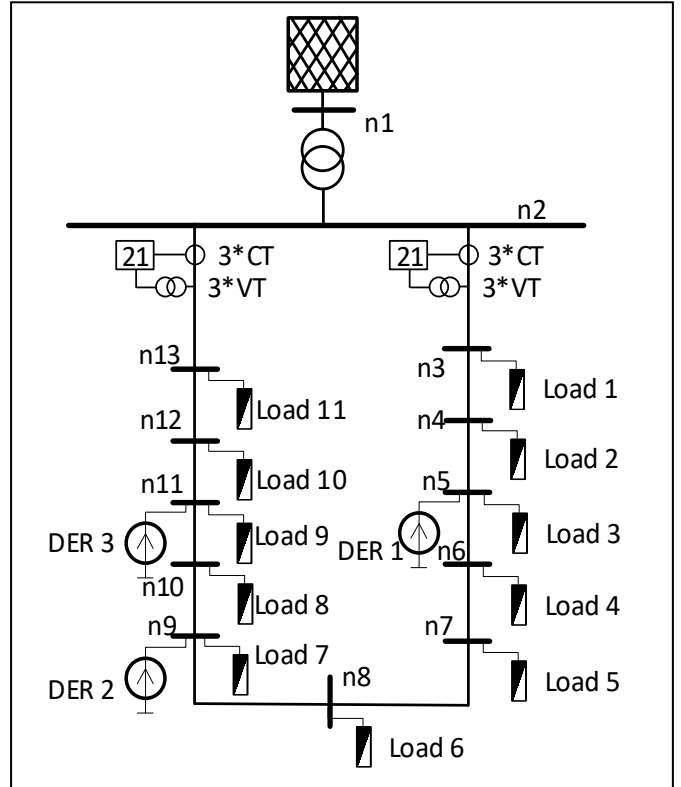


Figure 1. Network model

TABLE I. SCENARIOS OF DIFFERENT FAULT CONDITIONS

Scenario	Fault Impedances	Loads	DERs
1	No	No	No
2	Yes	No	No
3	No	Yes	No
4	No	No	Yes
5	Yes	Yes	Yes

II. MEASUREMENT ERRORS OF CURRENT AND VOLTAGE TRANSFORMERS

There are two sorts of current transformers, one for measuring purposes and the other for protection purposes. Naturally the second one is taken into consideration, because it has a better performance especially under the occurrence of

short circuit currents and enables the correct operation of protective relays. Most voltage transformers use the same core for measuring and protection purposes.

A. Current Transformers

Protection CTs are distinguished from metering CTs with better performance in the overcurrent range but less accuracy at the rated primary current. There are two typical classes, 5P and 10P, where P refers to protection and 5 or 10 refers to composite error at rated limit primary current in percent. The following table, extracted from IEC 60044-1, shows different ranges of error tolerances for this two classes.

TABLE II. PROTECTION CT ACCURACY CLASS [2]

Class	Current Error at Rated Primary Current	Phase Displacement at Rated Primary Current	Composite Error at Rated Limit Primary Current
5P	± 1%	± 60 minutes	5%
10P	± 3%	± 60 minutes	10%

In this paper CTs of class ‘10P10’, which is typical for European applications is chosen. Under nominal burden, the maximum current error is 1% at rated primary current and 10% at rated limit primary current. Since the number after P on the nameplate is 10, the rated limit primary current is 10 times the rated primary current [3]. If the burden is smaller than the nominal burden, the performance of the CT is better, or more accurate. Otherwise if the burden is greater than the nominal burden, the performance of the CT is worse, or less accurate. In order to simulate the measurement errors assumed for real CTs, a detailed error curve referring to [4] and [5] is used in the network calculations. Fig. 2 describes the applied measurement error in both current error and phase displacement. This error curve is discretized. It is plotted for nominal burden. In every current area the maximum current error and phase displacement are used.

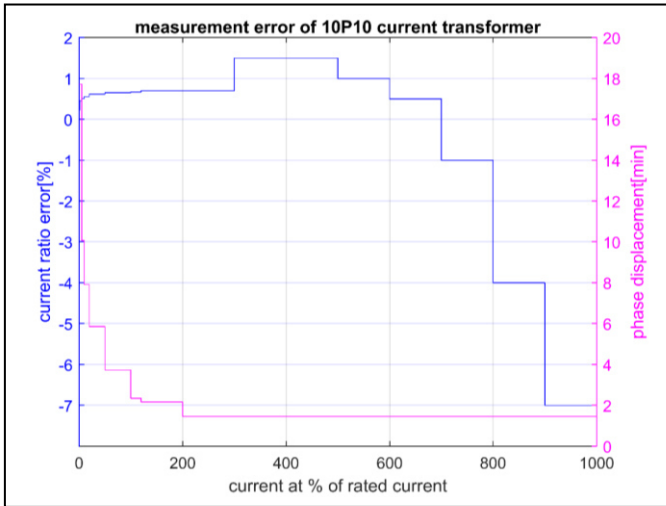


Figure 2. Measurement error of 10P10 current transformer

B. Voltage Transformers

When it comes to voltage transformers, the measurement error is divided into two areas. If the voltage is in the range from 0.8 times to 1.2 times the rated voltage, the measurement error depends on which of the five accuracy classes the VT can be assigned to (see table 3). If the voltage is smaller than 0.05 times the rated voltage or greater than 1.5 times the rated voltage, there are two accuracy classes, shown in table 4. Since most VTs use the same core for protection and measurement purposes, there is no information which describes the deviation from 0.05 to 0.8 times ratio voltage and from 1.2 to 1.5, because those areas are outside the regular voltage operation range.

TABLE III. MEASUREMENT VT ACCURACY CLASS [6]

Class	Voltage Error	Phase Displacement Error
0.1	±0.1%	±5 minutes
0.2	±0.2%	±10 minutes
0.5	±0.5%	±20 minutes
1	±1%	±40 minutes
3	±3%	Not sure

TABLE IV. PROTECTION VT ACCURACY CLASS [6]

Class	Voltage Error	Phase Displacement Error
3P	±3%	±120 minutes
6P	±6%	±240 minutes

III. ALGORITHM OF CONVENTIONAL DISTANCE PROTECTION METHOD FOR UNBALANCED FAULTS

The algorithm of conventional distance protection is using phase-to-phase and phase-to-ground voltages and phase currents to determine the impedance from the fault location to the distance relays [7].

A. Phase-to-Ground Faults

For phase-to-ground faults, the phase-earth loop is used in order to calculate the corresponding impedance, as shown in eq. (1). \underline{U}_{Ph-E} is the phase-to-ground voltage and \underline{I}_{Ph} the phase current of the line, in which the short circuit occurs. The residual compensation factor \underline{k}_E corresponds to the $\underline{Z}_E/\underline{Z}_L$ ratio of the overhead line, which is a complex number and \underline{Z}_E can be derived with eq. (2) and eq. (3). \underline{Z}_L is the total impedance from fault location to the distance relay. In theory, this factor should be calculated only with line impedances of the corresponding fault loop. Yet in practice this factor is calculated with the sum impedances of the whole ring, no matter where the fault actually happens. Consequently, the calculation of \underline{k}_E is also a source of error Eq. (4) shows the calculation of the ground current, which is the negative sum of three phase currents.

$$\underline{Z}_{Ph-E} = \frac{\underline{U}_{Ph-E}}{\underline{I}_{Ph} - \underline{k}_E \cdot \underline{I}_E} \quad (1)$$

$$\underline{k}_E = \frac{\underline{Z}_E}{\underline{Z}_L} \quad (2)$$

$$\underline{Z}_E = \frac{1}{3} \cdot (\underline{Z}_{L0} - \underline{Z}_{L1}) \quad (3)$$

$$\underline{I}_E = -(\underline{I}_A + \underline{I}_B + \underline{I}_C) \quad (4)$$

If the accuracy of the transformers is taken into account, not only measurement error of CTs but also of VTs have the impact of the result. The measurement error of each CT and VT arises differently with different values of current and voltage according to section 2. This may result in a false calculation of the distance which then does not equal the physical distance. In accordance with eq. (5) and eq. (6), eq. (1) and eq. (4) are rewritten including measurement errors, seen eq. (7) and eq. (8).

$$\underline{U}_{Ph-E,error} = \underline{U}_{Ph-E} \cdot (1 + \Delta \underline{U}_{error}) \quad (5)$$

$$\underline{I}_{E,A,B,C,error} = \underline{I}_{E,A,B,C} \cdot (1 + \Delta \underline{I}_{error}) \quad (6)$$

$$\underline{Z}_{Ph-E,error} = \frac{\underline{U}_{Ph-E,error}}{\underline{I}_{Ph,error} - \underline{k}_E \cdot \underline{I}_{E,error}} \quad (7)$$

$$\underline{I}_{E,error} = -(\underline{I}_{A,error} + \underline{I}_{B,error} + \underline{I}_{C,error}) \quad (8)$$

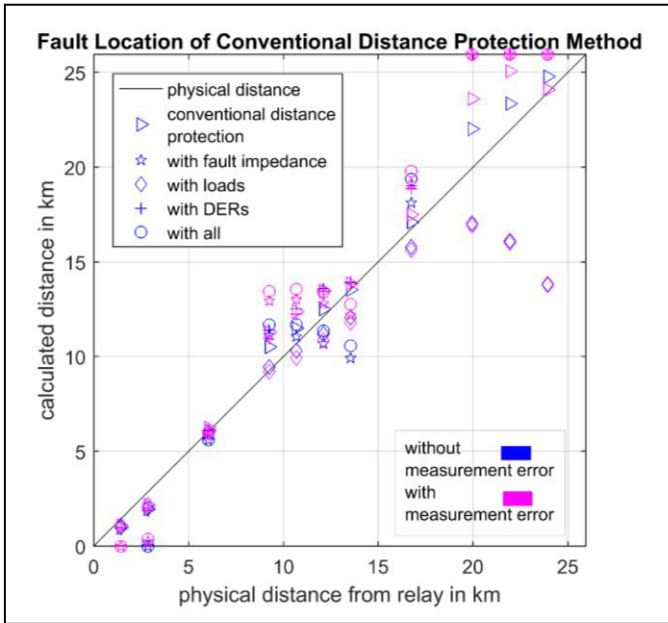


Figure 3. Distance calculation with conventional distance protection method for phase-to-ground faults

If the calculated distance is beyond 25.95 km, the distance is presented as 25.95 km in the diagram, since the total length of the ring is 25.95 km. For distances less than 0 km, 0 km are presented. This assumption is applied in all the simulations. According to the results from simulation in fig. 3, the calculated distance is strongly influenced by fault impedances, loads and DERs. Even though the conventional distance protection uses the reactance as indicator of the distance to the fault location to remedy adverse effects of fault resistances, the results show that the distance is strongly falsified.

B. Phase-to-Phase Faults

For phase-to-phase faults, the phase-to-phase loop is applied to calculate the distance. With eq. (9) the corresponding impedance can be calculated. \underline{U}_{PhA-E} , \underline{U}_{PhB-E} , \underline{I}_{PhA} and \underline{I}_{PhB} are the phase-to-ground voltages and phase currents of the faulty phases. With measurement errors the eq. (10) is derived.

$$\underline{Z}_{Ph-Ph} = \frac{\underline{U}_{Ph-Ph}}{\underline{I}_{Ph-Ph}} = \frac{\underline{U}_{PhA-E} - \underline{U}_{PhB-E}}{\underline{I}_{PhA} - \underline{I}_{PhB}} \quad (9)$$

$$\underline{Z}_{Ph-Ph,error} = \frac{\underline{U}_{Ph-Ph}}{\underline{I}_{Ph-Ph}} = \frac{\underline{U}_{PhA-E,error} - \underline{U}_{PhB-E,error}}{\underline{I}_{PhA,error} - \underline{I}_{PhB,error}} \quad (10)$$

Fig.4 indicates the simulation results for phase-to-phase faults and the conclusion is, that the conventional distance protection method strongly falsifies the results, especially under the occurrence of fault impedances, loads and DERs in this distribution network.

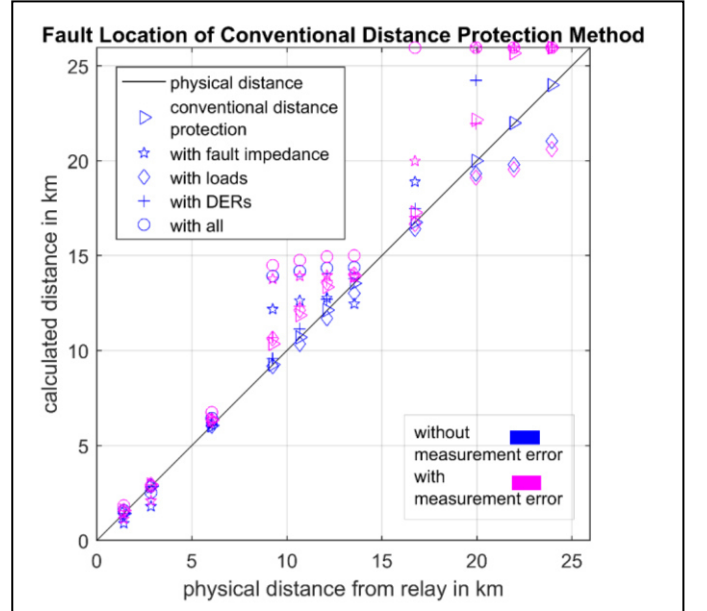


Figure 4. Distance calculation with conventional distance protection method for phase-to-phase faults

IV. PRINCIPLE OF NEW DISTANCE PROTECTION METHOD

In contrast to the conventional distance protection method, the new distance protection method uses negative-sequence currents to calculate the impedance from relay to fault. Since most of the installed DERs at medium voltage level are inverter-based and are controlled to provide symmetrical infeed only, they do not affect the negative-sequence current distribution [8]. The algorithm of the new distance protection makes use of the current divider rule and the fundamental theory is Kirchhoff's current law and the symmetrical components equivalent circuit [9]. The new method is explained on basis of the network model known from fig. 1.

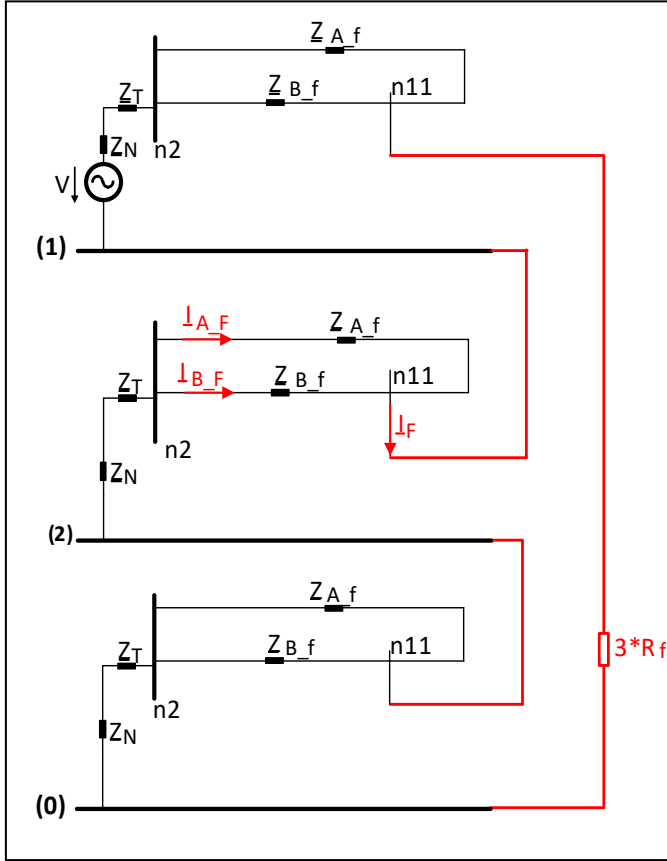


Figure 5. Symmetrical components equivalent circuit

A single-phase-to-ground fault on node n11 is applied. With use of the currents measured by the two distance relays and the sum impedance of the ring, the impedance from the fault location to the distance relays A and B can be calculated with the eq. (11) to eq. (14). Fig. 5 shows the corresponding symmetrical components equivalent circuit. Due to Kirchhoff's current law, the total negative-sequence fault current is the sum of the two negative-sequence currents measured by distance relay A and distance relay B (see eq. (11)). Based on the current divider rule, more current flows through the line with the smaller impedance to the fault location, which means the proportion of the impedance is inverse to the proportion of the current. The contribution of one relay to the total negative-sequence fault current is calculated in eq. (12). In this way the impedance from the distance relays to the fault location can be calculated with eq. (13) and eq. (14) respectively. The actual physical distance from

the distance relays A and B to the fault location can be derived using the reactance or the resistance of the line separately, because the fault resistance has no effect on the new method. For the application of this method, a communication channel between both distance relays is required.

$$\underline{I}_{F(2)} = \underline{I}_{A(2)} + \underline{I}_{B(2)} \quad (11)$$

$$\underline{\delta}_{A,B(2)} = \frac{\underline{I}_{A,B(2)}}{\underline{I}_{F(2)}} \quad (12)$$

$$\underline{Z}_{A,F(2)} = \left(1 - \underline{\delta}_{A(2)}\right) \cdot \sum_B^A \underline{Z}_{(2)} \quad (13)$$

$$\underline{Z}_{B,F(2)} = \left(1 - \underline{\delta}_{B(2)}\right) \cdot \sum_B^A \underline{Z}_{(2)} \quad (14)$$

Since the principle of new method is voltage-less only measurement errors from CTs have an impact on the method's accuracy. The rewritten eq. (11) to eq. (14) with regard to measurement errors of the CTs are given in eq. (15) to eq. (18).

$$\underline{I}_{F(2),error} = \underline{I}_{A(2),error} + \underline{I}_{B(2),error} \quad (15)$$

$$\underline{\delta}_{A,B(2),error} = \frac{\underline{I}_{A,B(2),error}}{\underline{I}_{F(2),error}} \quad (16)$$

$$\underline{Z}_{A,F(2),error} = \left(1 - \underline{\delta}_{A(2),error}\right) \cdot \sum_B^A \underline{Z}_{(2)} \quad (17)$$

$$\underline{Z}_{B,F(2),error} = \left(1 - \underline{\delta}_{B(2),error}\right) \cdot \sum_B^A \underline{Z}_{(2)} \quad (18)$$

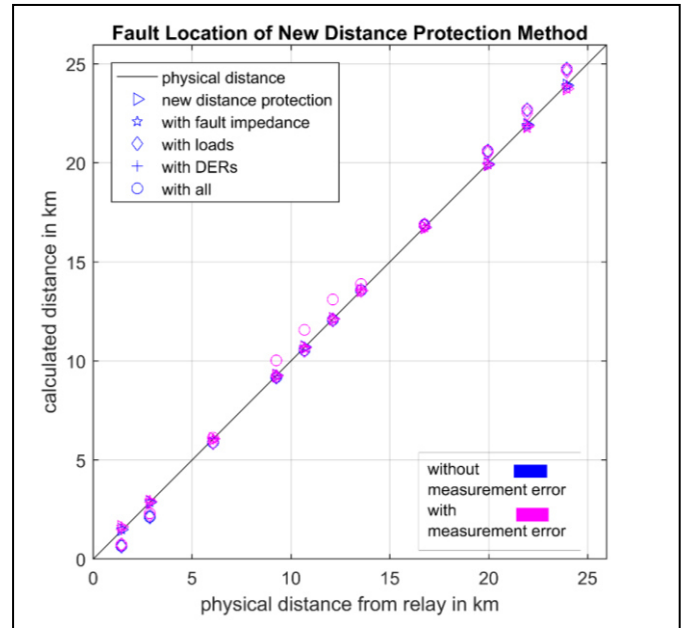


Figure 6. Fault location of new distance protection method for phase-to-ground faults

Fig. 6 indicates the influence of measurement errors on the new method for phase-to-ground faults. Basically, the impact of the accuracy from fault impedances, loads and DERs is not considerable if no measurement errors are applied (blue points in fig.6). Since the method applies negative-sequence quantities only, inaccuracies caused by deficient parametrization of the residual compensation factor have no effect on the result. Even if measurement errors from CTs are applied, this method is by far more reliable compared to the conventional distance protection method.

Fig. 7 represents the influence of different factors on the new method for phase-to-phase fault. The effect from fault impedances, loads, DERs and even measurement errors of CTs of the new distance protection is also not considerable as shown in the simulation.

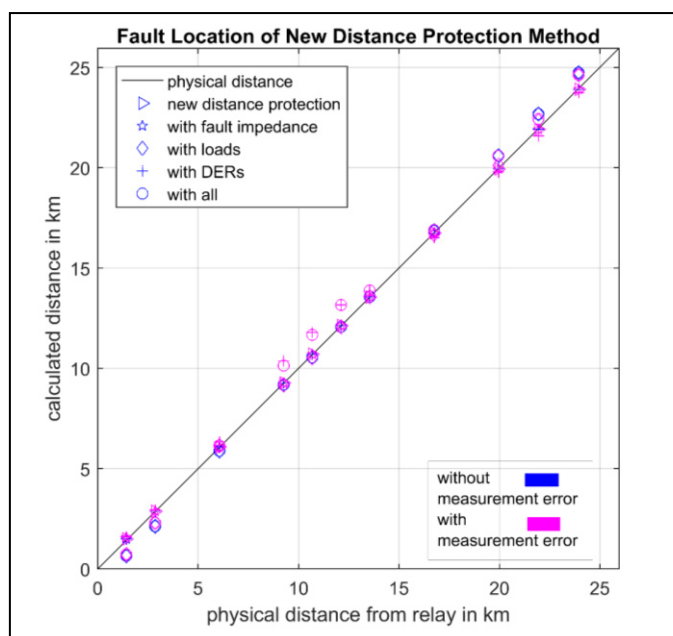


Figure 7. Fault location of new distance protection method for phase-to-phase faults

V. CONCLUSION

The influence on the accuracy of distance protection of measurement errors of CTs and VTs may not be neglected. The deviation from the real value to the measured value depends on the different classes of CTs and VTs, primary currents and voltages and how many phases are affected by the fault. In the steady-state simulation of the exemplary network, the influence of fault impedances, loads and DERs leads to inaccuracies and even false action of relays for the conventional distance protection method.

Compared to the conventional distance protection method, the new voltage-less distance protection method, which is based on negative-sequence currents, has advantages in accuracy in closed-ring networks with fault impedances, loads and also a high share of DERs. When it comes to the measurement errors

of transformers, on the one hand, VTs measurement are irrelevant, since no voltage signals are processed with the new method. On the other hand, the measurement errors of the CTs influence this method and lead to over-reach and under-reach to a certain extent. In order to provoke a worst-case scenario, the least accurate CT class "10P10" was chosen. However, in contrast to the conventional protection method the new method is by far more accurate and the simulations show the proper functionality for all scenarios.

REFERENCES

- [1] Bernd R. Oswald, "Berechnung von Drehstromnetzen", DOI 10.1007/978-3-8348-2621-3, © Springer Fachmedien Wiesbaden 2013.
- [2] International Standard, Current Transformers, CEI/IEC 60044-1, 2003.
- [3] CT Class Definitions, <https://store.gegridsolutions.com/faq/documents/239/GET-8418.pdf>, GE Power Management No. GET-8418A, Copyright © 2003 GE Multilin.
- [4] D.Braisch, Siemens AG, unpublished.
- [5] Technik-Wandler, <http://www.kiesewetter-mt.de/produkte/nssw/pdf/technik-wandler.pdf>, Rudolf Kiesewetter Messtechnik GmbH.
- [6] J.Jaeger, Script from "Schutz- und Leittechnik", 2015, Erlangen.
- [7] G.Ziegler, "Numerical Distance Protection", Publics Corporate Publishing, Erlangen, 2011.
- [8] BDEW Bundesverband der Energie- Wasserwirtschaft e.V., „Technische Richtlinie Erzeugungsanlage am Mittelspannungsnetz - Richtlinie für Anschluss und Parallelbetrieb von Erzeugungsanlagen am Mittelspannungsnetz“, BDEW, Berlin, 2008.
- [9] M.Biller, J.Jaeger, "Robust Distance Protection Algorithm for Closed-Ring Structures", in *Advancements in Power System Protection and Automation*, Jeju, 2017.

Investigation on Membership Function Design for Fuzzy Logic based Fault Classification

Nicholas Mohnlein, Jakob Schindler, Johann Jaeger
 Chair of Electrical Energy Systems
 Friedrich-Alexander-University Erlangen-Nuremberg (FAU)
 nicholas.mohnlein@fau.de

Abstract—In this paper, a fuzzy logic based fault classification in transmission lines is analyzed. For this, a fuzzy inference system relying only on current measurements from the literature is used. It is able to classify faults correctly in most cases, but still shows weaknesses for extreme line loadings and fault parameters. Besides changing the fuzzy logic operators, mainly the design of the membership functions is thoroughly analyzed. The impact of different line configurations like single and double lines as well as the impact of line transposition is discussed. Value ranges of fuzzy system input parameters are analyzed to optimize membership functions. Triangle and Gaussian type functions are studied and their classification performance is compared to mere boolean logic. Additionally, a universal fuzzy system is designed for optimal classification of all tested fault cases, as opposed to systems specifically adapted to a certain configuration. In total, the paper provides valuable insights into the functioning and design of fuzzy logic based fault classification.

Index Terms—fault classification, fuzzy logic, power transmission, protection

I. INTRODUCTION

To ensure reliable supply of electrical power a fast and selective fault clearing is important. One prerequisite for this is the classification of the fault type. Fuzzy logic is a form of logic in which the truth values are not only true (1) and false (0). Instead, fuzzy logic assigns so-called membership values to the logic variables, which can be any decimal value between 0 and 1. The combination of multiple such “fuzzy” truth variables on the basis of expert knowledge enables the decision making in complex systems in which a complete analytical modeling is unfeasible. Hence it is a promising approach for fault type classification in power systems and has already been investigated by previous works. The first attempts were made by Ferrero et al. [1]. In this work only a differentiation between phase-ground and phase-phase-ground fault was possible. Neither the involved phases nor a line-line fault without involving ground were considered. Das et al. [2] published an improved version which permits to determine all ten short circuit types including phase selectivity by using only the magnitude and angle of the three phase currents. The authors were able to classify all faults as long as there was no high system loading, distance or fault resistance. Adding three more inputs, calculated from the difference of current phase angles before and after the fault, Cecati et al. [3] achieved a successful classification even under these conditions. Another enhanced version was proposed by da Silva et al. [4]. Instead of using inputs based on stored pre-fault values like [3], three

new inputs based on the magnitude of the three phase currents were chosen. Besides a simple single line configuration, Cecati et al. and da Silva et al. considered also a double line with the mutual line coupling.

This work takes up the fuzzy system of da Silva et al. [4]. After presenting the general structure of fuzzy inference systems (FIS) and the functioning of the fault classification FIS from [4], the aim is to further investigate the design of membership functions and the sensitivity of the fuzzy inference systems with regard to line configurations. For this, exact parameter studies are done using three line configurations: single line, double line and double line with additional central busbar. Finally, the question whether a universal FIS for all configurations is possible is studied.

II. FIS FOR FAULT CLASSIFICATION

Fig. 1 shows the general process of a Fuzzy-Inference-System. With the help of the expert rule base, the output can be determined using suitable crisp (non fuzzy) input parameters. These input parameters are characteristic values which are either measured or calculated from measured values. The output is crisp again and gives an information about the phase in which the fault occurred.

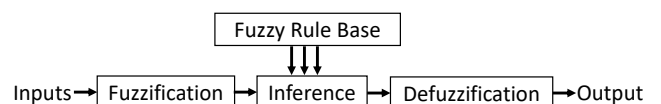


Fig. 1. Basic structure of a Fuzzy Inference System

In detail each crisp input x is evaluated against the membership functions $\mu(x)$ of the fuzzy variables associated to that input, which fuzzifies the crisp input. At the Inference process, the fuzzy rule base is applied to the fuzzy variables (so called inference) to yield fuzzy outputs for each rule. These are then aggregated to the output value. In the last step, the Defuzzification, this fuzzy output is converted to a crisp output.

A. Fuzzy Inputs

For this work, the same fuzzy input parameters as introduced in [2] and extended by [4] have been used. All of them are calculated from measurements of the three phase

current. The first five, first used in [2] are calculated from the current sequence components (Eq. 1 and Eq. 2), whereas the last three, added by [4] are related to the phase current magnitude. Herein, the inputs which can be computed by the sequence components, are shown in Eq. 1 and 2. The zero-, positive-, and negative sequence components of the currents relative to phase “a” are denoted as I_{a0f} , I_{a1f} , I_{a2f} and so forth.

$$\begin{aligned} Ang_A &= |\arg(\underline{I}_{a1f}) - \arg(\underline{I}_{a2f})| \\ Ang_B &= |\arg(\underline{I}_{b1f}) - \arg(\underline{I}_{b2f})| \\ Ang_C &= |\arg(\underline{I}_{c1f}) - \arg(\underline{I}_{c2f})| \end{aligned} \quad (1)$$

$$R_{0f} = \left| \frac{\underline{I}_{a0f}}{\underline{I}_{a1f}} \right| \quad R_{2f} = \left| \frac{\underline{I}_{a2f}}{\underline{I}_{a1f}} \right| \quad (2)$$

The three parameters Ang_A , Ang_B and Ang_C represent the amount of angle deviation of the positive sequence, related to phase a, b and c, from the angle of the negative sequence component. The parameters R_{0f} and R_{2f} are the zero and negative sequence magnitudes normalized to the positive sequence magnitude. To improve the fuzzy input set composed of the inputs deduced from the sequence component, three additional parameters introduced by [4], calculated from the phase current magnitudes, have been used (Eq. 3).

$$\begin{aligned} r_1 &= \frac{\text{abs}(\underline{I}_{af})}{\text{abs}(\underline{I}_{bf})} & r_{1n} &= \frac{r_1}{\max(r_1, r_2, r_3)} \\ r_2 &= \frac{\text{abs}(\underline{I}_{bf})}{\text{abs}(\underline{I}_{cf})} & r_{2n} &= \frac{r_2}{\max(r_1, r_2, r_3)} \\ r_3 &= \frac{\text{abs}(\underline{I}_{cf})}{\text{abs}(\underline{I}_{af})} & r_{3n} &= \frac{r_3}{\max(r_1, r_2, r_3)} \end{aligned}$$

$$\Delta_1 = r_{1n} - r_{2n}, \quad \Delta_2 = r_{2n} - r_{3n}, \quad \Delta_3 = r_{3n} - r_{1n} \quad (3)$$

These differences of normalized phase magnitude ratios are helpful to distinguish between line-ground (lg) and line-line-ground (llg) faults and help to improve the classification rate for fuzzy logic [4].

B. Fuzzy Variables

Previous papers [2], [3] and [4] have shown that the fuzzy variables of every input parameter given in table I provide effective means for fault classification. Therefore, they are also used in this study.

C. Fuzzy Rule Base

The fuzzy rule base represents the logical expert part of the FIS. All these rules are formed according to the following structure:

If *Condition* THEN *Conclusion*

TABLE I
CRISP INPUTS AND CORRESPONDING FUZZY VARIABLES

Ang_A	approx30°	approx90°	approx150°
Ang_B	approx30°	approx90°	approx150°
Ang_C	approx30°	approx90°	approx150°
R_{0f}	Low	High	
R_{2f}	Low	High	
Δ_1	Low	Medium	High
Δ_2	Low	Medium	High
Δ_3	Low	Medium	High

If there are multiple conditions in one rule they can be linked with an operator like AND or OR. In this work only the AND-operator is used to link conditions. The structure results as following:

If *Condition 1* AND *Condition 2* THEN *Conclusion*

Table II lists the rule for the classification of all ten fault types.

TABLE II
FUZZY RULE BASE (ONE RULE PER LINE)

Fault	Ang_A	Ang_B	Ang_C	R_{0f}	R_{2f}	Δ_1	Δ_2	Δ_3
a-g	30°	150°	90°	High	High	High	Med.	Low
b-g	90°	30°	150°	High	High	Low	High	Med.
c-g	150°	90°	30°	High	High	Med.	Low	High
a-b	30°	90°	150°	Low	High	-	-	-
b-c	150°	30°	90°	Low	High	-	-	-
c-a	90°	150°	30°	Low	High	-	-	-
a-b-g	30°	90°	150°	High	High	Low	High	Low
b-c-g	150°	30°	90°	High	High	Low	Low	High
c-a-g	90°	150°	30°	High	High	High	Low	Low
a-b-c	-	-	-	Low	Low	-	-	-

The b-c fault for example would be formulated like this:

If Ang_A is 150° AND Ang_B is 30° AND Ang_C is 90° AND R_{0f} is High THEN fault type is b-c-g

Because the prod method is used for the AND operator (see section II-D), every condition of one rule has to be greater than 0 for the rule to be active. Therefore, the value range is a decisive factor for a finely tuned FIS. For a better understanding of these facts, the following chapters describe the process of analyzing data and designing a membership function based on this data.

D. Fuzzy Operators

The FIS was implemented in *Matlab* using the *Fuzzy Logic Toolbox* which allows to make certain settings. The chosen operators influence the results by defining how the functions and membership values get handled. For the “Mamdani” FIS style the following settings were made:

AND-method set to **prod**
implication set to **min**
aggregation set to **max**
defuzzification set to **mom**

The settings differ from the ones made by [2] and [4]. For the AND-method the setting was changed from max- to prod-method, because using the max-method results in a reduction

of information as only the condition with the highest value determines the rule output. Another change is made by using the mean-of-maximum-method (mom) instead of the centroid-method to receive an exact result in case of two active rules, since any kind of averaging between two different fault types is not useful in our case.

III. MEMBERSHIP FUNCTION DESIGN (BASE CASE)

A. Power System Model and simulated Fault Cases

The base case to test and develop the FIS is a single line configuration with ideal transposition. It is illustrated in Fig. 2, the source and line data is given in the appendix. The measurement values for designing the membership functions were received by simulating the transmission lines in *Matlab Simulink*.

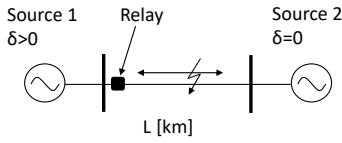


Fig. 2. Single line configuration (base case)

This paper focuses on membership function design, so an extensive knowledge of the possible system states is necessary. For this reason a study of parameters was done first to analyse the FIS inputs for a wide range of loadings and fault parameters for every fault type. These ranges are shown in table III.

TABLE III
PARAMETER-VARIATION

Transmission Angle [°]	δ	0, 10, 20, 30
Fault Resistance [Ω]	R_f	0.001, 5, 10, 25, 50, 75, 100, 200
Fault Location [km]	m	0.05L, 0.4L, 0.6L, 0.8L, 0.9L, 0.95L

Note that L stands for the length of the transmission line. With all combinations of δ , R_f and m $4 \times 8 \times 6 = 192$ fault cases were generated per fault type. Considering all ten fault types 1920 cases for each type of transmission-line are available to be classified by the proposed FIS. These parameter studies form the basis of designing the optimal membership functions.

B. Histogram of Fuzzy Variables

Table II shows which subset of the 1920 simulation cases should trigger a particular fuzzy variable (e.g. the variable “ Δ_1 is high” should be active in all a-g and all c-a-g faults). To help design suitable membership functions for each variable, each graph in Fig. 3 shows a histogram of the crisp inputs of all cases that should trigger the respective fuzzy variable. The first observation made from Fig. 3 is that the input ranges of the fuzzy variables indeed correspond roughly to the values implied by the names of the chosen fuzzy variables (e.g. approx. 90). While this is obvious for the diagrams on the left, the input ranges for the variables High of R_{of} and R_{2f} are very broad. Contrary, the input values corresponding to

Low are extremely small. This shows that the choice of inputs and fuzzy variables in table I seems reasonable and a fault classification according to table II is feasible. It has to be noted that the variables corresponding to Ang_A , Ang_B , Ang_C and Δ_1 , Δ_2 , Δ_3 do not have to be plotted separately, because the ideal symmetry of the line ensures that all parameters are the same regardless of the referenced phase.

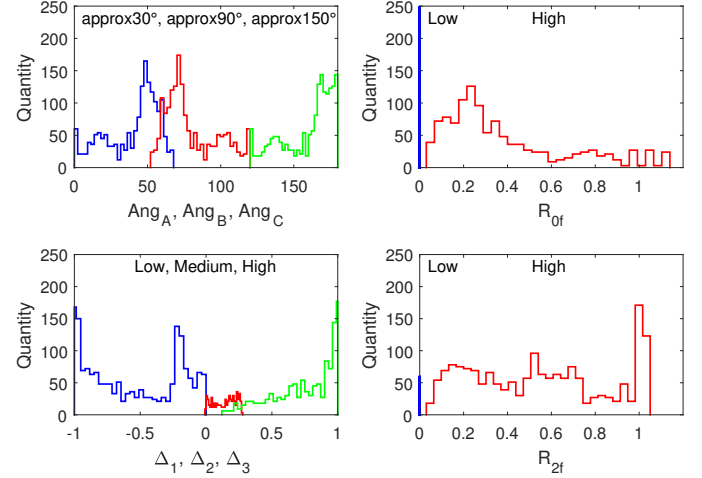


Fig. 3. Histogram of inputs corresponding to the different fuzzy inputs; single line configuration (base case)

C. Membership Functions

As shown in Fig. 3 there are some overlaps between the input histograms of different fuzzy variables. These overlaps can lead to two rules of the rule base being active at the same time. This can cause false classification when using boolean logic whereas fuzzy logic allows the correct rule to overrule the other one(s). To investigate on that, three types of membership functions are used: triangle type as the most simple fuzzy one, Gaussian as the most fuzzy one and rectangular for boolean logic.

1) *Triangle Type*: The most simple type of standard fuzzy membership functions is the triangle type. It is defined by a triplet of points P_1 (left corner) P_2 (top corner) and P_3 (right corner). Of these, P_1 and P_3 are the most important, as they determine the value range in which the fuzzy variable is non-zero. Using the rules mentioned in section II-C and the membership functions above, all cases are correctly identified. However, this is only possible if the borders of the membership functions are defined very precisely.

2) *Gaussian Type*: To observe the impact of other membership function types, the Gaussian type was used in a second step. This was accomplished by simply changing the settings in the *Fuzzy Logic Toolbox* to “gauss2mf”. The Gaussian type has two characteristics. Firstly, as it is defined as an exponential function, it cannot become zero. Secondly, in combination with the prod-method as the fuzzy AND operator, the membership values of the fuzzy rule outputs generally get closer to zero. As the value ranges rise compared to the triangle type, some manual corrections are necessary

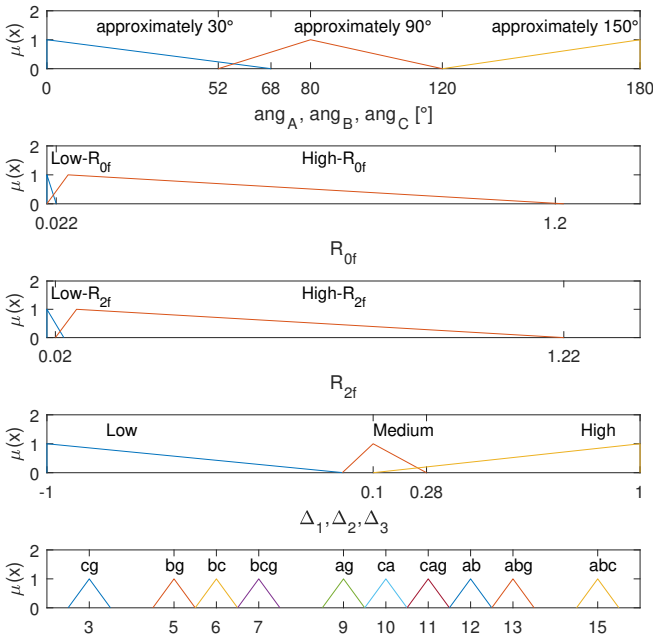


Fig. 4. Triangle type membership functions for symmetrical single line

to maintain optimal classification results. After adopting the curves 100% of the cases could be classified correctly again. Fig. 5 visualizes the difference between triangle and Gaussian membership functions.

3) *Rectangular Type*: To investigate how well a boolean logic with truth values of either 0 or 1 is able to classify the fault scenarios, another FIS was implemented. For this, rectangular membership functions (allowing only membership values of 0 or 1) were used, see Fig. 5. The selection of input variables, the rule base as well as the ranges of the membership functions stayed the same as for the triangle type. Surprisingly, all cases were classified correctly, showing that boolean logic is sufficient for fault classification in simple line configurations. Despite the overlaps in the variable ranges, the proposed rules are selective enough so that only the correct rule gets activated.

IV. ANALYSIS OF NETWORK CONFIGURATION INFLUENCE

A. Influence of Line Configuration

To analyze the influence of the line configuration on the fault classification of a given FIS, two further line configurations as shown in Fig. 6 and 7 have been considered in addition to the single line.

1) *Double Line*: The first step was similar to the base case. After the same parameter variation the value ranges were analyzed in histograms and compared to those from the base case. Although a slight change in the distributions was observed, the value ranges were almost the same. It was then tested, how well the base case membership functions performed with this new system configuration. When using the triangle type, 15 cases were wrongly classified. Very small changes in the value range of the variables led to this incorrect

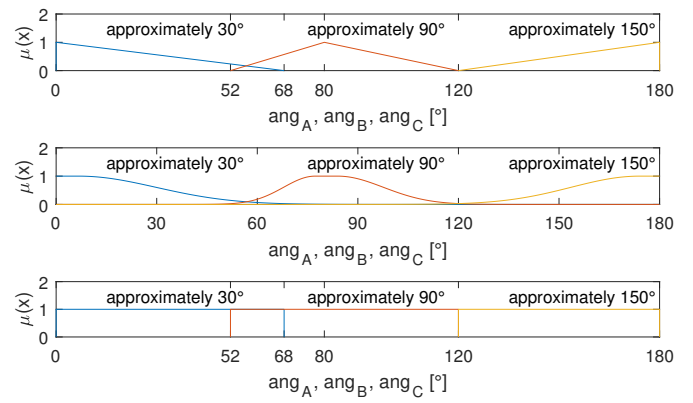


Fig. 5. Illustration of triangle, Gaussian and rectangular type membership functions for symmetrical single line

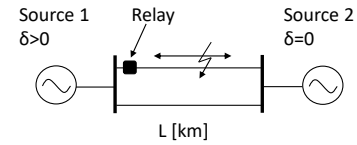


Fig. 6. Double line configuration

classifications. With an adapted triangle set, it was again possible to classify all cases correctly.

The same was tested with the Gaussian type. With the unadapted membership functions from the base case, the FIS classified all cases correctly. The infinite value ranges of the functions makes the FIS robust to small deviations in the input ranges.

While (adapted) triangle and Gaussian types could classify all cases correctly, the boolean logic represented by the rectangular membership functions misclassified three cases even when adapted optimally. The reason is that in some borderline cases of the double line configuration, two rules get active at the same time. As both rules are weighted equally with boolean logic, no correct classification can be made.

2) *Double Line with Central Busbar*: Another tested line configuration is the double transmission line with a central coupling busbar. If a fault occurs beyond the busbar, the healthy system feeds an additional current to the fault, which is not measured by the relay (intermediate infeed).

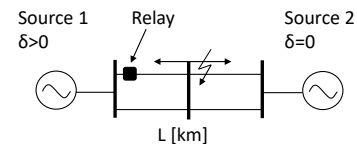


Fig. 7. Double line configuration with central busbar

Again, little changes in the value ranges and distributions are observed. The unadapted triangle type functions from the double line results in 27 mistakes. An adaptation of the triangle set allows to classify all faults correctly again. However

in this case it was not possible to reach 100% successful classification by only changing the value range as the overlap of $\Delta - Low$ and $\Delta - Medium$ was too big. Until now it was not necessary to define the second point of the triangle triplet which determines the slope of the triangle. But it shows now, at the borders of the overlapping zones this can become an important factor for receiving the right membership values. Determining the slope of the triangle by changing P_2 requires quite some trial and error effort for each line configuration.

Here again, the Gaussian type worked very well without any adoptions (still same membership functions as in the Base Case) with with a classification rate of 100%.

The problem of more than one active rule due to big overlaps of membership functions is observed again as described for the double line without additional busbar. Six cases are therefore classified incorrectly by boolean logic.

B. Analysis of unsymmetrical lines

So far all line configurations were assumed as symmetric with perfect transposition to balance the unsymmetry resulting from the geometrical arrangement of the three phases. In this chapter a single transmission line without any transposition was simulated (line data from [5] and given in the appendix). That leads to differing measurements of the currents and therefore the value range for each fuzzy variable will also change. These changes are illustrated in the Fig. 8.

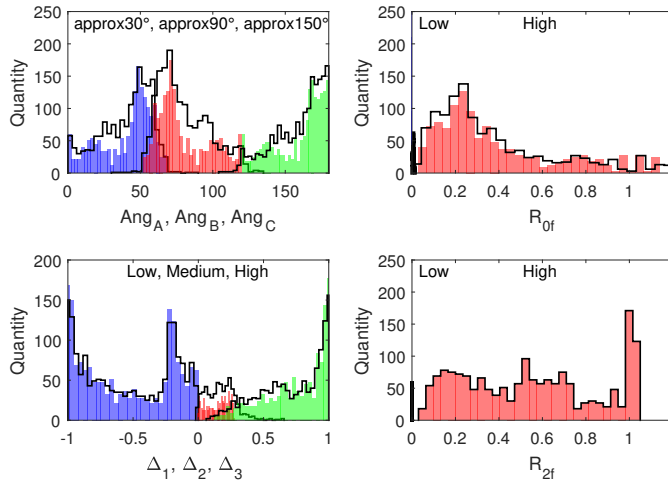


Fig. 8. Histogram for all eight fuzzy-inputs Base Case (coloured) versus unsymmetrical Base Case (black)

This time, the size of the overlapping zones raises significantly, so the old triangle sets will not fit. After adapting the triangle set to the new value range with maintained P_2 , all 1920 cases were classified correctly again. Until now the Gaussian set from the base case was able to classify all the scenarios correctly. However, under these unsymmetrical conditions this FIS decides incorrectly in more than 600 cases. It can therefore be concluded that only small changes in value range can be compensated by the Gaussian FIS. Bigger changes, for example produced by no transposition as compared to ideal transposition, lead to misclassification. To

test if there is a Gaussian set that works for all cases, the triangle set for the unsymmetrical single line is transformed into the “gauss2mf” type. Due to the bigger overlapping zones, some cases get the biggest membership of wrong variables. If two rules are compared with each other and the wrong rule often gets the bigger memberships, this rule gets active and the FIS classifies the fault incorrectly. In contrast, the triangle type with crisp borders is able to eliminate the wrong rule by assigning at least one variable with zero. In fact, it was not possible to create a Gaussian membership set which classifies all cases correctly. After adapting the Gaussian set, five incorrect decisions were still made. Compared with only a small number of misclassifications in previous scenarios, the boolean logic classifies more than 113 cases wrong. This can again be traced back to more than one active rule due to big overlapping zones.

V. UNIVERSAL FIS FOR ALL CASES

In the previous section, Gaussian and triangle type were compared. The triangle type has to be adapted each time because of the fixed value range, while the Gaussian type, once designed was able to classify almost all cases correctly. In this chapter one FIS is designed for all scenarios considered. For this purpose the parameter from each study were combined in one histogram, see Fig. 9.

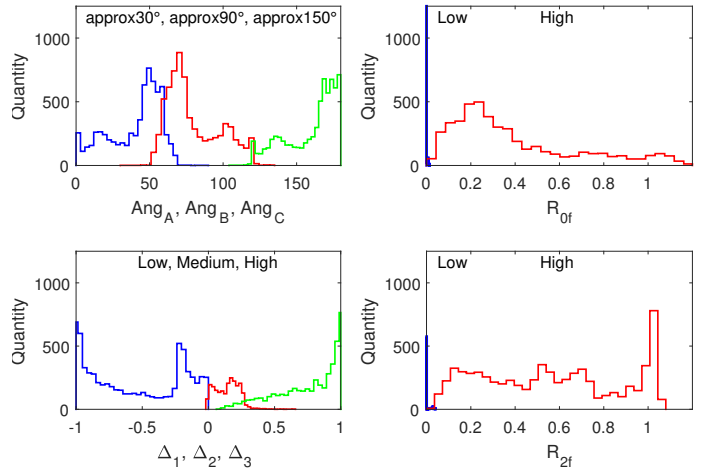


Fig. 9. Histogram for all eight fuzzy-inputs for all configurations

Based on these value ranges a triangle set was designed which has the same value ranges as the histograms and optimized points P_2 . This set was tested for the cases single line, double line, double line with busbar and unsymmetrical single line. It was in fact possible to classify all faults correctly with this system. However, this system is not quite robust against little changes which were not calculated before. If the value range changes, because of bigger unsymmetries in the network there will be a lot of mistakes in fault classification.

For comparison, another membership function set based on Gaussian membership functions was designed. This set classifies all faults correctly for the different symmetrical line configurations, while for the unsymmetrical line two

mistakes were made, equalling 99.89%. Even though two cases were misclassified by the Gaussian type, it is more robust against little deviations than the triangle type. The number of 113 misclassifications with rectangular membership functions shows that it is not possible to classify faults correctly with only using boolean logic. Table IV shows the results for each scenario classified with a FIS using membership functions adapted on the respective value range.

TABLE IV
NUMBER OF FAULTS FOR SPECIFIC VALUE RANGES ADAPTED

	single line	double line	double line busbar	unsym. single line	universal
triangle	0	0	0	0	0
Gaussian	0	0	0	2	2
rectangle	0	3	6	113	137

VI. CONCLUSION

In this paper, an analysis a fuzzy logic based fault classification for transmission lines is presented. Firstly, the used Fuzzy Inference System was explained in detail. Besides some changes to the settings of the FIS, the process of designing fuzzy membership functions was examined using the single line as a base case example. After this, the difference between triangle and Gaussian membership function types was tested. To evaluate the designed FIS, two more complex line configurations were tested with the same system, a double line and a double line with central busbar. As an additional aspect, the impact of an unsymmetrical line as opposed to a ideally transposed line was tested analyzed. Finally, a universal FIS was designed which can be used on all line configurations and classifies all faults correctly. For every line, it was possible to design a FIS, following the described procedure, which can classify all faults correctly. It was found that one Gaussian FIS, designed for a special case works also for other cases while the triangle FIS designed for one special case does only work for this specific case. If the value range is known, the triangle membership functions can also be used for all cases. By evaluating the boolean logic besides the fuzzy logic, this work showed that the use of fuzzy logic is indeed necessary as soon as more complex line configurations are considered. For future work, fuzzy logic for fault detection in addition to fault classification should be investigated in a similar manner. For this, especially the differentiation between the normal operation condition and the three phase fault needs to be realized, based on additional rules and/or new fuzzy inputs.

APPENDIX

Source Data (sending and receiving end)

Open Circuit Voltage	400 kV
Frequency	50 Hz
Short Circuit Power	10.6 GVA
Positive Sequence Impedance	1.31+j15.0 Ω
Zero Sequence Impedance	2.33+j26.6 Ω

Symmetrical Transmission Line Data

Length	100 km
Positive Sequence Resistance R1	0.0275 Ω
Zero Sequence Resistance R0	0.181 Ω
Zero Sequence Mutual Resistance R0m	0.152 Ω
Positive Sequence Inductance L1	0.8053 mH/km
Zero Sequence InductanceL0	2.9920 mH/km
Zero Sequence Mutual Inductance L0m	1.601 mH/km
Positive Sequence Capacitance C1	14.21 nF/km
Zero Sequence Capacitance C0	7.58 nF/km
Zero Sequence Mutual Capacitance C0m	-1.08 nF/km

Unsymmetrical Transmission Line Data

phase	x [m]	y[m]	type
1	11	31.2	1
2	14.2	22.2	1
3	7.8	22.2	1
earth	0	46.6	2

$$\rho_{\text{earth}} = 100 \Omega \cdot \text{m} \quad \text{max line sag: } 5.88 \text{ m}$$

Bundle Characteristics

type:	1	2
Conductor Outside Diameter [cm]	1.880	1.382
Conductor T/D ratio	0.310	0.197
Conductor GMR [cm]	0.775	0.608
Conductor DC resistance [Ω /km]	0.120	0.302
Conductor relative permeab.	1	1
Number of conduct.	4	1
Bundle diameter [cm]	56.568	0.000
Angel of conductor one [$^\circ$]	45.00	0.00

REFERENCES

- [1] A. Ferrero, S. Sangiovanni, and E. Zappitelli, "A fuzzy-set approach to fault-type identification in digital relaying," *IEEE Transactions on Power Delivery*, vol. 10, no. 1, pp. 169–175, 1995.
- [2] B. Das and J. V. Reddy, "Fuzzy-logic-based fault classification scheme for digital distance protection," *IEEE Transactions on Power Delivery*, vol. 20, no. 2, pp. 609–616, 2005.
- [3] C. Cecati and K. Razi, "Fuzzy-logic-based high accurate fault classification of single and double-circuit power transmission lines," in *International Symposium on Power Electronics Power Electronics, Electrical Drives, Automation and Motion*. IEEE, 2012, pp. 883–889.
- [4] E. da Silva Oliveira, A. H. Anzai, and W. A. Gaspar, "A high accuracy fuzzy-logic based fault classification in double-circuit transmission corridors," in *2014 11th IEEE/IAS International Conference on Industry Applications*. IEEE, 2014, pp. 1–7.
- [5] G. Herold, *Elektrische Energieversorgung II - Parameter elektrischer Stromkreise, Leitungen, Transformatoren*, 2nd ed. Wilburgstetten: Schlembach, 2008.

Influence of Meteorological Conditions on European Electricity Markets

S. K. Dankwah, L. Skiba

Institute of Power Systems and Power Economics
RWTH Aachen University
Aachen, Germany

S. K. Dankwah, W. Wangdee

Electrical Power and Energy Engineering Program
Thai-German Graduate School of Engineering
Bangkok, Thailand

Abstract— The electricity infeed of units based on renewable energies is mostly affected by different meteorological conditions. Subsequent to this, market results such as infeed of conventional power plants, market prices as well as imports and exports between market areas also depend on these meteorological conditions. Therefore, this paper presents investigations on how the European electricity market is affected by different weather conditions using European market simulations. Results for four different meteorological years of selected countries in Europe are described in this paper. The simulated results demonstrate that generation, import and export as well as electricity prices are all influenced by different meteorological conditions. Furthermore, the paper quantifies the possible effect of the use of different meteorological years in market simulations, underlining the importance of the choice of this input datum.

Keywords— Meteorological year, Power generation dispatch, Power system simulation, Renewable energy sources, Electricity prices.

I. INTRODUCTION

The world's aim and commitment to limit the rise in atmospheric mean temperature to below 2 °C above pre-industrial level [1] and maintain the concentration of greenhouse gas (GHG) at levels that would further not disrupt the climate system [2] cause a gradual increase in renewable energy sources (RES). RES, due to their negligible GHG emissions, provides hope in recent times to achieve these visions. Contrary to the increase in electricity consumption and public heating in Europe from 1990 to 2014 by 15%, there has been a decline in GHG emissions [3]. The significant rise in generation units based on RES in Europe is a major contributing factor to the lower GHG emissions [3]. The newly globally installed renewable power capacity was 9% higher in 2016 compared to 2015 [4].

Consequently, power generation based on RES units is expected to rise in the future due to low marginal cost, zero direct GHG emissions and the gradual reduction in technological price [4]. The infeed from these RES units is highly contingent on meteorological circumstances. If available, RES generation can be regarded as must-run infeed because of its low marginal costs and infeed prioritization in many countries. Hence, conventional power plants need to adjust their power output to meet the remaining demand. Therefore, RES units and meteorological circumstances have a large influence on power plant dispatch and wholesale electricity prices.

Market simulations are one possibility to quantify the effect of varying RES generation on power plant dispatch. In this context, RES generation is seen as must-run infeed and is input datum for the simulation. One possible approach is the use of consistent historical data to derive time-series for RES infeed, hydraulic storage inflow and load. In order to ensure consistency, data from one specific year can be used. The data of this so-called meteorological year can then be scaled and adjusted to fit the expected installed capacity and full load hours of the given scenario. Infeed and load can vary significantly from year to year. With that, the choice of a specific meteorological year can have a substantial influence on market simulation results.

Therefore, this paper illustrates the effects of different meteorological years on market simulation results. In order to do so, different meteorological years were analyzed and important differences and influences were then derived. Furthermore, a number of market simulations were parameterized, conducted and evaluated.

II. ANALYSIS

RES units have all their sources dependent on weather parameters. While photovoltaic units (pv) depend on solar radiation, wind turbines also generate power from the wind. Similarly, hydro power generation is relational to water potential. Renewable energy sources are moreover important elements for the price development on electricity markets hence the first part of the analysis focuses on discussions related to renewable energy sources.

A. Impact of weather conditions on electricity generation and consumption

The uncertain availability of RES is relational to factors such as temperature, solar radiation or light intensity, relative humidity, wind, and rainfall which are not perfectly predictable. Sources of biomass with their processes and power generation are affected to a lower extent by these weather parameters, hence, this work will not focus on electricity generation from biomass.

1) Impact on Must-run Units Generation

System operators commit some electricity generating units to be constant in operation, ensuring certain operational purposes are satisfied. These units are considered as must-run.

For instance, the covering of heating and control reserve power demand may lead to a must-run infeed of thermal power plants. Likewise, the prioritization of RES infeed results in their consideration as a must-run unit. This paper considers RES and combined heat power (CHP) plants as must-run units.

a) *Solar Energy*: Both the electrical efficiency and the power output of a pv module depend linearly on the operating temperature, and falls with decreasing cell temperature [5]. Minimum components of reflection exist in the atmosphere subjecting light striking solar panels to more losses. As humidity increases, both current and voltage reduce and hence the power [6]. The efficiencies of solar cells fall considerably with decreasing light intensity incident on solar modules and also rises with increasing light intensity. Fig. 1 illustrates how pv solar energy changed with the daily sun hours in the UK during 2015.

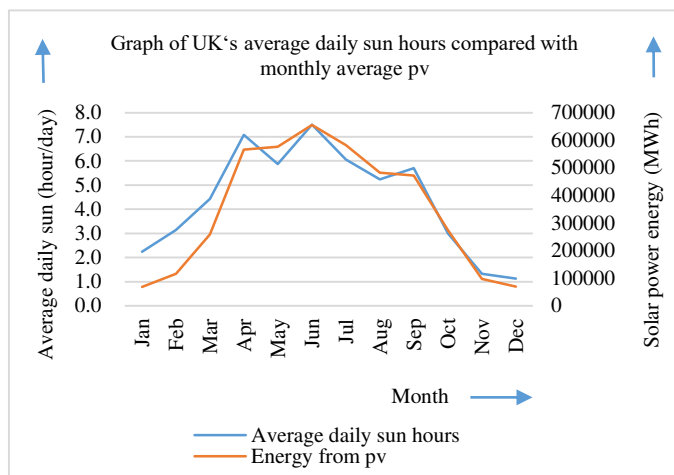


Figure 1. Comparison of daily sun hours to pv energy in the UK [7]

b) *Wind energy*: The amount of wind kinetic energy which could be converted into electricity by the wind turbine may fall during high temperatures due to the lower density of air. However, the output power from wind turbines increases mainly with increasing wind speeds between the cut-in and rated speeds. Almost constant output power of wind turbines is observed at levels above the rated speed. Fig. 2 shows how wind energy infeed varied with wind speed in the UK during 2014.

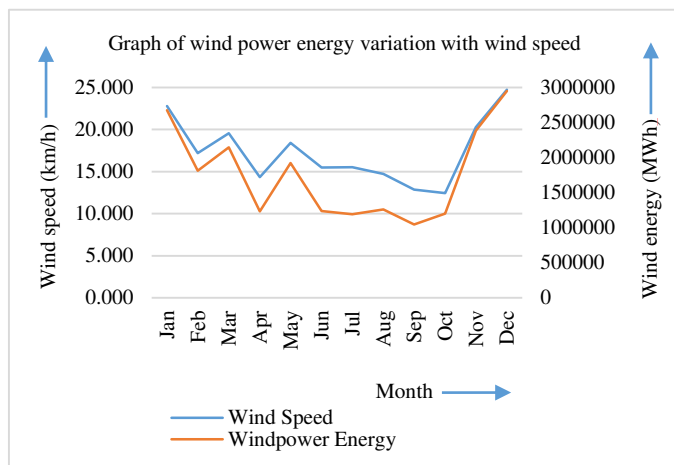


Figure 2. Comparison of wind energy to wind speed in the UK [7]

c) *Hydro Energy*: Alterations in precipitation and river discharge cause a varying Hydroelectric generation. A drop of one percent in precipitation leads to two to three percentage reduction in streamflow and each percentage reduction in streamflow ends up in a three percent fall in power generation [8]. The changes in energy generated during 2015 from hydro units due to the rainfall in the UK is shown in Fig. 3.

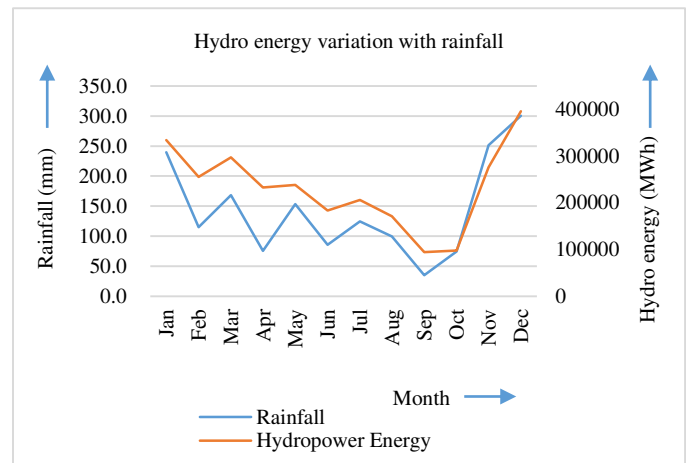


Figure 3. Comparison of hydro energy generation to average rainfall in the UK [7]

d) *CHP*: Industries and households have basic heating requirements such as industrial steam production, water and space heating which to large extents are supplied by CHPs. The volume of CHP dispatched to cover these demands changes with a change in demand. The dependency of heating requirement on the temperature therefore results in the variation of the output of CHPs.

Since the impacts of the weather on conventional power generation are minimal, compared to RES energy generation, only must-run generation from CHPs was analyzed with RES units because of the link between their generation and the weather.

2) Impact on Conventional Energy

On the electricity markets, must-run units bid at low prices and are usually successful with their bids. Hence, they are normally the first to cover portions of the available demand. The volume of load remaining is referred to as residual load. Conventional power plants dispatch to cover this residual load in accordance with the respective energy prices of running units. Since RES and CHP are influenced by the weather, their generation also varies, and this causes the residual load to alter with the output power of must-run units. Moreover, when consumption varies with the weather, the power dispatched from conventional power plants varies with the weather.

3) Impact on Consumption

Electricity generation follows the demand. Changes in consumption, therefore, cause the generation to vary. The variation in the residual load largely affects conventional and nuclear power generations while must-run units such as RES and CHP infeed are independent of the residual load. Fig. 4 shows a comparison of the amount of electricity consumed in Europe from 2012 to 2015. Consumption in 2012 on the average is the highest among all the other years. The graph also illustrates that,

in Europe, consumption in all years falls gradually from January to June, rises a little in July and falls back in August after which there is a gradual rise to December. These demand patterns largely follow the heat demand, with lower heating requirement during summer periods, i.e. from mid-May to August. Fig. 5 illustrates how the electricity consumption varied with heating degree days (HDD) for 2012. HDDs are quantitative indices usually used to determine the variation in consumption. The pattern of consumption in 2012 reflects that of the HDD. The graph also shows a rise in consumption in July higher than both June and August while the HDD during July was close to the least.

Power demand rose greatly in Europe during February 2012 as a result of temperatures dropping beneath seasonal average [9]. In 2014, the heating requirement was lower than previous years, which led to a reduction in power demand below the seasonal average. However, September and December had colder weather with increased demands [10]. Most countries experienced colder weather than the norm in October 2015 which increased the demand for electricity for residential heating [11].

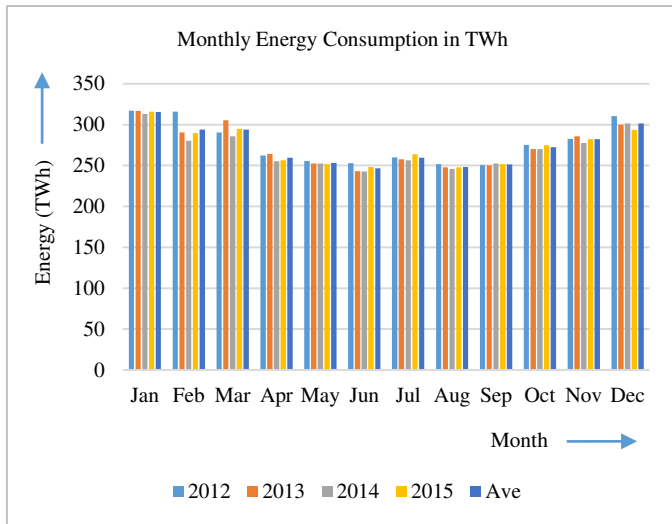


Figure 4. Monthly energy consumption for Europe from 2012 to 2015

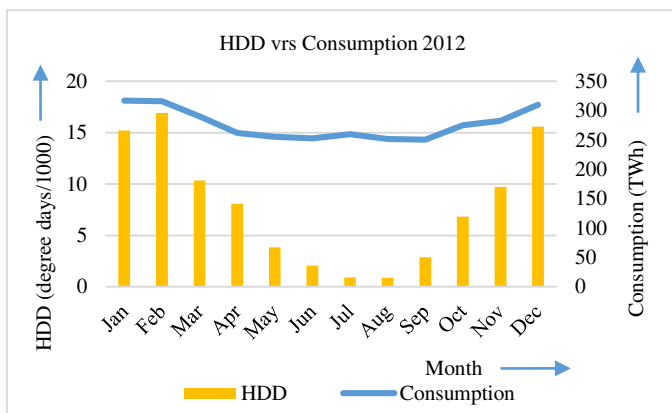


Figure 5. HDD and energy consumption

B. The European Electricity Price

The price of electricity is primarily determined by the cost of the primary energy, prices of emission allowances, the availability of power plants and the consumer demand. Other factors may include cross-border exchanges and weather conditions.

Increase in generation from conventional energies increases the cost of electricity. As prices of sources such as coal, oil or gas rises, generation costs also increase. When electricity generation from RES declines due to weather conditions, a greater volume of generation from primary energies is required to match the residual load resulting in a price increase of electricity. On average, electricity prices fall by €0.4/MWh when there is a percentage rise in the share of renewable energy in Europe [12].

During cold or hot spells when much power is consumed for heating or cooling purposes, electricity prices are affected. A greater demand causes rise in market prices since more conventional energy units need to be committed to supply the load.

Electricity markets in Europe are closely connected. One market area can buy electricity in another market area until the demand is covered or the transmission capacity is exhausted. This leads to a convergence of power prices in Europe. Different electricity prices between market areas emerge only when transmission capacities are insufficient. Markets with more interconnectivity or coupling, potentially gain lower power price compared to those with less coupling [12].

III. SIMULATION MODEL

In this paper, a market simulation model for European market areas is used [13]. The model optimizes complex problems to obtain an hourly infeed of every power plant, minimizing total generation costs. It solves the problem based on a four-step approach as illustrated in Fig. 6 using, among others, the following fundamental input data:

- generation stack of coupled market areas
- Must-run infeed (RES and CHP)
- constraints due to plant outages and variable cost of power plants
- prices of primary energy and emission certificate,
- balancing reserves and power demand
- dispatch constraints.

First of all, a linear approach is used to calculate the initial solution for power exchange between market areas and water reservoir levels. Afterwards, load coverage and reserve provision constraints are considered under Lagrangian relaxation to calculate appropriate start-up and operating decisions for each market area by dividing the complex problem into smaller hydraulic and thermal problems, computing and coordinating them iteratively. The third stage has calculations of electrical energy exchange between countries performed under thermal and hydraulic power plants constraint. Minimum plant dispatch cost, cross-border power exchanges and hourly market

load coverage are achieved under this step. Simulation of hourly market power prices is done by a linear approach as the last step.

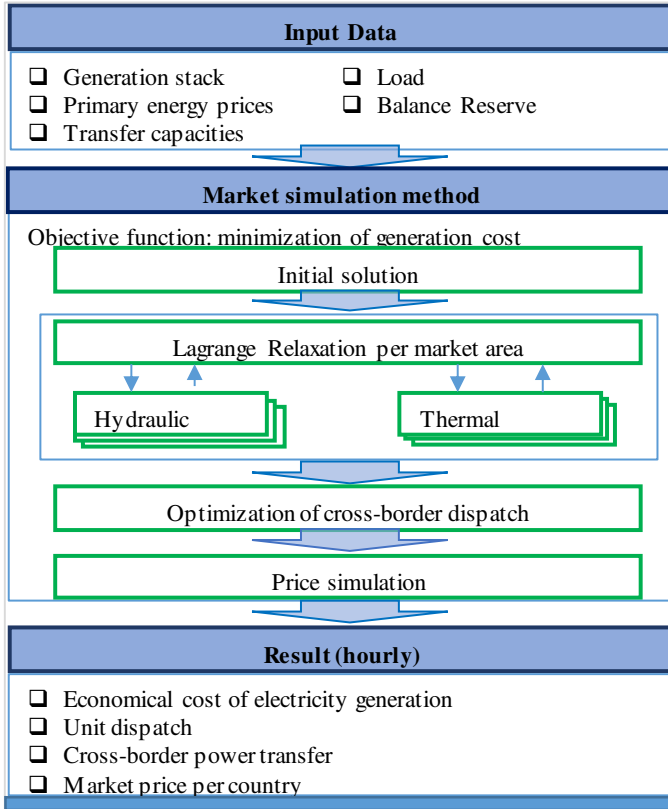


Figure 6. Four-step approach of the market simulation method [13]

IV. INVESTIGATIONS AND DISCUSSION

In order to better understand the influence of different meteorological conditions on market results, we aim to examine market simulation results for different meteorological years. First and foremost, the market result for the year 2014 was backtested with ENTSO-E historic data. Subsequently, three different sensitivity simulations with the reference simulation of 2014 were compared. In these sensitivities, the time series of wind, pv and CHP were adjusted to represent the meteorological conditions of 2012, 2013 and 2015. The remaining systems, including installed capacities for wind and pv, remain the same. Inflow to hydraulic basins was not varied because of insufficient data.

A. Input Data

In this research, data of wind and pv capacity factor time series from 2012 to 2015 were obtained from [14]. RES generation and net generation capacities (NGC) are based on ENTSO-E's yearly statistics and adequacy retrospect datasets [15] for the respective period. Consistent RES generation and NGCs of UK and Northern Ireland were acquired from the national statistics of the UK government [7]. The NGC with total power generation of every country were used to derive the full load hours for each year.

Acquired capacity factors were adjusted to fit the RES full load hours of each country. The newly adjusted capacity factors of different years together with NGCs of countries for 2014 were

then used to parameterize hourly generation portfolio of RES units for every year. Annual Eurostat's CHP values were dissolved into hourly profiles according to household and industrial heating demands and the average temperature for every year. Generation differences in the input data for pv, wind and CHP infeed are shown from Fig. 7 to Fig. 9 respectively.

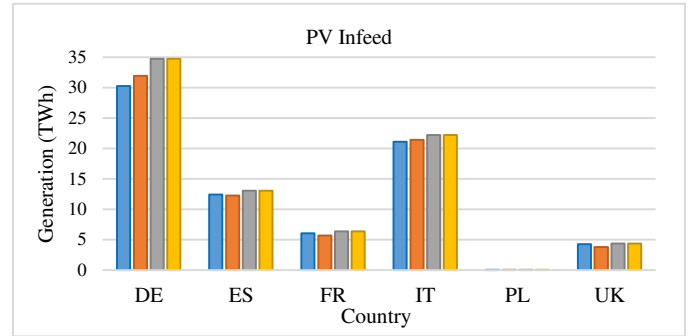


Figure 7. Total infeed of pv for different years in selected countries

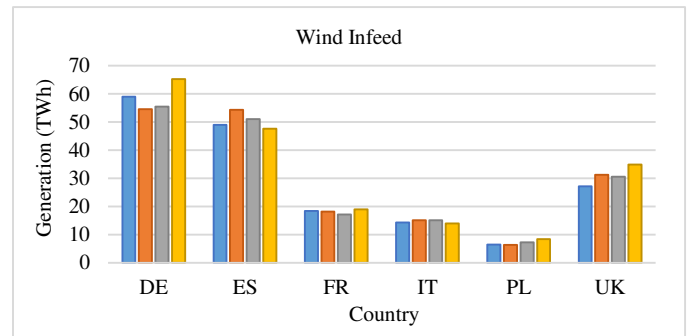


Figure 8. Total Infeed of wind for different years in selected countries

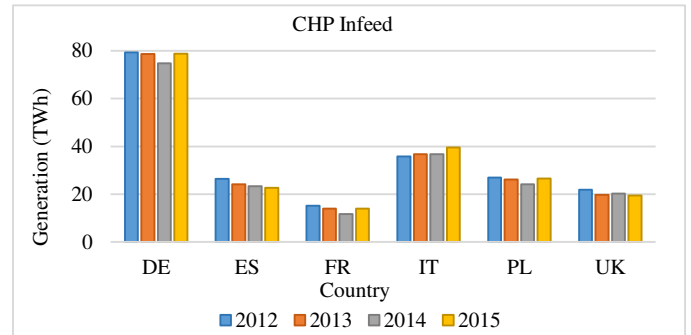


Figure 9. Total CHP infeed for different years in selected countries

B. Results

Due to a large number of countries in Europe, the discussion of results focuses on Germany and other selected countries. That is, Germany (DE), Spain (ES), France (FR), Italy (IT), Poland (PL) and United Kingdom (UK).

Fig. 10 shows a comparison of the resulting generation of 2014 to ENTSO-E 2014 historic data (HD). While the total generation of most countries is close to historic data, differences manifest in some market areas. Considering that CHP infeed is not specified in the historic data, but aggregated in the simulation, the biggest differences stem from infeed from hydraulic units. While these differences can be explained with simplified models of hydraulic systems in the simulation, other

differences in thermal generation can be attributed to simplifications in the modelling of primary energy or must-run restrictions. As a result, import and export figures differ between simulated and historic data. The main aim of this paper is to compare simulation results for different meteorological years rather than historical data. Hence, the used input data and model simplifications suite for this purpose. In the following, the simulation results of 2014 are used as the reference for further discussions.

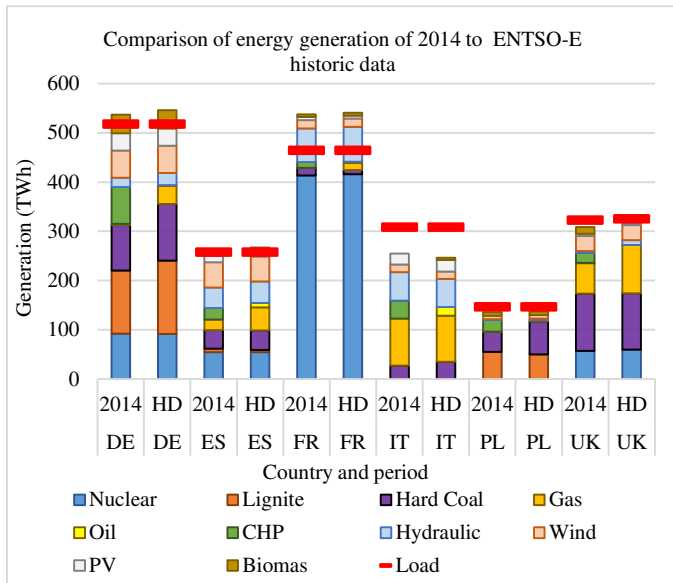


Figure 10. Comparison of simulated generation to historic data of selected European countries

The resulting yearly total thermal generation percentage deviation from 2014 (0%) of each country is illustrated in Fig. 11. The results clearly demonstrate different volumes of total thermal generation were dispatched. Moreover, the percentage rise in thermal generation is greater than its percentage reduction. Generation in France during 2012 which is the largest growth is 8.5% higher than in 2014 while UK’s thermal power production in 2015 fell below all others. This shows that the different weather conditions affected the output of thermal power plant. The result further indicates average thermal generation for 2012 is the highest compared to the other years. This could be associated with the high heating and consumption demand during 2012 as indicated in the analysis (3)II.A.3).

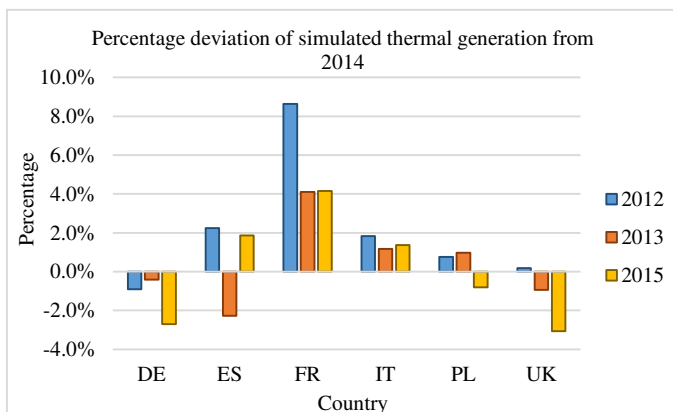


Figure 11. Percentage deviations of simulated thermal generation from 2014

The impact of different meteorological years on total import and export for the selected countries are presented in Fig. 12 and Fig. 13. Percentage import to Poland and Italy for all years are the closest to their import in 2014. In contrast, percentage export deviation of Poland is the largest while Italy remains the smallest. Poland exports 50% more electricity in 2013. The 8% import growth of Germany in 2012 compared to 2014 is largest among all import. However, the 50% export increment of Poland is due to a marginally low export in 2013 in which a substantial increase or reduction in export leads to huge percentage difference. The charts further show more negative percentage variance in France and UK for import and export respectively

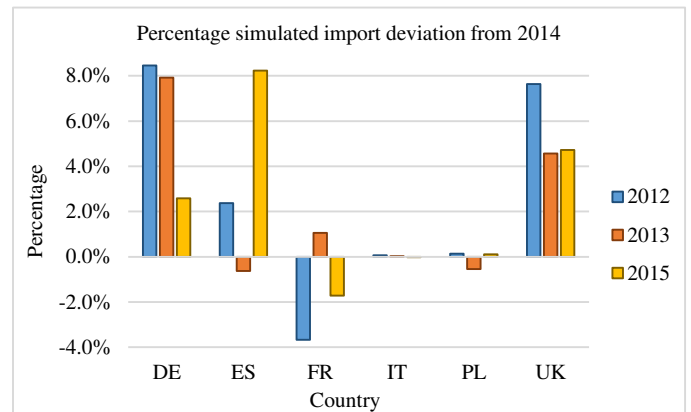


Figure 12. Percentage simulated electricity import deviation from 2014

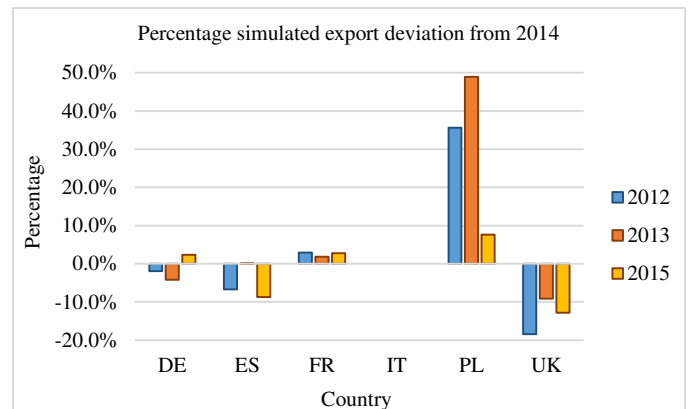


Figure 13. Percentage simulated electricity export deviation from 2014

Fig. 14 and Fig. 15 show the simulated price duration curves of Germany and Spain as influenced by the weather in different meteorological years. The two curves show price variation mostly at the cheapest and more expensive price hours. Meanwhile, more distinctiveness is noticed at cheapest hours than in expensive hours. Fig. 14 demonstrates most prices of all other years are lower than in 2014 on the German market. On the hand, Fig. 15 indicates that only prices of 2013 on the Spanish market are cheaper than prices of 2014. This signifies that different meteorological years do not necessarily have the same effect in all market areas.

Finally, in TABLE I, the total RES infeed, net electricity export and average electricity prices for Germany are depicted. It can be seen that the lowest (86.48 TWh) and highest (99.99 TWh) RES infeed can be found in 2013 and 2015 respectively. The highest RES infeed results in greatest net

export (21.301 TWh) and least average price (31.078€/MWh) whereas the lowest RES infeed leads to a lower net export and the most expensive average price. This illustrates that when the volume of RES infeed varies with weather conditions, electricity prices on the market also alters.

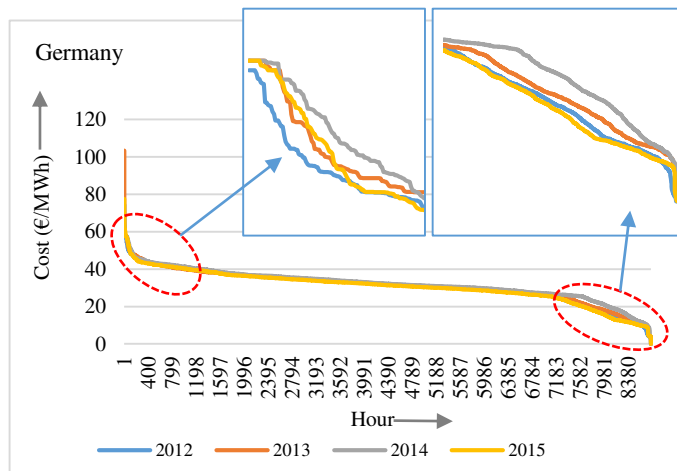


Figure 14. Simulated price duration curves for Germany

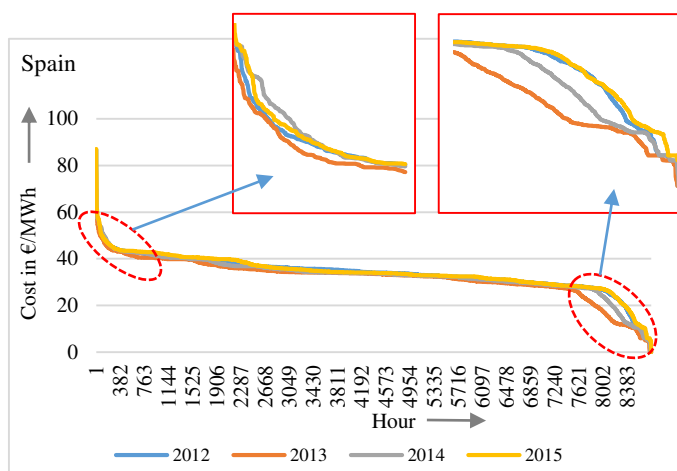


Figure 15. Simulated price duration curves for Germany

TABLE I. TOTAL RES INFEEED, NET EXPORT AND AVERAGE ELECTRICITY PRICES OF GERMANY

Year/Data	Total RES Infeed [TWh]	Net Export [TWh]	Yearly Average Price [€/MWh]
2012	89.30	17.026	31.686
2013	86.48	14.743	31.684
2014	90.44	21.292	32.618
2015	99.99	21.301	31.078

V. CONCLUSION

The European electricity market observes high volatility and varying prices due to the inclusion of the RES in the generation stack. The high expectancy of increase in RES calls for research into how RES, which is highly dependent on meteorological conditions, affects the market. In that vein, this research was undertaken to investigate how electricity markets are affected in different meteorological years by using market simulations. The

results show variations in generation as well as export and import for all analyzed meteorological years. In addition, different market prices are seen in the least and most expensive hours. This suggests that electricity prices which are determined on international markets vary less, unlike generation which has greater variation in individual countries when influenced by different meteorological conditions. Further work could be done to obtain more accurate historic data and incorporate these in further and more detailed simulations.

REFERENCES

- [1] United Nations, "Paris Agreement," United Nations, Paris, 2015.
- [2] United Nations, "Kyoto Protocol to the United Nations Framework Convention on Climate Change," United Nations, Tokyo, 1998.
- [3] Eurostat, "Eurostat Statistics Explained," European Commission, February 2017. [Online]. Available: http://ec.europa.eu/eurostat/statistics-explained/index.php/Climate_change_-_driving_forces. [Accessed 5 March 2018].
- [4] REN21, "Renewables 2017 Global Status Report," REN21 Secretariat, Paris, 2017.
- [5] E. Skoplaki and J. Palyvos, "On the temperature dependence of photovoltaic module electrical performance: A review of efficiency/power correlations," *Energy Procedia*, vol. 83, pp. 614-624, 2009.
- [6] M. K. Panjwani and D. G. B. Narejo, "Effect of Humidity on the Efficiency of Solar Cell (photovoltaic)," *International Journal of Engineering Research and General Science*, vol. 2, no. 4, pp. 499-503, 2014.
- [7] Department for Business, Energy and Industrial Strategy, UK, "Energy Trends," 9 January 2013. [Online]. Available: <https://www.gov.uk/government/statistics/energy-trends-section-6-renewables>. [Accessed 24 January 2018].
- [8] T. R. Karl, J. M. Melillo and T. C. Peterson, "Global Climate Change Impacts in the United States," Cambridge University Press, Cambridge, 2009.
- [9] European Commission, Directorate-General for Energy, "Quarterly Report on European Electricity Markets," European Commission, Brussels, 2012.
- [10] European Commission, Directorate-General for Energy, "Quarterly Report on European Electricity Markets," European Commission, Brussels, 2014.
- [11] European Commission, Directorate-General for Energy, "Quarterly Report on European Electricity Markets," European Commission, Brussels, 2015.
- [12] European Commission, "Report from the Commission to the European Parliament, the Council, the European Economic and Social Committee and the Committee of the Regions (Energy Prices and Costs in Europe)," European Commission, Brussels, 2016.
- [13] A. M. T. D. a. A. M. F. Grote, "Modeling of Electricity Pricing in European Market," in *IEEE*, Lisbon, 2015.
- [14] I. S. Stefan Pfenninger, "Long-term patterns of European pv output using 30 years of validated hourly reanalysis and satellite data," *Energy*, vol. 114, pp. 1251-1265, 2016.
- [15] ENTSO-E, "Yearly Statistics and Adequacy Retrospect," ENTSO-E, 29 05 2017. [Online]. Available: <https://www.entsoe.eu/publications/statistics/yearly-statistics-and-adequacy-retrospect/Pages/default.aspx>. [Accessed 8 February 2018].
- [16] M. E. Weber, "Water for Electricity Generation in the United States," in *Competition for Water Resources*, Elsevier, 2017, pp. 212-232.

Power Plant Dispatch Considering Heat Cogeneration

Lucas Bernhard Temmen, Timo Breithaupt, Lutz Hofmann
 Institute of Electric Power Systems
 Leibniz Universität Hannover
 30167 Hanover, Germany

Abstract—This paper illustrates how an Integrated Grid and Electricity Market Model (IGEM), which uses a mixed integer linear programming approach to calculate the optimal generation dispatch according to the marginal costs, can consider heat cogeneration in Germany’s power plant dispatch. The existing market model does not take the influence of district heating on electric power markets into account. Therefore, it underestimates the importance of integrated energy systems as cogeneration plants often have to produce power to cover their heat load. Thus, the power plants are organized in technical plant categories and their thermal output and operating behavior are assessed. Also, heating plants are created in order to improve the accuracy of the simulation. Subsequently, heating zones, for which temperature- and time-of-day-dependent thermal load curves are created, are introduced. Furthermore, the objective coefficients and the optimization variables of the mixed integer linear programming approach of IGEM are expanded and adjusted. New constraints, formulating the cogeneration plants’ characteristic operation diagram as well as the equilibrium conditions of thermal production and load, are described. Afterwards, a plausibility check of the simulation results, using statistical data about the total thermal bottleneck output and the yearly heat generation, is performed. Finally, the results of a case study of the district heating grid of the City of Leipzig is analyzed.

I. INTRODUCTION

In the Integrated Grid and Electricity Market Model (IGEM) of the Institute of Electric Power Systems of the Leibniz Universität Hannover, the energy markets in Europe in addition to an electrical grid simulation are analyzed. The active power and control reserve markets are modeled. Also, the power generation of renewable energies is considered using regional climate and plant data [1], [2]. The basic structure of IGEM is shown in Fig. 1. It is based on databases, e.g. a power plant database or regional data. Using these databases, a generation dispatch is modeled. Therefore, IGEM simulates electrical load curves and the operation behavior of power plants. It solves a mixed integer linear programming (MILP) optimization problem in order to find the economically optimal power plant dispatch considering factors like emission and fuel costs. Afterwards, a load flow simulation and a market price calculation are performed. Finally, IGEM evaluates the simulation results.

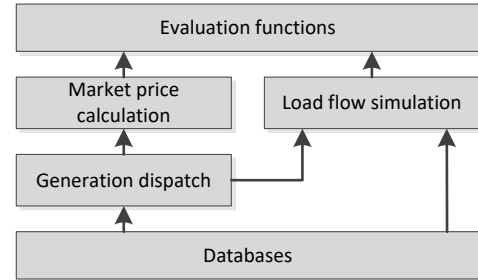


Fig. 1. Basic structure of IGEM

In Germany, 14 % of all households are connected to district heating grids [3]. Those grids are mostly located in conurbations; they supply the customers with heat using isolated steel pipes. The heat is generated with combined heat and power (CHP) plants or heating plants (HP).

In the present version of IGEM, the heat extraction of large thermal power plants is neglected. However, CHP has a significant influence on the power plant dispatch and is partly responsible for negative electricity prices [4].

CHP is also interesting from an ecological point of view, as a very low primary energy factor can be achieved. Therefore, the Federal Government’s objective is to increase the total electricity generation of CHP plants to 110 TWh by 2020 [5].

Besides the CHP plants and the consumers, there usually is at least one alternative heat supplier on each district heating grid. These HPs only generate heat. Furthermore, heat storage systems are often used to increase the flexibility of CHP plants. In today’s energy markets, a CHP plant not only competes with other power generators on the electricity market, but also with other heat generators in its district heating network. In order to reflect the impact of cogeneration on the electricity market, it is thus not sufficient to consider electricity generation costs alone; a holistic approach, which takes the total generation costs of the heat and electricity into account, should be used.

One goal of this paper is therefore the development of a model of large thermal power plants with heat extraction for their more precise consideration in the power plant dispatch. For this reason, an approach to model the operation behavior of CHP plants is presented in Section II-A. Furthermore, Section II-B shows the modeling of thermal

load curves. Afterwards, the implementation of the new constraints in IGEM is depicted (Section III). Section IV discusses the simulation results. Finally, a conclusion is made in Section V.

II. MODELING OF HEAT GENERATION AND LOAD

In this section, a description of the modeling of the generation plants and the thermal load is given. The classification into different power plant types and the estimation of the maximum heat output are shown. Also, a distinction between heat producers for the public supply and industrial plants for the provision of mainly process heat is made. Furthermore, the regional district heating demand is determined. For this purpose, temperature- and time-of-day-dependent coefficients are introduced in order to create thermal load curves.

A. Modeling of the Operation Behavior of CHP Plants

In this paper, large CHP plants are split into three main types:

- Back pressure steam turbine (BPST): Mostly small steam CHP plants, can only produce heat and electricity in a constant ratio
- Extraction condensing steam turbine (ECST): Large steam CHP plants, flexible production of heat and electricity
- Gas turbine with heat recovery (GTHR): Gas turbine with a boiler in order to use the waste heat of flue gases

Also, two coefficients, shown in (1) are important when modeling CHP plants. The CHP coefficient σ_N is the ratio of the nominal electrical output (P_N) to maximum thermal output (\dot{Q}_{\max}). Further, the power-loss-coefficient pl describes the losses of electrical power caused by the increase in heat power.

$$\sigma_N = \frac{P_N}{\dot{Q}_{\max}}, \quad pl = \frac{\Delta P_{el}}{\dot{Q}} \quad (1)$$

The power plant database of IGEM already contains information about the possibility of heat extraction of the power plants. In addition to that, for some power plants precise data on the maximum thermal output is available.

If this value is unknown, it is important to estimate this maximum heat output \dot{Q}_{\max} as precisely as possible in order to create a coherent simulation environment. It is then generated by dividing P_N by a typical σ_N . The nominal CHP coefficients used for power plant modeling are shown in table I. The given source provides this indicator as a range for each type of power plants. For the estimation of \dot{Q}_{\max} , the arithmetic mean of these ranges is assumed.

Furthermore, a division into systems with BPST, ECST or gas turbines with heat recovery is necessary since the operating behavior and the CHP coefficients of the power plant types differ significantly. The type of CHP plant

TABLE I
TYPICAL CHP COEFFICIENTS AND ELECTRIC OUTPUT OF DIFFERENT POWER PLANT TYPES [6]

Plant category	P_N	Type	CHP coefficient
Steam turbine	≤ 75 MW	BPST	0,45
	> 75 MW	ECST	1,65
Gas turbine		GTHR	0,5
Combined cycle		ECST	2,10

is allocated on the basis of the plant category and the nominal electrical output of the power plant.

Obviously, all combined cycle CHP plants are treated as ECST plants. This is mainly due to the lack of information in literature. A random sample of these plants in Germany showed that combined cycle plants with BPST are almost exclusively used in very large district heating grids with a continuously high thermal load (e.g. Berlin, [7]). The majority of combined cycle CHP plants is constructed as ECSTs; this is also due to the more flexible operating range.

The power loss index pl for each CHP plant is assumed to be 0.2; typical values are between 0.15 and 0.25 [8]. Since this coefficient depends on the ratio of thermal to electrical power, a simplified approach is needed. An exception are GTHR: here, a power loss index of 0 is assumed, since the thermal output of the flue gases used for heat generation is dissipated in exclusive electrical operation, the slight reduction in output due to the increased turbine outlet pressure is neglected.

Furthermore, the power plant database does not contain HPs, yet. However, these are indispensable for the operation of a district heating network in order to cover peak loads or to compensate an outage of a CHP plant, which is why they are introduced as follows. It is assumed that HPs can deliver at least 25 % of thermal capacity of each district heating network [9]. They produce only heat, their thermal efficiency is estimated at 90 %; start-up costs are neglected.

A further adjustment is necessary due to the information provided by the power plant operators. Often CHP plants and HPs are located on the same site and the cumulated electrical and thermal power is given. Therefore, at unrealistically low CHP coefficients of power stations, a separation into a CHP plant of lower thermal capacity and an HP is performed. The latter has the same core data as the associated CHP plant and is assigned the remaining thermal output. If it is not a biomass or waste-to-energy plant, it is treated as an HP with the energy source natural gas. This division allows a realistic representation of the operating behavior of the generating plants in every district heating network.

In order to display the thermal and electrical demand for a power plant, every plant has to be classified according to its operation objective. To meet this requirement, the power plant database of the German Grid Development

Plan is used [10]. Here, each plant is classified as either an industrial power plant or a power plant of public supply. In addition to this information, the power plants are allocated to the categories "Electricity-market-based", "CHP" or "Other supply". If a plant's category is "Electricity-market-based", the German TSOs evaluate its operation as power-driven; a coupling to the heat market or to other processes is neglected.

Plants in the "CHP" category not only contribute to the generation of electricity, they can also cover the public heat load. The systems can be operated in both, power- and heat-driven mode.

Public supply power plants in the category "Other supply" are operated by companies at industrial sites. They are necessary to maintain industrial processes, but they can also provide electricity and heat for the public supply. Examples of this category are lignite-powered plants that supply coal mines as well as waste-to-energy and biomass power plants that cannot store their fuel like other plant types [10]. For the optimization-based power plant dispatch of IGEM, only power plants that are not categorized as industrial power plants are considered for the coverage of public heat demand. Furthermore, the heat extraction from Electricity-market-based power plants is neglected. Plants in the category "Other supply" are treated the same way as those of the category "CHP", waste-to-energy and biomass power plants are assigned a must-run-condition. HPs and all other public supply power stations are not subject to must-run conditions.

B. Modeling of the Thermal Load Curves

The district heating demand is modeled individually for 39 government regions. This size of heating zones is chosen because the analysis of the systems at district-level often delivers inaccurate results, since heat consumption and generation in many district heating networks are located in different districts. For each heating zone, temperature- and time-dependent heat load curves are created.

To model the average heat demand for each day, a temperature-dependent approach is chosen. First, the hourly temperatures of each government region in Germany are imported from the climate analysis data of NASA (MERRA) [11]. These are increased by 2 °C to consider the formation of heat islands as they arise in conurbations, which are the main locations of district heating networks [12]. Subsequently, a weighted daily mean temperature, which includes the daily mean temperature of the previous day at 30 %, is calculated. This approach is also used in the Grid Development Plan as it considers the thermal inertia of the buildings [9].

The weighted daily mean temperatures are used to calculate a temperature-coefficient k_ϑ . This factor can reach values between 0 and 1; it decreases linearly with rising temperatures. At a weighted daily mean temperature of 16 °C, the heating limit is reached and k_ϑ drops to a base load of 0.09. This base load results from the hot water

demand of households. Below the weighted temperature $\vartheta_{\dot{Q}_{max}}$, the maximum heat output is required [9]. For the simulation, it is assumed that the temperature of maximum thermal load from [13] applies to all district heating networks. This results in a value of $\vartheta_{\dot{Q}_{max}} = -3.9$ °C.

Furthermore, the district heating load needs to be adapted to the heating habits of the users. Therefore, it is necessary to define typical daily load profiles and apply them to the temperature-coefficients. For this purpose, a time-of-day-coefficient k_{DT} is introduced. Therefore, typical daily heat demand profiles from [14] are normalized to the average output on the day under consideration. The resulting factor takes customer-related aspects like the "morning peak", which is caused by the high warm water demand in the morning hours, into account. The temporal courses of k_{DT} for winter and summer differ; the values for autumn and spring are created as the mean values of these seasons. In order to create a temperature- and time-dependent heating load coefficient, the two previously defined factors are multiplied with each other:

$$k_H = k_\vartheta \cdot k_{DT}. \quad (2)$$

To apply this heating load coefficient k_H , the maximum heating load in each district heating network must be determined. Therefore, the assumption is made that the proportion of maximum heating load to installed heat output is the same as in [13]. This results in a factor of 65 %. The location of each power plant is listed in the power plant database of IGEM; the heat output of each plant is known or has been estimated. The product of the maximum heating load of the region and the current heating load coefficient k_H determines the district heating demand in each region at any time. The thermal load curve and the outdoor temperatures of the City of Leipzig in the year 2014 are shown in Fig. 2.

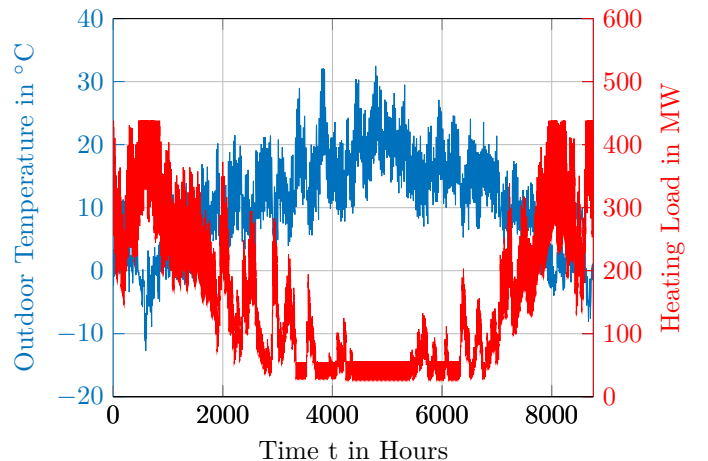


Fig. 2. Thermal load- and temperature curves of the City of Leipzig

It becomes clear that the maximum heating load of the district heating network is only needed a few times of the year. Furthermore, it can be seen that in summer,

there is only a very low heating load required. Here, only the hot water demand has to be covered; the influence of the consideration of the daytime-dependent load becomes visible. Thus, the load fluctuates between 30 and 60 MW within a summer day. In the transitional periods of the year, the heat requirement increases as the outside temperature drops.

III. MODIFICATION OF THE POWER PLANT DISPATCH MODEL OF IGEM

The power plant dispatch model of IGEM is described using a MILP approach. The associated objective function minimizes the total generation costs according to the marginal costs. It considers the wholesale electricity markets as well as the revenues from providing primary (PCR) and secondary control reserve (SCR). The model also calculates interdependencies between different markets, power trading and storages. This paper only shows some of the constraints concerning power plants, for further information and a complete description of the model, please see [1] and [2].

For the consideration of the heat extraction of large thermal power plants in the power plant dispatch model of IGEM, some adjustments are made and additional conditions are introduced. The objective function is shown in (3).

$$\min(\mathbf{f}^T \mathbf{x}) \quad (3)$$

Firstly, it is necessary to extend the optimization variables of the power plants. They are described by their active power production ($\mathbf{p}_{AP,PP}^T$), a binary variable indicating their operating status (\mathbf{op}_{PP}^T), a binary variable indicating whether they start-up at the respective point in time (\mathbf{st}_{PP}^T), as well as the symmetrical PCR ($\mathbf{p}_{PCR,PP}^T$), positive and negative SCR ($\mathbf{p}_{SCRpos,PP}^T$ and $\mathbf{p}_{SCRneg,PP}^T$). In this paper, "active power" means the power traded on wholesale markets in order to distinguish it from control reserve. Additionally, the vector $\mathbf{p}_{HP,PP}$ is introduced. It contains the heating power currently fed into the district heating network by each CHP plant and HP. The new vector of optimization variables is shown in (4). Each power plant n is represented with an own optimization variable for each point in time t .

$$\mathbf{x}_{PP}^T = \begin{bmatrix} \mathbf{p}_{AP,PP}^T & \mathbf{op}_{PP}^T & \mathbf{st}_{PP}^T & \mathbf{p}_{PCR,PP}^T \\ \mathbf{p}_{SCRpos,PP}^T & \mathbf{p}_{SCRneg,PP}^T & \mathbf{p}_{HP,PP}^T \end{bmatrix} \quad (4)$$

An adjustment is also necessary in the coefficients of the objective function in order to consider the costs of heat generation. It is extended by a vector of the specific heating costs \mathbf{hc} . The coefficients of the objective function are shown in (5). Here, the marginal costs of power generation (\mathbf{mc}^T) and start-up costs (\mathbf{sc}^T) are presented, the costs of the provision of secondary control reserve are implemented using \mathbf{os}^T .

$$\mathbf{f}_{PP}^T = \begin{bmatrix} \mathbf{mc}^T & \mathbf{0}^T & \mathbf{sc}^T & \mathbf{0}^T & \mathbf{os}^T & -\mathbf{os}^T & \mathbf{hc}^T \end{bmatrix} \quad (5)$$

The specific heating costs $hc_{PP,n}$ of CHP plants are calculated as the product of the power loss index $pl_{PP,n}$ and the marginal costs of power generation $mc_{PP,n}$ of the plants. The generated thermal power is therefore assigned an equivalent electrical power in order to determine the heat generation costs. (6) shows this connection. Costs of heat production for HPs are defined by (7) using their thermal efficiency $\eta_{th,PP,n}$, fuel and emission costs $C_{F,FT}$ and C_{CO2} , and a fuel-type specific emission factor EF_{FT} .

$$hc_{PP(CHP),n} = pl_{PP,n} \cdot mc_{PP,n} \quad (6)$$

$$hc_{PP(HP),n} = \frac{C_{F,FT} + (C_{CO2} \cdot EF_{FT})}{\eta_{th,PP,n}} \quad (7)$$

$$n = 1, 2, \dots, N$$

Furthermore, it is essential to adjust a constraint to consider the decreased electrical output when extracting heat from a CHP plant (8).

$$P_{r,PP,n,t} \geq P_{AP,PP,n,t} + P_{PCR,PP,n,t} + P_{SCRpos,PP,n,t} + P_{HP,PP,n,t} \cdot pl_{PP} \quad (8)$$

$$n = 1, 2, \dots, N; t = 1, 2, \dots, T$$

The constraints regarding the minimum output of a power plant are shown in (9). An extension for CHP plants is introduced, as it is assumed that the minimum output depends on processes in the steam generator.

$$0 \geq P_{\min,PP,n,t} \cdot op_{PP,n,t} + P_{PCR,PP,n,t} - P_{AP,PP,n,t} + P_{SCRneg,PP,n,t} - P_{HP,PP,n,t} \cdot pl_{PP} \quad (9)$$

$$n = 1, 2, \dots, N; t = 1, 2, \dots, T$$

In addition to that, the decreased maximum heat extraction in operating points with low electrical power needs to be taken into account. This can be achieved by assuming the following: the ratio between electrical and thermal output may never drop below the ratio in the operating point of maximum heat generation. At this point, the ratio is $\sigma_{N,PP,n} - pl_{PP}$. This constraint reproduces the back pressure line in the P- \dot{Q} diagram. The relation is illustrated in (10).

$$P_{AP,PP,n,t} - P_{HP,PP,n,t} \cdot (\sigma_{N,PP,n} - pl_{PP}) \geq 0 \quad (10)$$

$$n = 1, 2, \dots, N; t = 1, 2, \dots, T$$

Finally, heating zones hz , in which the generation must always be at least as great as the consumption, are introduced in (11). The load $P_{HL,hz,t}$ in each heating zone is determined in a separate program part for each time step of the simulation. In order to assign the power plants to the regions, a power-plant-heating-zone incidence matrix \mathbf{PHI} is created. This $N \times HZ$ matrix takes the value 1 if the power plant is located in the heating zone under consideration.

$$\sum_{n=1}^N phi_{n,hz} \cdot P_{HP,PP,n,t} \geq P_{HL,hz,t} \quad (11)$$

$$hz = 1, 2, \dots, HZ; \forall t = 1, 2, \dots, T$$

The displayed constraints apply to ECSTs. In order to describe the operating behavior of BPSTs, some adjustments are needed. First, the changes in (8) and (9) can be neglected. This is because the nominal and the minimum output of systems with BPSTs already take the heat extraction into account. For this reason and because BPST power plants have only one degree of freedom, (10) is adjusted as follows:

$$P_{AP,PP,n,t} - P_{HP,PP,n,t} \cdot \sigma_{N,PP,n} = 0. \quad (12)$$

$$n = 1, 2, \dots, N; t = 1, 2, \dots, T$$

IV. SIMULATION RESULTS AND DISCUSSION

In order to perform a plausibility check, an analysis of the input data and simulation results is needed. As a first step, the simulation results are compared to statistical data of Destatis and the AGFW of 2014. Table II shows the values of the installed heat power in GW as well as the total generated heat and the CHP heat in TWh.

TABLE II
STATISTICAL DATA CONCERNING DISTRICT HEATING [13], [15]

	AGFW	Destatis	INES
Installed heat power in GW	39.517	-	41.834
Generated heat in TWh	77.208	-	87.353
Generated CHP heat in TWh	64.083	103.010	84.702

One can recognize that the simulation result of the installed heat power fits very well with the statistical data of AGFW. The difference between the total generated heat in IGEM and the AGFW value is about 13 %. Also, the CHP heat of the German Federal Statistical Office is about 22 % higher than IGEM estimates. One reason for the deviation is the consideration of smaller CHP plants. The said statistic includes CHP plants with an electrical power of at least 1 MW, whereas IGEM assumes local heat production and represents those with an electrical output of less than 10 MW with time series [16]. Furthermore, the share of HPs in the total heat generation given by the AGFW is a lot greater than in the simulation. This is due to three main reasons:

- In IGEM, unplanned unavailabilities of power plants are considered by reducing their nominal power over the entire simulation interval to reproduce their yearly energy availability.
- The heating zones are defined as government regions. This is a large area and often leads to oversized district heating networks. Therefore, HPs in small district heating systems often compete with the much more efficient CHP plants of big cities.
- Thermohydraulic constraints of the district heating grid and the CHP plants, such as their reduced thermal output at low grid temperatures, are neglected.

In an analysis of a case study, the district heating network and the heat generation plants of the City of Leipzig

are examined. Subsequently, the thermal load curve of the city created by IGEM is described. Finally, a time interval in winter is evaluated in detail, so that the influence of the adjustments in the optimization model for the power plant dispatch can be shown. Within this framework, the operating points of CHP plants are analyzed in the P- \dot{Q} diagram and a comparison of the operating hours of the power plants with and without consideration of the heating load is made.

The period under study reaches from January 9 to January 25; this corresponds to the hours 217 to 600. As Fig. 2 illustrates, the lowest absolute outdoor temperature measured in this year is -12.7 °C.

Fig. 3 shows the course of thermal outputs of generating plants during the named period.

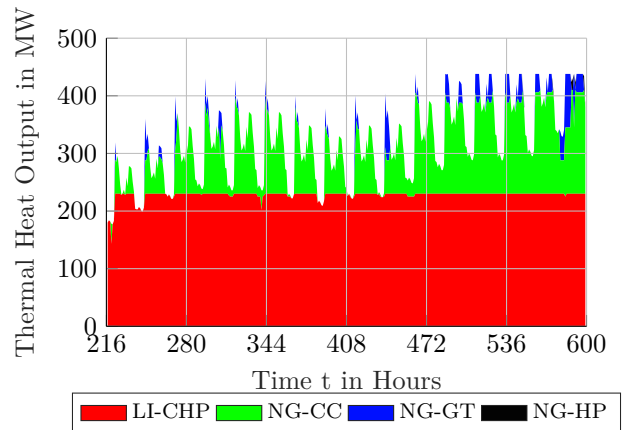


Fig. 3. Thermal output of CHP plants in a selected time interval

Obviously, most of the heat load is covered by the lignite-powered CHP plant. The largest share of the fluctuating heat demand is provided by a natural-gas-powered combined cycle plant. The gas turbine and the HP only cover a very small part of the load.

In order to analyze the operating points of the CHP plants, the P- \dot{Q} diagram of the combined cycle plant "Leipzig-Nord", created using the earlier stated constraints, is illustrated and the operating points are plotted into Fig. 4.

The plot shows the P- \dot{Q} diagram as a blue line, the operating points are plotted as purple asterisks. It is noticeable that the plant mostly operates on the lower lines of the diagram. This is a strong indicator of a heat-driven behavior, as in case of an economically viable power-driven operation, the plant would operate on the upper lines. This case occurs rarely when the asterisks do not touch the lower bound. In these moments, the upper bound is not reached since the CHP plant provides PCR as well.

Finally, the simulation results with and without the consideration of heat extraction are compared in Fig. 5. Regarding the lignite-powered CHP plant, only a small deviation can be noted. As the extraction of heat decreases

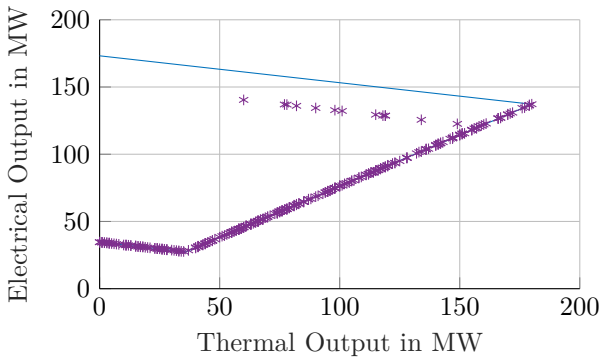


Fig. 4. P-Q diagram and operating points of the "Leipzig-Nord" CHP plant

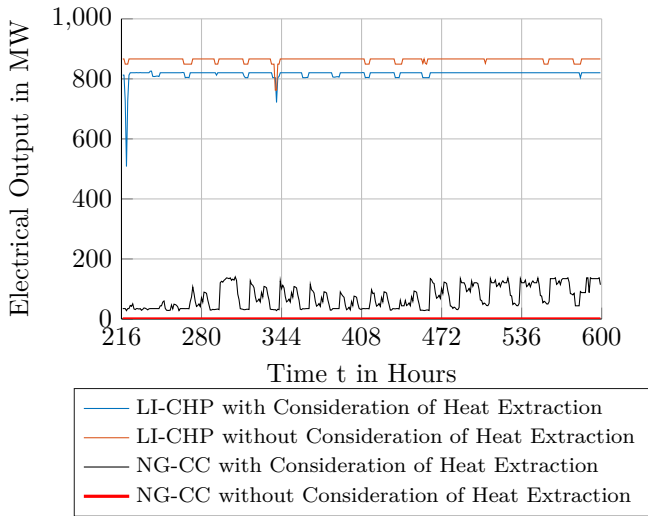


Fig. 5. Comparison between the electrical output of CHP plants with and without heat extraction

the maximum electrical output, the simulation with consideration of the heat demand results in a slightly lower curve. In contrast to this behavior, the combined cycle power plant is only providing electricity when the heat market is taken into account. This is due to its heat-driven behavior which was discussed earlier.

V. CONCLUSION

An approach for the consideration of heat extraction of thermal power plants in a power plant dispatch model has been presented. An existing power plant database was expanded by introducing new coefficients and categories. Therefore, the operating characteristics of CHP plants were modeled and HPs were implemented. Furthermore, temperature- and time-dependent thermal load curves were created for every government region. The power plant dispatch, described with a MILP approach, was extended by new variables and constraints.

Finally, a plausibility check, comparing the simulation results to statistical data and analyzing a detailed case study, was performed.

The adjustments have been fully implemented into the modeling framework and first simulation results were plausible. Even though the importance of HPs seemed to be understated, the influence of heat demands on the electricity markets could be demonstrated.

REFERENCES

- [1] T. Rendel, "Erweiterung und Plausibilisierung eines Modells für die integrierte Simulation des europäischen Verbundnetzes und Strommarktes," PhD thesis, Leibniz Universität Hannover, 2015.
- [2] T. Breithaupt, T. Leveringhaus, T. Rendel, and L. Hofmann, "A MILP Approach for the Joint Simulation of Electric Control Reserve and Wholesale Markets," in *SIMULTECH 2017*, Madrid, Jul. 2017.
- [3] Federal Cartel Office (Germany), *Sektoruntersuchung Fernwärme*, 2012.
- [4] P. Graichen, "Negative Electricity Prices: Causes and Effects," Agora Energiewende, Tech. Rep., 2014.
- [5] J. Arle et al., "Data on the Environment 2017," German Environment Agency, Tech. Rep., 2017.
- [6] Umweltbundesamt, *Kraft-Wärme-Kopplung*. [Online]. Available: <https://www.umweltbundesamt.de/daten/energie/kraft-waerme-kopplung-kwk>.
- [7] BEWAG, "Heizkraftwerk Mitte. Umweltschonende Energieerzeugung im Herzen von Berlin," Tech. Rep., 1998.
- [8] P. E. Grohnheit, "Modelling CHP within a national power system," *Energy Policy*, vol. 21, no. 4, 1993.
- [9] 50 Hertz Transimission GmbH, Amprion GmbH, TenneT TSO GmbH, and TransnetBW GmbH, *Grid Development Plan 2025*. [Online]. Available: www.netzentwicklungsplan.de.
- [10] 50 Hertz Transimission GmbH, Amprion GmbH, TenneT TSO GmbH, and TransnetBW GmbH, *Grid Development Plan 2030*. [Online]. Available: www.netzentwicklungsplan.de.
- [11] R. Gelaro et al., "The Modern-Era Retrospective Analysis for Research and Applications, Version 2 (MERRA-2)," *Journal of Climate*, 2017.
- [12] P. Hoffmann, "Quantifying the influence of climate change on the urban heat island of Hamburg using different downscaling methods," PhD thesis, Universität Hamburg, 2012.
- [13] "AGFW-Hauptbericht 2014," AGFW e.V., Tech. Rep., 2015.
- [14] S. Gill et al., "The Role of Electric Heating and District Heating Networks in the Integration of Wind Energy to Island Networks," *International Journal of Distributed Energy Resources*, vol. 7, no. 3, pp. 245–263, 2011.
- [15] Destatis, "Electricity and heat generation by energy sources (Code: 43311)," Tech. Rep., 2015.
- [16] A. Lübke, *Erstellung von regional aufgelösten Einspeisezeitreihen von wärmegeführten Blockheizkraftwerken in Deutschland*, 2018.

Security-constrained optimization of power plant dispatch in interconnected networks with several market areas and price zones

Nicola Gast, Andre Richter, Martin Wolter

Otto-von-Guericke-University Magdeburg

Chair of Electric Power Networks and Renewable Energy

Sources Magdeburg Germany

Abstract— During the last few years the renewable energy sources (RES) have been established in the German electricity market and became an important component of the electricity production. The increasing integration of renewable energies and the related spatially and temporally uneven energy generation far away from load centers often leads to transmission line overloading, which can be solved by costly redispatch measures. This overload results from several factors. Mostly the typical generation-profiles of RES are not equal to nations-consumption-load-profiles. For example, the production of photovoltaics is much higher at daytime than in the evening or at night. However, the peak load occurs in the evening and morning hours. Taking this asymmetric course into account, production/consumption balancing is a major challenge for the European electricity market. A possible solution is market coupling. In this paper a new approach for an automatic redistribution of load flows is presented. For this aim, five models are developed and simulated afterwards. The approach is performed and evaluated for a realistic German transmission system. The automatic redistribution is carried out as an example for Germany.

Keywords: *energy exchange, power systems, power grids, load flow, Net Transfer Capacity, unit commitment*

I. INTRODUCTION

In 2016, renewable energies acquired the biggest amount concerning the gross electricity generation in Germany. At the same time, the proportion of the conventional energies continuously decreased. Due to this combination of the growth of very volatile energy resources with the parallel occurring cut-off of coal power plants and nuclear power plants - the distribution system operators (DSO) as well as the transmission system operators (TSO) are put into challenges which shouldn't be neglected. In recent years, the percentage share of renewable energies has steadily increased. -it has reached the temporary maximum in 2016 with 29,06 % [1]. The enacted nuclear phase-out (2020) in combination with the planned and sequential occurring cut-off of all coal-fired power plants, aggregate the difficulties of a secure and reliable electricity supply [2]. According to the plans of the federal Government of Germany, it can be assumed that the share of conventional power plants will decrease and volatile energy sources will rise furthermore in the future. In 2050 a portion of 80 % of renewables of the gross-electricity generation is aspired. [1]

The aim of the generation is to cover load and keep the power balance in all situations. In principle, it has to be differentiated between three loads types: base, middle and peak. Two of the three loads are almost exclusively covered by conventional power plants. Most of the peak load can be covered by renewable energies [3]. The dominance of conventional power plants is omnipresent. Considering the planned decimation of the coal and nuclear power stations, a supply means for the basic and middle loads need to be addressed and restructured.

This means base and middle load must be guaranteed by renewable energies. During the last years, the active interventions (redispatch) in the predicted power station application planning (dispatch) by the transmission system operators strongly increases and lead to extensive additional costs [4]. To minimize these necessary corrections and the appearing costs, several alternatives, like the improvement of energy storage systems, net expansion (all voltage levels) and optimized distribution of the electric energy are available. One possibility of an optimized distribution is a price zone overlapping power plant dispatch planning. In the course of such a cross-zone power plant deployment plan, cross-border load flows can be optimally coordinated and distributed accordingly. An optimal distribution would have both technical and economic advantages. A technical advantage would be a reduction in the redispatch measures. This can lead to an increase of the respective asset lifetime and minimization of disturbances in the case of a line which is critical. This technical change can lead to a minimization of costs which can maximize the profits of the power plant owners. These possible changes and the resulting impact are part of this approach.

This paper highlights the question of optimal power plant dispatch in interconnected power networks, to reduce redispatch and increase power plant production. At the beginning, the current situation of the electricity market in Europe will be analyzed and evaluated. This gained knowledge serves as the basis for the automatic redistribution of excess loads. This is both, the technological and economical benefit for the operation of the power system.

II. APPROACH

In the previous section the topical challenges of the energy transition were indicated and illustrated. These challenges are known for a long time to the electricity sector, so that already different measures were developed to realize a stable electric system. Storage capacities, which are still under-dimensioned, have been compensated. One possible solution approach is an energy exchange. Thus, a bidirectional load exchange takes place not only nationwide, but also international. In case of Germany, the national energy exchange takes place between four TSOs. The international exchange occurs between the suitable TSO of the respective country. To realize an economically and technically optimized load exchange, as well as to ensure a stable and reliable system, the so-called market couplings have been set up in the European electricity market [5]. In a market connection, technical and market-related grid codes are further developed jointly. At the same time, a transnational coordination of system operation and network development takes place. The overall objective is to strengthen and unify the European electricity market and to promote sustainable energy supply. There are three different types (price coupling, tight volume coupling (TVC), loose volume coupling (LVC)) to realize such a coupling. While the TVC and LVC have a technical focus, there is an economic optimization in the price coupling in the foreground [10]. This paper follows this given approach.

Currently four market couplings exist, the CWE (Central-West Europe), NWE (North-West Europe), CEE (Central-East Europe) and MRC (Multi-Regional-Coupling). The MRC is currently the biggest market coupling. It is made up of the other three market couplings (CWE, NWE, CEE) and in addition the countries of Spain, Portugal, Italy, Switzerland, Austria and Slovenia. The composition of the four market couplings is illustrated in Fig. 1 [6].

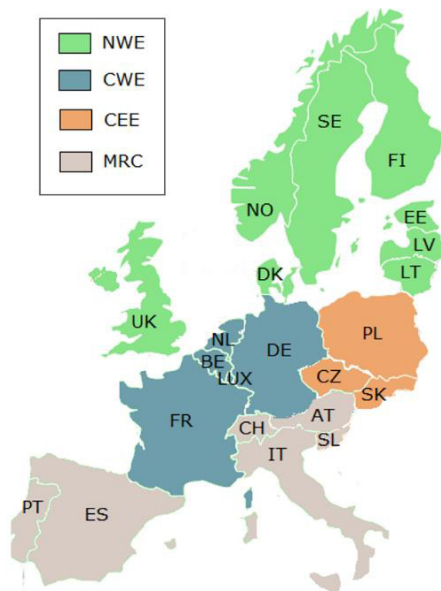


Fig. 1. Overview of market coupling. [6]

These zones were programmed in individual price coupling models in MATLAB. This allows the analysis of test scenarios. So, a solution that is technically and economically

optimized is found. The redistribution of the cross-border flows can also be controlled [7].

III. PROGRAMMING AND MODEL

The first model is used to simulate the load flows between Germany and its neighboring countries. Four further models are created for the other market couplings. To analyze the load flows in the ENTSO-E another model is created. Finally, the seventh model allows to analyze redistribution of the load flow surpluses. These surpluses are dependent on the respective Net Transfer Capacity (NTC) values. This automatic redistribution is the focus of this paper. Fig. 2 present the general flowchart for power redistribution in any market coupling model with respect to the NTC.

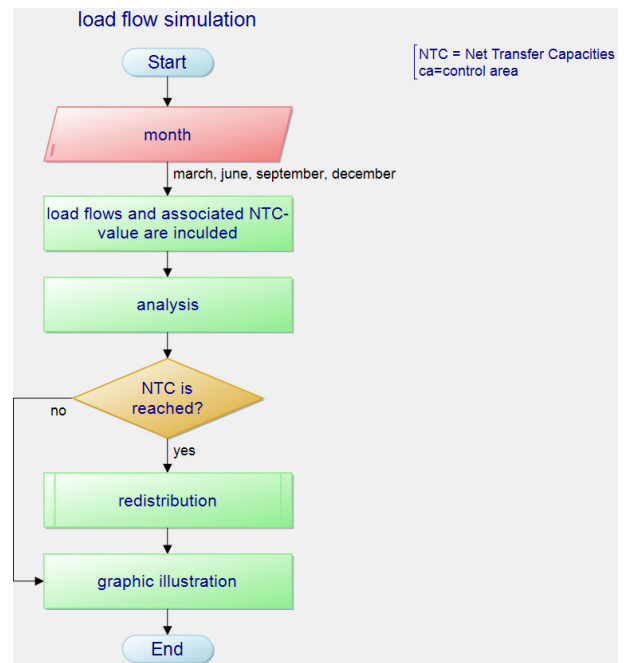


Fig. 2 Flowchart for redistribution.

Especially the volatile infeed of photovoltaic generation during the day has a high impact on the power system. Therefore, a uniform analysis of all models takes place over the months of March, June, September and December. This approach serves to illustrate the influence of renewable energies on cross-border load flows. In Germany, a quarterly-hour recording of cross-border load flows is required. These values are published by the TSO on the corresponding homepage. In the ENTSO-E, the load flows are recorded hourly and are also available on the homepage. The measured values serve as the basis of this analysis. The topological and geographical composition of the individual models are implemented in Simulink. The programming and the input for the analysis is done in MATLAB. The results are taken directly from Simulink and MATLAB. Those are tubular's in CSV-format and can be read and reused directly.

IV. UNIT COMMITMENT AND RESULTS

The overall aim of unit commitment is the regulation of optimal energy flows. It takes place on the operational level and the factors load-amount, load time span as well as form of available energy are considered. For the optimization, the mixed-integer linear optimization is used. A distinction must be made between the objective function, which involves minimizing costs, and the constraints that include the technical restrictions. The objective is as follows:

$$\begin{aligned} \text{Min!SumCost} = & \sum_t \sum_j (\text{varc}_j \cdot \text{prod}_{t,j}) + \\ & + \sum_t \sum_j (\text{startc}_j \cdot \text{start}_{t,j}) \end{aligned} \quad (1)$$

j	index power plant
t	index time
SumCost	sum of costs
varc _j	variable costs per power plant
prod _{t,j}	production per power plant and time
startc _j	start-up costs per power plant
start _{t,j}	start-up per power plant and time, binary (0/1)

In the example structure from [20] there are a total of seven constraints, the results from the automatic redistribution are included in the restriction, which deals with the load coverage.

$$\sum P_{\text{prod}} \geq \sum P_{\text{demand}} \quad (2)$$

demand the amount of electricity required

It is striven for an optimal utilization of the available power plants. Under this aspect, the market coupling is of particular importance. Among other things the transfer-costs, variable operating-costs and fuel-costs are considered too. This section presents a selection of the created models. At the beginning the cross-border load flows are analyzed. For this purpose, a model for the cross-border load flows of Germany is used. The principle of market coupling is also investigated. Therefore, an analysis of the bidirectional exchange of load flows in the existing market couplings takes place. The final goal is to develop an automatic balancing of load flow surpluses. These surpluses can be caused by a variation in the NTC values. Compensation can be achieved either by throttling production or by redistributing the load flows.

A. Germany

In Fig. 3 the TSO's of Germany and the neighboring states - where a bidirectional load flow takes place - are presented. In order to be able to analyze the influence of RES in the best possible way, all simulations take place in March, June, September and December. In summary, the analysis of the load flows show that the lowest export took place in June, except for Amprion. In March as well as in September there were recognizably more exports. The maximum export occurred in December. Considering the large share of the renewable energy in the production of electricity, the maximum export volume is expected in June, but the analysis of the load flows recalculates this. This can be explained by the annual revision of conventional power plants ([8] - [11]). It is remarkable that the

imports are increasing almost completely in June. The biggest increase can be seen in the neighboring countries which also own a very high share of renewable energies. Concerning Denmark this is due to the big portion of wind energy. The increase of the import from Switzerland can be led back on the thaw ([4], [7]). Thus, it can be stated that the influence of renewable energies is not seen in the export, but more clearly in the import from the individual control areas.

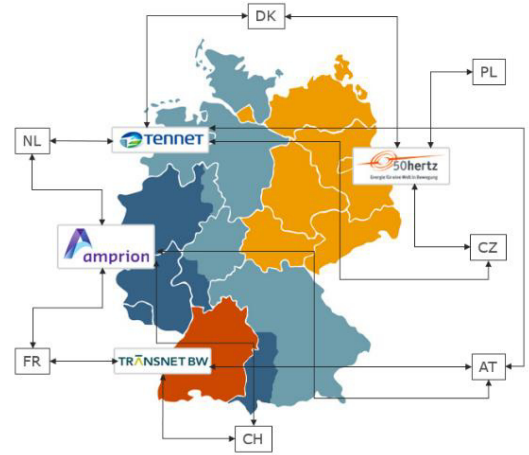


Fig 3. TSO and their neighboring states. [8] - [11]

B. Market Coupling

The individual national electricity transmission networks are linked to their respective neighboring countries, so that across whole Europe, a highly branched electricity network is generated, which is the basis for all market couplings. By means of the coupling of individual electricity markets, not only a reliable power supply can be guaranteed, but also a competitive price can be ensured. The overall objective is to make the most efficient use of the available transmission capacities between the involved countries, both technically and economically. In the market couplings CWE, NWE and MRC, a differentiation is necessary between the spot market and the OTC (Over the Counter) in terms of electricity trading [12]. In order to illustrate the principle of market coupling, this paper deals with CWE. In Fig. 3 the composition is shown. It should be noted that there is no direct link between Belgium and Germany as well as between France and Netherlands [8]. During the evaluation of the load flows within the CWE, it is treated as a whole. Accordingly, the individual trends are not discussed explicitly. In summary, it can be said that in the months of March, June, September and December certain procedures are repeated. As a matter of fact, the dynamics in the months of March and September almost coincide. Germany is continuously exporting to Netherlands, which also export almost constant power to Belgium. The only interchange, in the months of March, June, September and December, took place between Germany and France. Furthermore, with exception of March, France is always the main exporter of the CWE. In three out of four months, Belgium exports very irregularly and usually with low performance. That's why Belgium can be characterized as the main importer in the CWE. A loop flow could be observed in March and September that spreads the power from Germany across the Netherlands to Belgium. Thus,

it can be concluded that Germany is indirectly exporting to Belgium via Netherlands. Such loop flows are recognized throughout the ENTSO-E. In the West, for example, the Netherlands and Belgium are affected and in the East the countries of Hungary, Poland, Czech Republic and Slovakia. These loop flows can begin in Germany and end in Germany. This prevents the redispatch measures and which currently are not needed performance geographically dispersed. It can therefore be concluded that the RES strongly influence cross-border load flows.

C. Automatic redistribution

Regardless of whether a congestion is present or not, the respective physical transport limit between the respective states has to be taken into account. This limit corresponds to the maximum capacity to be transferred between two coupling stations and is known to the branch as NTC ([13] - [17]). The NTC corresponds to the difference between the TTC (Total Transfer Capacity) and the TRM (Transmission Reliability Margin or Security margin) [14]. It should be noted that the NTC is determined statically and corresponds more to a directive than to an absolute limit. The overall objective is the establishment of a secure and stable power grid in the respective market couplings and later in the European network of the ENTSO-E. Since April 23rd, 2015, the four German TSOs have been legally obliged to comply with the NTC values, which are calculated by means of an algorithm. These and other legal requirements are documented in decision BK6-13-162 [18]. The main focus is on the development of an automatically occurring redistribution of the excess load flows. The German model is not as complex as the rest. Consequently, this model acts as a basis for the discussion of automatic redistribution. This includes the four German control areas and the neighboring states, with which a bidirectional power flow exchange can take place. By adopting the number of parties, this algorithm can be used for the other models, too. Using these algorithms, both external influences and the resulting measures can be presented and analyzed. External influences are the variation of the NTC values and the current rates. The NTC value for this analysis is based on the forecast values of the individual TSOs. The considered electricity prices are taken from the ENTSO-E website [18]. Both influencing factors are based on real values. These factors can be changed individually or together. The resulting measures could be a redistribution or adaptation of the power plant implementation planning. In addition to the NTC, economical influences of the market must be observed. The principle aim is always the goal of profit maximization. Thus, the NTC limits with regard to the country which offers the currently best (highest) price, should be completely maxed out. In addition, all interventions in the dispatching and the corresponding costs should be avoided. This can be done by means of an automatic adjustment of the load flow. For visualizing the proceedings, the examples of the TSOs TenneT and 50Hertz Transmission are assumed. In Fig. 4, the responsible areas of TenneT TSO, 50Hertz Transmission and the corresponding couplings to neighboring countries are visualized.

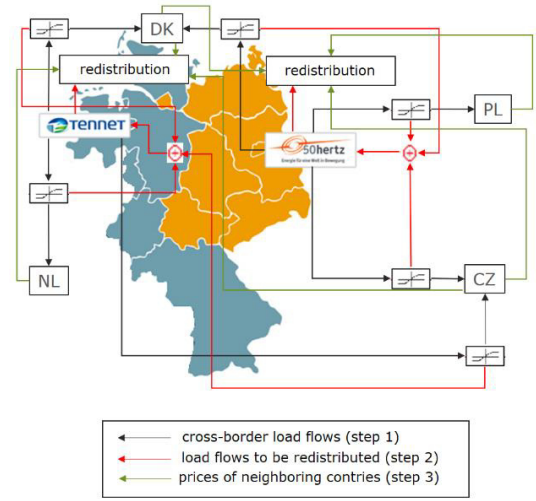


Fig. 4. Redistribution-model. [8] - [11], [13] - [17], [18]

This visualization is used to demonstrate the function of the algorithm that is created for this analysis. The complete algorithm consists of three steps and is explained in a simplified example. The structure of the algorithm is shown in Fig. 5. The export of electric power to Poland is aimed by 50Hertz Transmission (black arrows, Fig. 4). This export is limited by the NTC (symbolized by the limiter). In this case the desired export is higher than the export that took place. The resulting difference is returned into the control area of 50Hertz Transmission (red arrows).

$$P_{\text{free},i} = NTC_i - P_{\text{export},i} \quad (3)$$

i	index overhead power line
$P_{\text{free},i}$	available capacity
NTC_i	Net Transfer Capacity
$P_{\text{export},i}$	already existing export

The first step in the automatic redistribution algorithm involves an internal redistribution which means, that the redistribution takes place within the control zone of 50Hertz Transmission. For this purpose, the other couplings will be used for Denmark and Czech Republic. In order to be able to evaluate whether internal redistribution is possible, the other coupling plugs are analyzed for free capacities. If free capacities are available, a redistribution takes place within the own control area. In the case of 50Hertz Transmission, the coupling routes will come to Denmark and to Czech Republic. If both coupling sections still have free capacity, the system is redistributed again by a maximizing factor. In the following example, the price in Denmark is larger than in Czech Republic. That is why it would first be exported to Denmark. Subsequently the “new free capacities” and the “new redistributed load flows” have to be determined.

$$P_{\text{new},i} = P_{\text{free},i} - P_{\text{red},i} \quad (2)$$

$$P_{\text{red,new},i} = P_{\text{red},i} - P_{\text{new},i} \quad (3)$$

$P_{new,i}$ resulting capacity
 $P_{red,i}$ redistributed capacity

This redistribution takes place until either the free capacities are exhausted or all surpluses have been successfully redistributed. After this, a new check is carried out to determine whether there are any surpluses.

$$P_{red,i} > 0 \tag{6}$$

For this case, the second step in the algorithm is executed. In this step, the free capacity of the adjacent control area are interrogated. In the example with 50Hertz Transmission, the neighboring control area is TenneT TSO. Thus, in the second step, the free capacities are interrogated on the couplings between TenneT TSO and the neighboring countries (Netherlands, Denmark, Czech Republic). If free capacity is available, the excess of 50Hertz Transmission via TenneT TSO will be exported to the neighboring countries. Until this point, the procedure is identical to the internal redistribution with the aim to maximize profits. The abort condition is also identical. Thus, the redistribution stops when either all surpluses can be distributed or when the free capacities are exhausted. If free capacities are exhausted before a complete redistribution took place, the last step of the algorithm is performed. In this step, the load flows that are still to be redistributed are queried again. Subsequently, these load flows are forwarded to the power plant application planning and corresponding measures are proposed.

$$\text{Output}_{pp} = P_{red} \tag{7}$$

Output_{pp} information for the power plant

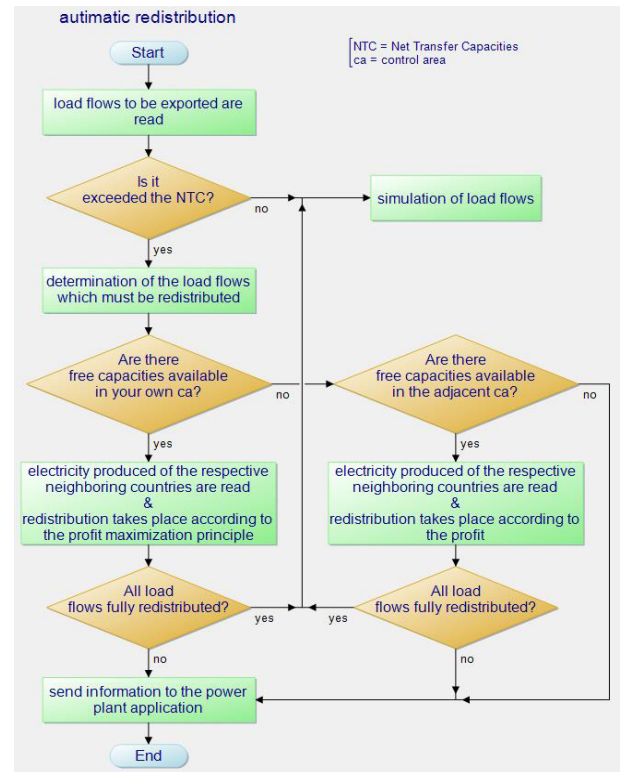


Fig 5. Algorithm for automatic redistribution. [8] - [11], [13] - [17], [18]

It should be noted that in the first two steps of the algorithm, there is no intervention in the schedule of the power stations. It is a pure displacement of the load flows. Furthermore, it must be pointed out that these are purely economic load flows. In Fig. 6 the effects of the individual steps of the algorithm are recognized. In the first bar chart, the resulting surpluses of 50Hertz Transmission are shown.

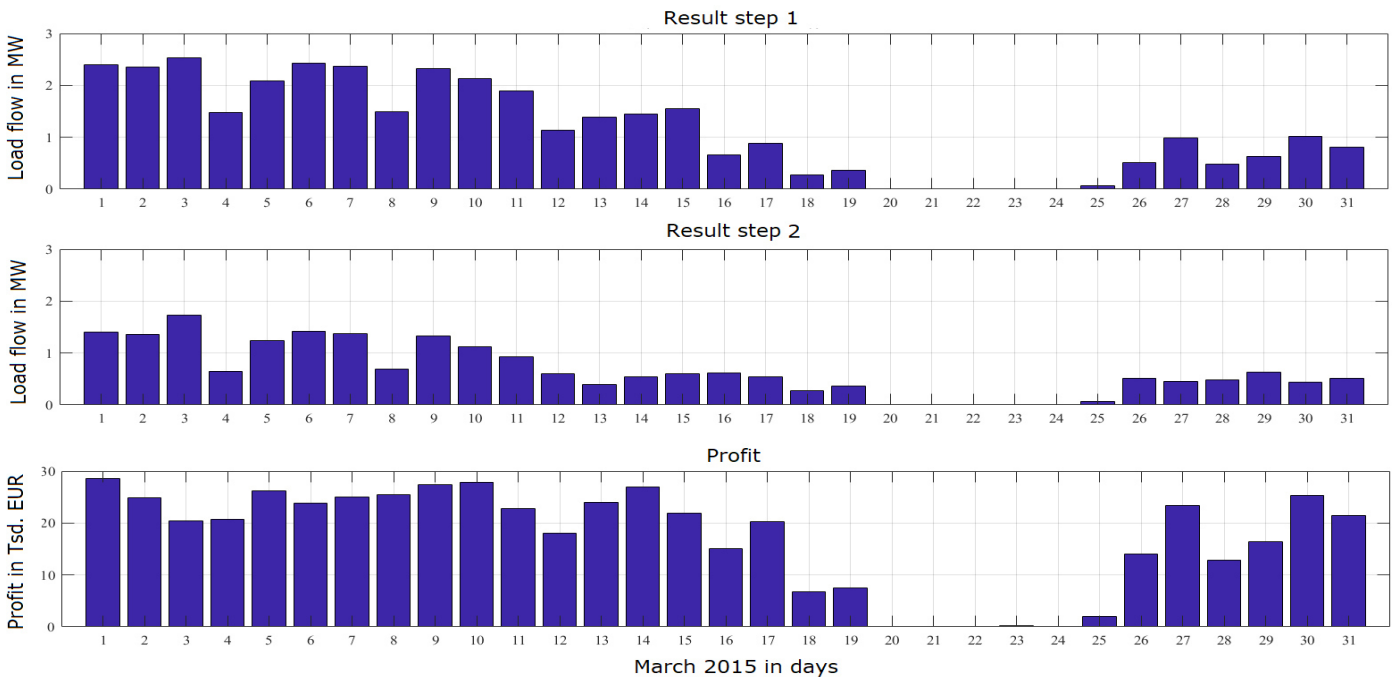


Fig. 6 Results of redistribution model.

This load flow could not be redistributed internally that the second step of the redistribution algorithm takes place. Although, it is not possible to redistribute all the load flows. A significant reduction of the surplus in the second diagram can be attributed. The remaining load flows must be compensated by means of an adaptation of the power plant deployment planning. The redistribution is always based on the profit maximization principle. Accordingly, the load flows that were redistributed through TenneT TSO into the respective neighboring countries were multiplied by the corresponding prices. The result is shown in the third bar graph. It should be noted that an automatic redistribution is realized with the aid of the algorithm. Furthermore, an additional profit of up to 30 thousand euros could be earned per day. This profit comes from the power plant operator. It can, for example, be used for the modernization of power station. A coverage of cost, which may be necessary by retrofitting could also be covered with this profit. The remaining load flows must be compensated by means of an adaptation of the power plant deployment planning. The redistribution is always based on the profit maximization principle. Accordingly, the load flows that were redistributed through TenneT TSO into the respective neighboring countries were multiplied by the corresponding prices. The result is shown in the third bar graph. It should be noted that an automatic redistribution is realized with the aid of the algorithm.

V. SUMMARY AND OUTLOOK

The overarching goal was to develop a concept for an optimized cross-zonal power plant dispatch. The focus is on the analysis of the load flow activities and the power exchange activities. The scientific value added and, at the same time, the result of this paper is a model for an automatic redistribution of the load flows. This model allows several considerations. On one hand, an analysis of the influence of NTC and current rates on the course of the load flows is possible. On the other hand, surpluses are automatically redistributed both technically and economically. Thus, an economic calculation is embedded in the potential additional gain. A detailed embedding of all resources of the transmission networks to be considered into the individual models would be the next step. Such an optimization is both the most economically profitable and technically desirable innovation.

REFERENCES

- [1] Destatis, „Erneuerbare Energien“ March 2017. [Online] Available: <https://www.bmwi.de/Redaktion/DE/Dossier/erneuerbare-energien.html> (01.06.2017)
- [2] Bundesregierung, „Bundesregierung beschließt Ausstieg aus der Kernkraft bis 2022“. [Online] Available: <https://www.bundesregierung.de/Content/DE/StatistischeSeiten/Breg/Energiekonzept/05-kernenergie.html> (10.08.2016)
- [3] oesterreichs energie, „Stromhandel in Europa“ Juli 2017. [Online] Available: <http://jugend-und-schule.oesterreichsenergie.at/3-4-schulstufe/stromhandel/> (01.09.2017)
- [4] Bundesnetzagentur, „Redispatch,“ 08. August 2016.[Online] Available: https://www.bundesnetzagentur.de/DE/Sachgebiete/ElektrizitaetundGas/Unternehmen_Institutionen/Versorgungssicherheit/Stromnetze/Engpassmanagement/Redispatch/redispatch-node.html (10.08.2017)
- [5] Bundesnetzagentur, „Market Coupling - Marktkopplung der europäischen Stromgroßhandelsmärkte,“ 16. August 2016. [Online] Available: https://www.bundesnetzagentur.de/DE/Sachgebiete/ElektrizitaetundGas/Unternehmen_Institutionen/HandelundVertrieb/EuropMarktkopplung/MarketCoupling.html?nn=266476 (31.08.2016)
- [6] EPEXSPOT, „MARKTKOPPLUNG EIN WESENTLICHER SCHRITT ZUR MARKTINTEGRATION“. [Online] Available: http://www.epexspot.com/de/Marktkopplung/ein_wesentlicher_schritt_zur_marktintegration (10:09:2016)
- [7] Entose, “DETAILED ELECTRICITY EXCHANGE (IN GWh) “. [Online] Available: <https://www.ENTSO-E.eu/db-query/exchange/detailed-electricity-exchange> (31.08.2015)
- [8] TransnetBW, „KENNZAHLEN“. [Online] Available: <https://www.transnetbw.de/de/transparenz/marktdaten/kennzahlen> (15.07.2016)
- [9] 50Hertz Transmission „Lastflüsse“. [Online] Available: <http://www.50hertz.com/de/Anschluss-und-Zugang/Engpassmanagement/Lastfluesse> (16.07.2016)
- [10] TenneT TSO, „Grenzüberschreitende Lastflüsse / abgestimmte Fahrpläne“. „Grenzüberschreitende Lastflüsse / abgestimmte Fahrpläne“. [Online] Available: <https://www.tennetso.de/site/Transparenz/veroeffentlichungen/netzkennzahlen/grenzueberschreitende-lastfluesse> (17.07.2016)
- [11] Amprion, „GRENZÜBERSCHREITENDE LASTFLÜSSE “. [Online] Available: <https://www.amprion.net/Netzkennzahlen/Grenzueberschreitende-Lastfluesse/index-3.html> (19.07.2016)
- [12] NEXST KRAFTWERKE, „Was ist Spotmarkt?“. [Online] Available: <https://www.next-kraftwerke.de/wissen/strommarkt/spotmarkt-epex-spot> (10.07.2016)
- [13] 50Hertz Transmission, „Allgemeines Modell der 50Hertz Transmission GmbH für die Berechnung der Gesamtübertragungskapazität und der Sicherheitsmarge“. [Online] Available: <http://www.50hertz.com/Portals/3/Content/Dokumente/Anschluss-Zugang/Engpassmanagement/Methodik/Allgemeines-Modell-Berechnung-Uebertragungskapazitaet.pdf> (08.09.2016)
- [14] 50Hertz Transmission „Jahresvorschau Kapazitätsvergabe“. [Online] Available: <http://www.50hertz.com/de/Anschluss-und-Zugang/Engpassmanagement/Kapazitaetsvergabe/Jahresvorschau> (05.09.2016)
- [15] TenneT TSO, „Vorschau auf die Kapazitätsvergabe (NTC)“. [Online] Available: <https://www.tennetso.de/site/Transparenz/veroeffentlichungen/engpassmanagement/vorschau-kapazitaetsvergabe> (06.09.2016)
- [16] TransnetBW, „ENGPASS“. [Online] Available: <https://www.transnetbw.de/de/strommarkt/engpassmanagement/engpass> (04.09.2016)
- [17] Amprion, „NETZENG PÄSSE “. [Online] Available: <https://www.amprion.net/Strommarkt/Engpassmanagement/Netzengp%C3%A4sse/> (08 09 2016)
- [18] Entose, “Day-ahead Prices“. [Online] Available: [\(https://transparency.ENTSO-E.eu/transmission-domain/t2/dayAheadPrices/show?name=&defaultValue=false&viewType=GRAPH&areaType=BZN&atch=false&dateTime.dateTime=08.05.2017+00:00|CET|DAY& biddingZone.values=CTY|10Y1001A1001A83F|BZN|10Y1001A1001A63L&dateTime.timezone=CET_CEST&dateTime.timezone_input=CET+\(UTC+1\)+/CEST+\(UTC+2\)](https://transparency.ENTSO-E.eu/transmission-domain/t2/dayAheadPrices/show?name=&defaultValue=false&viewType=GRAPH&areaType=BZN&atch=false&dateTime.dateTime=08.05.2017+00:00|CET|DAY& biddingZone.values=CTY|10Y1001A1001A83F|BZN|10Y1001A1001A63L&dateTime.timezone=CET_CEST&dateTime.timezone_input=CET+(UTC+1)+/CEST+(UTC+2)) (01.09.2016)
- [19] Bundesnetzagentur, „Aktuelle Mitteilungen der Beschlusskammer 6,“ Dezember 2015. [Online] Available: https://www.bundesnetzagentur.de/DE/Service-Funktionen/Beschlusskammern/Beschlusskammer6/BK6_01_Aktuelles/BK6_Aktuelles_node.html (05.08.2016)
- [20] Universität Duisburg-Essen, „Management der Stromerzeugung,“ Dezember 2015. [Online] Available: https://www.tdr.wiwi.uni-due.de/fileadmin/fileupload/BWL-ENERGIE/Lehre/EFE_VL/EFE_WS0708_Kap_2_3.pdf (01.06.2016)

Evaluation of a Transition Path to a Future Scenario of Lower Saxony's Energy Supply under Variation of Storage Capacity and Power

1st Thomas Wolgast

*Institute for Electrical Power Systems
Leibniz Universität Hannover
Hanover, Germany*

2nd Christoph Blaufuß

*Institute for Electrical Power Systems
Leibniz Universität Hannover
Hanover, Germany*

3rd Lutz Hofmann

*Institute for Electrical Power Systems
Leibniz Universität Hannover
Hanover, Germany*

Abstract—Currently huge transformations of the energy provision in Germany and throughout the world take place. The power system switches to renewable energies within a few centuries. German federal state Lower Saxony is a forerunner in that transformation. A main part of the renewable share in Lower Saxony and worldwide will be provided by fluctuating wind and solar energy. That results in major uncertainties regarding the future energy supply. Therefore the application of large energy storage systems will be necessary most likely. In this paper a transition path of Lower Saxony's energy supply until 2050 is created. This transition path is simulated in 10 year increments with a market simulation tool and the results are presented and analyzed. A main focus in the analysis is on the use of energy storages and the technical consequences of different sized storage systems within the intermediate steps.

Index Terms—Transition Path, Energy Scenarios, Market Simulation, Energy Storages, Lower Saxony, NEDS

I. INTRODUCTION

The German federal state Lower Saxony plays an important role in the so called "Energiewende", the transformation of the German power system from conventional to sustainable technologies. The German government plans to increase the renewable share in production to 80% until 2050. Especially the fluctuating energy supply by wind turbines and solar plants will be extended. Some renewable energy sources could provide base load, too. For example hydroelectric power plants and biomass power plants. But because of its flatness Lower Saxony is almost completely unsuitable for hydro-power. Biomass plants lead to mono-cultures and to competition between agricultural and energy correlated use of the available areas [1].

Furthermore the non urban Lower Saxony must prospectively provide energy for the bordering federal states, too, especially the city states Bremen and Hamburg.

Since wind and solar power plants provide only an fluctuating energy supply it is assumed that in the long term large energy storage systems are required to achieve reliable energy supply without fossil power plants. The technical consequences and possibilities of large energy storage systems

need to be analyzed with regard to the storage capacity and installed power of the facilities.

Within the NEDS project ('Nachhaltige Energieversorgung Niedersachsen') in this paper a transition path until 2050 is developed and simulated to examine the future development of the energy supply in Lower Saxony, Bremen and Hamburg and the consequences of its change [2]. This area will be simulated and examined detached from the rest of Germany. Further the effects of different sized energy storage systems within the intermediate transition path steps will be analyzed, too. For the economical and technical simulation INES is used, an market simulator which has been developed by the Institute for Electrical Power Systems at the University of Hanover.

II. MODELING OF THE TRANSITION PATH

The data from 2015 as starting point for power plants, power grid, load and feed-in by wind and solar facilities is already known. The data for 2050 is taken from [3] where a scenario of 2050 with -80% CO₂ emissions is described. With the data for 2015 and 2050 three intermediate steps are developed: 2020, 2030 and 2040.

Tab. I shows the used input data. The development of the wind and solar energy feed-in is assumed to be linear between the starting point 2015 and 2050. The supply of hydro-power and biomass power is assumed to stagnate at present status for the reasons given in section I. Therefore these two are not listed. The increase of the gross domestic product (GDP) is assumed to be steep in the first years and then flattening till 2050 [4]. Because of the strong correlation between load and economic performance the same goes for the development of the load.

The data for the development of the fuel costs are estimations from the Institute for Environmental Economics and World Trade of the Leibniz Universität Hannover. The current fuel costs are known and the data for the intermediate transition path steps are assumed to develop linearly again [4]. For waste and other energy sources (sewage sludge for example) no estimates were available. So an increase of 2% per year was assumed. Uranium is not listed because of the German nuclear

TABLE I
INPUT DATA, [3] [4]

Year	2015	2050
GDP	360.35 bil. €	429.63 bil. €
Total load	68.889 TWh	89.246 TWh
Total wind feed-in	12.744 TWh	56.763 TWh
Total solar feed-in	2.952 TWh	52.274 TWh
CO ₂ certificate cost	13.5 €/t CO ₂	101.15 €/t CO ₂
Fuel costs NG	25 €/MWh	35 €/MWh
Fuel costs HC	13 €/MWh	19.5 €/MWh
Fuel costs WA	25 €/MWh	50 €/MWh
Fuel costs FU	28 €/MWh	56 €/MWh

NG: Natural gas, HC: Hard Coal, WA: Waste, FU: Other

phase-out in 2022 [5]. For lignite coal applies a similar case. At the moment only one lignite fired power plant is active in Lower Saxony, which is planned to be shut down in 2020. Because of the German governments objectives to reduce CO₂ emissions it is unlikely that another lignite fired power station will be built in Lower Saxony in the future.

The costs for CO₂ certificates are assumed to stagnate in the short term and then increase rapidly until 2050. Again these data are assumptions from the Institute for Environmental Economics and World Trade [4].

The future power grid expansion is not known completely. Therefore the state of the grid within the intermediate steps cannot be generated like the other data before. Instead in every step a power flow calculation will be carried out before the analysis. Based on the results the necessary grid expansion measures will be derived. Thereby only the extra-high voltage grid is considered. In Germany this voltage level is divided into two sub-levels, the 220-kV-level and the 380-kV-level. On long term it is sought to disestablish the 220-kV-voltage level. For this reason, when an overload of an electrical line in the 220-kV-level takes place, the corresponding area will be converted to 380 kV. If the overload could not be cleared this way or takes place in the 380-kV-voltage level from the start, the corresponding line will be enhanced until the overload is removed. Within the intermediate steps there is a possibility that overload situations take place only in one of the different storage configurations. In this case the same grid will be used for all setups nevertheless to maintain comparability. Possible overloads of electrical lines will be accepted in this case. After the grid expansion the new grid is used as a base grid for the following time step. This procedure is repeated step by step until 2050.

III. STORAGE MODELING

The secondary objective of this paper is the analysis of the implications of differently sized energy storage systems within the time steps. Therefore in each of the steps three different configurations of the energy storages will be simulated: small, medium and large storage systems with different assets in storage capacity and power. All other parameters remain the same to maintain comparability.

In accordance with [3] the energy storage is assumed to be realized by hydrogen synthesis (power-to-gas) with an

overall efficiency of 33.7%. Because in total no fuel is consumed the marginal costs for storing in and out are presumed as 0 €/MWh. But in praxis the energy losses, while storing in and storing out, restrict the storage use nevertheless.

The energy storage model in INES manages the storage operations based on economic criteria with the highest profit for the operator of the storage systems. For this the assumption is made that the electricity price is linearly dependent on the residual load [6]. With that assumption and the objective of energy storage system operators to make the highest possible profits, the storages store out while the residual load is high and store in while the residual load is low (or even negative).

For this work the storage model of the appropriated market simulator INES was adjusted for an usage in future scenarios, which was not possible before. The storage model receives the residual load of a time frame, the storage power in MW and storage capacity in MWh as input data. Thereby all storages of the regarded area are viewed as one cumulated energy storage system. The cumulated power is allocated to the individual storages afterwards. Quadratic programming is used to find the most economical solution for storage usage whilst taking into account certain constraints. The pursued economic optimum is found with the minimum of the summed up quadratic residual load RL_{new} after storage use. That new residual load is the sum of old residual load RL_{old} and the storage output/input P_S .

$$\text{Min}_{P_S} \sum_{t=1}^T (RL_{old,t} + P_{S,t})^2 \quad (1)$$

The practical execution of this minimization problem is only possible when the storages are large enough. In that ideal case the exemplary residual load in Fig. 1 results, which corresponds to the solution of eq. (1).

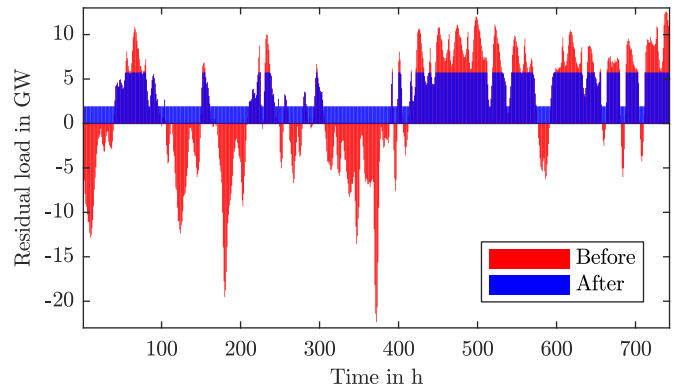


Fig. 1. Exemplary residual load before and after storage use

The old residual load before storage use is pictured in red, the new residual load in blue. The difference between old and new residual load is the storage power in each time step. It can be seen that the use of the storages flattens the course. But no complete straight course is achieved. Instead the residual load now oscillates between an maximum and an minimum

amplitude. The reason for this are the energy losses of the storages. A further flattening of the residual load does not bring any economic advantage. This can be demonstrated with a simple calculation.

The profit P for the storage operator is the difference between gain from storing out and costs from storing in. The gain is the product of supplied energy E_{out} and the obtained electricity price p_{out} at that moment. The same thing applies for the costs.

$$P = Gains - Costs = E_{out} \cdot p_{out} - E_{in} \cdot p_{in} \quad (2)$$

Losses occur in these processes. Therefore more energy has to be stored in than can be stored out. The storage efficiency η_S must be included.

$$P = E_{out} \cdot p_{out} - \frac{E_{out}}{\eta_S} \cdot p_{in} \quad (3)$$

An use of the storages only makes sense, when the resulting profit is positive. Therefore the following inequality results.

$$P \geq 0 \implies p_{out} - \frac{p_{in}}{\eta_S} \geq 0 \quad (4)$$

Considering the assumption made, that the electricity price p_{el} is linearly dependent to the residual load RL :

$$p_{el} \sim RL \quad (5)$$

In consequence the proportion of the amplitudes of the new residual load (after storage use) while storing out RL_{out} and storing in RL_{in} must be higher or equal than the inverse storage efficiency.

$$RL_{out} - \frac{RL_{in}}{\eta_S} \geq 0 \implies \frac{RL_{out}}{RL_{in}} \geq \frac{1}{\eta_S} \quad (6)$$

The residual load cannot be lowered under RL_{out} by storing out and cannot be elevated over RL_{in} by storing in. Finally this leads to the residual load course shown before in Fig. 1. The ratio between maximum and minimum amplitude is approximately three, the inverse of the efficiency of 33.7%, corresponding to eq. (6). Further storing processes and flattening of the residual load offer no economical advantage, because the costs for the losses surpass the gains for supplying energy.

The scale of required future energy storage systems in Lower Saxony is difficult to predict and depends on various factors. For that reason first of all in each time step it will be tested which maximum configuration of the energy storages still increases the profits of the storage operators. These maximum values for storage capacity and power are then used as a scale for the three different configurations. In the large configuration the installed storage capacity in MWh and power in MW both are set as 90% of the maximum values. For medium 60% are chosen, and 30% for the small storage configuration.

In the long term energy has to be stored seasonally to balance fluctuations in the feed-in of wind and solar energy. Therefore the operational planning of the energy storage systems will be scheduled for periods of four months. Longer

periods would suit the seasonal character of the problem even better, but the computation time for storage operational planning depends exponentially on the length of the scheduled period.

IV. INTEGRATED GRID AND ENERGY MARKET SIMULATOR INES

The simulations of the transition path steps will be carried out with the Integrated Grid and Energy Market Simulator INES. The INES first models the energy market and determines the use of renewable energies, storages and power plants to cover the electrical load at any time. According to German law the renewable energies get priority access to the energy market. The load and the feed-in of wind and solar power is deposited with time series, which have been scaled to match the input data for total load and feed-in. The difference between load and renewable input power then defines the residual load, which lays the basis for the operation of the energy storages in INES, as described in section III. After storage use the power plant resource planning takes place. The planning functions by the merit order principle. Starting with the power plant with lowest marginal cost one after another plant gets added until the total load is covered. The power plant with the highest marginal cost, that contributes to the energy market, then defines the electricity price. After the market simulation is finished, a power flow calculation is conducted in order to determine the power flow in the extra-high voltage grid [6]. These simulations lead to results for energy losses, electricity prices, energy mix in production and other data.

V. SIMULATION OF THE TRANSITION PATH

In this paper the time steps 2015 as starting point, 2030 as main intermediate step and 2050 as ending point will be presented and their simulation results analyzed. For each time step one year (8760 h) is simulated at hourly intervals.

A. Starting Point 2015

The simulation results of the starting point 2015, serving as reference, are shown in Tab. II. The present storage capacity and power is used here. The used efficiency factor of the storages is approximately 80%, because mainly pumped-storage power plants are in use currently. Only in the future time steps the lower storage efficiency of 33.7% is used.

Overall an maximum of about 10.37 GW of power plant output is required to cover the added up load of Lower Saxony, Hamburg and Bremen. That corresponds with the minimal required installed capacity of the power plant stock. Most of the load is covered by hard coal power plants. The reasons for this are the medium marginal cost of these power plants and their high installed total power. Nuclear and lignite fired power plants have lower marginal costs, but in the regarded area there are only one lignite fired plant and two nuclear plants. That is why the share in production is lower than that of hard coal, although all three run in full load almost the whole year. Gas fired plants only provide 3.8% because of their high marginal cost. The renewable energies supply about

TABLE II
STARTING POINT 2015 - RESULTS

Parameter	Result
Total energy feed-in	70.07 TWh
Maximum residual load	10.37 GW
Energy mix (share in total feed-in)	NU: 26.43% LI: 3.09% HC: 29.12% NG: 3.79% FU: 0% SO: 4.21% WI: 18.19% BM: 13.83% HY: 1.34% WA: 0% RE: 37.36%
Average electricity price	42.36 €/MWh
CO ₂ emissions	19.18 Mt CO ₂ 0.274 t CO ₂ /MWh
Energy losses (share of total feed-in)	EHVG: 0.65% Storage: 0.07%
Export of Energy (share of total feed-in)	0%

NU: Nuclear, LI: Lignite coal, HC: Hard coal, NG: Natural gas, FU: Other, SO: Solar, WI: Wind
BM: Biomass, HY: Hydro power, WA: Waste, RE: Renewable energy, EHVG: extra-high voltage grid

37% of the electricity production. Most of it is provided by wind turbines and biomass power plants. These data form a basis to evaluate the results for the future time steps.

B. Intermediate Step 2030

In 2021 both Lower Saxony's nuclear power plants Grohnde and Emsland are planned to be decommissioned. The same applies for the lignite fired power plant Buschhaus in 2020. Therefore all three plants are removed from the power plant stock. In addition to that all power plants built before 1970 are removed, too, because of an estimated maximum lifetime of 60 years. Overall the installed power plant capacity decreases by 3.3 GW. Partly that loss in capacity will be compensated by the increasing feed-in of wind turbines and solar plants. Additionally it is presumed that the planned hard coal power plant Stade (900 MW) will be completed until 2030 [7]. No further power plants are added.

The simulation results of 2030 with all three energy storage configurations are shown in Tab. III. The electricity prices and the CO₂ emissions are now listed relatively to the values in 2015.

Compared to 2015 the share in production of the renewable energies has increased significantly. As a result the CO₂ emissions decrease, although the total load has increased and the CO₂-neutral nuclear power plants have been decommissioned. On the downside the loss of cheap base-load power plants results in higher electricity prices. It is noticeable that the share of hard coal is decreasing, although these power plants now provide the electrical energy with the lowest marginal cost. That is because the hard coal fired plants are already almost permanently at full load. That results in a higher share of natural gas power plants, because they have to cover not only peak load but also partially base load, too. The high utilization of the hard coal power plants indicates that additional plants

TABLE III
INTERMEDIATE STEP 2030 - RESULTS

Storage configuration	Large (90%)	Medium (60%)	Small (30%)
Storage capacity	1.62 TWh	1.08 TWh	0.54 TWh
Storage power	12.96 GW	8.64 GW	4.32 GW
Total energy feed-in	90.35 TWh	90.1 TWh	89.55 TWh
Maximum residual load	6.64 GW	7.11 GW	7.83 GW
Energy mix	HC: 21.79% NG: 5.96% FU: 0.00013% SO: 26.66% WI: 34.99% BM: 9.56% HY: 1.03% WA: 0.00028% RE: 72.24%	HC: 21.77% NG: 5.95% FU: 0.00028% SO: 26.74% WI: 35.08% BM: 9.42% HY: 1.04% WA: 0.00024% RE: 72.28%	HC: 21.86% NG: 6.11% FU: 0.00012% SO: 26.9% WI: 35.3% BM: 8.79% HY: 1.04% WA: 0.00036% RE: 72.03%
Average electricity price (cmp. to 2015)	116.71%	114.52%	114.49%
CO ₂ Emissions (cmp. to 2015)	Tot.: 91.03% Rel.: 70.44%	Tot.: 90.67% Rel.: 70.44%	Tot.: 90.82% Rel.: 70.8%
Energy losses	EHVG: 0.71 % Storage: 9.12%	EHVG: 0.73 % Storage: 8.81%	EHVG: 0.69 % Storage: 7.08%
Energy export	0%	0.07%	1.23%

Cmp.: Compared, Tot.: Total, Rel.: Relative (per MWh)

have to be added to the power plant stock in future time steps after 2030.

The comparison of the three storage configurations shows that the difference between them is marginal in most of the cases. For example the shares of the renewable energies deviate by only 0.25%, the emissions of CO₂ by only 0.07 million tons per year. The only differences worth mentioning are the maximum residual load and the energy losses of the storages. The large configuration of the energy storages allows more storage operations and a better flattening of the residual load. On the one hand that leads to a lower maximum residual load, which defines the minimum necessary installed capacity of the power plant stock. On the other hand these additional storage operations result in higher losses.

In 2030 larger energy storages provide only small advantages and also some disadvantages. With the smallest configuration even the required exports (or shut downs) of energy are very low. This could lead to the consideration that in 2030 extended storage systems are still not necessary for an ensured energy supply. For that reason a further simulation was performed with the data of 2030 but only the storage capacity and power of 2015: 1.43 GWh and 101.68 MW. This storage configuration resulted in a failure of load covering in various periods of time throughout the year. In that case INES just reduces the residual load by load shedding and continues the simulation. But in reality a failure in load covering would be disastrous for industrial Germany. Therefore if no large storage facilities will be installed, the power plant stock has to be extended instead. Most likely fossil power plants would be necessary for this. In addition the simulation showed that the average electricity prices rise to values over 90 €/MWh

and also over 7% of the supplied energy has to be exported, because of negative residual loads. All three consequences are not desirable. This proves that already in 2030 an extension of storage systems is necessary, but not in a large scale and only if an expansion of the power plant stock is undesired.

It is worth mentioning that even the small storage configuration (0.54 TWh) corresponds to an increase of storage capacity by a factor of about 380 compared to 2015. This would require an enormous and expensive build-up of energy storage systems in Lower Saxony or Germany in general. Also it is questionable if that build-up can be carried in out just 12 years. But the dimension of required storage capacity is not unrealistic. A potential storage capacity of over 1700 TWh with hydrogen storage in caverns is estimated for whole Germany [8].

C. Scenario 2050

For scenario 2050 all power plants built before 1990 get removed from the power plant stock. The total installed power plant capacity is reduced by about 5.5 GW this way. Already in 2040 the problem occurs that the load cannot be covered throughout the whole year. For that reason additional modern gas and steam turbine power plants are added, overall about 4 GW in 2040 and 2.4 GW in 2050. These new plants are assumed to be evenly distributed in the considered area. Gas and steam turbine power plants are chosen, because of their low CO₂ emissions. In the long term exponentially growing CO₂ certificate costs were assumed. Therefore gas and steam turbine power plants are probably the best solution in that period of time. Also a ban of coal fired power plants until 2050 is not unlikely. Tab. IV shows the results for Scenario 2050.

TABLE IV
RESULTS - SCENARIO 2050

Storage configuration	Large (90%)	Medium (60%)	Small (30%)
Storage capacity	4.95 TWh	3.3 TWh	1.65 TWh
Storage power	31.5 GW	21 GW	10.5 GW
Total energy feed-in	120.21 TWh	120.48 TWh	123.9 TWh
Maximum residual load	2.56 GW	3.31 GW	5.02 GW
Energy mix	HC: 0.17% NG: 4.39% FU: 0.0536% SO: 43.49% WI: 47.22% BM: 3.87% HY: 0.779% WA: 0.0317% RE: 95.38%	HC: 0.161% NG: 4.5% FU: 0.056% SO: 43.39% WI: 47.11% BM: 3.98% HY: 0.78% WA: 0.027% RE: 95.29%	HC: 0.21% NG: 6.74% FU: 0.0727% SO: 42.19% WI: 45.81% BM: 4.19% HY: 0.756% WA: 0.0363% RE: 92.98%
Average electricity price (cmp. to 2015)	68.84%	64.97%	98.51%
CO ₂ emissions (cmp. to 2015)	Tot.: 10.22% Rel.: 5.95%	Tot.: 10.38% Rel.: 6.06%	Tot.: 15.54% Rel.: 8.76%
Energy losses	EHVG: 0.64% Strg.: 24.63%	EHVG: 0.64% Strg.: 23.72%	EHVG: 0.73% Strg.: 18.1%
Energy export	0.0096%	1.09%	8.79%

The share in production of renewable energies has increased to over 90% in all three storage configurations. The total emissions of CO₂ is lowered by over 80% compared to 2015. The emissions per megawatt hour are lowered even more markedly. Also the necessary installed power plant capacity is lowered significantly compared to 2015 and 2030, from over 10 GW to under 3 GW with the large storage configuration. After the rise of the electricity price in 2030 it now continues its current decreasing development again. The storage losses rise to about 20% of the supplied electrical energy.

Contrary to 2030 major differences can be monitored between the energy storage configurations. It is especially noticeable that the small storage configuration provides no longer any advantages aside from the lower energy losses. Instead it results in the highest average electricity prices, CO₂ emissions, maximum residual load and the highest exports of surplus energy. Even the highest amount of total electrical energy must be generated because the additional exports surpass the saved energy losses, compared to the other two configurations. Additionally the exported energy often results in overloading of the electrical lines. The large configuration of the storages provides only minor advantages compared to the medium sized storages. All that indicates that the small configuration with 1.65 TWh and 10.5 GW is too small for Scenario 2050 and that the large configuration is over-sized. The medium configuration seems to be closest to the optimal solution. But no further statements can be made without an additional economic view on the case.

VI. EVALUATION

The simulations confirm that the energy supply of Lower Saxony and surrounding area will change dramatically the next few decades, if the schedule for the "Energiewende" will be fulfilled. Exemplarily some selected characteristic values will be presented to demonstrate these changes.

Fig. 2 shows the increase of the renewable energy share in production of electricity until 2050. For the representation the medium energy storage configuration was chosen, but the other two configurations in principle show the same development with only slight deviation. The figure shows that the share in production of the renewable energies is increasing steep at first and then flattening. Since the renewable feed-in was assumed to rise linearly the flattening is due to the increasing total load, exports and losses, which result in higher total feed-in. In Scenario 2050 a renewable share of over 90% is achieved which surpasses the objective of the German government for 2050 and is close to a fully renewable energy supply.

The same figure also displays the development of the electricity price and the CO₂ emissions relative to the starting point 2015. Overall the current decreasing trend of the electricity price is continuing. But after the nuclear phaseout in 2022 it increases temporarily. From 2030 on it is decreasing again and eventually falls to about 65% of the price at starting point 2015. It is important to mention that in the INES the marginal costs for wind and solar supply are assumed to be 0 €/MWh. Therefore the rising renewable share in supply

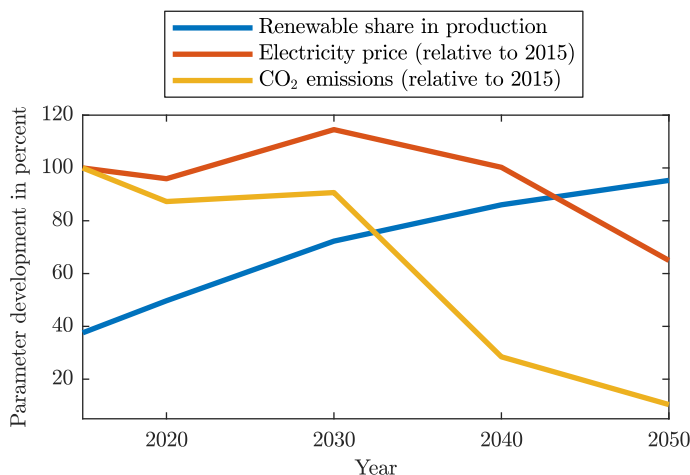


Fig. 2. Development of renewable share, electricity price and CO₂ emissions

results in the decreasing prices. The decrease of the CO₂ emissions resembles the development of the electricity prices. On the whole the emissions are decreasing steadily. But again this development temporarily stops between 2020 and 2030 due to the nuclear phaseout. In 2050 the total emissions have decreased by over 80%. That matches with the objective in [3].

The simulations show that until 2030 only minor differences between the three considered energy storage configurations occur. That indicates that energy storage systems in that scale are not necessary in the next few years. After 2030 the differences scale up and the medium and large storage configurations show significant advantages in comparison to the small configuration.

Three general correlations could be found in the process. Larger energy storages lower the necessary power plant capacity and exported (or shut down) energy due to excess power. To achieve that much energy has to be stored in and out again, which leads to high energy losses. The other parameters do not directly correlate with the scale of the storage systems. Instead the effects of different sized storages depend primarily on the regarded time step as second influencing factor.

VII. CONCLUSION AND FUTURE WORK

In this paper different time steps of Lower Saxony's energy supply from the present until 2050 were created and simulated with the market simulation tool INES. These simulations allowed to assess the future development of Lower Saxony's energy supply. Secondly the impact of different sized energy storage systems on the regarded parameters was investigated within the separate intermediate steps. Thereby mainly technical parameters were analyzed. So advantages and disadvantages of different sized storages could be identified. But that approach could not determine the optimal size of the energy storages and their cost savings potential. To find these also an economical analysis has to be carried out. The costs of storage systems (investment, operating, losses) have to be juxtaposed with the savings potential in the grid expansion, the power plant stock and other areas.

Generally the energy losses in the storages surpass the losses in the extra-high voltage grid by far. Up to 25% energy losses in the storages are economically and ecologically unjustifiable. Therefore the storage of energy through hydrogen synthesis in this scale is not a viable solution for the future, at least not with the assumed efficiency factors of 33.7%. In most of the cases the energy must be stored only for hours and days. Therefore an combination of short-term and long-term energy storages might lead to better results. For example batteries with a much higher efficiency could perform the day/night balancing, where most of the energy gets stored in and out and most of the losses occur. Conversely the seasonal balancing, where high storage capacity is required, would be executed with hydrogen synthesis.

ACKNOWLEDGMENT

The research project 'NEDS Nachhaltige Energieversorgung Niedersachsen' acknowledges the support of the Lower Saxony Ministry of Science and Culture through the 'Niedersächsisches Vorab' grant programme (grant ZN3043).

REFERENCES

- [1] L. Hofmann, M. Sonnenschein, Smart Nord - Final Report, Institute of Electric Power Systems Leibniz Universität Hannover, Department of Computer Science, Carl von Ossietzky Universität Oldenburg, April 2015.
- [2] M. Blank, C. Blaufuß, M. Glötzel, J. Minnemann, A. Nieße, F. Pothen, C. Reinhold, J. S. Schwarz, K. Stahlecker, F. Wille, T. Witt, T. Rendel, F. Eggert, B. Engel, J. Geldermann, L. Hofmann, M. Hübner, S. Lehnhoff, N. Paech, M. Sonnenschein, Process for Simulation-based Sustainability Evaluation of Future Energy Scenarios, NEDS Whitepaper, December 2015.
- [3] H.-P. Beck, C. v. Haaren, J. Kuck, M. Rode, J. Ahmels, F. Dossola, J. z. Hingst, F. Kaiser, A. Kruse, C. Palmas, G. Römer, I. Ryspaeva, H.-H. Schmidt-Kanefendt, W. Siemers, R. Simons, J.-P. Springmann, C. Yilmaz, Szenarien zur Energieversorgung in Niedersachsen im Jahr 2050, Niedersächsisches Ministerium für Umwelt, Energie und Klimaschutz, 2016.
- [4] Institute for Environmental Economics and World Trade, Protocol of e-mail correspondence, March 2018.
- [5] T. Gaßmann, Netzentwicklungsplan - Kraftwerksliste Szenariorahmen 2030, Federal Grid Agency Germany, January 2018.
- [6] T. Rendel, Erweiterung und Plausibilisierung eines Modells für die integrierte Simulation des europäischen Verbundnetzes und Strommarktes, Institute of Electric Power Systems Leibniz Universität Hannover, September 2015.
- [7] G. Penn-Bressel, Daten und Fakten zu Braun- und Steinkohlen, Federal Environment Agency Germany, December 2017.
- [8] Scientific Services - German Bundestag, Sachstand: Entwicklung der Stromspeicherkapazitäten in Deutschland von 2010 bis 2016, January 2017.

Detection and Localization of Power Plant Outages using Machine Learning Algorithms

M.Sc. Bharathwajanprabu Ravisankar and M. Sc. Stefan Dalhues
 Institute of Energy Systems, Energy Efficiency and Energy Economics ie³
 TU Dortmund University
 Dortmund, Germany

Abstract—For power network operators worldwide, one of the common leading problems that requires efficient handling is the mitigation of large scale network failures due to power outage. As such, instances of failing power plant or transmission line raises complication in smooth network operation. This requires handling huge amounts of live data which can only be solved by using intelligent mechanism. One such efficient mechanism is the use of Machine Learning (ML) algorithms for classification of power outage scenarios. To gather an overview, in this paper, wide comparison are made on the classification results of five different ML algorithms, namely Decision Tree (DT), Ensemble methods, k-Nearest Neighbors (k-NN), Neural Network (NN) and Support Vector Machine (SVM). These supervised learning algorithms determines the cause of power outage, either due to a failing power plant or transmission line and approximately locates the outage area. The underlying problem involves generating data sets using DigSILENT PowerFactory simulations, noise free feature extraction, ML algorithm development, training and testing of classification models. The analysis and comparison of classification results at the end reveals the effectiveness in using such ML algorithms to solve power outage prediction problems. The developed ML algorithms and models has been validated by using data sets and classification results from different network configurations with varying load change conditions.

Index Terms—Big Data Classification Machine Learning Power Outage Supervised Learning

I. INTRODUCTION

Owing to interconnection of complex power transmission grids, it is vital to have network operation procedures that can understand and suggest progressive solutions to arising problems. Thus, it becomes necessary to put in place a non-destructive online system to monitor, alert and diagnose network demands. This in turn reduces operational costs, enhances optimal usage, improves reliability and accuracy of network assessment [1]. But, in a real world scenario, the possibilities of network outages caused by power generating stations and transmission lines are most likely due to consistent operational stress. An economically reliable system to detect such failures provides greater assistance to smooth operations [2].

The outage detection systems available as yet requires bringing the failing system to a halt for maintenance and inspections, thus affecting its operation as well as impacting power demands and requirements throughout its interconnected network. Even though forecasting power demands helps

in proper planning of power transmission, it still lacks in potential to distinguish demands during urgent or emergency conditions. A planned outage can be compensated appropriately due to known demands whereas unplanned or unexpected power outage requires immediate action. Some times the reason for such outages are not known for long and failing network creates problems that are tedious and time consuming to solve.

To address this issue, several multiagent system methods [3] are designed to establish communication. Information interchange through network of communication agents feeds data to algorithms which are used to understand the ongoing network operation. This makes way for the use of multiple Artificial Intelligence (AI) methods to detect faults and outage conditions. The AI methods thus developed requires improving the detection and location of power outages in some ways to compensate power demands, subsequently rectifying the faults as quickly as possible [1] [2] [4] [5]. But, to detect outages for a vast network of interconnected power transmission systems, there exists less number of AI methods that employ algorithms directly onto busbar. Also, it is important for the intelligent algorithms to be autonomous for effective operation and assistance when the data are read through Phasor Measurement Unit (PMU).

Hence, there is a need for systematic approach to process huge amount of data that are generated throughout the network grid. This demands higher levels of understanding about the operation and planning of existing systems, higher computational resources, full-scale algorithmic routines and schemes. The crucial part of this paper is to find such autonomous intelligent solutions for detection and localization of power outages.

II. OUTAGE DETECTION IN POWER SYSTEMS

To enhance reliability, the interconnected network of the European Network of Transmission System Operators for Electricity (ENTSO-E) has been created to maintain system stability even in critical situations. However, failures and malfunctions can affect the whole interconnected transmission system and can cause blackouts throughout the whole system. In case of power plant outages, it is important for the transmission system operator to detect the event and localize the failure and apply countermeasures, even in case of a

distant failure. One way to detect the outage is to monitor the measurements from PMU across the network. For example, the oscillations caused by generator outages provides the readings necessary to detect the outages caused due to generator failure. Likewise, the transmission line failures can also be monitored and detected based on the available data from the measuring devices. In practise, measured data from the devices are so huge in a way that it is not possible for human operators to process in a time bound manner. This leads to complications during network problem detection. The need for processing large data is thus required.

Machine Learning approaches are the most prominent techniques available today that are capable of handling problems with vast ranges of complexity and computation. Owing to sustained surge in computing hardware and software designs, ML has improved drastically to next levels of futuristic intelligent solutions. This paper examines the solutions to complex network problems by utilizing robustness and vast computing capabilities of ML. The data classification thus forms the basis for recognizing patterns and detection of outages. Few effectual outage detection and localization models are designed and established to utilize the potentials of ML algorithms for classification through supervised learning which are capable of classifying datasets after training. Following machine learning algorithms are developed, models trained and tested for both detection and localization of outages in this paper: Complex Decision Tree (CDT) [6], Random Forests (RanFors) [7], Medium k-Nearest Neighbor (MKNN), Weighted k-Nearest Neighbor (WKNN) [8], Neural Network [9], Linear SVM One vs One (LSVMovO), Linear SVM One vs All (LSVMovA), Quadratic SVM One vs One (QSVMOvO) and Quadratic SVM One vs All (QSVMOvA) [10]. The training algorithms are modelled based on available datasets and its respective classification classes. Several combinations of training are carried out by training several times and choosing the best classifier that suits the application.

III. DESCRIPTION OF THE PROPOSED METHOD

The proposed method compares various machine learning classification models for the detection and localization of power outages. The first part of classification involves the detection of outage in the network, either due to failure of generator or transmission line. The next part is to find the source or area of such an outage. It is necessary to know how classifier models are utilized to understand the outage type detection and localization process. After training, the best classifier models are selected and are exported. For outage type detection, the classifier models which are capable of detecting both generator and transmission line outages are used. But, the location classification is triggered only after detection of outage type and hence the process of obtaining the location involves location specific classifier models. Such a setup is described in figure 1.

Once the input data is fed into outage classifier, it determines whether there is an outage due to generator failure or transmission line failure or no outage at all. If an outage is

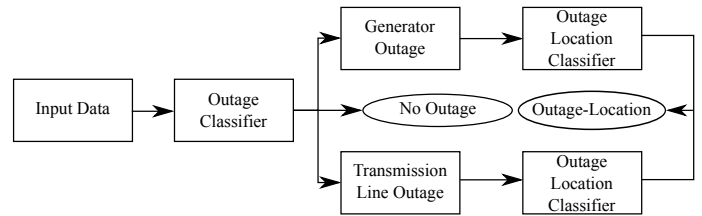


Figure 1. Outage Detection and Localization Work-flow

detected, then based on the outage type, either the generator location classifier model or transmission line location classifier model is triggered to obtain the outage location.

The development of ML method consists of five parts namely generating data sets, data preprocessing, algorithm development, model training and testing and validation. The data sets can be obtained from live systems or through simulation. The data generated by such means needs a data preprocessing step where the data set is analysed thoroughly to clean out data, eliminate irrelevant data points and noises. In data preprocessing, the vital part that concerns to ML is the extraction of features. Features defines the properties of data very clearly than raw data themselves. Also, obtaining features is better in terms of computational efficiency. Because, instead of processing raw data, it is economical to process only the needed features and obtain the relevant outcomes with better accuracy. Feature selection leads to data which are relevant to problem and enhances predictability. For problems with numerical computations, one of the best and easier way is to extract and select features by employing statistical analysis.

A. Statistical Data Analysis

In statistical analysis, the basic forms of mathematical components of data are estimated. For the data with waveforms, the following list of statistical components are important and provides the necessary information:

- Maximum Value
- Minimum Value
- Mean
- Variance
- Standard Deviation
- Range

An illustrative example of voltage magnitude for a transmission line outage plotted against simulation time is shown as an sample trapping of waveform on to statistical features in figure 2. SD-XAxis and SD-YAxis denotes the standard deviation of waveform along x and y axes. Also, Mean-XAxis and Mean-YAxis denotes the mean value of waveform along x and y axes. Similarly, other statistical features can also be estimated to trap the waveform. Trapping of a waveform within statistical limits provides a wide range of possibility to compute and derive similar patterns. Principal Component Analysis is another significant statistical method that transforms the correlated observations to linearly uncorrelated observation according to orthogonal transformation procedures. Every data vector is the linear combination of the

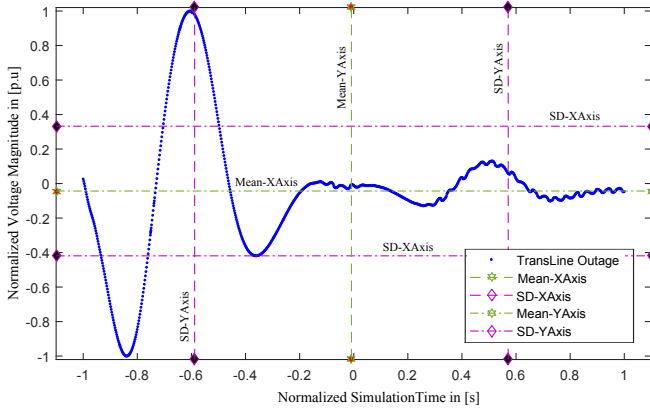


Figure 2. Statistical Analysis

principal components. The principal component or orthogonal vectors are usually ordered in terms of decreasing strength and are sorted by reduction or elimination of weak components. The weak components are nothing but those observations with low variance. Due to elimination of weak components, it is possible to reconstruct the original data with proper approximation.

B. Data Preprocessing

Highly debated step in data preprocessing is data normalization. Data normalization can be considered as a mathematical scaling or reduction technique that manages to calibrate different measurement scales into a single common scale. The normalization helps in the reduction of data variability and introduces integrity to data. Two of the widely used normalization forms are shown in equation 2 with y as the input data to be normalized.

$$y' = \frac{y - \min(y)}{\max(y) - \min(y)} \quad (1)$$

$$y' = 2 \left(\frac{y - \min(y)}{\max(y) - \min(y)} \right) - 1 \quad (2)$$

Using the normalization forms in equation 2, the data can be scaled to ranges between $[-1, 1]$.

The supervised learning in particular requires the training set to contain both the data points and respective labels for the data points. Hence, the data sets which are preprocessed in the previous steps are labelled and the whole data set is split into training dataset and testing dataset. Those in the training dataset are used only for training and those in the testing datasets are kept separately and are used only for testing of the trained model to determine its performance.

Now, the processed input data consists of features to classify the outage. It is fed to the outage classifier which contains the necessary classifiers for detection and localization of outages. If there are no outages, then no classifiers are activated. If there is an outage, the outage classifier determines the type of outage. For example, if a generator outage occurs, then the classifier detects the generator outage and activates the location classifiers. The location classifiers in turn finds the

area of generator outage and provides the user with outage location. Similar operation is carried out if the classifier detects transmission line outage.

The crucial part in the ML is the development of algorithms based on the requirement. Upon iterative training of the model, the algorithms are fine tuned to obtain accurate results. During initial stages, the classifier models are trained iteratively using the training datasets. After each training, the outcomes are evaluated and the one with better accuracy and good performance is selected as the classifier model. The selected classifier model is then tested using testing datasets. The testing of classifier models shows whether a classifier model is performing well by classifying the data correctly. If the classifier model performs well, then the classifier model can be used in real time deployments.

IV. SIMULATION SETUP

Simulation of outage conditions for a network model is initiated by the user using a Matlab script which communicates with DIgSILENT PowerFactory via a python script and initiates the simulation. One way of simulating outage is by making a generator or a transmission line as 'Out of Service (OoS)' at user specified time. For example, taking a transmission line as OoS at time t seconds. This replicates a real time outage situation in a simulation environment. PowerFactory simulates load flow conditions for such scenarios and generates outputs. Out of many available properties of electrical systems to analyse with, the following three properties are chosen as output from PowerFactory simulations: Frequency, Voltage Angle and Voltage Magnitude. The generated outputs from each BusBars (BBs) consisting of frequency, voltage angle and voltage magnitude are stored and later processed. Similarly, simulations are carried out with different OoS situations. These data sets forms the basis for input data and are sent for data preprocessing, training and classification. Upon receiving the output file, Matlab scripts retrieves BB data, allocates variable names and forms initial datasets. These datasets as it is are not capable enough to be used for classification training directly and requires data preprocessing. The Nordic Network as shown in figure 3 is used in this paper to obtain different datasets. The network consists of 20 generators and 33 transmission lines out of which generator G20 is used for simulation stability and is never taken OoS. The training dataset after data preprocessing as explained previously consists of 400 predictors from 57 BB readings. To solve the classification problem, training dataset requires different labelling for detection and localization. For the part of outage detection, the training datasets are labelled as 'Generator Outage' and 'Transmission Line Outage'. The dataset with normal operating data are labelled as 'No Outage'. Similarly, for location of outage, the names of the respective zones are labelled and the data for which location are not known are labelled as 'Unknown Zone'. A typical example of such labelling in terms of location classifier is shown in figure 4.

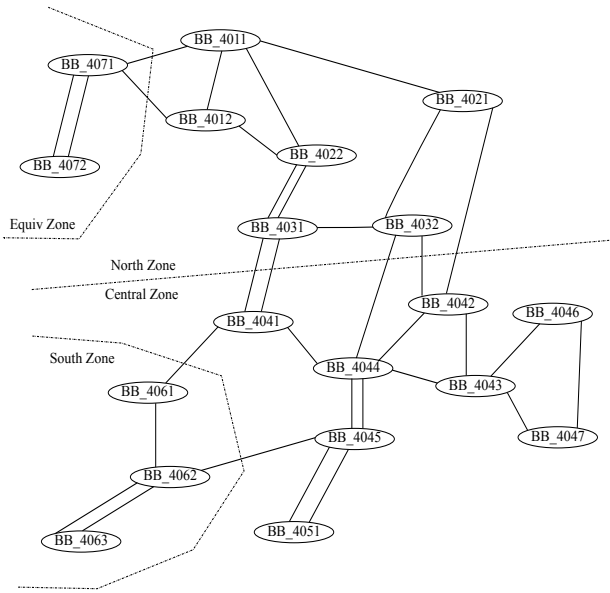


Figure 3. Nordic 400kV Transmission Network (based on [11])

A simulation example is as follows: The generation of input data is carried out by taking G_01 as OoS at time $t = 5$ seconds and the simulation is run for a total of 30 seconds in PowerFactory. Similarly, other generators are taken out and simulated. This step is carried out for transmission lines as well. The list of possible generators and transmission lines that can be taken OoS are 19 and 33 respectively. In this paper 14 generators and 14 transmission lines are taken OoS for the purpose of training data generation. This generates a total of 400 predictors and are fed as input to the classifier.

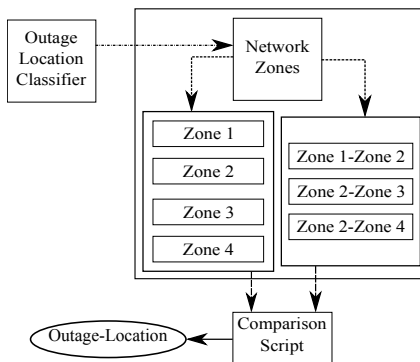


Figure 4. Outage-Location Classifier Model Work-flow for Nordic Network

Figure 4 shows the labelling of Nordic Network Model zones with respect to location classifier. The four zones, namely 'Zone 1', 'Zone 2', 'Zone 3' and 'Zone 4' as well as three between zones, namely, 'Zone 1 - Zone 2', 'Zone 2 - Zone 3' and 'Zone 2 - Zone 4', specifies the labels for their corresponding zones. Once, the location classifier classifies the zones, the labels are taken in to be compared with other zone data to arrive at location of outage.

V. RESULTS

The interpretation of classifier model results consists of two main parts, namely interpretation of detection classification and interpretation of localization classification. The first part, detection of outage, holds the key for activation of second part, localization of outage. As an example, the test results of the QSMOvO detection classifier model is shown in figure 5. The result shows the data points before classification and after classification by the detection classifier. The captured results in figure 5 shows the classification of data points for a given interval of time. The classifier algorithm utilizes all live data points to perform live classification. During live classification, each data points traversing through the classifier are classified, thus giving the operator a clear view of ongoing operating condition of power plants and transmission lines.

The first row with red data points of the result portrays the better detection of normal operating condition or no outage. The Second row with green data points hints the accurate classification of Generator Outage condition. Similarly, the Transmission line Outage can be seen in third row. Even though there is a short period of misclassification of outage condition at first, the classifier is able to get the outage correct from the subsequent data points.

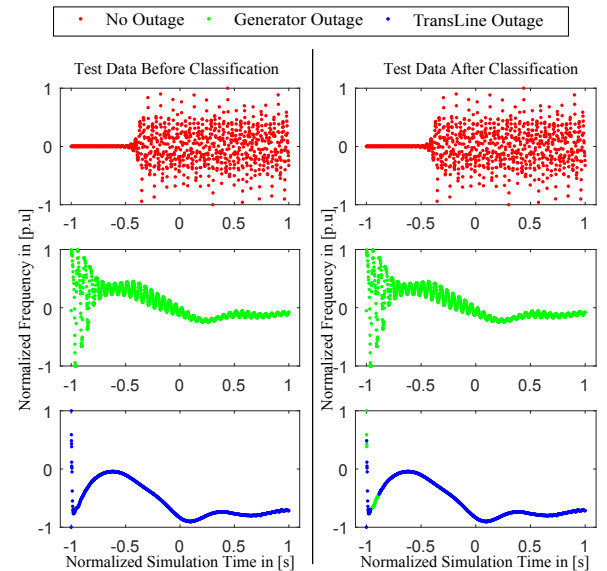


Figure 5. Result of QSVN One vs One Detection Classifier model

From figure 5, it can be clear that the classifier works as intended. The red color classification result represents no outage or normal operating condition whereas green and blue represents generator and transmission line outages respectively. Similarly, varying classification results, can also be seen and analysed with the other classifier models as well. Based on the results, the efficiency of the classifier can be determined and the best classifier can be selected for deployment.

The classifiers are also tested with a different configuration of Nordic Network by changing the loads to 0.8 scaling factor, thus simulating varied loading conditions of power

transmission system. Similar to previous testing, the generator and transmission lines are taken OoS and the testing data are generated. The classification outcome of QSVMOvO is shown in figure 6.

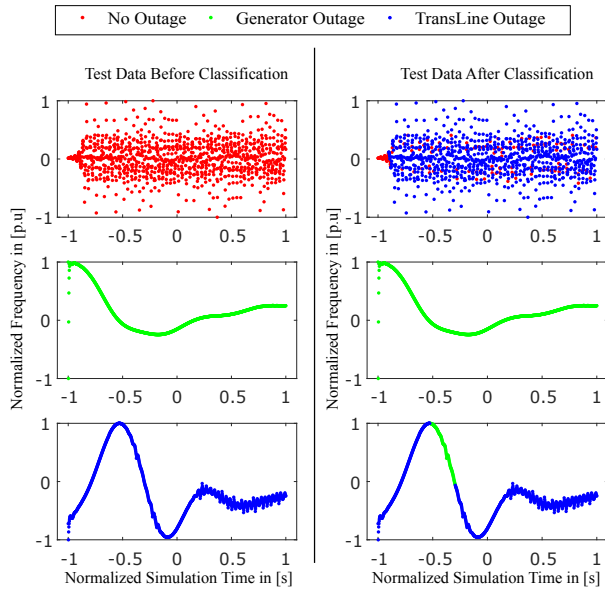


Figure 6. QSVMOvO Detection Classification with Load Changes

It can be seen clearly in Figure 6 that there are some hiccups in the detection of no outage. But, there are significant improvement for transmission line outage. With most of correct classification, it can be understood that the transmission line outage detection at the initial stages are good. Now, in a straightforward way, it can be clearly noted that the generator outage detection has far better correct classification. This shows that the classifier is capable of detecting the outages and requires further training to improve accuracy. Similar results can also be seen from other BB's perspectives.

A. Result Analysis

With reference to box plot figure 7 and figure 8 for detection classification, the CDT method has overall average performance compared to other classifiers. While considering localization of outage, one can easily see that the performances of CDT classifier for all the zones and inter zones are good. This implies that the combined localization classification has better scope for CDT than individual detection classification. Based on the results, the following significant observations about CDT classifier can be compiled: CDT classifier can only be used for trial detection and to understand the model. For localization, it is possible to be used for low memory computations. Due to crucial obstacles in data split and average performing classification, there is an imminent need for an alternative search tree algorithm. Hence, it is worthy to try ensemble method with decision tree algorithms. But, it can be noted that the random forests classification algorithm performs far better than decision tree. Further, it can be said that RanFors classifier can be used for both detection and

localization of outage but only with less complex datasets. RanFors classifier also suffers from CDT's obstacles in data split as mentioned previously though this can be overcome by finding the optimal number of random trees through iterative training and testing.

Both MKNN and WKNN with euclidean distance vector and 10 nearest neighbor has shown good performance for varying conditions as seen in figure 7 and figure 8. The reasons are because of convergence metrics and the number of nearest neighbor. The main drawback of this method is the execution time as it takes around 235 seconds in average to detect and locate the outage. Due to long execution time, it is not suitable for real time applications. It also requires more computing memory and hence might not be economical. The neural network classifiers, widely recognized for pattern

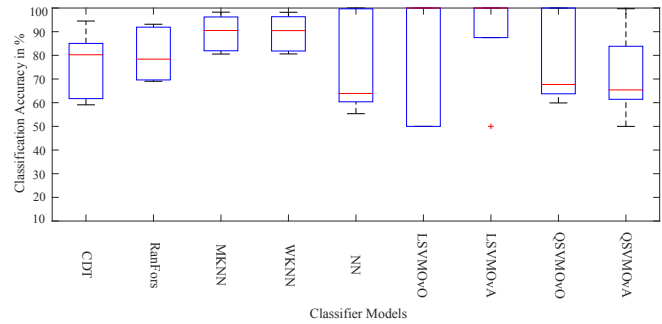


Figure 7. Detection Classification: Generator Outage Classification Accuracy

classification shows above average results for detection as illustrated in figure 7. The training of neural network are cumbersome but worthy. During training several iteration of repeated training as well as trainings with different numbers of hidden layers were performed. By understanding the performance results of various iterative training, suitable hidden neurons need to be selected. The NN classifiers are better than search tree classifiers as well as a good contender against other classification methods, but requires more computational capacity and exhaustive training.

Through box plots, it can be observed that the SVM methods performance are consistent, good and competitive. Due to the use of quadratic kernel function, it is possible to expand the concept of binary classification to multi class classification. Though the execution time and performances are better, it is worth noting that SVM methods require prolonged time to train. Also, it requires good training datasets. Apart from this pitfalls, QSVM classifiers are noteworthy to explore further to take advantage of multi class classification. Further, it can be added that the testing of classifiers with load change scenarios strongly implies the need for extensive training and testing with different kinds of scenarios. When the load changes it affects the core structure of the datasets with respect to the load change factor. This leads to masking of outage from classifiers. Due to this, even the classifier with better classification accuracy on different outages finds difficulties facing datasets from load change. A good example of such load

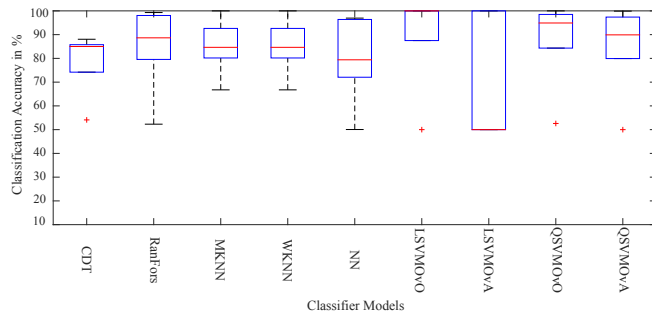


Figure 8. Detection Classification: Transmission Line Outage Classification Accuracy

change scenario is shown in Figure 6. Here, the result shows the masking of transmission line outage over no outage data. This implies that the classifier couldn't distinguish between a normal operating condition and an outage condition. Hence, the load change is recognized as an outage even at normal operating condition. To mitigate this problem, the classifiers has to be trained with load change scenarios too.

In case of different configuration of network models, it is very difficult for the classifier to detect data points that are actually outages. This is due to various factors like distinct topologies, modes of operation, load scenarios, etc., Even though the classifiers are to classify unseen data, it is more difficult to classify unseen day that are of entirely different operating conditions.

Though there are many features to select, it is in the interest of scope of this paper, that only these three measurements alone were considered.

VI. CONCLUSION

From observation and evaluation of results it can be concluded that the SVM, NN and k-NN methods holds significant application on classification of power outages. Even though the medium and weighted k-NN methods has significant practical implications due to increased execution time to classify data, it is well understood that the algorithms perform nevertheless. The SVM on the other hand requires more time to train the classifier, which is quite a vital task for ML methods. But, the classification and quick execution assists the SVM and has more reasons to further explore to utilize its capabilities. The computationally intensive neural networks, which has been researched for several decades now has shown good performance. The training of the classifier models were hard to achieve perfection. It is time consuming when the data is too big or complex. Due to the requirement of iterative training, the classifiers were trained carefully to avoid generalization towards a particular network model or datasets. The classifiers modelled in this paper had minimal information from the grid. Due to minimal information, there was restricted training which largely influenced the overall outcome. Even with such restricted minimal datasets, the classifiers has exhibited encouraging results. The results from the simulation provided a glimpse of real world problem where load changes are

repetitive. It gave a detailed understanding on the effects of changing loads on normal operation. It also lead to a reasoning that the classifier requires large datasets with different load condition at different times of the day.

Through observation of training process, testing with different conditions and through extensive analysis of various classifier models, it can be evidently justified that the classifiers are capable of handling and solving power outage detection as well as localization of outage source. It is also capable of pointing out the area of outage as close to the outage source zone by using minimal information from the grid. The classification models would perform better if the models are trained well with data sets from real time systems. But, obtaining data from real time systems requires extensive measurement spectrum, which are comparably rare. Also, a very precise model of the system is required that is capable of generating the needed data by simulation. Since a lot of parameters in the power system are unknown, it is quite hard to achieve the exact dynamic behaviour of the system.

Further developmental works regarding the outage classification problem can involve in the improvement of locating the source of outages by expanding feature datasets, training and more electrical devices.

REFERENCES

- [1] N. S. Coleman, C. Schegan and K. N. Miu, *A study of power distribution system fault classification with machine learning techniques*, North American Power Symposium (NAPS), 2015.
- [2] X. Zhang, *Neural Network-Based Classification of Single-Phase Distribution Transformer Fault Data*, 2006.
- [3] S. C. Müller, U. Häger and C. Rehtanz, *A multiagent system for adaptive power flow control in electrical transmission systems*, IEEE Transactions on Industrial Informatics, vol.10, no.4, 2014.
- [4] Y. Zaho, R. Sevlian, R. Rajagopal, A. Goldsmith and H. V. Poor, *Outage detection in power distribution networks with optimally-deployed power flow sensors*, Proc. of IEEE Power and Energy Society General Meeting, 2013.
- [5] D. Watts and H. Ren, *Classification and discussion on methods for cascading failure Analysis in Transmission System*, IEEE International Conference on Sustainable Energy Technologies, 2008.
- [6] J. R. Quinlan, IEEE Transactions on Systems, Man, and Cybernetics, Decision trees and decision-making, vol.20, no.2, 1990.
- [7] T. G.Dietterich, Ensemble methods in machine learning, International workshop on multiple classifier systems, 2000.
- [8] T. Cover and P. Hart, Nearest neighbor pattern classification, IEEE transactions on information theory, vol.13, no.1, 1967.
- [9] C. M.Bishop, Neural networks for pattern recognition, 1995.
- [10] V. N.Vladimir and V. Vapnik, The nature of statistical learning theory, 1995.
- [11] T. C. Van and L. Papangelis, Description, modeling and simulation results of a test system for voltage stability analysis, 2013.

Contribution to Distribution System State Estimation with Hachtel's Augmented Matrix Approach

Tobias Hoffmann, Annika Brüggemann, Florian Rewald, Christian Rehtanz
 ie³ – Institute of Energy Systems, Energy Efficiency and Energy Economics,
 TU Dortmund University, Dortmund, Germany

Abstract— The procedure of state estimation calculates the static state based on real-time measurements for the transmission system. Due to differences in measurement and network infrastructure, employing the conventional approach of the weighted least squares approach for the distribution system, the estimated static state leads to an ill-conditioned state estimation, which can result in convergence problems or an inadequate estimated static state. This paper analyses and evaluates the application of Hachtel's augmented matrix approach as an alternative means of static state estimation for medium and low voltage networks with variations in the distribution system of decentralized feed-ins or the network topology, and hereupon deduces recommendations for the application of state estimation with Hachtel's augmented matrix approach in distribution systems.

Keywords— *Distribution System State Estimation, Hachtel's augmented matrix approach, ill-conditioning*

I. INTRODUCTION

Monitoring power systems, the essential information for further analysis is the static state, e.g. dispatch studies, verifying the (n-1) security or optimal power flow. The static state includes the voltage magnitude and voltage angle of the network busses and initially shows potential risks of the voltage range. Determining a consistent and definite state vector based on different measurements, state estimation (SE) is necessary and has been used at the control centers for the transmission system for more than 40 years [1]-[3]. However, due to the change towards more and more decentralized feed-in the relevance of Distribution System SE (DSSE) is increasing and requires adjustments of the so-called conventional SE used at the transmission system. Differences in the measurement infrastructure and network topology of the distribution systems make these adjustments necessary.

Handschin summarized four main requirements for SE [4]: 1) the static state must be consistent and stable; 2) the SE filters measurement errors as the errors are distributed Gaussian random variables; 3) unknown parameter are calculable with the SE; 4) huge measurement errors must be identified and eliminated. Besides these requirements the knowledge of the network topology, the network parameter and the telemetered measurements are essential input data for the SE. Hence, the conventional SE implementing the iterative weighted-least-square (WLS) approach solves the estimation problem. A

potential risk that the SE with the WLS method faces is the sensitivity to erroneous input data that can lead to an ill-conditioned SE problem, i.e. a small erroneous measurement results in serious deviation in the estimated static state [5].

First studies to the ill-conditioning problem of SE were done 1976 by Duff and Reid [6] who recommended the use of Hachtel's augmented matrix approach for sparse matrixes as an alternative to the WLS approach. Moreover, the authors of [7] and [8] validated also Hachtel's augmented matrix approach as a good alternative and made various studies with transmission test systems. As mentioned before the significance for DSSE is increasing, i.e. distribution systems can be operated more efficiently and e.g. react to a dispatch situation in the transmission system.

Distribution systems are characterized by a different measurement infrastructure and network topology as compared to transmission systems, e.g. with a high R/X ratio or limited power measurements. Therefore, it is necessary to validate the use of SE with the WLS approach or the alternative Hachtel's augmented matrix approach in the distribution system. In 1996 the authors of [9] suggested to solve the problem of the few power measurements by counting zero-injections as power measurements with a high accuracy. Based on this idea Nussrat compared the implementation of different approaches for the SE in distribution systems [10]. Nussrat diagnosed that the ill-conditioned SE problem in distribution systems is related to the high R/X ratios and short power lines. The studies of Nussrat and the authors of [11] show that the use of Hachtel's augmented matrix approach is a good compromise for the distribution system and numerically more stable compared to the WLS approach. Nevertheless, they do not show the impact of changes in the distribution system to the SE solution, e.g. meshed networks, a feed-in or load overweight.

Accordingly, this paper provides an overview for SE in distribution systems with changes in the network topology and changes in the amount of the power injections. For this paper both approaches, the WLS and Hachtel's augmented matrix approach, are implemented in MATLAB and the results are compared by means of different criteria.

The next Section presents the mathematical formulations of the WLS approach and the Hachtel's augmented matrix approach. In Section III the simulation scenarios are explained. The results of the comparison of both approaches are presented

in Section IV while a conclusion and ideas for consequent studies are summarized in Section IV.

II. STATE ESTIMATION ALGORITHM

SE is based on a redundancy of measurements and calculates a complete, consistent and definite static state with less state variables [5]. Handschin suggested a redundancy for the input data, i.e. the number of measurements doubles the number of state variables [4].

For the conventional SE, input data are understood as real-time measurements in the transmission system with a known accuracy. Following the approach to establish a measurement infrastructure in the distribution system as in the transmission system, the economic efficiency would not be given, due to the high number of busses in the distribution system [5][10]. Hence, there is an approach to raise the number of measurements by adding non-real measurements and classifying them in three categories [5][10]: *pseudo*-, *virtual* and *real* measurements. Real measurements are at least physical measurements and can be power flow or currents in power lines, power injections or bus voltage measurements. However, pseudo-measurements are e.g. based on historical data and forecast for loads or generation while virtual measurements e.g. are supposed at passive busses with no generation or load, having network their zero-injection. The accuracy of the virtual measurements is supposed to be error-free [5].

The different measurements gathered by a supervisory control and data acquisition (SCADA) system can be summed up in the vector \mathbf{z} [5]:

$$\mathbf{z} = \begin{bmatrix} z_1 \\ z_2 \\ \vdots \\ z_m \end{bmatrix} = \mathbf{h}(\mathbf{x}) + \mathbf{e}, \quad (1)$$

where z_i is the measurement at bus i and m is the amount of measurements. The vector $\mathbf{h}(\mathbf{x})^T = [h_1(\mathbf{x}), h_2(\mathbf{x}), \dots, h_m(\mathbf{x})]$ contains the non-linear network equation for measurements i in every $h_i(\mathbf{x})$. Additionally, the measurement error e_i is given. The first order state variables for n busses are defined as [5]:

$$\mathbf{x}^T = [x_1, x_2, \dots, x_n]. \quad (2)$$

Second order state variables are calculated with the first order state variables and describe values that have not been measured, e.g. a non-measured power-flow.

Like for power flow calculation the voltage angle in the reference bus is in accordance with [4] set as $\theta_1 = 0^\circ$. With m measurements and n busses the redundancy request as mentioned before is [4]:

$$\eta = \frac{m}{2n-1} \approx 2. \quad (3)$$

The measurement errors are statistically independent of each other and do not interact. Hence, the variance σ_i^2 is different for every measurement and is summed in the matrix of the weights \mathbf{R} [5].

A. Weighed-Least-Squares (WLS) approach

The most common way to solve the SE problem is the iterative WLS approach with the aim to minimize the weighted sum of the squared measurement error [5]:

$$\min J(\mathbf{x}) = (\mathbf{z} - \mathbf{h}(\mathbf{x}))^T \cdot \mathbf{R}^{-1} \cdot (\mathbf{z} - \mathbf{h}(\mathbf{x})). \quad (4)$$

The condition for optimal results of first order $\mathbf{g}(\mathbf{x}) = \partial J(\mathbf{x}) / \partial \mathbf{x} \stackrel{!}{=} 0$ leads with linearizing of the network equations and the TAYLOR expansion to [5]:

$$\mathbf{G}(\mathbf{x}^k) = \frac{\partial \mathbf{g}(\mathbf{x}^k)}{\partial \mathbf{x}} = \mathbf{H}^T(\mathbf{x}^k) \cdot \mathbf{R}^{-1} \cdot \mathbf{H}(\mathbf{x}^k). \quad (5)$$

The variable \mathbf{x}^k refers to the value of the state variable at the k th iteration and $\mathbf{H}(\mathbf{x}^k) = \partial \mathbf{h}(\mathbf{x}) / \partial \mathbf{x}$ is the Jacobian of the network equations in $\mathbf{h}(\mathbf{x})$. The matrix $\mathbf{G}(\mathbf{x}^k)$ is known as the gain-matrix and is characterized as a sparse, square, symmetric and positive definite matrix for an observable system [5]. At the k th iteration the state variable \mathbf{x}^k is solved with the WLS approach:

$$\mathbf{G}(\mathbf{x}^k) \cdot \Delta \mathbf{x}^k = \mathbf{H}^T(\mathbf{x}^k) \cdot \mathbf{R} \cdot [\mathbf{z} - \mathbf{h}(\mathbf{x}^k)], \quad (6)$$

$$\Delta \mathbf{x}^k = \mathbf{x}^{k+1} - \mathbf{x}^k. \quad (7)$$

For solving the SE, the convergence criterion is defined as

$$|\mathbf{x}^{k+1} - \mathbf{x}^k| < \varepsilon_x \quad (8)$$

and is set to the begin of the iterative WLS approach.

B. Hachtel's-augmented matrix approach

Large gain-matrices for systems with many bus numbers tend the whole SE problem to become an ill-conditioning problem. The condition of a matrix is defined as the increase of an erroneous input data to the output, i.e. the static state variable for SE [5][7][8]. A measurable factor for any matrix \mathbf{A} is the condition number κ :

$$\underbrace{\text{cond}(\mathbf{A})}_{\kappa} := \|\mathbf{A}\| \cdot \|\mathbf{A}^{-1}\|. \quad (9)$$

An ill-conditioned matrix leads to κ approaching infinity; whereas for a well-conditioned problem the condition number κ is unity or close to one. One reason that a gain-matrix becomes ill-conditioned may be that the weights of the measurement are high, e.g. with virtual measurements. [5][7][8]

Solving the problem of the high weights Hachtel's augmented matrix approach is suited as an alternative for the SE. The virtual measurements with the high weights are treated as constraints. The optimizing problem of the WLS approach in (4) changes to:

$$\begin{aligned} & \text{minimize} && J(\mathbf{x}) = \mathbf{r}^T \cdot \mathbf{R}^{-1} \cdot \mathbf{r}, \\ & \text{subject to} && \mathbf{c}(\mathbf{x}) = 0, \\ & && \mathbf{r} - \mathbf{z} + \mathbf{h}(\mathbf{x}) = 0. \end{aligned} \quad (10)$$

The residual variable is set as $\mathbf{r} = \Delta \mathbf{z} - \mathbf{H} \cdot \Delta \mathbf{x}$ and defines the deviation between the different measurements and the net equations, where $\Delta \mathbf{z} = \mathbf{z} - \mathbf{h}(\mathbf{x})$ [5]. Solving the optimizing problem in (10) with the use of the Lagrange multipliers the optimization $\mathcal{L} = J(\mathbf{x}) - \boldsymbol{\lambda}^T \cdot \mathbf{c}(\mathbf{x}) - \boldsymbol{\mu}^T \cdot (\mathbf{r} - \mathbf{z} + \mathbf{h}(\mathbf{x}))$ leads to:

$$\begin{aligned}
\frac{\partial \mathcal{L}(\mathbf{x})}{\partial \mathbf{x}} = 0 &\Rightarrow \mathbf{C}^T \cdot \boldsymbol{\lambda} + \mathbf{H}^T \cdot \boldsymbol{\mu} = 0, \\
\frac{\partial \mathcal{L}(\mathbf{x})}{\partial \boldsymbol{\lambda}} = 0 &\Rightarrow \mathbf{c}(\mathbf{x}) = 0, \\
\frac{\partial \mathcal{L}(\mathbf{x})}{\partial \mathbf{r}} = 0 &\Rightarrow \mathbf{R}^{-1} \cdot \mathbf{r} - \boldsymbol{\mu} = 0, \\
\frac{\partial \mathcal{L}(\mathbf{x})}{\partial \boldsymbol{\mu}} = 0 &\Rightarrow \mathbf{r} - \mathbf{z} + \mathbf{h}(\mathbf{x}) = 0.
\end{aligned} \tag{11}$$

The Jacobian for the virtual measurements is defined as $\mathbf{C} = \partial \mathbf{c}(\mathbf{x}) / \partial \mathbf{x}$; whereas $\mathbf{H} = \partial \mathbf{h}(\mathbf{x}) / \partial \mathbf{x}$ is the Jacobian for the pseudo- and real measurements. Linearizing (11) the following linear system of equations is obtained [5]:

$$\begin{bmatrix} \mathbf{R} & \mathbf{H} & 0 \\ \mathbf{H}^T & 0 & \mathbf{C}^T \\ 0 & \mathbf{C} & 0 \end{bmatrix} \cdot \begin{bmatrix} \boldsymbol{\mu} \\ \Delta \mathbf{x} \\ \boldsymbol{\lambda} \end{bmatrix} = \begin{bmatrix} \Delta \mathbf{z}^k \\ 0 \\ -\mathbf{c}(\mathbf{x}^k) \end{bmatrix}. \tag{12}$$

A variable factor α presents the opportunity to improve the condition of the problem and changes (12) to the following equation system:

$$\underbrace{\begin{bmatrix} \alpha^{-1} \mathbf{R} & \mathbf{H} & 0 \\ \mathbf{H}^T & 0 & \mathbf{C}^T \\ 0 & \mathbf{C} & 0 \end{bmatrix}}_{\mathbf{K}} \cdot \begin{bmatrix} \boldsymbol{\mu}_s \\ \Delta \mathbf{x} \\ \boldsymbol{\lambda}_s \end{bmatrix} = \begin{bmatrix} \Delta \mathbf{z}^k \\ 0 \\ -\mathbf{c}(\mathbf{x}^k) \end{bmatrix}. \tag{13}$$

The left-hand coefficient matrix is known as the Hachtel matrix \mathbf{K} and is symmetric [5]. Depending on the number of measurements, the dimension of the Hachtel matrix \mathbf{K} is increasing or decreasing. Both Lagrange multipliers $\boldsymbol{\mu}_s$ and $\boldsymbol{\lambda}_s$ are scaled compared to (12), due to the factor α . If the factor α is set as $\alpha = 1$ the condition number κ of the matrix \mathbf{K} can become higher than for gain-matrix of the NE [10].

The convergence criterion for the Hachtel's augmented matrix approach is set to that of the WLS approach in (7) before the start of the iterative approach.

III. IMPLEMENTATION AND SIMULATION SCENARIOS

To compare the Hachtel's augmented matrix approach with the conventional WLS approach for DSSE several simulation scenarios are investigated. Besides the implementation of both approaches the following section describes the simulation scenarios and the evaluation criteria.

A. Implementation

Based on an existing test environment in MATLAB for the WLS approach the Hachtel's augmented matrix approach is implemented and adjusted [12]. We distinguish the different measurement categories using the measurement vector, the Jacobian for the net equations $h_i(\mathbf{x})$ using the Hachtel's augmented matrix approach contains the real and pseudo-measurements; whereas the virtual measurements are included in the Jacobian \mathbf{C} . Therefore, the weighting matrix \mathbf{R} is reduced compared to the weighting matrix \mathbf{R} to the WLS approach. Another difference is the variable factor α for the Hachtel's augmented matrix approach. The used weights in this paper are shown in Table I. Further distinctions regarding the accuracy of the real measurements are neglected in this paper. The used convergence criterion is set to $\varepsilon_x = 1 \cdot 10^{-6}$ for both

approaches with a maximum iteration count $k_{max} = 100$. Furthermore, this paper uses the flat start in accordance to [5].

TABLE I. WEIGHTS OF MEASUREMENT CATEGORIES

Variance	Real measurement	Pseudo-Measurement	Virtual measurement
σ_i^2	40,000	10,000	20,000 ^a

a. Only for the WLS approach

Assumed measurements for this paper are real time measurements of the voltage magnitude V_i at the reference bus and the power flow measurements P_{ij} and Q_{ij} to the surrounding busses. At every known zero-injection, the power balance measurement is assumed as a virtual measurement. Completing the three categories, pseudo measurements are set in this paper to power balance measurements P_i at every bus in the distribution test system.

B. Simulation scenarios

For the comparative simulations this paper uses the 15 nodes medium voltage (MV) European benchmark network from CIGRÉ [13]. System parameter are chosen as given in the technical elaboration from CIGRÉ. Hence, the basic scenario has two radial feeders. The frequency is 50 Hz with a nominal voltage of 20 kV. Another characteristic of the power system is the $R/X > 1$ ratio for all power lines except for the power line between the reference bus and the transformer to the MV system. The reference bus is connected to a fixed 110 kV network.

The total amount of feed-ins and loads is summed up as given in (14) and (15). Besides the apparent power of the MV network, both sums include the apparent power of the subordinate low voltage network. In the basic scenario they are scaled with respect to the feed-ins with $S_{feed-in} = 3.11$ MVA and for the loads with $S_{load} = 46.61$ MVA. Without further scaling the basic scenario is modelled as a load case. This constitutes a characteristic of a distribution system with a few decentralized feed-ins.

$$S_{feed-in} = S_{feed-in}^{MV} + S_{feed-in}^{LV} \tag{14}$$

$$S_{load} = S_{load}^{MV} + S_{load}^{LV} \tag{15}$$

As mentioned before the focus of this paper is to compare the two different approaches for the SE with various system parameters of the same distribution system.

- The first adjustment to the basic scenario is that the power injections at the busses are scaled with $s_{C_{feed-in}}$ in 10%-steps from 40% up to 100%. Independent from the voltage level in which the power injections are connected the feed-ins are observed: the total amount of $S_{feed-in}$ is scaled.
- Distribution systems nowadays are characterized by many decentralized feed-ins. Hence, the impact of feed-in or load overweight to the SE solution is part of this paper. Whereas the basic scenario is scaled as a load situation, a feed-in situation is generated with $S_{feed-in} > S_{load}$. As the feed-ins are in the load

situation already at the operating limits, the scaling for the loads is $sc_{load} = 5\%$. The values for both situations are shown in Table II.

TABLE II. SIMULATION SCENARIOS

	Feeder Situation	Load Situation
$S_{feed-in}$	3.11 MVA	3.11 MVA
S_{load}	2.33 MVA	46.61 MVA

C. Three criteria to compare

Evaluating the results of the SE a comparative criterion is needed. To distinguish the deviation of the estimated static state more accurate, the state variables are observed separately in voltage magnitude V and voltage angle θ . At this stage the exact static state is known in the variables V_{exact} and θ_{exact} . Hence, the first criterion is the average deviation β over all busses n :

$$\beta_V = \left| \frac{V_{exact} - V_{SE}}{V_{exact}} \cdot 100 \cdot \frac{1}{n} \right|, \quad (16)$$

$$\beta_\theta = \left| \frac{\theta_{exact} - \theta_{SE}}{\theta_{exact}} \cdot 100 \cdot \frac{1}{n} \right|, \quad (17)$$

where V_{SE} is the estimated voltage magnitude and θ_{SE} the estimated voltage angle. The elapsed time t in s observes the performance of the SE approaches for the iterations step to solve the SE problem.

Another criterion in order to compare both SE approaches is the condition number κ as mentioned in (9). Depending on the approach, the observed matrix is the gain matrix \mathbf{G} as in (5) or the Hachtel matrix \mathbf{K} as in (13). The last criterion used in this paper is the maximum deviation b from the estimated static state to the exactly known static state. Like in (16) and (17), the observed maximum deviation is separated in voltage magnitude V and angle θ :

$$b_V = \left| \max \frac{V_{exact} - V_{SE}}{V_{exact}} \right|, \quad (18)$$

$$b_\theta = \left| \max \frac{\theta_{exact} - \theta_{SE}}{\theta_{exact}} \right|. \quad (19)$$

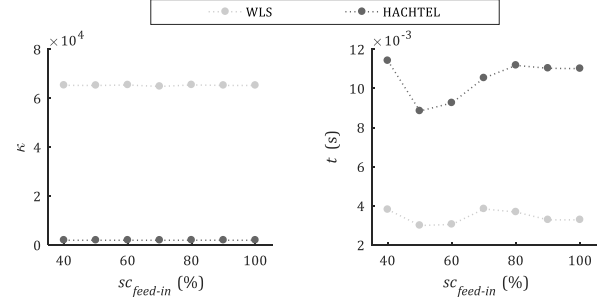
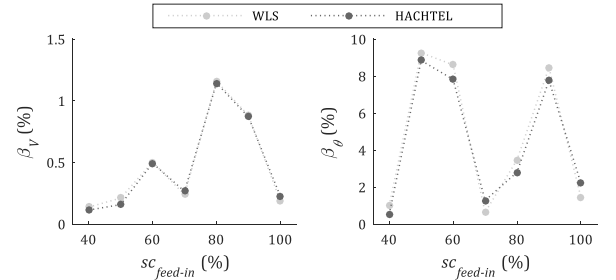
IV. RESULTS AND DISCUSSION

A. Results with the scaling factor $sc_{feed-in}$

As mentioned before the power injections of decentralized feeders can vary in medium and low voltage networks, e.g. due to different weather conditions. The criteria of the condition number κ and the elapsed time t shown in Fig. 1 are influenced by different scaling factors $sc_{feed-in}$. The grey lines present the SE using the WLS approach while the green line shows the results of the Hachtel's augmented matrix approach. The color allocation with grey for the WLS approach and green for the Hachtel's augmented matrix approach are equally defined in the whole paper.

Almost independent of the scaling factor $sc_{feed-in}$ the condition numbers κ for both approaches are constant with respect to Fig. 1. Nevertheless, the condition number κ of the Hachtel matrix \mathbf{K} is lower in every simulation than to the condition number κ of the gain matrix \mathbf{G} . The condition number

κ of the Hachtel matrix \mathbf{K} is around $\kappa \approx 1,900$. As the condition number κ , the elapsed time t does not react to a change of the scaling factor $sc_{feed-in}$. Even if the WLS approach is the faster SE approach, due to the small distribution system with 15 nodes, the aspect of speed performance is negligible.

Figure 1. Impact of scaling factor $sc_{feed-in}$ on the condition number κ and the elapsed time t Figure 2. Impact of scaling factor $sc_{feed-in}$ on the average deviation β in voltage magnitude V and voltage angle θ

Evaluating the same simulations with the criteria of the mean deviation β in voltage magnitude V and voltage angle θ the results in Fig. 2 show that the accuracy performance of both approaches is almost similar. Furthermore, the higher deviation β_θ may be explained by the high R/X ratio nature in distribution systems with very small voltage angle differences. Hence, a small absolute deviation might be already a high percentage deviation.

Summarizing the results of the first simulations, it shows that the scaling factors $sc_{feed-in}$ do not influence the condition number κ or the elapsed time t significantly. The accuracy of both approaches is almost similar under the aspect of the scaling factors $sc_{feed-in}$. However, the condition number κ as a criterion of identifying the condition of a SE problem, shows that the Hachtel's augmented matrix approach is more stable than the WLS approach.

The evaluation of the condition number κ and the elapsed time t confirm previous studies of the authors of [5] and [10]. Hence, the further simulations evaluate the performance of both SE approaches with the criteria of the deviation.

B. Results of the changing feed-in/load situation of the distribution system

Further comparisons of the SE approaches assume different feed-in and load situations of the distribution test system. The idea to perform such a comparison stems from the development of many distribution systems nowadays which produce more power with the decentralized feed-ins than consumed. Hence, the traditional top-down power flows might change in several situations to bidirectional power flows. The system parameters for the distribution test system are described in Section III.

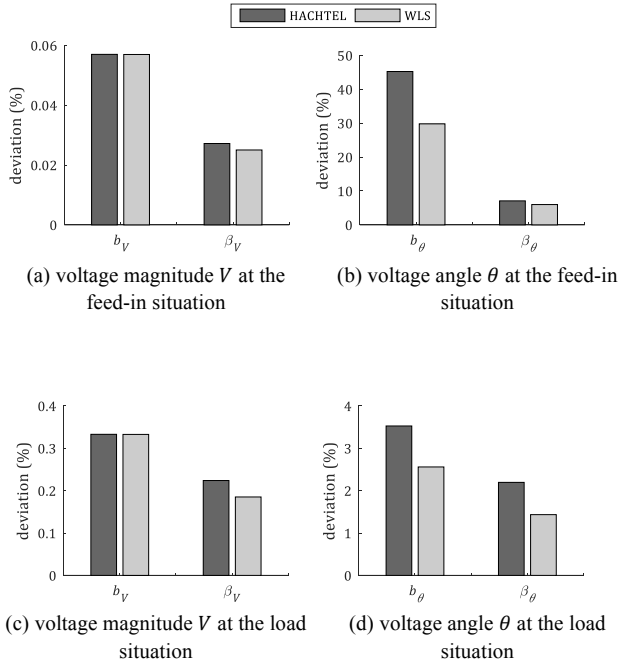


Figure 3. Maximum deviation b and average deviation β

In Fig. 3 the comparison of both situations is shown. While the maximum deviation b_V is almost similar in both situations, the criterion of the average deviation β_V leads to a better result in the case of the WLS approach. Furthermore, the results of the estimated voltage magnitude V presents again better results compared to the results of the voltage angle θ . The cause might be the same as before: the small voltage angle differences in distribution systems combined with a high R/X ratio. Hence, the relevance of the voltage angle θ at distribution systems is different compared to the voltage angle θ in transmission systems where the real power flow depends more of the voltage angle θ .

Comparing independently the results for the voltage magnitude V with respect to Fig. 3 (a) and Fig. 3 (b) it shows that both SE approaches lead to produce more accurate results in the feed-in situation. Even the maximum deviation is with respect to Fig. 3 (a) $b_V < 0.06$. Furthermore, the accuracy of the WLS approach produces in both situations a more accurate average deviation β_V . Nevertheless, the results for the voltage

magnitude V are in both situations with both SE approaches at the point of the maximum deviation $b_V < 1\%$.

V. CONCLUSION

A comparison of the conventional WLS approach with the Hachtel's augmented matrix approach has been presented. Besides the mathematical formulations the focus on this paper are further simulations in a MATLAB test environment. Especially the changing characteristic of distribution systems towards more and more decentralized feed-ins and their impact to the solution of the SE are simulated and discussed.

Comparing this paper with others the simulation to the changing feed-in or load situation are one new contribution for the DSSE with the use of the Hachtel's augmented matrix approach. Hence, further studies with real test networks are necessary to expand the evaluation of the Hachtel's augmented matrix approach for the DSSE. Another field of study might be to evaluate optimal measurement placement algorithm for DSSE with the Hachtel's augmented matrix approach.

REFERENCES

- [1] F. C. Schweppe and J. Wildes, "Power System Static-State Estimation, Part I: Exact Model", *Power Apparatus and Systems, IEEE Transactions on*, no. 1, pp. 120-125, 1970.
- [2] F. C. Schweppe and D. B. Rom, "Power System Static-State Estimation, Part II: Approximate Model", *Power Apparatus and Systems, IEEE Transactions on*, no. 1, pp. 125-130, 1970.
- [3] F. C. Schweppe, "Power System Static-State Estimation Part III: Implementation", *Power Apparatus and Systems, IEEE Transactions on*, no. 1, pp. 130-135, 1970.
- [4] E. Handschin, *Elektrische Energieübertragungssysteme*, 2nd ed. Heidelberg: Hüthig, 1992.
- [5] A. Abur and A. G. Exposito, *Power System State Estimation Theory and Implementation (Power Engineering (Willis))*, 1st ed. CRC Press, 2004.
- [6] I. S. Duff and J. K. Reid, "A comparison of some methods for the solution of sparse overdetermined systems of linear equations", *IMA J Appl Math on*, vol. 17, pp. 267-280, 1976.
- [7] A. Gjelsvik, S. Aam and L. Holten, "Hachtel's augmented matrix method – a rapid method improving numerical stability in Power System State Estimation", *Power Apparatus and Systems, IEEE Transactions on*, vol. PAS-104, pp. 2987-2993, 1985.
- [8] L. Holten, A. Gjelsvik, S. Aam, F. F. Wu and W. H. E. Liu, "Comparison of different methods for state estimation", *Power Systems, IEEE Transactions on*, vol. 3, pp. 1798-1806, 1988.
- [9] W.-M. Lin and J.-H. Teng, "State Estimation for distribution systems with zero-injection constraints", *Power Systems, IEEE Transactions on*, vol. 11, pp. 518-524, 1996.
- [10] N. Nussrat, "Development of novel electrical power distribution system state estimation and meter placement algorithms suitable for parallel processing", *Brunel University London, Brunel Institute of Power Systems (BIBS), Dissertation*, 2015.
- [11] D. Waersch, R. Brandalik, W. H. Wellssow, J. Jordan, R. Bischler, N. Schneider, "Bad data processing for low voltage state estimation systems based on smart meter data", *CIGRE Workshop 2016, Helsinki in Finland*, 2016.
- [12] A. Brüggemann, K. Görner, C. Rehtanz, "Evaluation of extended Kalman filter and particle filter approaches for quasi-dynamic distribution system state estimation", *24th International Conference & Exhibition on Electricity Distribution (CIRED) 12-15 June 2017*, 2017.
- [13] CIGRÉ Task Force C6.04, "Benchmark systems for network integration of renewable and distributed energy sources", *Technical Brochure 575, CIGRÉ*, 2014.

Impact Analysis of Decentralized Energy Devices Participating in Load Frequency Control

X.Song, Y.Zeng, H.Cai, T. Jiang, S. Schlegel and D. Westermann

Power Systems Group
Technische Universität Ilmenau
Ilmenau, Germany

Abstract— Load frequency control is an essential ancillary service to balance the generations and demands of active power. However, due to declining profitability and new climate policy in recent years, increasing number of planned conventional power plants face shutdowns and consequently, transmission system operator (TSO) risk the loss of controllable power generation required for load frequency control. Controllable power from the distribution system operator (DSO) levels with decentralized energy devices can provide TSOs a new concept to maintain the necessary control reserve. This paper demonstrates the impact of decentralized energy devices participating in load frequency control under different system restrictions.

Index Terms—mid-term model; load frequency control; electric vehicles

I. INTRODUCTION

The responsibilities of system operation can be divided into four main categories and include the transmission system operators (TSO) and distribution system operators (DSO). However, some responsibilities are limited exclusively to the TSO (characterized by *) as their coordinating authority:

- monitoring and switching operation
- voltage stability*
- system security*
- system balance*

To meet the last three tasks, the TSO makes use of ancillary services, which are historically provided by large-scale fossil-fuel based power plants. Among these services, load frequency control (LFC) is used to maintain the active power balance for system frequency stability. With the aim to reduce CO₂-emissions and the sustainability of power generation, the number of renewable energy generation units is rising steadily. Consequently, more and more conventional power plants are becoming uneconomical or do not meet the limits imposed by the climate policy, which results in planned shutdowns [4]. This loss of controllable power generation requires new concepts, especially for the provision of ancillary services like balancing power. So far, this balancing power is provided by easily manageable conventional and pumped storage power plants. The challenge is to compensate the loss of such controllable power especially in times when the need for ancillary services like load frequency control is rising due to increased deployment of volatile renewable energy sources. Besides

remaining power plants, new actors like electric vehicle (EV) fleets, storage systems or other controllable decentralized energy devices (DED) could be used for ancillary services provision. The operational challenge comes from their decentralized nature, predominantly in the distribution system operator's (DSO) area of responsibility (shown in the figure. 1). Thereby, there is a need for detailed communication between TSO–DSO and pool operator–DSO.

Keeping in perspective the announced one million EVs till 2020 and six million EVs by 2030 by the German Federal Government, this paper investigates the impact on the system of decentralized energy devices participating in LFC, described exemplarily for electric vehicles. Section II of the paper introduces the background and structure of the LFC and shows the overview of the approach. Section II is developed to describe the simulation model of the DED and the electrical power system. This is then parameterized and validated based on real measurement data. Afterward in section IV, key performance indicators are derived and defined. Based on numerical case studies, a sensitivity analysis is performed and the results are discussed regarding the control performance and impact in section V.

II. ANALYSIS APPROACH

Load frequency is jointly controlled in the European synchronous area by the member TSOs of the Union for the Coordination of Transmission of Electricity (UCTE). The process of load frequency control in the synchronous areas is divided into quotation phase and online allocation phase. This approach has to be applicable for both phases, while a strong communication is suggested. Unlike conventional balancing power providers, the DED are deployed mainly in the distribution grid at the medium and low voltage level. The available capacity is coordinated between DSO and pool management system through a constant communication. Figure 1 describes the signal flows of this approach.

Initially, the transmission system operators put their balancing power demands for the following weeks on a market platform as shown by *quotation process 1* (figure 1) based on the forecast. After reaching an agreement of maximum permissible capacity with their responsible DSO, all qualified DED operators and pool operators apply for their planned

*This work is funded by the German Federal Ministry for the Environment, Nature Conservation and Nuclear Safety (“Gesteuertes Laden V3.0: Netzintegration von Elektro-Mobilität auf dem Weg zu ersten kommerziellen Lösungen” - “Smart Charge V3.0: Grid integration of electric mobility on the way to the first commercial solutions”)

provision of control reserve as shown in as *quotation process 2* (figure 1).

After the registration period expires, the DSO processes data and calculates an optimal power flow (OPF). The algorithm determines the maximum permissible operating point for each DED based on the DEDs' input information, generation and load forecasts (\underline{Q}). The derived restrictions are defined as grid operation limits (GOL), which must always be fulfilled (see figure 2). Then, every operator receives a time series for the next week of permissible operation points in 15-minute intervals as shown by *quotation process 3* (figure 1). Consequently, in the entire time horizon, the limitation of the objectives has to be considered; the approach of providing balancing power has to be constrained in the range of any technical restrictions of the distribution grid as well as the operating limits of the DED. In any case, the provision of balancing power should not violate the grid restriction (standardized for Europe by EN50160) or result in critical grid situations.

Afterwards, the pool operators determine their offer including the price as well as capacity, taking into account the input information on the permissible operation point of the DEDs by the DSO and submit this to the market platform (shown in figure 1 as *quotation process 4*).

At the end of the quotation process, each TSO determines a Merit-Order-List based on the price and accepts the cheapest offers to fulfill their published demand (shown in figure 1 as *quotation process 6*). After that, all bidders get a notification of acceptance published on the market platform (shown in figure 1 as *quotation process 7*). In the last step, all operators with

During this continuous process, it has to be checked whether any grid GOL is violated due to the inaccuracy of the forecast or unexpected load changes. In such circumstance, the DSO has to restore normal conditions, e.g. by using grid actions or

reducing the REGUs' infeed considering the general generation situation, type and location of the violation.

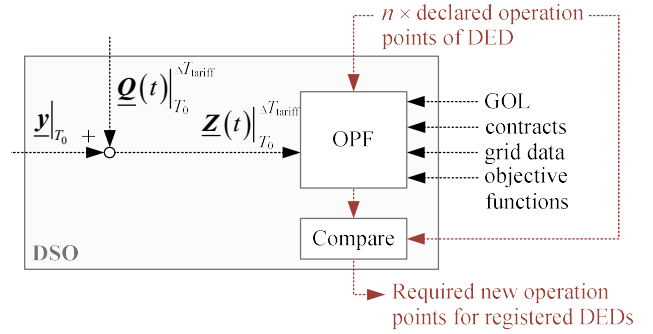


Figure 2: Recalculation process

The OPF reduces the absolute of each operation point X of the concerning DEDs (sketched in equation 1).

$$X_{\text{new}} = \frac{X_{\text{old}}}{|X_{\text{old}}|} \cdot \left| |X_{\text{old}}| - \Delta \right|, \Delta \in R^+ \quad (1)$$

In case of a GOL violation in the allocation process, the declared DEDs' operating points for the specific time steps have to be recalculated (sketched in figure 2). The input variables refer to actual system state (\underline{y}), the generation and load forecasts (\underline{Q}) and additional objectives like weighing functions of the DEDs' operation points of the remaining period (T_0 till ΔT_{tariff}). Afterwards, the new and "old" declared operation points are compared, and a list of the modified operation points for each DED is created, and all are sent to the responsible operators.

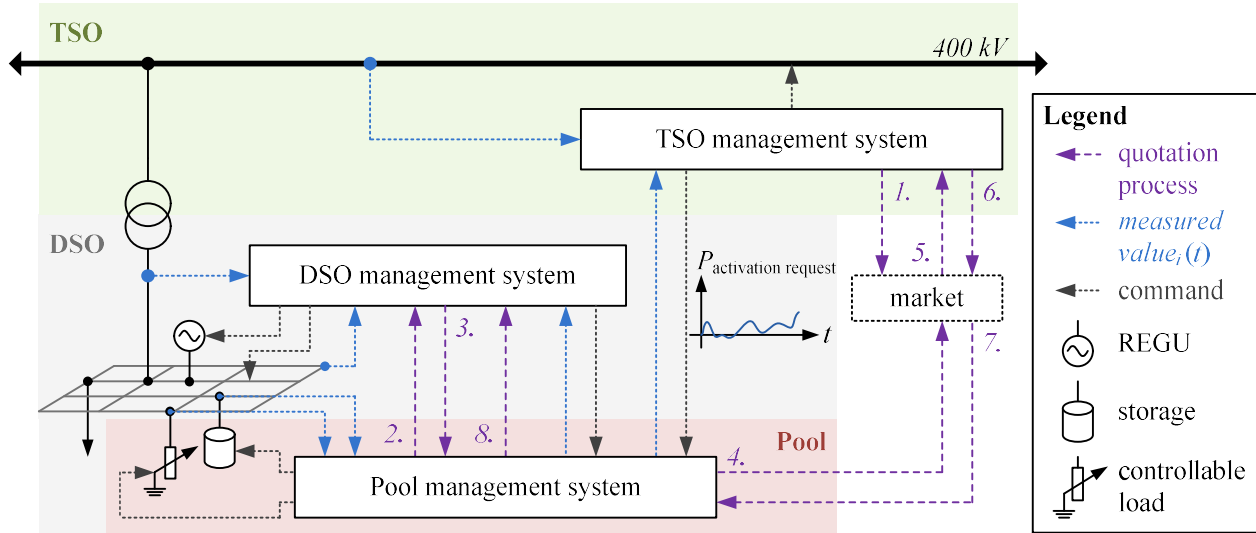


Figure 1: Sketch of the proposed approach signal flows

III. SIMULATION MODEL

To design a simulation model for load frequency control analysis, firstly, the general requirement of the process for this model has to be defined. For this reason and regarding the validation respectively, the simulation system of the whole control process is described in the following paragraphs.

The main purpose of primary control is to limit the frequency deviation. Consequently, to act as fast as possible, the primary control governor (PC Gov.) is set locally at the power plant and operates directly on the steam valve. Thus, governor of primary control is characterized as a proportional controller. Its gain V'_r represents the power plant's speed droop characteristic. Thus, the transfer function of the primary control reserve results as sketched in figure 3. The parameter T_s describes the mechanical dynamics of the valve and is in the range of 0.1-0.3s. The dynamic of the turbine depending on its type and size is represented by T_T in a range of 2.5-5.5 s.

According to the frequency deviation, the primary (local) and secondary control (central) determines the reference values for the generation units. The principle system is visualized in figure 2.

To control the frequency deviation, the TSO makes use of the secondary control reserve. To restore f_0 , the governor of the secondary controller is characterized as a gain K_i combined with an integrator. With the consideration of the boiler's dynamic represented by K_B , the following transfer function can be derived.

$$\Delta P'_{ref\ sec} = K_B \cdot K_i \int \Delta f'(t) dt \quad (2)$$

Regarding the equation of motion [5] the change of frequency reflects the mismatch of electrical power and mechanical power.

$$\ddot{\delta} = \frac{\omega_0}{2H} \cdot (\overline{T}_m - \overline{T}_e - K_D \Delta \overline{\omega}_r) \quad (3)$$

Hence, for area n with j rotational load and i generators the equation has to be adapted by the moment of inertia of generator J_{gi} in area and the moment of inertia of load J_{lj} in the area n (shown in equation 7).

$$T_{inr}(n) = \frac{4\pi^2 f_0^2 (\sum J_{gi} + \sum J_{lj})}{P_\Sigma} \quad (4)$$

The load response to frequency deviation is expressed by V'_L . Thus, the transfer function of the grid can be described as in equation 8.

$$G_{grid} = \frac{1}{1 + \frac{1}{sT_{inr}} \cdot V'_L} = \frac{1}{sT_{inr} + V'_L} = \frac{1}{1 + \frac{sT_{inr}}{V'_L}} = \frac{K'_L}{sT_{grid} + 1} \quad (5)$$

The nominal frequency f_0 of system operation for the European synchronous area is 50Hz. Primary control activation is triggered if the frequency deviation exceeds ± 20 mHz. Based

on the reference disturbance of UCTE Operation Handbook, where 3000MW of primary balancing power reserves has to be fully activated at the maximal permissible quasi-steady-state frequency deviation ± 200 mHz [8]. V'_r can be calculated with equation 2 [5]. The gain of the governor is normalized to the nominal capacity of the control area P_0 and f_0 .

Figure 4 shows the resulting structure of the power plant with the described controller. The upper half is the primary control loop while the lower half is the secondary control loop. Both signals are summed and form the normalized reference value of turbine.

Here, the system inertia is defined with:

$$T_{inr} = \frac{4J\pi^2 f_0^2}{P_0} \quad (6)$$

The reference value is sent from the secondary controller of the TSO to the DEDs (sketched in figure 5). Hence, the model has also to consider the communication link.

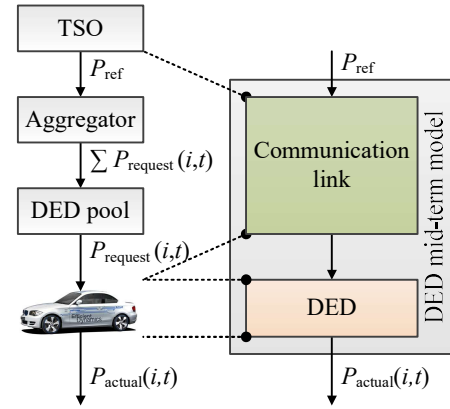


Figure 3: The signal flow of the DED pool

The authors propose a mid-term model based on two elements. A time delay represents the whole communication link between TSO and DED and linear time-invariant system (Pt1) element simulate the charging dynamic.

$$G_{DED}(s) = G_{kom}(s) * G_{DED}(s) = e^{-sT_D} * \frac{K_{DED}}{1 + T_{DED} \cdot s} \quad (7)$$

The parameters K_{DED} and T_{DED} which describe the dynamic of the charging process are estimated based on the samples of step response using the method of least squares. Table 1 shows the value of K_{DED} , T_{DED} and T_D as well as their dispersion. The gain is smaller than 1. This is attributed to the voltage drop caused by charging process. In contrast to K_{DED} , and T_D , the time constant T_{EV} has a larger standard deviation because the most of its measured values are located between 0.7 and 1.05.

TABLE I. PARAMETER DEFINITION

	K_{DED}	T_{DED}	T_D
arithmetic mean μ	0.9458	0.8940	8.0810
standard deviation σ	0.0656	0.5117	0.3745

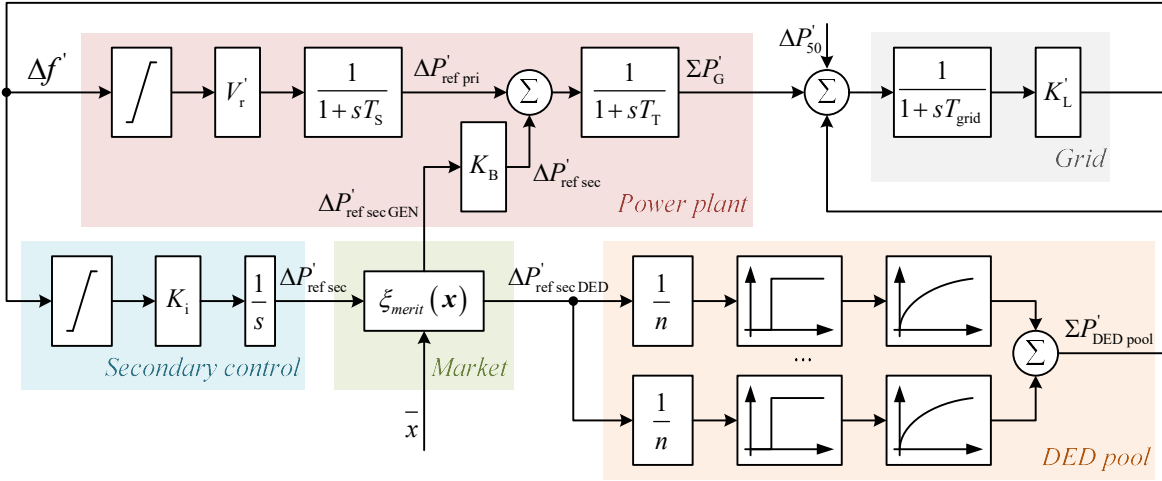


Figure 4: Sketch of the proposed approach signal flows

IV. SIMULATION RESULTS

This chapter focuses on the system performance of this new concept based on the UCTE reference disturbance cases. Therefore, the key performance indicators are described first. Afterwards, numerical case studies are analyzed by simulation.

A. Key Performance Indicators

- Maximum frequency deviation $|\Delta f'_{\max}|$

This indicator describes the maximum frequency deviation, which is caused in the control area by a positive or negative change of load or power generation. It is dependent on the inertia of the control zone, which is determined physically by the number and the mass of the synchronizing flywheels.

- Total frequency disturbance TFD

$$\text{TFD} = \int_{T_1}^{T_2} |f(t)| dt \quad (8)$$

In addition to the maximum frequency disturbance, the sum of the disturbance over the disturbance clearing time T_1 (begin of the disturbance) to T_2 (system frequency back to tolerance band) is also essential. This ratio is a measure of the speed of the control devices in response to the deviation with regard for the influence of the disturbance. The smaller the sum of the frequency deviation, the faster the control unit consequently responds, and the less the system suffers from the frequency disturbance.

- Total Balancing energy

$$E_{\text{sum}} = \int_{T_1}^{T_2} (p_{\text{pri}} + p_{\text{sec}}) dt \quad (9)$$

Total balancing energy is defined as the sum of activated primary and secondary control power between time T_1 and T_2 .

It indicates the total energy required to cover the unexpected change of load or power generation. It is consequently also an indicator of the financial cost.

B. Numerical Case Studies

In the following section, a generation deficit of 3 GW from the ENTSO-E reference case is investigated. Figure 11 shows the development of system frequency as well as the primary and secondary balancing power after a 3GW disturbance [8].

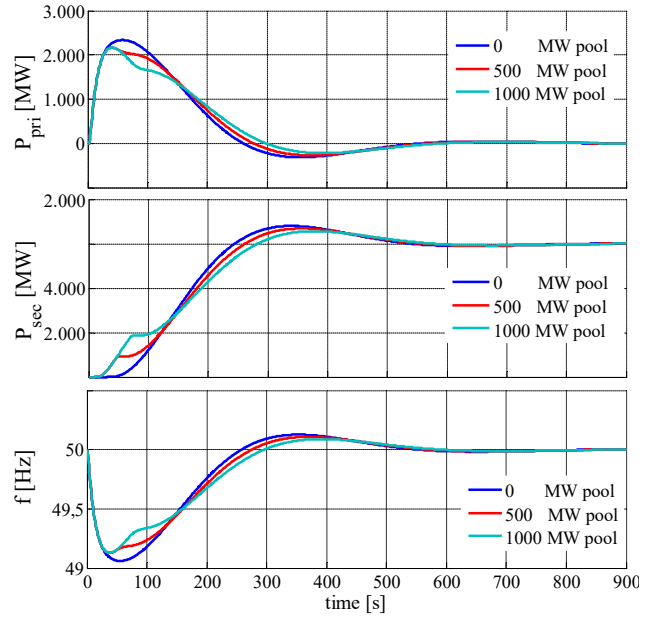


Figure 5. Balancing power provision in control area 1

The primary balancing power is activated immediately after detection of a frequency deviation. Meanwhile, the secondary

control calculates the reference value of secondary balancing power. After the merit-order-list of the market, the DED pool and the power plant get the reference value of balancing power accordingly. After the system frequency returns into the tolerance band, the disturbance is under control, and the primary controller is switched off.

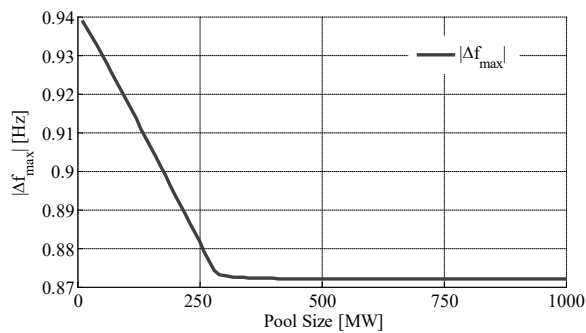


Figure 6: The signal flow of the DED

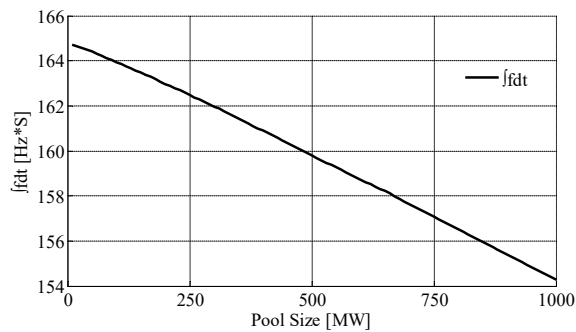


Figure 7. Total frequency disturbance

As mentioned in section III, the DED pool has better dynamic performance than conventional power plants. The DED pool acts much quicker to put its secondary balancing power into the power system, so that it not only reduces the maximum frequency deviation (shown in figure 6), but also reduces the demand of primary control power. Hence it could reduce the total frequency disturbance, which means, with DED as the provider of secondary control power, the power system suffers less frequency deviation during the disturbance. This phenomenon increases with the size of the pool. Certainly, these effects are also limited by technical restriction of the DED, as shown in Figure 6, due to the delay of the communication link, the reduction of the maximum frequency deviation reaches saturation with pool size of 270 MW.

V. CONCLUSION

Faced with new challenges, the characteristics of electrical power systems are subjected to significant changes. While the number of renewable energy generation units steadily increases, more and more conventional power plants are planned to be shut down. As a result, there is a loss of controllable power generation. Nevertheless, the transmission system operator (TSO) has to ensure system stability, which requires adequate control reserve. Pooling of DEDs is an alternative concept, which can provide TSOs the necessary reserve to maintain the control power. With the excellent dynamic performance shown

by the measurements during the field test, the DED pool is a proper supplement to conventional power plants by providing secondary control power, as well as partial primary control power. The simulation shows that the DED pool could reduce the total frequency deviation as well as the maximum frequency deviation due to a system disturbance, and hence provide a better system performance.

REFERENCES

- [1] Data for control reserve. regelleistung.net, [Online]. Available: <https://www.regelleistung.net/ip/action/abrufwert?language=en>
- [2] European Commission, *A policy framework for climate and energy in the period from 2020 to 2030*, 2014
- [3] *Energy Concept – for an Environmentally Sound, Reliable and Affordable Energy Supply*, Federal Ministry for the Environment, Nature Conservation and Nuclear Safety, 2010
- [4] List of power plant closure notifications. Bundesnetzagentur, [Online]. Available: http://www.bundesnetzagentur.de/cln_1431/EN/Areas/Energy/Companies/SpecialTopics/List_of_closure_notifications/List_of_closure_notifications_node.html
- [5] P. Kundur, *Power system stability and control*, vol I. NewYork McGraw-Hill, 1994.
- [6] Data for control reserve. regelleistung.net, [Online]. Available: <https://www.regelleistung.net/ip/action/abrufwert?language=en>
- [7] *National Electromobility Development Plan*, German Federal Government, 2009
- [8] German Federal Ministry of Economics and Technology, *Energy Industry Act (EnWG)*, Mar. 2011
- [9] *UCTE Operation Handbook Policy 1*, Mar. 2009
- [10] European Commission, *A policy framework for climate and energy in the period from 2020 to 2030*, 2014
- [11] *Energy Concept – for an Environmentally Sound, Reliable and Affordable Energy Supply*, Federal Ministry for the Environment, Nature Conservation and Nuclear Safety, 2010
- [12] List of power plant closure notifications. Bundesnetzagentur, [Online]. Available: http://www.bundesnetzagentur.de/EN/Areas/Energy/Companies/SpecialTopics/List_of_closure_notifications/List_of_closure_notifications_node.html
- [13] Data for control reserve. regelleistung.net, [Online]. Available: <https://www.regelleistung.net/ip/action/abrufwert?language=en>
- [14] R. Schwerdfeger, S. Schlegel, T. Jiang, D. Westermann *Approach for load frequency control participation by decentralized energy devices 2015 IEEE Power and Energy Society General Meeting*
- [15] *National Electromobility Development Plan*, German Federal Government, 2009
- [16] Y.G. Rebours, D.S. Kirschen, M. Trotignon and S. Rossignol, "A Survey of Frequency and Voltage Control Ancillary Services - Part I:
- [17] Y.G. Rebours, D.S. Kirschen, M. Trotignon and S. Rossignol, "A Survey of Frequency and Voltage Control Ancillary Services - Part II: Economic Features," *IEEE Trans. on Power Systems*, vol.22, no.1, pp.358,366, Feb. 2007
- [18] A.M. Pirbazari, "Ancillary services definitions, markets and practices in the world," in *Proc 2010 IEEE Power Engineering Society Transmission and Distribution Conf and Exposition: Latin America (T&D-LA)*, vol., no., pp.32,36
- [19] German Federal Ministry of Economics and Technology, *Energy Industry Act (EnWG)*, Mar. 2011
- [20] *TransmissionCode 2007*, VDN, Berlin, 2007
- [21] *Voltage characteristics of electricity supplied by public distribution networks*, DIN EN 50160, Feb. 2011

Application of a pseudo value generation tool for loads in low voltage state estimation

Patrick Gassler

Chair of Energy Systems and Energy Management
 Technical University Kaiserslautern
 Kaiserslautern, Germany

Abstract—The increasing number of volatile electrical energy generation and the increasing penetration of electric vehicles can result in operating limit violations in low voltage grids which stay mainly undetected due to the unknown state. This situation makes the network operation challenging. Supervision of these grids becomes therefore necessary. Different research activities showed that with an appropriate estimation algorithm and with enough measurements from smart meters the system state of low voltage grids can be determined sufficiently accurately. However, in Germany, the measuring of consumer-related data is prohibited by law, thus not enough measurements are available. To overcome this limitation, a tool has been developed which synthesizes realistic pseudo-values. With the application of these pseudo-values, it should be investigated if the estimation of the system state still provides usable results. The simulation results show that on average the errors are acceptable, but some high errors occur as well. Therefore, the application of this state estimation in the network control is possible, but with some limitations.

Linear state estimation; low voltage grids; distribution grids; pseudo measurements; smart meters; volatile energy feed-in;

I. INTRODUCTION

To stay in line with their CO₂ emission target values, the German government introduced in 2000 the “Erneuerbare Energien Gesetz” (EEG) translated: law of renewable energies, which lead to a considerable increase of electrical energy production from renewable sources [1]. An important part of this energy is produced from volatile power plants like wind turbines and photovoltaic (PV) plants. Especially PV installations feed their energy mainly in the low voltage (LV) grids [2]. This can lead in grids with a strong penetration of such systems to voltage magnitude over the operating limit (set by the norm DIN EN 50160) and could also lead to line overload.

Another important development in Germany in the near future is the increasing number of electric vehicles (EV). These vehicles draw their energy from the LV grids and therefore will represent a considerable increase of load.

In the original planning of LV grids, these new operating states could not be considered since the planning occurred long before the present changes of the power grid. Some of these LV grids needs to be extended to satisfy the current and future usage.

Also, because supervision of LV grids was in the past not necessary measurement and monitoring equipment were not installed. Due to the unknown state, operating limit violations stay undetected and operation and extension of LV grids is challenging. Therefore, supervision of those grids becomes indispensable but without measurements was until now not possible.

With the introduction of smart meter, measurements like voltage magnitudes and active or reactive power flows can be gained directly at the house buses of a LV grid. In Germany the smart meter rollout has already been settled within a law [3] and could make the estimation of a LV grid state possible. It was already showed in [4] that with those measurements and an appropriate linear SE algorithm, the state of a LV grid can be estimated sufficient accurately. However, in Germany the law prohibits the measurement and collection of consumer-related data for privacy reasons. Therefore, only voltage magnitudes can be measured. The power values are missing and must be replaced by pseudo data. For this reason, a tool has been developed which generates realistic pseudo values for the power consumption of households.

In this paper, the usability of the pseudo values generated from this tool for the SE is investigated. This was achieved with several computer simulations. These simulations were performed on a LV grid model and with a linear SE algorithm presented in [5]. In chapter II the theoretical background of the SE introduced. In chapter III the simulation environment is presented and also the process of generating pseudo values for power usage of households. In chapter IV the simulation results are evaluated. The paper is finally concluded with a summary in chapter V.

II. LINEAR STATE ESTIMATION

A. Reason for the state estimation

For many years state-of-the-art in transmission grids, the SE hasn’t been deployed until today in LV grids. In the past, the operation of LV grids was easily predictable and no supervision was needed. Therefore, no measurement and monitoring devices were installed in those grids. Additionally, due to the vast number of such grids the supervision would have been way to expensive. Today the situation as changed and smart meter could represent a cheap solution to gather measurements in a LV grid for the SE.

Generally, the SE has to achieve following tasks: reliable estimation of the state at all times, filtering out measurement noise from measurement devices and calculating non-measured values [6].

In a load flow calculation, the load buses are represented as PQ nodes as well as the generation buses like the PV systems which cannot be regarded as PV nodes, so the voltage magnitude measurements cannot be included in the calculation process. This is one of the reasons why the SE is chosen over the load flow calculation.

B. State estimation

Conventional state estimation is based on equation (1) where z is the vector of all measured variables, x is the state vector, e is the vector of the measurement errors and h are the equations relating the state and the measurements. The task of the SE is to solve this equations system. [6]

$$z = h(x) + e \quad (1)$$

The state vector usually consists of voltage magnitudes and angles of every node of the grid. The measurements which represent the input data of the SE can differ but usually consist mainly of active and reactive power balance and flow, of voltage magnitudes and sometimes of current magnitudes. Angle measurement are until now not common in the SE. [6]

Furthermore, due to the inaccuracy of the measure device every measure has an error included in the vector e . This error can be represented as gaussian distributed with an expected value of zero.

C. Linearisation of the measurement functions

The functions h which relate the measurements values and the state are shown in (2) and (3). To simplify the representation the notations in (4) are introduced. Because of the trigonometric relation these functions are nonlinear.

$$P_v^{ij} = U_v^i \cdot \sum_{w=1}^3 \left\{ U_w^i \cdot [G_{v,w}^{ij} \cdot c_{v,w}^{ii} + B_{v,w}^{ij} \cdot s_{v,w}^{ii}] - \dots \right. \\ \left. U_w^j \cdot [G_{v,w}^{ij} \cdot c_{v,w}^{ij} + B_{v,w}^{ij} \cdot s_{v,w}^{ij}] \right\} \quad (2)$$

$$Q_v^{ij} = U_v^i \cdot \sum_{w=1}^3 \left\{ U_w^i \cdot [G_{v,w}^{ij} \cdot s_{v,w}^{ii} - B_{v,w}^{ij} \cdot c_{v,w}^{ii}] - \dots \right. \\ \left. U_w^j \cdot [G_{v,w}^{ij} \cdot s_{v,w}^{ij} - B_{v,w}^{ij} \cdot c_{v,w}^{ij}] \right\} \quad (3)$$

$$\Delta\varphi_{v,w}^{ij} = \varphi_v^i - \varphi_w^j, v, w \in [1,2,3] \\ c_{v,w}^{ij} = \cos(\Delta\varphi_{v,w}^{ij}), s_{v,w}^{ij} = \sin(\Delta\varphi_{v,w}^{ij}) \quad (4)$$

Non-linear equation system must be solved with iterative algorithm which can be really time and resource consuming. Also, these algorithms don't always lead to a solution which could be problematic to deal with.

In transmission grids the state estimation occurs at the control center and is performed by powerful computers. Due to the high number of LV grids, a simpler system would be more suitable for an automated grid supervision.

With linear equations the system can be solved in one iteration and a solution will always be calculated. However, some accuracy will be lost because of the linearization error.

The measurement functions can be linearized with a Taylor approximation. The complete linearization can be found in [5]. They are not further discussed in this paper.

D. Redundancy of the measured values

A pre-condition of the SE is the positive redundancy of measurements defined with η in equation (5). [6]

$$\eta = \frac{M}{2N-1} - 1 \geq 0 \quad (5)$$

Basically, there must be twice as much measurements M than grid nodes N . In transmission grids, system variables can be measured at almost every node, hence the redundancy is easily sufficient. For LV grids this is not the case as these are often build as underground cable networks where no measurement can be performed at the cable joints. Only measurement at the distribution station and at the house connection are possible which are unfortunately not sufficient.

However, at some inaccessible grid nodes the value of some variables can be known through physical law like for example the Kirchhoff current law. With the introduction of these values as virtual measurements in the SE the redundancy would be sufficient. Virtual values are considered exact and do not have a measurement error. [7]

The introduction of virtual measurement requires an adjustment of the algorithm. A solution is introduced in [7] with the augmented matrix method.

III. SIMULATION ENVIRONMENT

A. Low Voltage Grid Model

For the simulation a modelled grid based on a real LV grid represented in Figure 1. was used. This grid has 234 nodes, 236 transmission lines, 116 house connections and 17 PV systems. Furthermore, the grid is operated radial and as such will be assumed for the simulations. For the verification it was important that the grid had only households as loads and a high number of PV systems.

B. Benchmark and real measurements

The verification of the simulations was performed using an exact model or so-called benchmark. This benchmark was gained computationally with a load flow calculation using real power measurements (P and Q) for the households as well as the PV systems. These values originate from the SmartSCADA project [4] and were measured directly from different households and PV system over a whole year using smart meters.

For the SE the required input values for the voltage magnitudes at the house connections and the values for the voltage magnitudes as well as the power at the transformer were taken from the benchmark. To simulate the measurement

noise from the smart meters the values were furthermore superposed with a Gauss distributed random value.

C. Pseudo Measurements

The applied pseudo values as replacement for missing real measurements were generated by a MATLAB® Tool. This tool presented in [8] can synthesize power load profiles (LP) for buildings and households. For this paper, only profiles for households were generated. The number of person in a household can be defined as well as the type of household (detached house or apartment building). The simplified diagram in Figure 4. shows the flowchart of a profile generation process. In contrast to other method for the reproduction of the power consumption like standard load profiles (SLP) which delivers only periodic and average values, the tool generates unique and probabilistic values based on statistic usage of power from households. The use of random variables through the generation process leads to unique profiles.

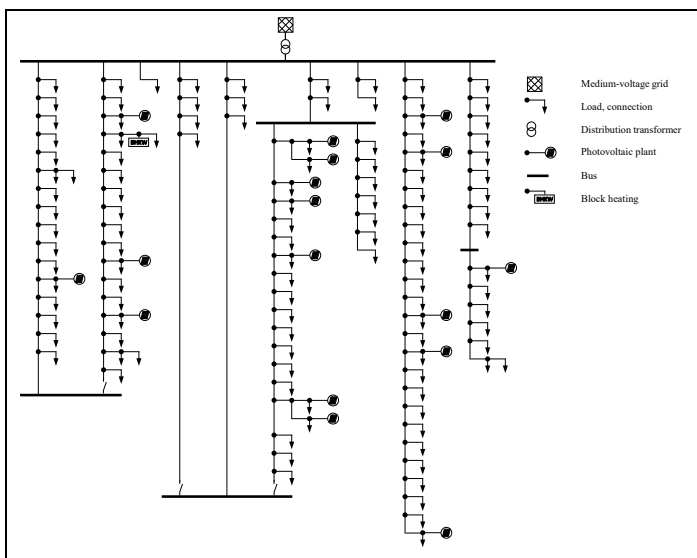


Figure 1. Wessum-Riete modelled LV grid

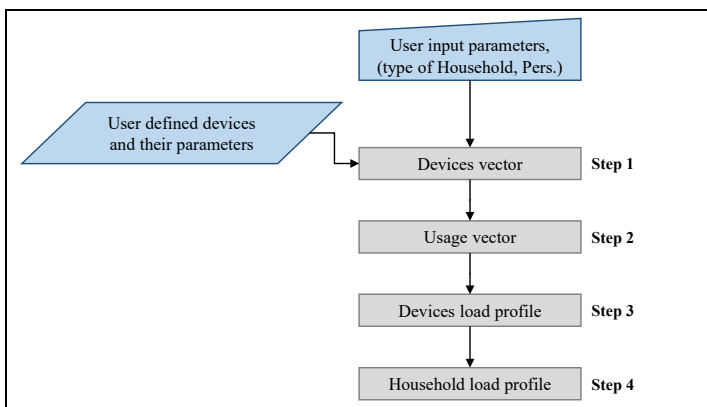


Figure 2. Generation process of a load profile

To achieve these realistic LP the tools considers the power usage from individual home devices like e. g. a fridge, a television or a washing machine. Important parameters for a device are the penetration rate for different household's types,

the load curve, the power factor, the annual energy demand and the usage frequency distribution.

The devices and their parameters are defined by the user. A list of the most usual devices is already suggested. Their parameters are based on statistic data. Additionally, the user need to specify the number of persons in the household, the time and the time step for the generation of a new profile.

The generation process of a synthetic LP can be basically split in four steps for better understanding. In the first step the tool determines which devices are present in the household and creates a so-called device vector. This vector is created by comparing the penetration of each device with a uniform distributed random variable. The penetration specifies the probability of the presence as well as the amount of a specific device in a household. In the next step the usages of every individual device based on the usage frequency distribution and the annual energy demand is determined. The tool determines how many times a device is used in the desired time period and distributes these usages using also a uniform distributed random variable over the period.

For every device in the household an individual LP is then generated. In the final step these LP are summarized to form a household LP.

Due to unsymmetrical loads in LV grids, the tool generates a unique LP for every phase. The distribution of the devices to the phases is random. The tool also generates a reactive power LP for each device as well as for the whole household based on the active power LP and the power factor of the devices.

Another method to generate pseudo measurements called "Approximate active power distribution" (AAPD) presented in [] was used for this paper. This method uses another approach to represent the power consumption of household and will not be discussed further in this paper.

D. Configuration of the profiles in the grid

The assignment of the LP to the house buses of the LV grid was performed in different ways. Every synthetic LP is unique therefore the assignment is important. For the majority of the simulations the assignment occurred randomly as this was the simplest way and didn't require additional information about the consumers. For one simulation the configuration was based on the annual energy consumption of the households as this is the only consumer-related information the grid operator can get in accordance of the law.

E. Simulation process

Each simulation consists of the computational SE of the LV grid model for every instant of the time period. The chosen period was a year and the time step was 10 minutes. That way every season of the year was included in the simulation.

The simulations were performed in MATLAB® with the algorithm presented in [5].

IV. VERIFICATION

A. Simulation configuration

For the verification, the results of six simulations were considered. TABLE I. summarize the input data for each simulation. In this paper the focus was to analyze the usage of pseudo values in the SE only for households. For PV systems the law is different and allows the measurement of plants with an installed power over 1kW and it is far easier to predict the power generation from unmeasured systems. Hence the same power generation profiles with the same configuration for the PV systems in the grid were used for every simulations. These profiles as already mentioned originates from the SmartSCADA project. The difference of all six simulations are in the used LP for households and their assignment to the grid buses.

TABLE I. OVERVIEW OF THE SIMULATIONS

Simulation number	Load Profiles	LP Configuration
S1	SmartSCADA	As in benchmark
S2	SmartSCADA	Random
S3	AAPD	Random
S4	Tool	Random
S5	Tool	Random
S6	Tool	Based on average load

In simulation 1 the same real values from the benchmark with the same assignment in the grid were used. This simulation shows the results of a SE with only real measurements as they could be gather completely from smart meter. This situation could be possible in other countries than Germany with weaker laws about data privacy. The remaining errors in this case comes only from the linearization of the SE.

In simulation 2 the same real values are still used but this time with another random assignment at the households of the grid. In other words, the power consumption of the households in the grid were reproduced with the power consumption of other households in the same grid. This simulation should show the accuracy of using real measurements for power load reproduction.

In simulation 3 the pseudo values from the AAPD were used to reproduce the power usage. In the remaining simulations the synthetic LP from the tool were applied for the SE. In this context a database with enough different LP generated with the tool was created. For simulation 4 and 5 the assignment of the LP occurred randomly. The reason two simulations with a random assignment were performed was to analyze the effect of different assignments.

In the last simulation the configuration was based on the annual energy consumption. For every household in the grid and for every available synthetic LP the annual energy consumption was calculated and the assignment of the LP to the grid load buses and LP was according to most similar values. Hence the overall annual power consumption of the grid should stay almost the same.

B. Evaluated data

As every simulation results in more than 30 million values, for a given system variable, only average and maximal errors were considered. Maximal errors can help detect system variable operating limit violations. Average values are necessary for regulation tasks (as e. g. for a regulated distribution transformer). Also, only voltage and current magnitudes were considered as they give a direct statement about the grid operating state.

To calculate the error of a given value from a simulation, the same value from the benchmark is subtracted from the value. The absolute value of the error was than calculated to obtain only the absolute difference between model and simulation. To consider only the average and maximal values, the time reference was remove by calculating the average error over a year and by selecting the maximal error over the whole year. Subsequently the result is an error value for every node in the grid.

The three phases were considered independently and represented next to each other on different graphs.

C. Voltage magnitudes

Figure 3. shows the voltage magnitude mean errors of all six simulations represented as boxplots. A remarkable difference can be observed between the first and the other simulations. The replacement of the missing measurement with pseudo values lead as expected to higher errors in respect to the benchmark. However, the errors didn't exceed 0.35 V which is tolerable considering the operative voltage of 230 V in LV grids. The results for simulations 2 to 6 are almost the same. Both the used pseudo values and the placement of these values in the grids didn't had much influence on the results.

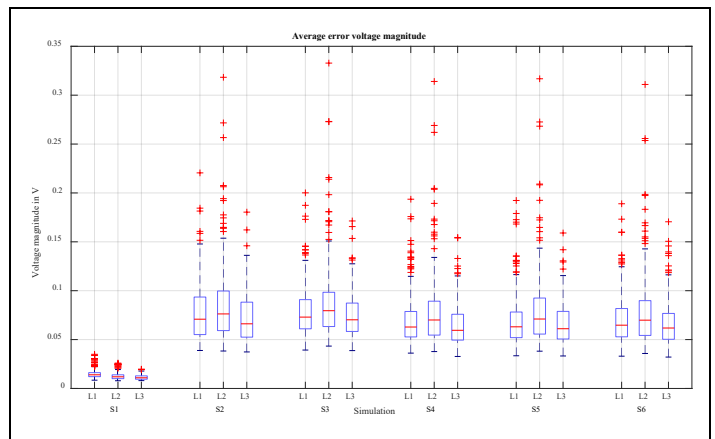


Figure 3. Boxplot of the average voltage magnitude error

For the maximal errors shown in Figure 4. the behavior is quite similar. The maximal observed outlier lies at 3.5 V which represents about 1.5% of the nominal voltage. Considering the allowed voltage range of $\pm 10\%$ (set by the DIN EN 50160 norm) in which the operative voltage value has to be, the SE could in the most cases detect a limit violation if the band was reduced by these $\pm 1.5\%$.

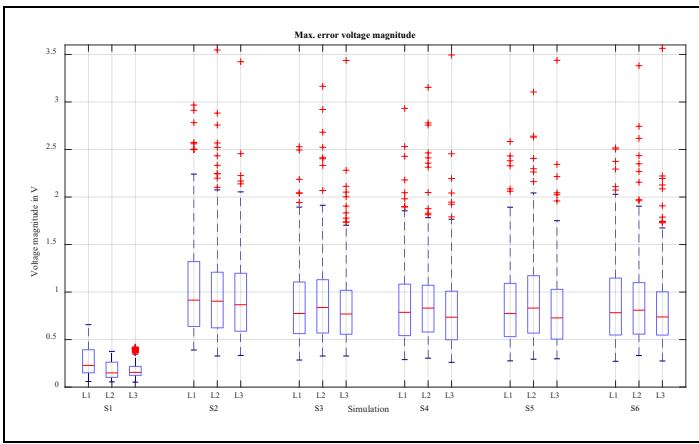


Figure 4. Boxplot of the max. voltage magnitude error

Furthermore, if assumed an error of 2.3 V is still tolerable, the occurrence of an error above this value as shown in TABLE II. would be for all simulations less than 0.0011% of all values, which represent less than one case in three days.

TABLE II. NUMBER OF OCCURRENCE OF A VOLTAGE ERROR ABOVE 2.3 V

Phase	S1	S2	S3	S4	S5	S6
L1	0	38	4	10	7	5
L2	0	107	135	79	75	88
L3	0	35	28	30	33	29

D. Current magnitudes

In Figure 5. the maximal errors of the current magnitudes are shown. One again the use of pseudo values in simulations 2 to 6 lead to much higher deviations with the benchmark. The highest current error lies at about 60 A which is assuming a current carrying capacity of about 219 A for a main line about 25 % of the line capacity. Such error can be really problematic in grids which have a high power load or generation, because a fuse could be triggered without warning from the SE. To ensure the SE doesn't miss a line overload the grid operator could reduce the maximal allowed current for the main lines. But this would only be possible in grids with low load.

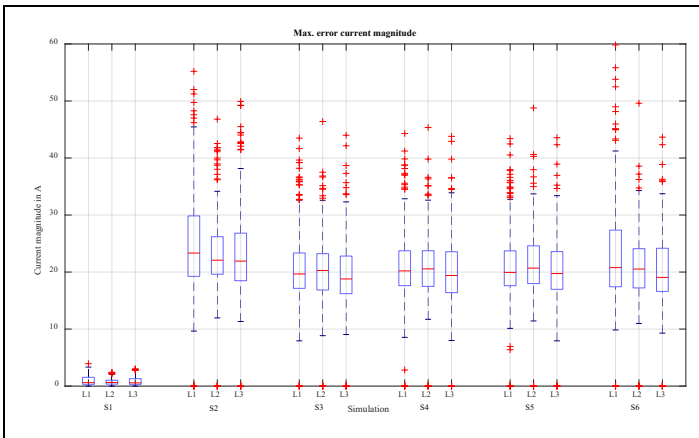


Figure 5. Boxplot of the max. current magnitude errors

Now assuming errors of 30 A are still tolerable, errors above this value as shown in TABLE III. would occur only

every three days (for the best case scenario S4 with pseudo-values). Furthermore, it should take into consideration not every occurrence of a high leads to a line overload.

TABLE III. NUMBER OF OCCURRENCE OF A CURRENT ERROR ABOVE 30 A

Phase	S1	S2	S3	S4	S5	S6
L1	0	447	152	139	136	132
L2	0	139	64	41	43	49
L3	0	363	86	77	66	66

V. CONCLUSION

In this paper the accuracy of the SE of a LV grid using a high number of pseudo values was investigated. For this task, a tool was used to generate synthetic LP for household which were applied in an existing linear algorithm to perform an estimation of the state. The results were then compared to a benchmark.

The results showed that the average error for voltage magnitudes were tolerable. For the maximal errors of voltage and current magnitudes some high values could be observed however with a really minor overall occurrence.

The SE method showed in this paper could be used in LV grid supervision although the operator should consider the possibility of high error.

Furthermore, the algorithm should be examined with other grid models. Also for more accuracy in the SE of LV grids the focus should be on other method more suited for SE tasks to predict, estimate or calculate the load of households.

REFERENCES

- [1] Die Bundesregierung, Erneuerbare-Energien-Gesetz (EEG), 2012
- [2] Fraunhofer, „Aktuelle Fakten zur Photovoltaik in Deutschland“, www.pv-fakten.de, 2018
- [3] Die Bundesregierung, Gesetz zur Digitalisierung der Energiewende (GDEW), 2016
- [4] D. Waeresch, R. Brandalik and W. H. Wellssow “Linear State Estimation in Low Voltage Grids based on Smart Meter Data”, PowerTech, 2015 IEEE Eindhoven
- [5] R. Brandalik, D. Waeresch, W. H. Wellssow and J. Tu ‘Linear three phase state estimation for LV grids using pseudo measurements based on approximate power distributions”, CIRED, Glasgow 2017
- [6] A. Abur, *Power System State Estimation*, CRC Press, Boca Raton, USA, 2004.
- [7] A. Gjelsvik, S. Aam, L. Holten, “Hachtel’s augmented matrix method – a rapid method improving numerical stability in power system static state estimation”, IEEE Transactions on Power Apparatus and Systems, 1985
- [8] N. Nau, ‘Synthesis of domestic load curves for low voltage grid simulations’, PESS Erlangen 2017

Investigation of Real-time Performance Using OPAL-RT and Acceleration Methods based on different Power Converter Models

H. Cai, Y. Zeng, X. Song, T. Jiang, S. Schlegel, D. Westermann

Power Systems Group
Technische Universität Ilmenau
Ilmenau, Germany

Abstract—Since 2010, Germany has enacted the Energy Strategy 2050, whose goal is to increase the share of renewable energy from wind or solar. To this end, new grids and the connection between the renewable energy installation and the low-voltage and medium-voltage grid will be set up. This requires various power electronic elements and their simulative investigation. Traditional simulation techniques are limited because of a large number of power electronics and the complexity of the system. Due to the low computational speed of conventional simulation methods, the simulation results are distorted. In this case, real-time simulation is efficient because it has fast computational speed. Therefore, the results of the real-time simulation are similar to the realism. Also, real-time is the prerequisite for communication between simulators and physical equipment. The first goal of the seminar paper is to investigate real-time capability through real-time simulation based on the three inverter models in different scenarios. The second objective is to examine the effectiveness of the acceleration methods offered by the software of the real-time simulator.

Index Terms: Real-time simulation, OPAL-RT, HIL Simulation, distribution grid, power converter model

I. INTRODUCTION

According to the Energy Strategy 2050, the consumption of traditional energy resources in Germany will decrease in the future and at the same time increase the proportion of renewable energies such as wind energy, biomass, solar energy [1] [2] [3].

To increase the amount of renewable energy, the development of more grids and the connection between renewable energy plant and low-voltage and medium-voltage grid is necessary [4], [5]. For this purpose, different Power electronic elements in different time periods and their simulative investigation are needed. Conventional simulation techniques are limited because of a significant amount of power electronics and the complexity of the system. Due to the low speed of traditional simulation methods, the simulation results are inaccurate. However, the real-time simulation can solve the problem because it has high operating rate [6]. With the high operating speed, the simulation behavior from the real-time simulation is particularly close to reality [6] [7]. Also, the real-

time simulation and physical time have the same clock, which is the requirement for being able to couple the renewable energy system with a simulated environment [8]. For such reasons, real-time simulation is needed.

Power Converters as an essential power electronic element has a significant contribution to the expansion of renewable energy or to increase the fed-in power. To make sure that the application of a high proportion of converter-based generators and loads in the future distribution system, the power converter models must be investigated. For the highly complicated renewable energy system, the phasor model is not enough with low model depth. Other models, such as the detailed model with high model depth are taken into consideration. However, the behaviors in real time of different models are not the same, so it is necessary to simulate the models with varying depths and then to compare their behavior in real time.

In this paper, the first goal is to investigate the real-time performance of models with different model depths in different scenarios. The modeling and simulation of the converter are based on the example of three-phase inverter. The second goal is to improve the effectiveness of acceleration method offered by OPAL-RT.

For these purposes, first, the introduction of Opal-RT and motivation of this paper was explained. After that, the standard hardware and software for simulation will be summarized in chapter 2. In chapter 3, the real-time performance of converter models at different modeling levels in RT-Lab will be presented and compared. Also, the efficiency of acceleration methods was improved to optimize the property of real-time. At last, Chapter 4 includes a conclusion.

II. HARDWARE AND SOFTWARE IN REAL-TIME SIMULATION

The investigations in this paper are based on the three models of the power converter with different model depth in Simulink. The modeling and simulation of the three-phase converter are based on an existing seminar paper and will be presented in this chapter. The real-time simulator builds a

simulative environment so that the real-time performance of the power converter models can be investigated. The following sections explain the standard hardware and software include the real-time simulator and the acceleration methods that needed for successful real-time simulation.

A. Converter Model

To investigate the real-time behavior, three in Simulink constructed inverter models, a detailed model (DEM), an average model (AVM), and a phase model (PM), are implemented in the real-time simulator. The general topology of the power converter model is shown as followed in Fig 1.

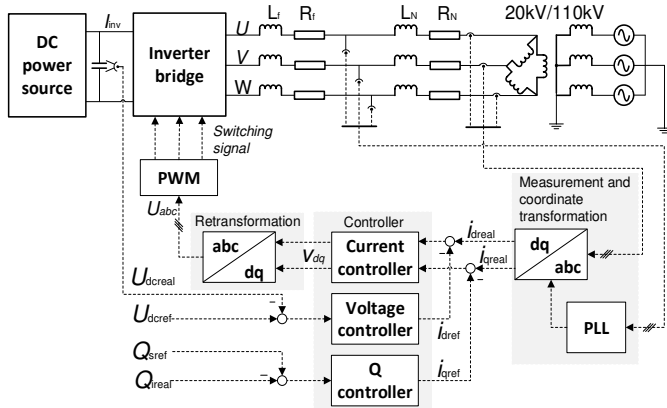


Fig. 1 Converter model structure [9]

The modeling consists of the grid circuit and the control circuit of each current converter model [9]. In addition to a three-phase inverter with an intermediate voltage circuit, the grid circuit includes a filter choke, the grid impedance, a transformer and the interconnected grid. The controller circuit consists of a phase locked loop, voltage controller, and current controller, etc. The controller is collected in a subsystem. The input of the controller is the active power P and reactive power Q . The three converter models are created with three different concepts. The DEM has the highest model depth and highest detail level of all three models. It bases on the physical circuit with detailed components. Thus, it has a complex structure but a high accuracy. The AVM works not with instantaneous values but with the averaged values. The outputs of the inverter model of the PM are amounts and phases of the three phase currents and voltages [9]. It has the lowest model depth of these three models.



Fig. 2 Real-time simulator series OP5600

B. Standard Hardware and Software

The real-time simulator series OP5600, as shown in Fig. 2, was produced by OPAL-RT. It has an eight-core CPU for operating the task, FPGA (Field-programmable gate array) for input/output management [10]. There are 112 monitoring

interfaces in front. On the back of the simulator are the real-time interfaces, which can connect not only with a monitor but also with controller/microcontroller. The Simulator OP5600 and its expansion device enables real-time simulation- and I/O-signals to be delivered via Mini-BNC connectors without compromise [11]. OPAL-RT offers four software, as shown in this 2-dimensional Figure 3. The choice of software depends on the size of the model, that is to say, how many connecting points are there in a model, and it also depends on sampling interval.

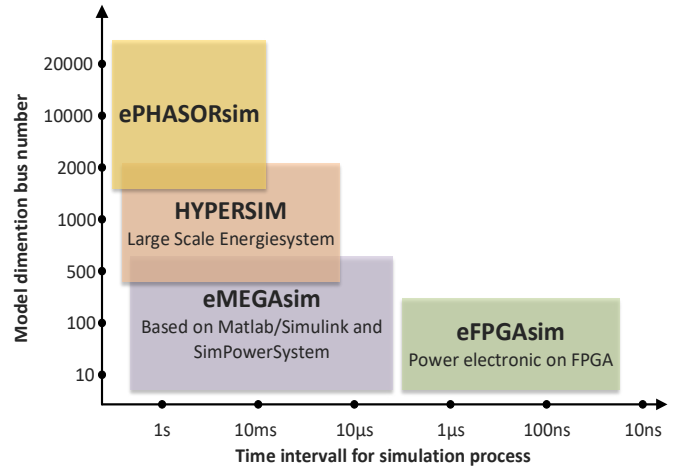


Fig. 3 OPAL-RT standard software

In this paper, eMEGAsim is used. eMEGAsim bases on Matlab / Simulink and it is suitable for Power System Model or Power Electronics Model. With eMEGAsim, the data stream will be first calculated in CPU and then executed in the FPGA for coordinating and cooperating with the I / O ports. RT-LAB is the platform offered by OPAL-RT, where the model can be programmed and simulated under eMEGAsim. Fig. 4 shows the procedure to run the real-time simulation.

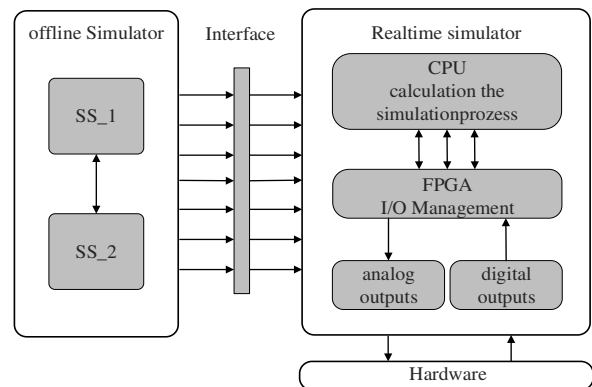


Fig. 4 The process of the real-time simulation

Applying the real-time simulator requires the Hardware-in-the-Loop (HIL) simulation, which is the key to connecting the plant to a simulated environment. In addition, HIL is a method to test and protect during the development or early startup of machinery and equipment [11].

C. Acceleration methods

Real-time is the requirement of communication between the equipment and simulator. Real-time cannot be achieved in the case of a computer with low operating speed, or an

oversized model. OPAL-RT offers the acceleration methods that can accelerate the simulation process and achieve real-time simulation. There are two methods: parallel computer and ARTEMiS Toolbox.

Parallel computing reduces calculation time by distributing the calculation task on several cores of one CPU and all cores execute the simulation process simultaneously. That is why parallel computing is ideal for processing large amounts of data. Exploiting the full power of the parallel computer, the entire model must be divided into several subsystems. Each subsystem obtains a core. The calculation task in the subsystem will be operated by the core it owns. The number of cores CPU limits the maximum number of subsystems. By assignment the subsystem appropriately the effectiveness of parallel computing for reducing simulation operation time will be enhanced. Fig. 5(a) presents the whole system without using parallel computing. In Fig 5(b) the system is divided into two subsystems, each one owns a core in CPU. It shows a system using parallel computing.

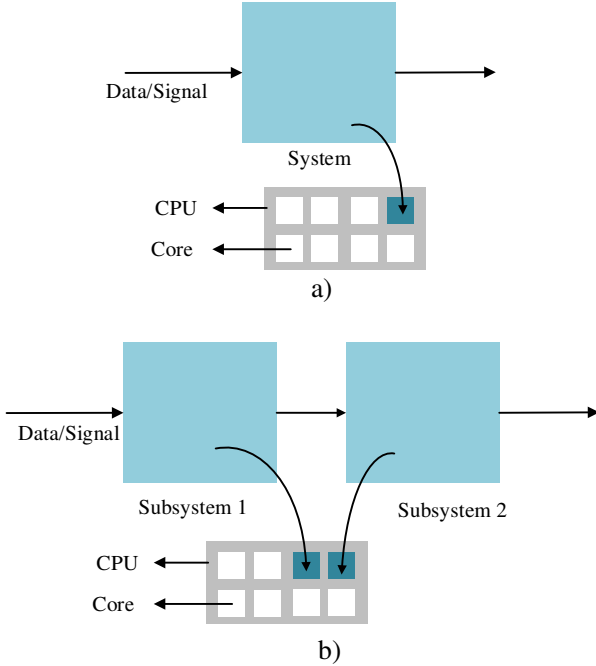


Fig. 5 The concept of parallel computing

The second acceleration method is ARTEMiS Toolbox, which can also enable real-time simulation. ARTEMiS provide available decoupling methods, such as SSN(state-space-nodal), Artemis Distributed Parameter Line(DPL), and Stublines. These decoupling methods are used for single core and multi-core simulation. In this paper, only DPL is investigated, which is shown in Figure 6.

DPL in a single core (inside subsystem): it divides the model's large state space equation (1) into several smaller state-space matrices with replacing C1, C2, D1, D2 with 0, then reduces the total size of the matrix, thereby making the overall simulation faster.

Group Equation:

$$x_{n+1} = \begin{bmatrix} A1^m & C1 \\ C2 & A2^n \end{bmatrix} x_n + \begin{bmatrix} B1^m & D1 \\ D2 & B2^n \end{bmatrix} u_n \quad (1)$$

Compared with SPS, operations C1, C2, D1, D2 are saved with using DPL.

DPL in multi-cores (between subsystems): Using DPL to implement the parallel computation which makes sure the effectiveness and the accuracy of the computation. With DPL each core is independent during the timestep and they exchange data at the end of the timestep.

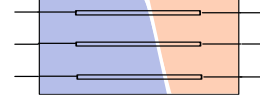


Fig. 6 ARTEMiS Distributed Parameters Line Block

Figure 6 shows a 3-phase distributed transmission line model optimized for real-time simulation. This block allows system decoupling into smaller subnets, each having a CPU core. Therefore, parallel computers are set up, and the computation process is accelerated. But ARTEMiS DPL can only be replaced on PLC line that supplies SPS signal.

III. SIMULATION

Based on the presented theory, the characteristics of real-time simulations are investigated in the medium voltage distribution grid. Fig. 7 shows the reference network. It builds upon the Cigré benchmark [12], which presents the topology of the European version of the medium-voltage network. In this network, both feeders of the open ring topology are operated at 20 kV and are fed via separate transformers from the 110 kV sub-transmission system. On the right side of the open ring topology of 20kv grid, three inverters with different load relate to it, while on the left side of the medium voltage ring remind unchanged [9]. The inverter models, which parameters are given in Appendix, are modeled with three different model depths in MATLAB and all implemented into the real-time simulator.

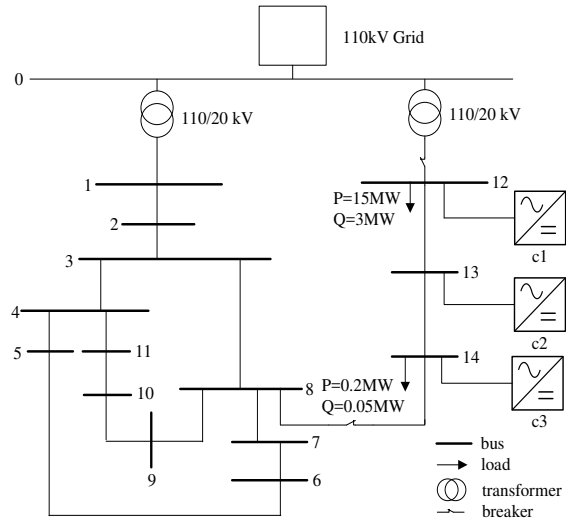


Fig. 7 General system topology for simulations

The effects of the two presented acceleration methods, namely parallel computing and ARTEMiS, are examined. For parallel computing, the system can be one calculation subsystem or split into two or four calculation subsystems. Fig. 8 shows the

arrangement of a four-subsystem topology.

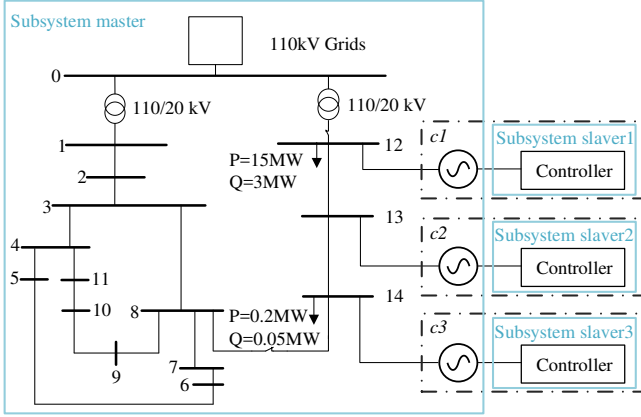


Fig. 8 Simulation with parallel computing

For ARTEMiS, it can only be implemented in the AVM. ARTEMiS cannot work in PM because it must be under the discrete environment, but the PM environment is Phasors. ARTEMiS can also not work in DEM because three-level bridge block is used as the inverter in DEM and there are 18 switches, resulting in memory overflow in the calculation of switching matrix permutations, which is not allowed in MATLAB. In this paper, ARTEMiS line has been used to replace distributed parameter line in SPS. It has two functions; one is direct to accelerate the simulation, and the other is, because of the replacement of distributed parameter line, a complete inverter can be separated from net independently as one subsystem slaver, which means with ARTEMiS converter does not need to divide into controller and voltage source. That makes the separation of model easier. Fig.9 shows the arrangement of a four-subsystem with three ARTEMiS DPL topology.

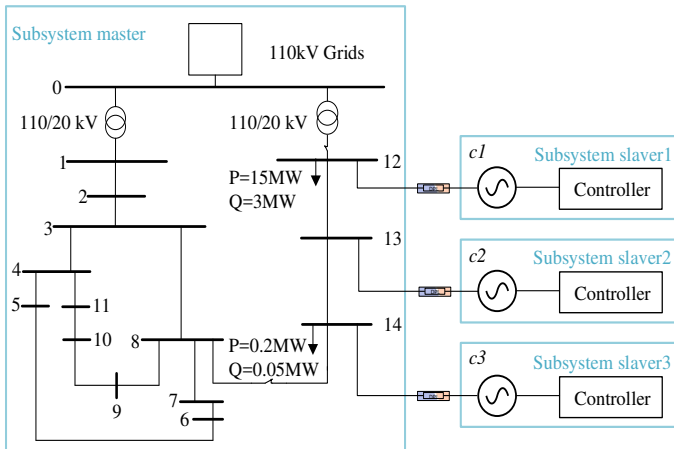


Fig. 9 Simulation with ARTEMiS DPL

The simulations can be done with the different number of subsystems model because the numbers of calculation subsystems commonly have effects only on calculation time but not on the resulting forms of voltage, active and reactive power, etc.

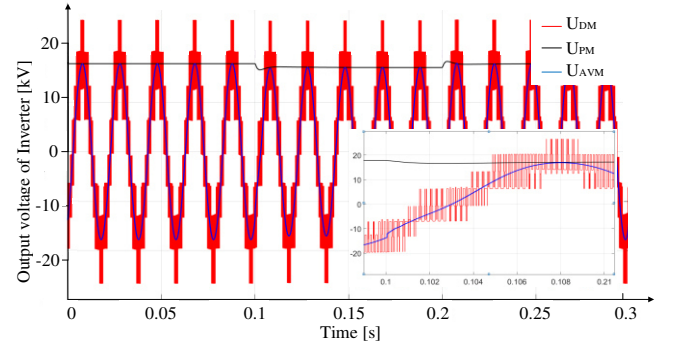


Fig. 10 Comparison of simulation results at changing of an operating point: A phase output voltage of the corresponding inverter

Fig. 10 shows the simulation results of the output voltages of the inverters, which amplitude is $\frac{\sqrt{2}}{\sqrt{3}} \cdot 20kV = 16.3kV$. Because of the switching mode of operation in DEM, the waveforms of the output voltages (red line in Fig. 10) show a pulsed signal. This distorted voltage contains the high-frequency component in addition to the fundamental frequency component. By contrast, in AVM and PM, only the fundamental frequency component is presented because the switch behaviors are ignored. The voltage curves are completely adjusted here. While the output voltages of the inverter in AVM (blue line in Fig. 10) are ideally sinusoidal, the phase model considers only the peak value and the phase angle. The phase angle is not marked in Fig. 10.

TABLE I REAL-TIME CAPABILITY OF PARALLEL COMPUTING

Model type	Numbers of subsystems	Time interval [μs]	Usage-value [%]	Running time [μs]
DEM	1	200	96	192
	2	200	89	133.5
	4	200	87	78.3
AVM	1	50	90	45
	2	50	75.98	37.5
	4	50	40.62	20.5
PM	1	50	70.7	35.35
	2	50	38.7	19.35
	4	50	22.9	11.45

The whole simulation run-time comprises calculation time T_R of CPU and command time T_K in FPGA. If this running time is smaller than a predetermined time interval T_S , it is real-time capable. If the running time is greater than the time interval T_S , the interval T_S can be extended to achieve real-time capability. A disadvantage of an enlarged interval T_S is a reduced accuracy. The software RT-LAB from the developer OPAL-RT Technology offers real-time simulators and acceleration methods. With acceleration methods, the calculation time T_R can be reduced thereby the running time is reduced. The Usage-value of RT-LAB provides information about the real-time capability. If Usage-value is below 100%, the simulation is running in real time. If this value is above 100%, there is an

overrun. Overrun in the simulation cause highly biased results. Also, the behavior of the system becomes uncertain. Therefore, the main part of this work is to avoid overrun and even to reduce the running time of the simulation.

TABLE I shows the calculation time of three model types with three scenarios of parallel computing. The number of subsystems, different time intervals T_s , the *Usage*-value and the calculation time T_R is shown in this table. The time intervals T_s are chosen so that the real-time capability is guaranteed. The *Usage*-value shows the degree of capacity utilization.

TABLE II shows the calculation time of AVM with the different number of ARTEMiS DPL in one, two and four subsystems. The number of DPL, the time interval T_s , the *Usage*-value and the calculation time T_R is shown in this table. The *Usage*-value indicates the utilization ratio.

TABLE II REAL-TIME CAPABILITY WITH ARTEMIS DPL

Model type	Numbers of subsystems	Numbers of DPL	Time interval [μ s]	Usage-value [%]	Running time [μ s]
AVM	1	0	50	90	45
		1	50	63.47	31.74
		2	50	57.28	28.64
		3	50	52.88	26.44
	2	0	50	75.98	37.99
		1	50	45.47	22.74
		2	50	41.88	20.94
	4	3	50	37.45	18.73
		0	50	40.62	20.31
		1	50	26.35	13.18
		2	50	23.85	11.93
			3	50	21.21

IV. CONCLUSION

In this paper, the real-time capability was examined by real-time simulation based on the three inverter models in different scenarios. Besides, the effectiveness of the acceleration methods offered by the software of the real-time simulator was investigated. The simulation of the system with small disturbance has been carried out with the DEM, AVM, and PM, which are examined with OPAL-RT 5600. According to the simulation result as well as the system performance, we could add up to following conclusions:

- PM shows the best real-time capability amount three models, shows in the table I, under the same condition, the PM cost almost one third of the system calculation capacity as the AVM or DEM.
- Parallel computing has a significant effect on the reduction of computing time (see in Table I).
- Using DPL to replace distributed parameter line in SPS has two ways to reduce the computing time. On the one hand, using DPL in the model with only one calculation subsystem, that means no parallel computing, can directly make the computing time shorter (see in Table II). On the other hand, DPL makes the separation of model easier. The

inverter does not need to divide into controller and voltage source anymore. In other words, DPL facilitates parallel computing. However, ARTEMiS can only be used in AVM. Further investigations with dynamical models of power grids with the connection to medium and high voltage grids can be implemented and realized with this real-time simulator.

APPENDIX

The parameters of the simulation are in Table III.

TABLE III USED PARAMETERS FOR SIMULATIONS

Parameter	DEM	AVM	PM
Nominal power and frequency [S (W), f (Hz)]	[5e6, 50]	[5e6, 50]	[5e6, 50]
Nominal supply voltage U_{AC} (V)	20e3	20e3	20e3
Nominal dc voltage U_{DC} (V)	40e3	40e3	40e3
Intermediate circuit capacity C (F)	80e-6	80e-6	80e-6
Filter choke [R (Ω), L (H)]	[0.2 0.005]	[0.2 0.005]	[0.2 0.005]
U_{AC} -controller [Kp, Ki]	-----	[1 3000]	[1 3000]
U_{DC} -controller [Kp, Ki]	[70 700]	[70 700]	[70 700]
Q -controller [Kp, Ki]	[5 300]	[5 300]	[5 300]
I -controller [Kp, Ki]	[0.3 20]	[0.3 20]	[0.3 20]
PLL-controller [Kp, Ki]	[40 10]	[40 10]	[40 10]

REFERENCES

- [1] Bundesverband erneuerbare Energie, e.V. Available: <https://www.bee-ev.de/home/>.
- [2] Das Energiekonzept 2050, Die Bundesregierung [OnLinie], Available: <https://www.bundesregierung.de/>.
- [3] Agentur für erneuerbare Energie (Hrsg.): Bundesländer in der Übersicht-Installierte Leistung Photovoltaik [OnLinie]. <http://www.foederal-erneuerba.de>, Dezember 2011.
- [4] Energiekonzept für eine umweltschonende, zuverlässige und bezahlbare Energieversorgung[OnLinie]. <https://www.nachhaltigkeit.info/media/1285831803phpz9Rqi2.pdf>, 28. September 2010.
- [5] "Photovoltaics Report" 19", *Fraunhofer Institute for Solar Energy Systems*, October 2015.
- [6] J. Lundsgaard-Hansen, „Energiestrategie 2050 - das Eis ist dünn,“ *Neu Zürcher Zeitung*, 24 08 2013.
- [7] M. Zhou, V. A. Centeno, J. S. Thorp and A. Phadke, “An Alternative for Including Phasor Measurements to State Estimators”, *IEEE Trans. Power Syst.*, vol. 21, no. 4, pp. 1930–1937, Nov. 2006.
- [8] H. Hu, X. Fang, F. Chen, Z. J. Shen, and I. Batarseh, “A Modified High-Efficiency LLC Converter with Two Transformers for Wide Input-Voltage Range Applications,” *IEEE Trans. Power Electron.*, vol. 28, no. 4, April 2013, pp. 1946–1960.
- [9] Zheng Liu, “Realisierung von Umrichtermodellen und deren Untersuchung auf dynamisches Verhalten im Verteilernetz“, 07, Dezember, 2016.
- [10] Federico Milano, *Power system modelling and scripting*, London, 2010.
- [11] Opal-RT Technologies, Montreal, QC, Canada, H3K 1G6[Online]. Available: www.opal-rt.com.
- [12] "CIGRE Task Force C6.04.02", *Benchmark Systems for Network Integration of Renewable and Distributed Energy Resources*, Apr. 2014.

Concept of an Adaptable Protection Device for Low Voltage Networks

Kevin Alexander Egle, Florian Grumm, Marc Florian Meyer, Maik Plenz, Detlef Schulz (Senior Member, IEEE)
 Helmut-Schmidt-University /
 University of the Federal Armed Forces Hamburg
 Hamburg, Germany

Abstract—This paper presents a concept for a solid-state power controller for low voltage electrical grids, which is able to deal with different short-circuit powers present in the electrical grid it is utilized in.

Keywords short-circuit power; solid-state power controller; short-circuit detection; islanding grids

NOMENCLATURE

SCC	short-circuit current
SSPC	solid-state power controller
MOSFET	metal-oxide-semiconductor field-effect transistor
λ_{total}	total failure rate
λ_{MOSFET}	MOSFET failure rate
π_T	temperature correction factor
N	Number of parallel MOSFETS
L	inductance
R	resistance
S_K''	short-circuit power
\hat{u}	voltage amplitude
φ	phase angle
i_0	initial current value of a coil
ω	Radial frequency of the grid

I. INTRODUCTION

The increasing share of distributed energy resources (DER) raises the possibility to operate partial networks in islanding mode. There are two different islanding scenarios:

- unintentional islanding as an unwanted network state, which needs to be shut down or securely operated; in either case it has to be detected
- intentional islanding, e.g. as a kind of emergency power supply of critical infrastructure like hospitals, fire departments, etc.

In the case of an islanding operation of a partial network, the protection requirements change. Islanded networks are most likely supplied by wind and photovoltaic plants, which are connected to the grid via inverters. According to VDE 0102 [1] the short-circuit currents (SCC) of inverters are almost equal to their rated currents. Hence, the short-circuit power in networks operated in islanding mode is reduced essentially compared to

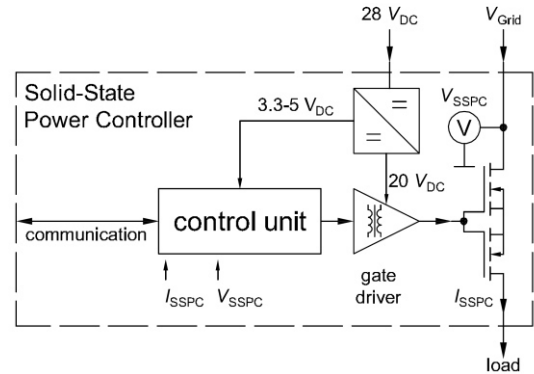


Figure 1. Block diagram of a solid-state power controller

normal operation. The standard primary protection device is the fuse. Its reliable operation highly depends on a sufficiently high short-circuit power. Hence, in islanding mode of partial networks, fuses may not trigger in case of a fault.

If islanding scenarios become more frequent in the future, an adaptable protection device is needed in order to ensure a reliable network operation. Adaptable refers to the variation of parameters and characteristics, such as:

- voltage characteristics (e.g. voltage limit settings)
- current characteristics (e.g. over current settings)
- I^2t characteristics (fuse characteristic)
- grid frequency (allow varying frequencies)

In the following, a concept for such a protection device is presented, which is based on solid-state power controllers (SSPC) used in aircraft applications. A typical structure of a SSPC is depicted in Fig. 1.

II. PRELIMINARY CONSIDERATIONS

First, the typical short-circuit powers of low-voltage grids are evaluated, in order to determine the required current load capacity of the SSPC.

A. Evaluation of the Short-Circuit Current

Fig. 2 presents a statistical evaluation of short-circuit powers present in different connection points in German low voltage grids. The data set cuts right across the fields of typical rural and

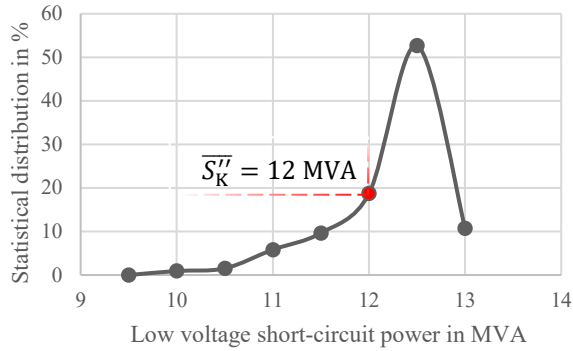


Figure 2. Typical short-circuit power in low voltage grids derived from data of a German distribution grid operator

urban areas in mid Germany. Data from over 10,000 localities was analyzed. As a result, it can be concluded, that the average short-circuit power in German low voltage grids is approximately 12 MVA.

Additionally, grid impedance measurements at two different connection points in the laboratory (16 A and 32 A, three-phase) were conducted in order to validate these values. The impedance measurement device NIM1000 [2] was used for this purpose. This measurement device allows the determination of the short-circuit current and grid impedance in compliance with DIN EN 61557-3 and VDE 0413-3 [3]. The loop impedances L1-N, L2-N, L3-N, as well as L1-L2, L1-L3 and L2-L3 were determined, with an accuracy of three percent. The frequency range of the measurement results ranges from 0 to 500 Hz. Tab. I shows the resulting measurement data. The highest measured prospective short circuit current ($I_K'' \cdot \sqrt{2}$) amounts to 3.55 kA.

TABLE I. MEASUREMENT VALUES OF 2 CONNECTION POINTS IN THE LABORATORY.

Connection Point	Loop	I_K'' in kA	$R@50\text{Hz}$ in m Ω	$X@50\text{Hz}$ in m Ω	$Z@50\text{Hz}$ in m Ω
16 A	L1-N	1.67	131	23	133
	L2-N	1.69	129	24	132
	L3-N	1.65	132	24	134
	L1-L2	2.46	153	27	156
	L1-L3	2.51	149	30	152
	L2-L3	2.52	150	26	153
32 A	L1-N	0.69	319	31	320
	L2-N	0.69	320	32	321
	L3-N	0.69	317	34	319
	L1-L2	1.13	331	40	333
	L1-L3	1.17	338	37	324
	L2-L3	1.15	332	35	334

B. Design Requirements

1) MOSFET vs. IGBT

In order to ensure a high reliability of the SSPC, a self-test is to be incorporated into the design concept. A possible solution is proposed in [4]. This self-test does not interfere with the power supply of the load, because it operates without interruption during a self-test procedure. For this concept, only MOSFETs are applicable, because several semiconductor switched need to operate in parallel and a secure parallel operation of IGBTs is much more complicated due to their

negative temperature coefficient. Therefore, an architecture consisting of several anti-serial MOSFET pairs connected in parallel form the power switch unit is used.

2) Galvanic isolation

The presented SSPC is controlled by a real time system, which ensures a high flexibility in programming protection algorithms. In order to protect the real time system from high voltages, only galvanically isolated voltage and current sensors are to be used. Furthermore, all digital control signals need to be galvanically isolated as well.

3) Current and Voltage Specifications

Prior to the concept-phase the rated currents and voltages of the SSPC were specified. The voltage ratings correspond to those of German low voltage grids specified in DIN EN 50160. The size of the temporary over-voltages the SSPC needs to withstand is specified in chapter III.B. The rated current and the rated pulsed current of the SSPC are predefined. The amount to 50 A_{RMS} and 200 A_{RMS}, respectively.

III. AIMS OF INVESTIGATION: PROTECTION REQUIREMENTS

A. Limiting of current transients

The maximum SCC determined in the course of the impedance measurements exceeds the pulsed current stability of a typical Power-MOSFETs by approximately the factor 18. To cope with such high currents, several MOSFETs may be connected in parallel. However, a high amount of MOSFETs would be necessary. Since short-circuit failures are rare events, such a parallel connection would be inefficient and uneconomical. Moreover, connectors, conducting paths of printed circuit boards and the cooling system have to be dimensioned disproportionately compared to the rated value of the current, in order to withstand the thermal stress of a short-circuit failure. Hence, a protection unit which detects short-circuit events before the maximum value of the SCC is reached is needed.

Here a detection algorithm based on the current slew rate (di/dt) is proposed. Since one of the design requirements is the usage of galvanically isolated sensors, such as hall-sensors, a software based detection algorithm cannot manage such a problem in admissible time due to sensor latencies. Sensor latencies also propose a problem in case the grid is fed by low inductive sources such as big accumulators. Thus, the current slew rate measurement is implemented with the help of analogue hardware components. Since the voltage drop over a coil is proportional to the current slew rate di_L/dt and the coil's inductance L (1), this proposes placing a coil in series to the SSPC and measuring the voltages drop V_L :

$$V_L = L \frac{di_L(t)}{dt} \quad (1)$$

B. Temporary Over Voltages in Low-Voltage Grids

The nominal phase-to-neutral and phase-to-phase voltages of German low-voltage grids is 230 V_{RMS} and 400 V_{RMS}, respectively. According to DIN EN 50160 [5] the maximum permanent deviation from nominal voltages are +/- 10%. Therefore, the maximum permanent voltage V_{\max} is 565 V_{peak}.

MOSFETs are very sensitive to over-voltages during which they can easily be destroyed. In order to have a safety margin that includes voltage peaks caused by switching events and voltage raises caused by single pole failures, V_{\max} is multiplied with a safety factor of 2. This results in a voltage rating of 1243 V, which was rounded down to 1200 V. The minimum required voltage stability of 1200 V serves as a reference value for the part dimensioning. During operation, over-voltages of this level have to be avoided by using an appropriate protection circuitry.

C. Inrush Currents

When capacitive loads are to be protected by the SSPC, high inrush currents may occur during turn on. The height of the inrush current highly depends on the value of the load capacity, the wire or path capacities, the ohmic resistances of wires, paths and loads as well as inductances of coils, chokes or power-inductances. As a simplified equivalent network, this results in a series resonant circuit [6] as shown in Fig. 3.

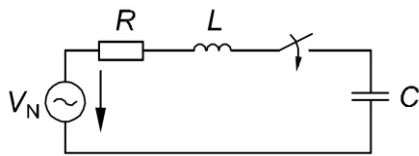


Figure 3. Series resonance circuit

D. Summary

Based on the requirements presented above, the main parts and functions of the SSPC, which are to be designed, are as follows:

- Withstand over-voltage ($V_{\text{peak,max}} = 1200 \text{ V}$)
- Short circuit detection
- Inrush current limiter
- Over-voltage protection

IV. BASIC CONCEPT

The requirements review of chapter III is followed by the concrete development. The SSPC had to fulfil the highest operational standard in modularity and flexibility and comply with the requirements of the task and the factors resulting from the requirements review. The SSPC consists of one module per phase. The single modules are connected with an adapter plate. The adapter has two grid connectors and a 24 V supply pin. Moreover, the adapter plate has an internal circuit that realized a synthetical neutral point and the voltage respectively current supply of the control circuit. The abstract setup with the elements of the SSPC is depicted in Fig. 4.

A. Power Switch

The power switch of each SSPC module consists of nine parallel anti-serial n-channel MOSFET-pairs of the model Cree C3M0075120J. One MOSFET-pair is driven by one gate-driver. Because of the high-side configuration, the voltage supply had to be realized with galvanic isolated DC-DC-converters.

To manage the rated current of 50 A and the pulsed current of 200 A, three parallel MOSFET-pairs would have been sufficient. By raising the number of parallel MOSFET-pairs up to nine, the reliability was increased because of the lower junction temperature. Normally the reliability would decrease with higher count of parallel MOSFETs. Hence, the failure rate λ of the anti-serial configuration rises in accordance with (2) proportional to the number of parallel MOSFET-pairs:

$$\lambda_{\text{total}} = 2 \cdot \lambda_{\text{MOSFET}} \cdot N \quad (2)$$

The Siemens Norm SN29500-3 gives reference values for the failure rates of Power-MOSFETs. With the aid of a temperature specific correction factor π_T the failure rate at a specific junction temperature can be determined. The direct comparison between three and nine parallel MOSFET-pairs

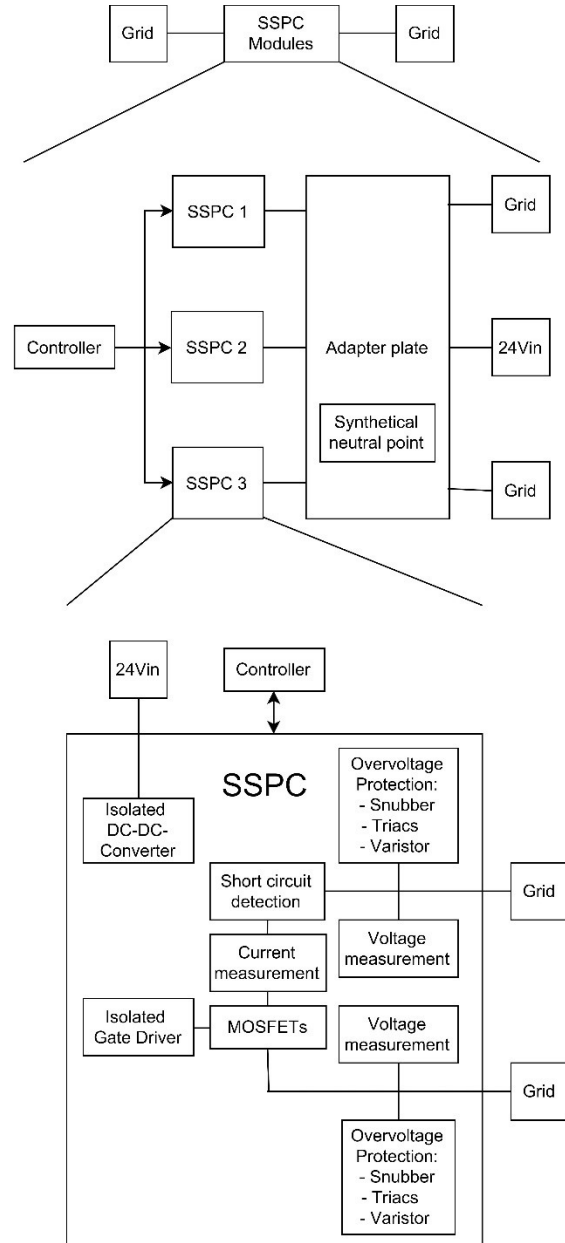


Figure 4. Concept overview. The interconnection of the single SSPC modules and the structure of a single SSPC are depicted.

showed a reduction of the failure rate by 70%. This is caused by the smaller junction temperature:

$$\lambda_{\text{total}} = \pi_T \cdot 2 \cdot \lambda_{\text{MOSFET}} \cdot N \quad (3)$$

B. Inrush Current Limiter

A separated pair of MOSFETs in series with two NTC-thermistors and one pulse stable ceramic-compound-resistor were connected in parallel to the power switch in order to limit the inrush current during turn on. The inrush current limiting path is able to absorb the energy of two sinus waves of 50 Hz. When the SSPC is switched on, the load is firstly supplied via the inrush current limiting path. After approximately 40 ms the main switch turns on and the inrush current limiter is switched off. The structure of the current limit path and its integration into the power switch is depicted in Fig. 5.

C. Over Voltage Protection

The designed over-voltage protection consists of three stages and is placed both at the load and grid side of the SSPC.

A snubber circuit damps short transients. Its resistor and capacitor were dimensioned with the information retrieved with the help of the grid impedance measurements. To face voltage-peaks caused by high inductances (exceeding the measured grid inductance), a TRIAC circuit is used. A DIAC triggers two parallel TRIACs connected in series to a pulse stable ceramic-compound-resistor and a fuse in case the rated voltage is 10 % higher than allowed. The resistor limits the current of the TRIACs to the rated current of the SSPC. Hence, repetitive triggering is possible. In case of permanent over-voltages caused by failures, the fuse triggers and opens the circuit.

Voltage transients, which the snubber circuit is not able to handle, and which are too steep for triggering the TRIACs respectively (di/dt is too high), are problematic. This problem is solved using varistors. They were chosen such that they only trigger when both the snubber circuit and the TRIAC circuit fail to filter the voltage transients. A major disadvantage of varistors

is, that their lifetime reduces with every triggering event and as a consequence their leakage current increases until the varistor is destroyed. Since the varistor then acts as a short circuit, a fuse is connected in series to the varistor. To ensure, that the controller is able to detect whether the fuse is triggered (varistor destroyed), an AC opto-coupler is used to decouple a voltage signal from the fuse. As long as the fuse is intact the opto-coupler is switched on and supplies a capacitor via a isolated DC-DC-converter. The controller can then measure the voltage of the capacitor in order to detect a maloperation of the varistor.

D. Short-Circuit Detection

As described above the short-circuit detection is realised via a measurement of the current slew rate. The current slew rate is not measured directly, but rather via a measurement of the voltage drop over a coil, see section III.A.

The basic idea is, that the short circuit detection is able to detect a short-circuit failure before the maximum value of the short-circuit current is reached. Unlike voltages, currents cannot jump at inductances as the following equation shows:

$$i_L(t) = \frac{1}{L} \int u_L(t) dt \quad (4)$$

In case of a short-circuit event on the load side of the SSPC and the assumption, that R_{Load} is much smaller than 2 Ohm, the voltage is divided between the SSPC and the grid impedance. In order to predict the time response of the coil and the amplitude of the voltage drop over the coil in case of a short-circuit event, the network is transformed into its Laplace representation, which is depicted in Fig. 6.

The Laplace representation results from the assumption, that the short-circuit failure occurs in the most disadvantageous case, at the maximum or peak value of the current. The grid voltage is described as a sinusoidal signal with a phase difference angle φ . Transformed into the image section this leads to the following equation for the voltage (6).

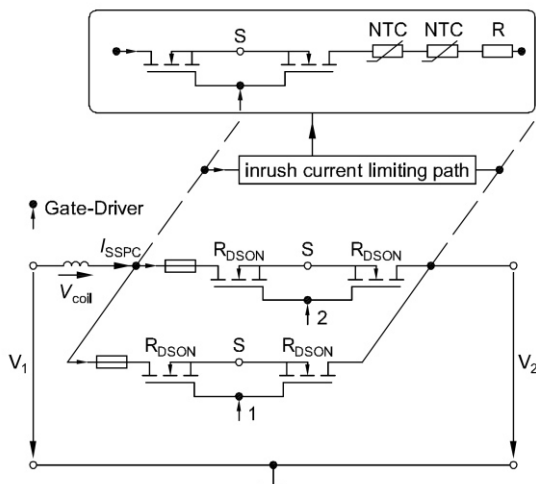


Figure 5. Laplace representation of the network. The dashed line represents the short-circuit path.

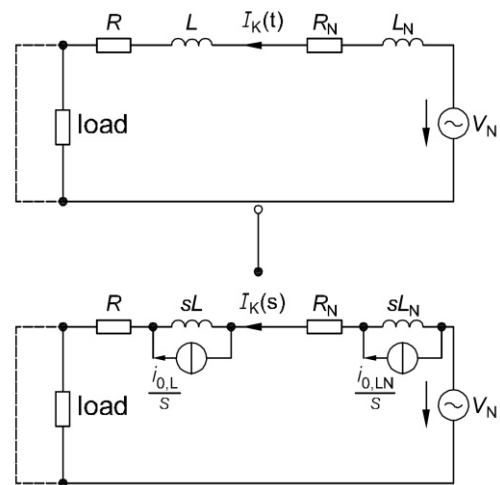


Figure 6. Laplace representation of the network. The dashed line represents the short-circuit path.

$$v(t) = \hat{u} \cdot \sin(\omega t + \varphi) \quad (5)$$

$$V(s) = \frac{\hat{u} \cdot (s \cdot \sin(\varphi) + \omega \cdot \cos(\varphi))}{s^2 + \omega^2} \quad (6)$$

To determine the short circuit current $I_K(s)$, the superposition principle was used. The short circuit current $I_K(s)$ in the image section has been determined by the summation of the partial short-circuit currents. The inverse transformation, back into time domain, leads to the following equation:

$$I_K''(t) = \frac{\hat{u}}{R_N + R} \cdot \frac{1}{1 + (\omega\tau)^2} \cdot \left[-\omega\tau \cdot \cos(\omega t + \varphi) + \sin(\omega t + \varphi) + e^{-\frac{t}{\tau}} (\omega\tau \cos(\varphi) - \sin(\varphi)) \right] + i_N e^{-t/\tau} \quad (7)$$

$$\tau = \frac{L_N + L}{R_N + R}$$

The inductance of the SSPC may not disturb the operation by producing a noticeable voltage drop or negative influence on the phase difference angle. Inductances with a magnetically soft core can be build considerably more compact, because of the higher permeability. The inductivity may not become saturated in any operation case. Furthermore, a too small distance from the saturation during switching on has to be avoided due to remanence effects. The chosen inductivity has a saturation current of 280 A, an inductivity of 2,2 μH and a resistance of 0,22 $\text{m}\Omega$. Depending on the current and its slew rate the voltage drop over the inductance can be determined by:

$$U_L(t) = U_{\text{ind}}(t) + U_R(t) = L \cdot \frac{\partial I_K(t)}{\partial t} + I_K(t) \cdot R_{\text{coil}} \quad (8)$$

By varying the values of the grid impedance in the equations above, the occurring voltages over the coil in case of a short-circuit event may be determined analytically. Using a galvanically isolated logic circuit with back coupling to the control circuit of the power MOSFETs, the voltage supply of the gate-drivers is disconnected in case of a short-circuit event. This results in the opening of the power switch. The interruption of the gate-driver's supply only lasts for a few milliseconds. However, during the interruption the controller measures a current near zero via the hall-sensor even though the controller sends a high signal to power MOSFETs driver circuit. Hereby the controller is able to detect the failure as a short-circuit event and starts sending a zero volt signal to the drive circuit of the power-MOSFETs in order to shut of the SSPC permanently.

V. CONCLUSION

This paper presents a concept for a solid-state power controller which can be used in low voltage electrical grids with either high or low short-circuit powers. Hence, it is ideal for grid regions that are exposed to the risk of unintentional islanding. This is achieved via a limitation of current transients using a

current slew rate measurement and via an adaptable design, where voltage, current and I^2t characteristics are adjustable.

Furthermore, the SSPC may be used for grid protection in electrical networks that may either be operated with a connection to the mains supply or as a stand-alone emergency supply network. This is realized by a novel short-circuit detection unit, that is capable to limit the short-circuit current and switch off short circuit failures, before the SCC reaches a thermal harmful value. Advantageous for this purpose is the fast switching ability of the MOSFETs.

The developed SSPC may be used in one and multi-phase operation, with or without a neutral point. For each phase, one SSPC module is necessary. With the help of an adapter (printed circuit board) the SSPC modules are installed into a 19-inch rack combined in order to form a three-phase SSPC. A 3D model of the setup is depicted in Fig. 7.

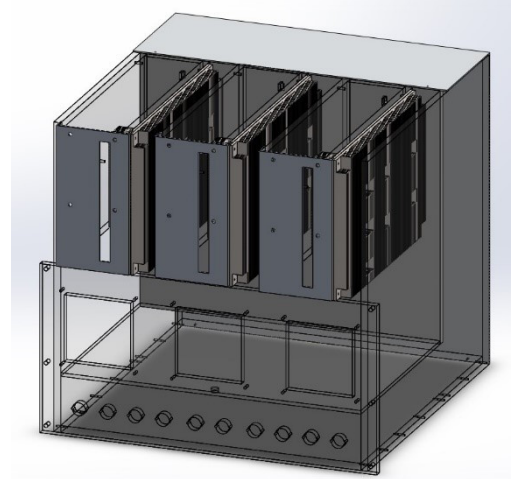


Figure 7. 3D model of the 19-inch rack designed to combine three SSPC modules in order to form a three-phase SSPC.

REFERENCES

- [1] DIN EN 60909-0, VDE 0102:2016-12, Short-Circuit Currents in Three-Phase Systems (German title: Kurschlussströme in Drehstromnetzen)
- [2] Megger GmbH: NIM1000, 2017. <https://de.megger.com/netzimpedanz-pruefgerat-nim1000>, [Online; Last accessed: 15. Februar 2018]
- [3] DIN EN 61557-3:2017-12, VDE 0413-3:2017-12, Electrical safety in low voltage distribution systems up to 1000 V a.c. and 1500 V d.c. – Equipment for testing, measuring or monitoring of protective measures (German title: Elektrische Sicherheit in Niederspannungsnetzen bis AC 1000 V und DC 1500 V – Geräte zum Prüfen, Messen oder Überwachen von Schutzmaßnahmen)
- [4] F. Grumm, M. F. Meyer, E. Waldhaim, M. Terörde, D. Schulz, Self-testing Solid-State Power Controller for High-Voltage-DC-Aircraft Applications, NEIS Conference 2016, Conference on Sustainable Energy Supply and Energy Storage Systems, Hamburg, Germany.
- [5] DIN EN 50160:2011-02, Voltage characteristics of electricity supplied by public distribution networks (German title: Merkmale der Spannung in öffentlichen Elektrizitätsversorgungsnetzen)
- [6] J. Specovius, Fundamental Course on Power Electronics: Components, Circuits and Systems (German title: Grundkurs Leistungselektronik: Bauelemente, Schaltungen und Systeme). Springer-Verlag, 2017.

Demand Side Integration Architecture for low voltage smart grids

Sara Mohammadi

Energy System and Energy Management
University of Kaiserslautern
Kaiserslautern, Germany

Abstract—Utilities around the world have been considering Demand Side Integration (DSI) in their strategic planning. The main aim of Demand Side Integration is to assist users to be engaged in attenuating peak demands and costs on the electricity network and change their nominal consumption patterns. This results in increasing sustainability of the smart grid, the use of renewable energy and reducing overall operational cost and carbon emission. Demand side management (DSM) and Demand Response (DR) are the main techniques which are involved in the integration of the demand side. As the penetration of DSM and DR increase, incorporating the network model into the DSI analysis algorithm becomes necessary. Most of the existing strategies used in traditional energy management systems handle only a limited number of loads of limited types. This paper focuses on the demand integration architecture based on day-ahead load shifting technique with a large number of devices and discusses some practical considerations associated with this approach. The load shifting methods proposed in this work are time of use (TOU), real time pricing (RTP) and direct load control (DLC) which change the turn-on time of devices according to usage probability.

Keywords-component; Demand Side Management; Demand Response; Load shifting; TOU; RTP; DLC

I. INTRODUCTION

Maintaining the balance between generation and consumption in the power system is generally based on the controllability of the generated energy of power plants. The other balancing method is the control of loads. It is more reasonable in the power sector to manage electricity demand than to increase power supply or transmission capacity.

Demand Side Integration programs are used to reduce the need of additional peak or base load generating capacity or distribution facilities and includes the algorithms of demand response (DR) and Demand Side Management (DSM). Demand Side Integration (DSI) is an important feature of smart grid to manage energy.

DR refers to the costumers' reactions to monetary incentives like time dependent tariffs and DSM mostly defines as the direct influence on the load by decreasing or increasing the energy demand at a certain time. The point in DSM/DR is to efficiently shift the load to some other point in time. This causes inconvenience to the customer and therefore it should be minimized.

In this work, the architecture of demand side integration is proposed based on demand side management and demand response strategies. Efficient demand side integration can avoid the construction of an under-utilized electrical infrastructure in terms of distribution networks, generation capacity and transmission lines. Controlling energy demand can decrease the overall peak load demand and increase the grid sustainability and security by reducing the overall cost, carbon emission levels and global warming.

II. TECHNIQUES AND METHODS

A. Demand Side Management

Demand side management focuses [1] on utilizing power saving technologies, electricity tariffs, monetary incentives, and government policies to mitigate the peak load demand instead of enlarging the generation capacity or reinforcing the transmission and distribution network. DSM aims to reduce or shift the load from peak hours to off-peak hours. DSM is associated with the long-term changes in the electricity consumption achieved through investments in energy efficiency or changes in customer behavior.

In DSM, load can be projected as a curve (load profile curve) and has six main techniques used for load shaping which is shown in Fig. 1 [2]. Generally, these are the possible DSM techniques that can be employed in the grids.

- a. Peak clipping: Reduction of loads during the electricity rush hour. Peak clipping [3, 4] is a direct load control technique to make reduction of the peak loads.
- b. Valley filling: Construction of loads during off-peak hours by applying direct load control.
- c. Load shifting: Takes advantage of time independence of loads and Shifts loads from peak hours to off-peak hours.
- d. Load conservation: Conservation of power by reducing the complete load for a long term (in hours or in days).
- e. Load growth: [3, 4] optimizes the daily response in case of large demand introduction beyond the valley filling technique and increases the consumption of power with certain limit.

- f. Flexible load shaping: Redistribution of load to various time slots for On-Demand Service. It is mainly related to reliability of smart grid.

The combination of the mentioned techniques enables the load curve to follow generation as close as possible. Example of programs in this category is Direct Load Control (DLC). DLC allows utilities to remotely manage demand by directly modifying the operation of end-use devices. Ordinarily, DLC programs involve a utility or equipment that allows them to switch specific appliances on and off for a short time during peak periods. In return, consumers are usually rewarded by way of a financial incentive. It could decrease the amount of assets needed to fulfill current demand using existing methods of power generation (mostly fossil-fuel) and would significantly increase the load factor [2].

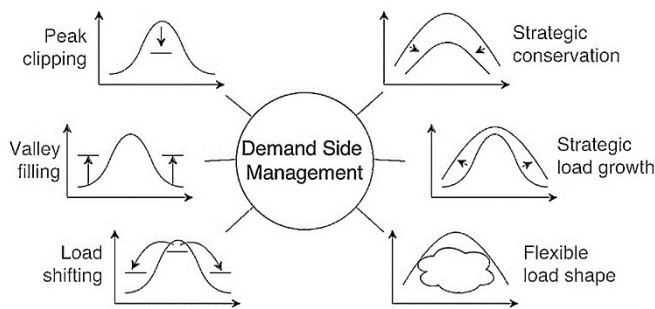


Figure 1. Load shaping techniques [3]

B. Demand Response

Electric demand response (DR) refers to the changes in the electricity usage by the end-use customers from their nominal consumption patterns in response to changes in the price of electricity over time, or to incentive payments designed to induce lower electricity use at times of high wholesale market prices or when the system reliability is jeopardized [4]. Demand response is often associated with the short-term changes targeted for the critical hours during a day/year when the demand is high or when the reserve margin is low.

Demand response programs can be categorized into two major groups in this paper. Each mentioned group can also be categorized into some sub-sets as illustrated below:

- Incentive-based methods Utility offers a flat price, which is defined on a yearly basis. In this category a set of demand reduction signals are issued by the aggregator and sent to the participating customers in the form of voluntary demand reduction requests or mandatory commands.
- Price-responsive methods are based on dynamic pricing rates in which electricity tariffs are not flat; the prices fluctuate following the real time cost of electricity. The aim of these programs is to flatten the demand curve by offering a high price during peak periods and lower prices during off-peak periods. The most common rates

are defined as Time of Use (TOU) and Real Time Pricing (RTP) programs in this work.

- Time-of-use (TOU): Price is based on three different time periods (i.e. off-peak, shoulder, on-peak) each day, and is fixed at least for two years. The simplest rate involves just two pricing periods, a peak period and an off-peak period.
- Real-time-price (RTP): This rate design features prices that vary hourly or sub-hourly all year long, for some or a customer's entire load. Customers are notified of the rates on a day-ahead or hour-ahead basis.

Fixed electricity tariff is very archaic and introduces cross-subsidies between customers. There is simply no incentive for customer to contribute in making the system more efficient [5]. Fig. 2 shows how price-based incentives changes price elasticity and how small reduction in demand will result a big reduction in generation cost and, in turn, a reduction in electricity price.

If real-time pricing was implemented, the price would become elastic on the demand side opposed to fixed price tariff. On the other hand, increased number of renewable would also reshape the supply curve. During the times when green energy is scarce, the price for the same amount of energy would increase, shifting the curve up. That happens because renewable energy, like wind or solar, has very low running costs. All in all, demand response techniques would allow customers to participate both saving money and being more environmentally friendly.

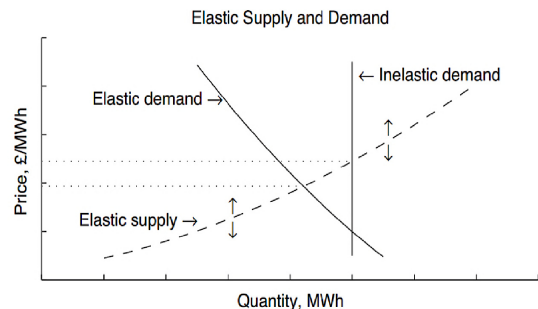


Figure 2. Supply and demand of electricity [2]

III. RELATED WORK

In recent many Demand Side Management and Demand Response strategies have been proposed and improved. The main objective of all these techniques is minimizing the cost and peak load demand. In [6] evolutionary algorithm is used to schedule a large number of appliances. This algorithm makes the load curve and the objective curve closer, which is the given electricity price signal. Different types of loads are handling in this work, i.e., residential, commercial and industrial loads. To tackle a large number of loads, the results show this method is more efficient compared to mathematical approaches.

An Integer Linear Programming (ILP) based appliance scheduling scheme to shift the load from on-peak to off-peak to reduce cost and peak load is proposed in [7]. In [8] author

proposed the architecture of DSM, which integrates renewable energy in the power system to minimize the expense of the users. To minimize overall cost, Linear Programming (LP) based Optimization-based Residential Energy Management (OREM) scheme is proposed in [9]. A Mixed Integer Linear Programming (MILP) method is used for scheduling various types of appliances to reduce the electricity cost in [10].

To avoid distribution system overloading, an algorithm is proposed in [11], which checks the priority of appliance and shut them down. Avoiding distribution system overloading is discussed by proper load shedding. Optimal Stopping Rule (OSR) is proposed in [12]. This method is a mathematical optimization technique which helps user to schedule its appliance at the time where the price is low. This strategy reduces the electricity consumption cost. Stochastic optimization-based cost minimization problem with the integration of renewable energy is proposed in [13] by using LYAPUNOV optimization approach.

To increase the efficiency of network, an integration of renewable energy in the power system is proposed in [14], user minimize its monetary expenses by trading grid energy. In [15], author presents a method of synthesizing domestic load profiles as a better solution compared to standard load profiles. This method is implemented in a tool developed in MATLAB.

Almost all of the techniques and methods mentioned above were developed using OSR, ILP, LP and MILP cannot tackle a large number of appliances. In addition, the distribution of loads is over several hours, i.e., the duty cycles of all load types are different. Comparing to other strategies, the method proposed here is able to handle all these parameters in an efficient and fast way. Annual consumption, distribution of energy requirements, frequency distribution, etc. are presented and probability distribution is the main algorithm in this work.

IV. LOAD SHIFTING METHOD DESCRIPTION

The DSM and DR change user behavior so that users choose to use their devices at different times. These times are calculated from load curve. The load curves can be created as a standard load profile. The standard load profile is the average load curve of a device valid for a high number of devices. To create the standard load profile first a time vector of a specific year is created. By multiplying the usage statistic of a week with the corresponding day the values result with respect to the weekday, a resulting probability density vector. The density vector is the basic standard load profile so far.

To have dynamic load profile and to avoid the discontinuity between the winter and summer probabilities at the transition of the seasons the density vector should be dynamised. For example, At the transition from winter to summer the value of dynamic density vector has to become the average of winter and summer probability weighted by time [15].

The difference between three types of days a week (Monday-Friday, Saturday and Sunday) and 24 hours a day results the standard load profile dynamization of a single device. Finally, the density vector is normalized to the sum of it. Then the density vector is multiplied with the devices energy demand and results the device's standard load profile. By summing up the density

vector it results probability distribution that its value is from close to zero rising to one. The devices energy demand divided by the energy content of a single use profile provides the number of the devices usages per year. To create synthetic load curve a random number between zero and one is generated. The random number compared with the probability vector returns an index at which previous values are smaller and following values are larger than random number. The same index value in the previously created time vector shows the time the device is used. This timing refers to the energy median of a single use curve. Then the single use profile is added to the load curve at a specific time and this process is repeated but there are some restrictions. If the device is already running at the new generated timing the new date is discarded to avoid overlapping. These operations are repeated until enough valid usage times are found and the load curve is completed. Afterwards this iterates for all devices in every household [15].

For load shifting of electrical appliances, their requirements must be taken into account. Usually, the requirements consist of two factors: the amount and quality of the energy. This means supplying the household appliance with sufficient energy to perform a specific process, while ensuring the voltage, continuity of the current, and other factors within a given interval. For example, the washing machine is a very high requirement for the quality of energy. Therefore, shifting the starting point of the washing machine is a suitable measure for demand side integration. In contrast, e.g. the hot water tank is a high demand on the amount of energy, but a relatively low-quality requirement. In this case, the interruption of the energy supply during the process is also a possible measure for the load shift. The most important methods using in this work is described as follows.

A. Time of Use (TOU)

In the context of this work, TOU rates apply only to the operating time or the switch-on time of washing machines, dishwashers and tumble dryers. According to the project Moma, in city model of Mannheim [16], 107 households participated in the project between October 2010 and August 2011, and two-thirds of the participants have changed their electricity consumption patterns since the beginning of the project, according to the final survey. Therefore, it is assumed that this customer reaction is transferable to this work as parameter (K) if the price difference between low tariff and high tariff does not change. Therefore, customer reaction can be saves as (K) which describes the will of a household to save money. In the algorithm, the customer response K results as a random value from 1 to 3, the same reaction probability users had in the project Moma. If the customer response K of a household is less than 3, this means that this household wants to save money through TOU tariffs, as two-thirds of the subscribers.

In this case, the program will always give the household a new start time, randomly chosen according to the frequency distribution, until the associated operating time is in the low tariff. It should also be noted that if a household wants to save money through TOU tariffs, but the operating time e.g. the washing machine in this household coincidentally lies in the low tariff, then this operating time remains unchanged. Considering the German current electricity price of 28.8 ct/kWh, the prices

for the low and high tariffs used in this work are set at 25.2 ct/kWh and 34.8 ct/kWh. In this case, the average electricity price of one day still remains at 28.8 ct/kWh.

B. Real Time Pricing (RTP)

Real time pricing is a time-based pricing method, and indirectly influences the load profile via the consumer. Therefore, RTP tariffs are only valid for the operating time or the switch-on time of washing machines, dishwashers and tumble dryers. For RTP rates, prices change more frequently than at TOU rates, e.g. hourly or within shorter periods of time, whereby prices are usually based on prognostic consumption and prognostic feed-in [17]. In this case, the price structure of RTP tariffs depends on the weather conditions, the season, etc. Therefore, the following data are relevant to the analysis of the impact of RTP tariffs on electricity consumption:

- prognostic load and feed taking into account the weather conditions
- Price differences between the rates
- the associated customer reaction

According to the final report of E-DeMa project [17], the tariff structure consists of 5 tariffs in a day: low tariff (ST), secondary tariff (NT), main tariff (HT), high tariff 1 (HHT1) and high tariff2 (HHT2). In contrast to TOU tariffs, the tariff structure of RTP tariffs changes daily. In addition, the prices are offered within one day only in hourly blocks, as shown in Fig 3.

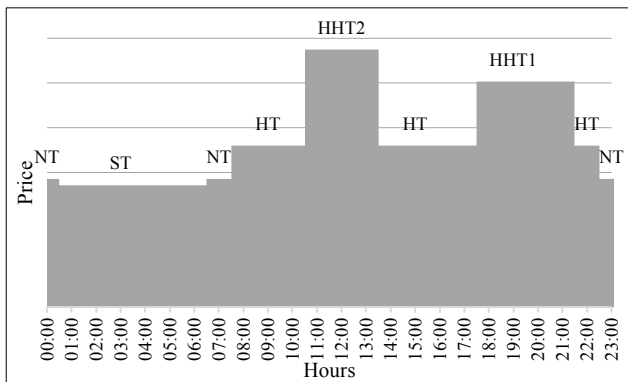


Figure 3. RTP-Tariff structure on Saturday, winter

Because of too many uncertain impacts on consumption, the best way to determine and communicate the structure of RTP tariffs is day-ahead, so that network operators can more accurately forecast consumption and provide customers with better RTP tariffs. Due to the frequent changes in prices in RTP tariffs and the short duration between the announcement of the price and the valid day, the use of Information and Communication Technologies (ICT) is required. With the help of ICT, customers can better track and use the RTP tariffs so that these RTP tariffs can reach the target of load shifting [17].

If the structure of the RTP tariffs is calculated, the price differences and the associated customer responses must be coordinated. The E-DeMa project has used the criteria shown in table I to match the price for each tariff and switch-on probability. The prices for the tariffs consist of the NT price and a surcharge depending on the spread. Spread is the average

difference between the peak load price and the baseload exchange price in the period under consideration. For the customer response, the turn-on probability of the devices in table I is used. If e.g. A household uses its washing machine in HHT2, it changes its consumption behavior with the probability $K = K_{ST} + K_{NT} + K_{HT} + K_{HHT1} = 0,99$. When a household uses its washing machine in the HT, the probability is $K = K_{ST} + K_{NT} = 0,65$. If a household already uses its washing machine in the ST, it changes its consumption behavior with the probability $K = 0$. Through this process, the program can know if the household wants to save money through RTP tariffs. If so, the program must now use the frequency distribution to determine the switch-on time adapted to RTP tariffs.

TABLE I. TARIFF, PRICE AND CUSTOMER REACTION [17]

Tariff's Name	Price	Turn on probability of controllable devices
ST	NT-Price-1,00 ct/kWh	0,44
NT	NT-Price	0,21
HT	NT-Price+5×Spread	0,29
HHT1	NT-Price+5×(2,00 ct/kWh+Spread)	0,05
HHT2	NT-Price+5×(3,00 ct/kWh+Spread)	0,01

C. Direct Load Control (DLC)

While TOU tariffs and RTP tariffs affect power consumption indirectly through the consumer, Direct Load Control is the direct control of the equipment. For the task-driven devices, a central computer provides the customer with a control signal about the start time of use. For the program-driven devices e.g. Heat pump and refrigerator, the automatic loads shifting to adapt to the electricity supply or to avoid overloading is realized by a suitable controller, whereby the operating limit of the respective devices (e.g. the internal temperature of the refrigerator) must not be exceeded [18].

Currently, the control signals are tuned by the power grid operators. To carry out DLC, customers must first sign a contract with the grid operator. In this case, the power grid operator is able to remotely control some home appliances (heat pump, electric heater, room air conditioner, etc.) in their home. In addition to the task-driven electrical appliances, the following electrical appliances are suitable for Direct Load Control: refrigerators, freezers, night storage heaters, heat pumps and hot water storage tanks. Air conditioning and electric direct heating are also suitable for DLC.

To implement DLC, a load profile of the other electrical appliances that are not suitable for Direct Load Control must first be generated. It is understandable that DLC is a DSM measure which is very optimized for load shifting but it is unpleasant for the customer because the switch-on times and operating times of the devices are only coordinated by the computer or operator and not by the customers themselves. The impact on the load depends heavily on the number of customers participating in DLC program. To control electrical appliances, grid operators must adhere to the operating limits of each electrical appliance while minimizing customer comfort.

Therefore, Direct Load Control has a very big demand on the sensors, measuring devices, control devices, etc. [18].

D. Integration of the methodes

Fig. 4 shows the main steps of algorithm architecture for the day-ahead demand side integration strategy. According to the algorithm there are two types of DSI-capable device in the house. In case that the device is DSI capable, and user wants to decrease their electricity consumption cost, one of DR algorithms, according to the pricing method start to work.

In other cases that the device is only computer-controlled type, the central controller of the smart grid can use DSM algorithm to optimize the load profile in pick hours and save energy. Therefore, the computer-controlled devices are only suitable for DLC method. Operator starts using DSM algorithm mostly for other purposes except cost reducing and can inform the user in advance.

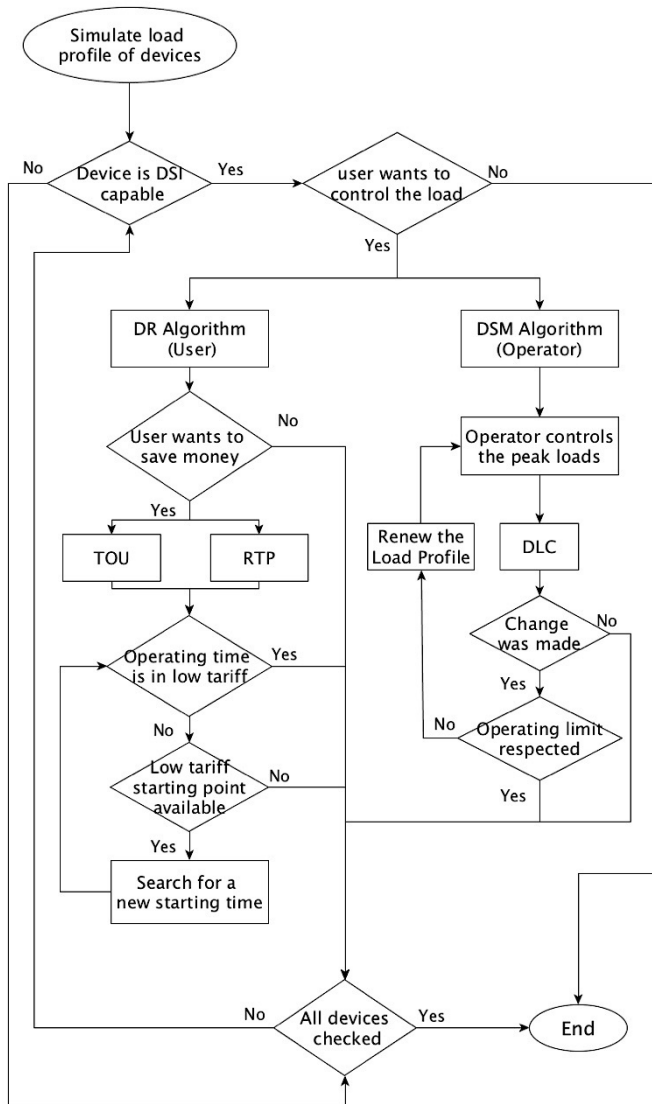


Figure 4. Main steps of the algorithm

This method is implemented to a toolbox in matlab which can be used to analyses electricity usage and price for demand side in smart grids.

V. OTHER DEVICES

There is another type of device, the user-driven devices, e.g. room lighting, kitchen appliances, televisions, etc. Unlike DSI-enabled household appliances, these user-driven domestic appliances have a relatively fixed on-time due to the environment and habit and shifting their load profile is very inconvenient or impractical for users. Therefore, this type of devices is not suitable for demand side integration and will not be considered a priority. But to replicate the daily load, these devices must be considered.

VI. CONCLUSION

Demand side integration has potential to provide many benefits to the distribution network level. The purpose of the integration could be maximizing the use of renewable energy resources, maximizing the financial benefits, minimizing the power imported from the distribution grid, or reducing the peak load demand. This paper presents a strategy that can be employed in the future smart grid. The proposed strategy is a generalized technique based on load shifting, which has been mathematically formulated as a minimization problem. Therefore, this strategy can be easily implemented to simulations and case studies. Since the electricity consumption is controlled by three different algorithms, from both operator side and user side, it can ensure a proper minimization in peak demand and bill. This strategy is capable to handle a large number of devices in a wide area of time and therefore performs efficient in smart grids.

REFERENCES

1. Maharjan, I.K., *Demand side management: Load management, load profiling, load shifting, residential and industrial consumer, energy audit, reliability, urban, semi-urban and rural setting*. 2010: LAP Lambert Academic Publ.
2. Gelazanskas, L. and K.A. Gamage, *Demand side management in smart grid: A review and proposals for future direction*. Sustainable Cities and Society, 2014. **11**: p. 22-30.
3. Gellings, C.W. and J.H. Chamberlin, *Demand-side management: concepts and methods*. 1987.
4. Commission, F.E.R., *Assessment of demand response and advanced metering*. 2008.
5. Tiptipakorn, S. and W.-J. Lee. *A residential consumer-centered load control strategy in real-time electricity pricing environment*. in *Power Symposium, 2007. NAPS'07. 39th North American*. 2007. IEEE.
6. Logenthiran, T., D. Srinivasan, and T.Z. Shun, *Demand side management in smart grid using heuristic optimization*. IEEE transactions on smart grid, 2012. **3**(3): p. 1244-1252.
7. Zhu, Z., et al. *An integer linear programming based optimization for home demand-side management in smart grid*. in *Innovative Smart Grid Technologies (ISGT), 2012 IEEE PES*. 2012. IEEE.
8. Costanzo, G.T., et al., *A system architecture for autonomous demand side load management in smart buildings*. IEEE Transactions on Smart Grid, 2012. **3**(4): p. 2157-2165.
9. Erol-Kantarci, M. and H.T. Mouftah, *Wireless sensor networks for cost-efficient residential energy management in the smart grid*. IEEE Transactions on Smart Grid, 2011. **2**(2): p. 314-325.

10. Agnetis, A., et al., *Load scheduling for household energy consumption optimization*. IEEE Transactions on Smart Grid, 2013. **4**(4): p. 2364-2373.
11. Shao, S., M. Pipattanasomporn, and S. Rahman, *Demand response as a load shaping tool in an intelligent grid with electric vehicles*. IEEE Transactions on Smart Grid, 2011. **2**(4): p. 624-631.
12. Yi, P., et al., *Real-time opportunistic scheduling for residential demand response*. IEEE Transactions on smart grid, 2013. **4**(1): p. 227-234.
13. Guo, Y., M. Pan, and Y. Fang, *Optimal power management of residential customers in the smart grid*. IEEE Transactions on Parallel and Distributed Systems, 2012. **23**(9): p. 1593-1606.
14. Yang, P., et al., *Parallel load schedule optimization with renewable distributed generators in smart grids*. IEEE Transactions on Smart Grid, 2013. **4**(3): p. 1431-1441.
15. Nau, N., *Synthesis of domestic load curves for low voltage grid simulations*. p. 6.
16. Kiessling, A., *Modellstadt Mannheim (moma)—Abschlussbericht: Beiträge von moma zur Transformation des Energiesystems für Nachhaltigkeit, Beteiligung, Regionalität und Verbundheit*. Final Report, 2013.
17. Laskowski, M., *Abschlussbericht E-DeMa, Entwicklung und Demonstration dezentral vernetzter Energiesysteme hin zum E-Energy-Marktplatz der Zukunft*. RWE Deutschland AG, 10/2013.
18. Sonnenschein, M., B. Rapp, and J. Bremer, *Demand side management und demand response*. Handbuch Energiemanagement, 2010. **3**.

Practical Approach of Realizing Co-simulation by Using eMEGASIM and ePHASORSIM based on Inverter Dominated Grid

X.Song, T. Jiang, S. Schlegel, D. Westermann
 Power Systems Group
 Technische Universität Ilmenau
 Ilmenau, Germany

Abstract— The co-simulation by combining Electro-Magnetic-Transient(EMT) model with Phasor Model(PM) has opened a new opportunity to the field of simulation in power system. The combined model also called hybrid model takes both advantages, which owns the high accuracy from EMT model and the fast execution speed from PM. Based on the traditional theory of co-simulation, this paper provides a more practical approach to realize the hybrid model, which is carried out by using of EMT solver eMEGASIM and PM solver ePHASORSIM based on the OPAL RT platform. In this paper, the inverter model that belongs to EMT will be simulated by connecting with eMEGASIM and the network is realized through ePHASORSIM. For the purpose of researching the results, the CIGRE benchmark medium voltage network will be used and then applied in the real-time simulation. Through the real-time simulation, the voltage and current dynamic characters and the advantage of hybrid model in real-time capability will be presented.

Index Terms—co-simulation, hybrid model, real-time simulation.

I. INTRODUCTION

Recently, the increasing number of power electronic based devices, such as photovoltaic, wind generation device and HVDC is interfaced with the power network [1]-[4]. Due to the inherent quick switching characteristic and non-linear nature of electronic-based controllers and devices, these power electronic converters have brought the significant challenges to the dynamic simulation of power system [1]-[2]. The conventional stability analysis of power system is usually presented by the using of performance model in quasi-steady-state (QSS) according to the fundamental frequency [5]. However, in general, the QSS models are not enough to simulate some critical fast, nonlinear dynamic behavior such as inverter commutation process [6]. Inadequate modeling of these power electronic devices could lead to erroneous simulation results regarding the system transient stability

[2],[3],[6]. While EMT models have a better accuracy to support modeling power electronic devices and AC power systems. Although they can represent network components at various levels of detail, they are computationally too burdensome for simulating a large-scale power system, compared to simplified models. Nevertheless, dynamic phasor models can be as accurate as EMT models and at the same time, faster to simulate, compared to the complicated models, when the waveforms represent the dynamic behaviour of QSS. This reduced equivalent model can be used, for instance, in the form of a low-frequency equivalent model, while the detailed EMT model simulates the sub-system, the dynamic behavior of which needs to be observed in detail [7]. By using this method, the simulation will be faster than the full EMT simulation, whereas the accuracy in somewhat decreases. The most simplistic model and the fastest solver is Phasor-Mode(PM), which are usually based on the positive-sequence phasors and used in stability studies [8]. The idea of the hybrid model can be dated back to [9]. This hybrid simulation is considered as an effective alternative to solve the challenges in the modeling and simulation. Previously, the research about the hybrid simulation was focused on the methods and techniques for combining the EMT model and PM model [3],[10] and the development of hybrid simulation tools and programs [4],[11]. In spite of significant progress in hybrid simulation, it has not been widely applied in industry or academia. One of the most important reason is that, until now, there exist no simulation tools which can testify the feasibility. The appearance of real-time simulator OPAL RT can make this testification possible. ePHASORSIM and eMEGASIM can respectively simulate the large scale over layer grid in phasor domain and in EMT based detailed equivalent model. Besides, in order to prove the feasibility, in reality, the hardware can be connected with the real time simulator, which can not only research on interaction between the model and hardware but also certify the adaptability of the hybrid model.

In this paper, the hybrid model through combining the EMT and PM will be realized by using ePHASORSIM and

eMEGASIM. In order to investigate the accuracy, the simulation speed and other characters of hybrid simulation, the paper can be organized as follows: In chapter II, this paper provides a brief overview of model classification in power system. The idea about how to realize the hybrid model will be also mentioned in this chapter. In afterward, the reason about why the real-time simulation can be used here is explained in chapter III. It follows the simulation and the discussion of the results in chapter IV, before concluding in chapter V.

II. THE SHORT REVIEW OF MODEL CLASSIFICATION AND HYBRID MODEL THEORY

The Cigré working group B4.57 published a simulation model guideline in 2014 [4]. The overall time range of power system transients is generally classified into fast electromagnetic transients (EMT), slow electromechanical transients and quasi-stationary state. Different time-domain simulation models are used for studying the different dynamic phenomena in power systems [3][4][5]. The report differentiates in total seven model types varying in depth and purpose. The models for the proposed combination in this work are focusing on types are the detailed equivalent model (DEM), average value model (AVM) and phasor model

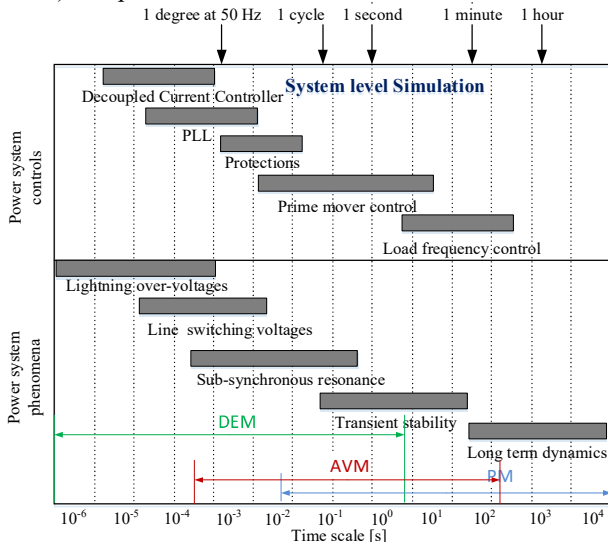


Figure 1: Model classification with time domain

A. Detailed equivalent model (DEM)

The detailed equivalent model treats the IGBTs and diodes as two-state resistive devices, while the capacitor is represented by a voltage source in series with impedance. The detailed equivalent models (DEM) are expressed as differential equations. The main usage of the DEM is to perform EMT studies, e.g. analyses on the AC and DC side or to design and to tune the low-level controllers (e.g. capacitor balancing algorithms).

B. Average value model

Based on the switching functions, the AC and DC side is modeled as a controlled current or a voltage source with harmonic content. The instantaneous values of discontinuous cells contain ripple caused by switching. AVM uses

continuous blocks, which represent the averaged behavior of the switching cell within a switching interval. The main usage of this model is to perform transient studies involving large disturbances on AC grids or to design and tune high-level control systems.

C. Phasor model

The phasor model is a fundamental frequency approach, without switching harmonics. It is often used for medium-term studies (400 milliseconds to 10 seconds). In phasor model, the converter is modeled as a controlled three-phase AC-voltage source. Network voltages (U) and branch currents (I) are expressed by complex phasors. Capacitances (C) and inductances (L) are described by their complex algebraic equations. Generally, the simulation with detailed equivalent models provides more information than average value models and phasor models.

D. Hybrid model theory

The realization of the hybrid model is by using an equivalent model through boundary condition. One of those subsystems is needed to be substituted. One feasible method is to replace the subsystem with an ideal voltage or current source. The drawback of this method is that it neglects the current or voltage change in conjunction bus [13]. Another method is to replace the EMT subsystem with a current source and the PM Subsystem with a current source parallel to an FDNE (Frequency Dependent Network Equivalent) admittance. The FDNE method produces results with higher accuracy especially with large frequency changes if the system is disturbed [14]. To represent the EMT Subsystem with updated impedance every iteration is another method, the disadvantage of it is subsystems do not offer a satisfactory performance on sensitivity, and the current change cannot be adjusted until the next time step [15].

In general, the process of the combination of PM subsystem and EMT subsystem that has the different simulation period has 5 steps, which is shown in Fig.2.

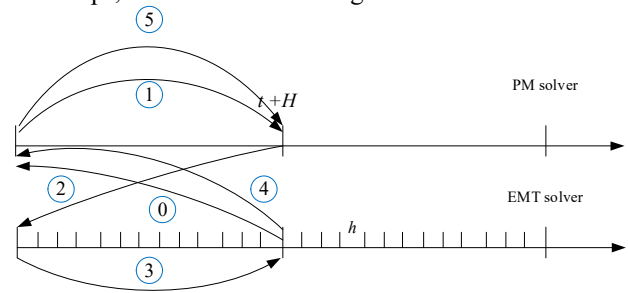


Figure 2: Calculation procedure with interaction between PM and EMT solver

Fig. 2 shows the calculation procedure with interaction between PM and EMT solver. It is recognizable that both processes have different precise over time ranges. PM's time range is H and EMT's time range is h . One iteration is finished between the time range $t \in [t_0, t_0 + H]$ for both solvers. The calculation process begins with a prediction of the EMT solver (step 0). Afterwards, the PM solver calculates results for the

time step (step 1). These results are used by the EMT solver (steps 2 and 3) and the new results are used by the PM solver again (step 5). The steps 2 to 5 are repeated until the results converge to a value.

1) From PM to EMT through time interpolation

Through the time interpolation, the voltages and currents of PM form can be transformed to EMT form with the smaller time step. In time interval $t \in [t, t + H]$, the voltage can be calculated by Thevenin equation at time $t + H$ as follows:

$$\bar{E}_{pm}(t + H) = \bar{V}^{k+\frac{1}{2}}(t + H) - Z_{pm}I^{k+\frac{1}{2}}(t + H) \quad (1)$$

The large time step H is a multiple of the small-time step h or $H = ph$ with $p \in \mathbb{N}$. The interpolated voltage magnitude at time $t + mh$ ($m = 0, \dots, p$) is defined as follows:

$$\begin{aligned} \|\bar{E}_{pm}(t + mh)\| &= \|\bar{E}_{pm}(t)\| \\ &+ \frac{m}{p} (\|\bar{E}_{pm}(t + H)\| - \|\bar{E}_{pm}(t)\|) \end{aligned} \quad (2)$$

$$\begin{aligned} \angle \bar{E}_{pm}(t + mh) &= \angle \bar{E}_{pm}(t + H) \\ &+ \frac{m}{p} (\angle \bar{E}_{pm}(t + H) - \angle \bar{E}_{pm}(t)) \end{aligned} \quad (3)$$

Consequently, the voltage Thevenin equation in EMT form can be calculated out in three-phase:

$$\begin{aligned} e_a(t + mh) &= \sqrt{2} \|\bar{E}_{pm}(t + mh)\| \cos(\omega_s(t + mh) \\ &+ \angle \bar{E}_{pm}(t + mh)) \\ e_b(t + mh) &= \sqrt{2} \|\bar{E}_{pm}(t + mh)\| \cos(\omega_s(t + mh) \\ &+ \angle \bar{E}_{pm}(t + mh) - \frac{2\pi}{3}) \\ e_c(t + mh) &= \sqrt{2} \|\bar{E}_{pm}(t + mh)\| \cos(\omega_s(t + mh) \\ &+ \angle \bar{E}_{pm}(t + mh) - \frac{4\pi}{3}) \end{aligned} \quad (4)$$

2) From EMT to PM through the phasor extraction

This process will use the three-phase current signals in EMT system. Firstly, the current will be projected into dq axis, which is applied in PLL [16]. With the transformation matrix

$$\begin{aligned} T &= \frac{\sqrt{2}}{3} \begin{bmatrix} \cos \theta & \cos(\theta - 2\pi/3) & \cos(\theta - 4\pi/3) \\ -\sin \theta & -\sin(\theta - 2\pi/3) & -\sin(\theta - 4\pi/3) \end{bmatrix} \\ i_{abc} = \begin{bmatrix} i_a \\ i_b \\ i_c \end{bmatrix} &= \sqrt{2} I_a \begin{bmatrix} \cos(\omega_s t + \varphi_a) \\ \cos(\omega_s t + \varphi_a - 2\pi/3) \\ \cos(\omega_s t + \varphi_a - 4\pi/3) \end{bmatrix} \end{aligned} \quad (5)$$

It follows:

$$i_{xy} = \begin{bmatrix} i_x \\ i_y \end{bmatrix} = I_a \begin{bmatrix} \cos \varphi_a \\ \sin \varphi_a \end{bmatrix} \quad (6)$$

With the magnitude $I_a = \sqrt{I_x^2 + I_y^2}$ and phase $\varphi_a = \arctan(I_x/I_y)$. This form is the representation of PM.

III. REVIEW OF REAL-TIME SIMULATION

A. Theory of real-time simulation

The types of digital simulation are usually divided as a simulation with the discrete-time and constant step or variable time steps. During discrete-time simulation, time moves forwards in steps of equal duration. This is commonly known as fixed time-step simulation [17]. The simulation with variable time steps is used for solving high-frequency

dynamics and non-linear systems. But it is not suitable for the real-time simulation. Accordingly, real-time simulation can only be applied in the fixed time-step simulation. The following figures 3 represent these two possibilities and explain the real-time simulation.

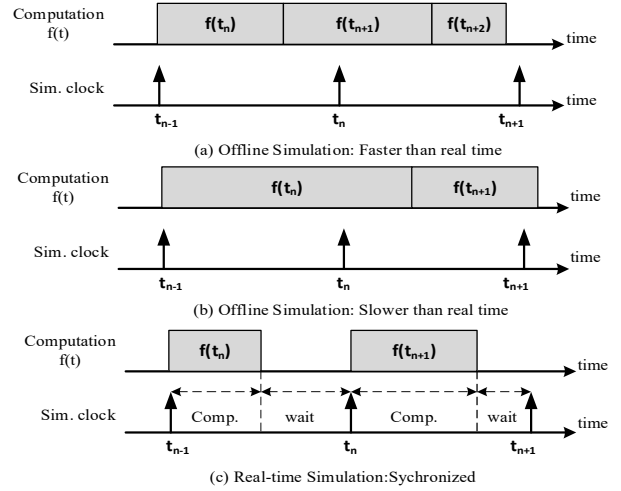


Figure 3: Comparison of Real-time simulation requisites and other simulation

In (a), the computation time is shorter than a fixed time-step, which is referred as the real time-step, while in (b), the computing time is longer. These two situations are mentioned as offline simulation. Normally, the objective is to obtain results as fast as possible, when performing the offline simulation. The solving speed depends on the computation ability and the mathematical complexity of systems.

On the contrary, the accuracy and the speed of computation of real-time simulation not only depends upon the precise dynamic of representation of the system but also on the length of the time-step used to produce the results. Figures 3 (c) illustrates the principle of the real-time simulation. For the sake of ensuring the validation of real-time simulation, the internal variables and outputs of simulation should be accurately calculated out by the real-time simulator within the same length of time that its physical counterpart would be. From the figure 3, it is apparently that the time required to compute the results at a fixed time step must be shorter than the simulation clock duration of the time-step. However, if simulator operations are not all achieved within the required fixed time-step, the real-time simulation is considered erroneous, which is normally described as an ‘overrun’.

B. Application of real-time simulation

The advantages of the real-time simulation permit the simulator to perform all operations necessary to make a real-time simulation relevant, including driving inputs and outputs to and from externally connected devices. Accordingly, real-time simulation is typically used in three different application categories, which are introduced in part (1) and (2)

1) Rapid Control Prototyping(RCP)

In RCP application, a designed controller is implemented using a real-time simulator and then is connected to a physical device. The advantages offered by RCP can avoid many

problems by implementing an actual controller. It is more flexible and faster to develop a prototype of the controller by using a real-time simulator. With just a few mouse clicks, the controller prototype can be tuned or completely modified.

2) Hardware-in-the-Loop(HIL)

Comparing with RCP, in HIL application, a physical controller is connected to a virtual plant executed on a real-time simulator, instead of to a physical device. The following figure 4 illustrate a small variation to HIL.

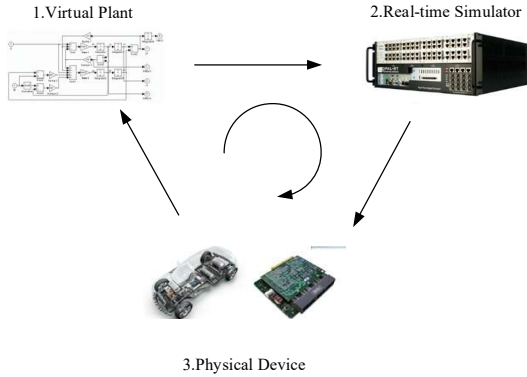


Figure 4: Process of HIL

In addition to the advantages of RCP, HIL can give controllers an early test when physical test benches are not available, the cost of which is usually less and the test of which is normally more stable. According to these, the repeatable results are allowed by using HIL and some testing conditions that are unsuitable on the physical device can be operated.

3) eMEGASIM and ePHASORSIM

For the sake of realization of hybrid simulation, two simulation systems will be applied: eMEGASIM and ePHASORSIM. These two systems correspond to the different time range. eMEGASIM offers direct platform compatibility with ePHASORSIM, procuring maximum versatility from large power grid simulation to highly detailed power electronic simulation. ePHASORSIM allows the simulation of massive grids going up to 20k buses on a single core computer and its capability of performing parallel computing allowing unleashed performances for larger real-time simulation. The typical time step of these two systems will be displayed by the following figure 5.

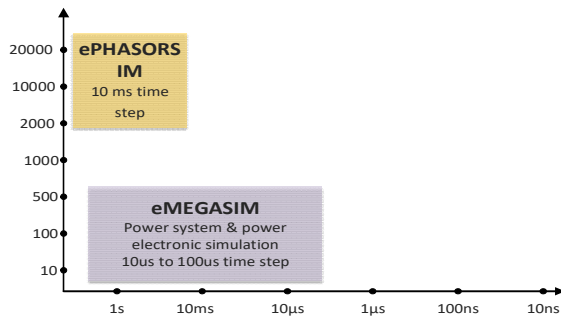


Figure 5: Period of transient phenomena simulated

From this figure, it is obviously to see that the typical time step by eMEGASIM is usually between 10us and 100us, while ePHASORSIM can only realize the simulation with the time step from 1ms to 10ms.

C. Operation of real-time simulation

The compatible modeling environment of above simulation system is adaptable in Simulink. For successfully operating the simulation, the subsystems should be divided into two parts at first: Computation subsystems and GUI subsystems, which is necessary for the RT-LAB platform. The aim of this division is to assign the computation subsystems into different CPU cores. This is shown in figure 6.

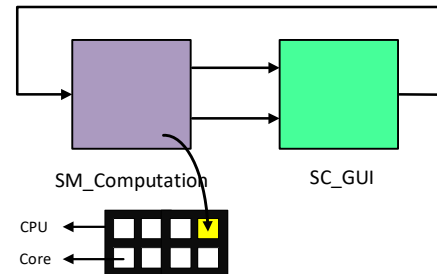


Figure 6: Two subsystems in RT-LAB platform

IV. MODEL AND SIMULATION RESULTS

To show the potential of hybrid simulation, the simulation is carried out in different scenarios and the results are compared with the results of EMT and PM models. The simulations focus on the comparison of modeling accuracy and real-time capability.

The model of the grid is constructed as follow. A 20-kV distribution grid is modeled aligning Cigré benchmark and is implemented in ePHASORSIM. Both feeders of the open ring topology operate at 20 kV and are fed via separate transformers from the 110 kV sub-transmission systems, which is a typical form of medium-voltage networks in Europe (cf. fig. 7).

The 20 kV Grid includes 16 buses, three of them are active buses, at which the converter models are connected. The converter consists of an I -control-loop, a U -control-loop and an upper-level reactive power controller for the voltage support. The converter can work bidirectionally.

For researching the accuracy of the hybrid model an operation point change is simulated. The change in current is transformed from EMT model to phasor solver for updating the grid state.

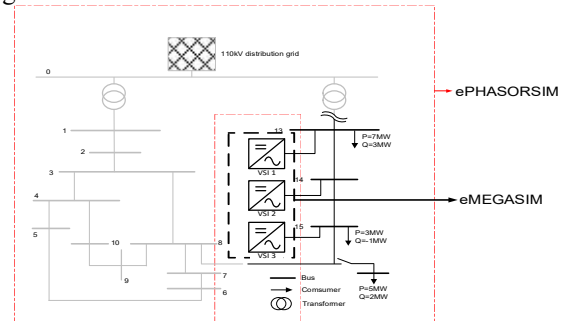


Figure 7: Grid topology with two different simulation parts[18]

In the simulation, the part of network will be simulated through the ePHASORSIM, while eMEGASIM realizes the simulation of control loop in inverter. The control structure of inverter is

shown in figure 8. As shown in table 1, the time step of control solution is usually below 100us, which is only available by eMEGASIM.

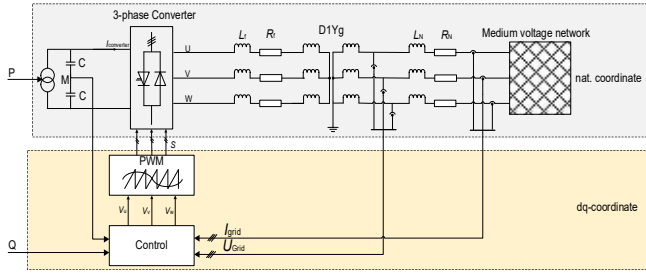


Figure 8: Control loop topology of Inverter
The current behavior at the connection point is shown in Fig. 9, the power flow caused by an operation point change is compared. The stationary behavior of the models has only relatively small deviations, though they differ in dynamical behavior. The phasor model can correct disturbances directly because of the neglected sinusoidal period. But the accuracy of the EMT model is better because of the smaller time step. The hybrid model behaves nearly like the EMT Model.

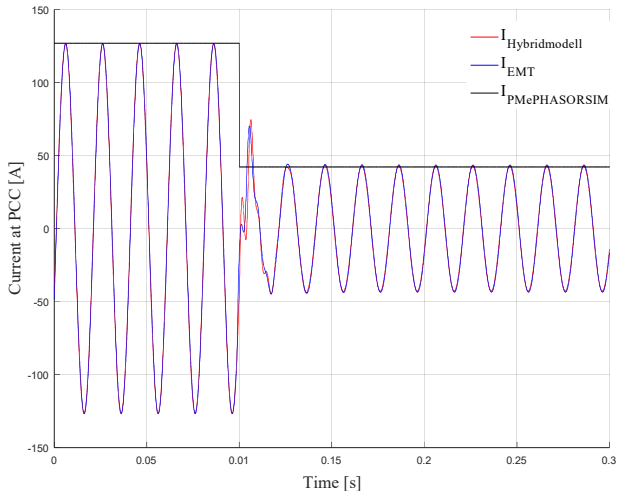


Figure 9: Current behavior at the point of common coupling (PCC)
The comparison of the voltage behavior because of the change of working state is shown in Figure 10. From the static state, there is no difference between EMT and hybrid model. Although the deviation in dynamic behavior is larger than in stationary, this little difference represents that hybrid model has comparatively high accuracy.

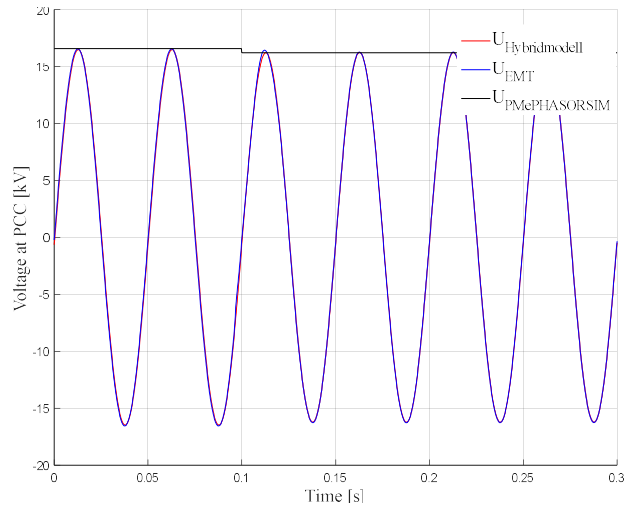


Figure 10: Voltage behavior at PCC
The power relationship on account of changing the working state is presented in fig.11. From the perspective of the static condition, the performance of the hybrid model and EMT model is same, because there is no deviation between them (see blue and red line). On the other hand, the PM model describes the dynamic process through a one-time step-down. The hybrid model because of including the part of the PM model has more sensitivity, which will lead to a bigger fluctuation (see the blue line and the red line between 0.1s and 0.11s, 0.12s and 0.13s). Despite it, the changed behavior of both models are alike and the deviation between them is smaller as 5%.

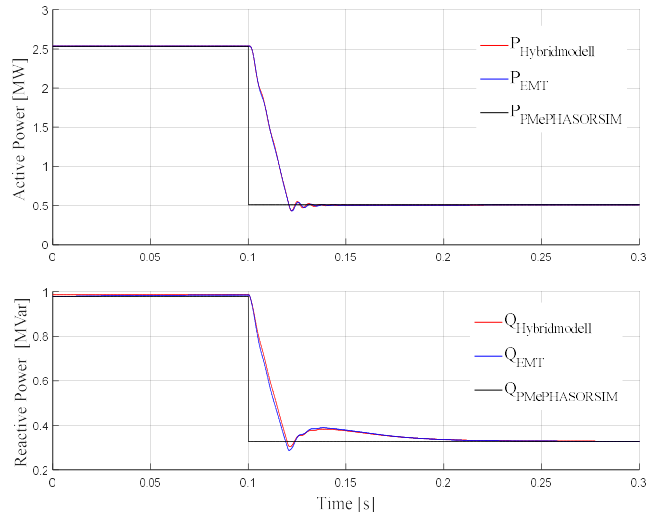


Figure 11: Behavior of active and reactive power at PCC
Table 1: Comparison of real-time capability

Model type	Number of Subsystems	Sampling time T_s	Number of inverter	U_{sage}	Runtime T_r
Hybrid Modell	1	100 μ s	1	8,45%	8,45 μ s
			3	27,45%	27,45 μ s
EMT Modell (AVM)	1	100 μ s	1	9,45%	9,45 μ s
			3	62%	62 μ s
PM	1	100 μ s	1	9,51%	9,51 μ s
			3	38.7%	38,7 μ s
PM (ePHASORSIM)	1	100 μ s	1	0.08%	0.08 μ s
			3	0.1%	0.1 μ s

Another important index is the real-time capability, which is shown in table 1. As is discussed above, the advantage of the hybrid model is that the simulation speed is faster than the EMT model and the accuracy is higher than PM. From fig.10 to fig 12, the voltage, current and power curve of the hybrid model has an only small deviation in the dynamic state with EMT model, which consequentially has higher precision than PM. From the table 1, the results of real-time simulation have presented the speed of different model type clearly. With the increasing of the inverter that is also the rise of the complexity of the model, the usage of CPU core has a different growth rate. EMT Model has the biggest rate, from 9.45% to 62%, when the number of converter increases from one to 3, which means that EMT Model is more easily to reach the overrun. However, the growth rate of hybrid model change from 8.45% to 27.45%. PM (ePHASORSIM) possesses the smallest usage of CPU core.

V. CONCLUSION

The purpose of this paper is to research on the real-time capability and characteristics of a hybrid model which combines EMT model that connects the solver with eMEGASIM and PM which simulated in ePHASORSIM. By using ePhASORSIM from OPAL-RT, it simplifies the modeling of a network because it only needs to import the grid parameters like voltage, current, impedance and so on into the document of ePHASORSIM. The connection of eMEGASIM and ePHASORSIM is possible by using the traditional co-simulation theory like time interpolation and phasor extraction. The voltage of ePHAORSIM is transformed into three phase voltages by time interpolation and then delivered to eMEGASIM. The three-phase current of eMEGASIM kann be transformed into phasor form by phasor extraction.

Compared to EMT model (AVM), the accuracy of the hybrid model in stationary operation is near to reality (relative deviation is smaller than 2%). The dynamic behaviors of EMT and hybrid model are close to an operation point change. They differ in an initializing process. About real-time capability, the hybrid model is more efficient than the EMT model. The real-time simulation of EMT model with three inverters needs about 62% CPU core usage while the hybrid model only uses 27% CPU core usage.

REFERENCES

- [1] J. Beerten, O. Gomis-Bellmunt, X. Guillaud, J. Rimez, A. van der Meer, and D. Hertem. "Modeling and control of HVDC grids: a key challenge for the future power system." *Proc. PSCC 2014*: 1-21.
- [2] A.A. van der Meer; M. Gibescu, A.M.M. van der Meijden; W.L. Kling, J.A. Ferreira, "Advanced Hybrid Transient Stability and EMT Simulation for VSC-HVDC Systems," *IEEE Transactions on Power Delivery*. vol. 30, no. 30, pp.1057-1066, 2015
- [3] Y. Zhang, A. M. Gole, W. Wenchuan, Z. Boming, and S. Hongbin, "Development and Analysis of Applicability of a Hybrid Transient Simulation Platform Combining TSA and EMT Elements," *IEEE Transactions on Power Systems*, vol. 28, pp. 357-366, 2013.
- [4] G. D. Irwin, C. Amarasinghe, N. Kroeker, and D. Woodford, "Parallel processing and hybrid simulation for HVDC/VSC PSCAD studies," in *10th IET International Conference on AC and DC Power Transmission*, 2012, pp. 1-6
- [5] V. Jalili-Marandi, V. Dinavahi, K. Strunz, J. A. Martinez, and A. Ramirez, "Interfacing Techniques for Transient Stability and Electro-magnetic Transient Programs IEEE Task Force on Interfacing Tech-niques for Simulation Tools," *IEEE Transactions on Power Delivery*, vol. 24, pp. 2385-2395, 2009.
- [6] M. D. Heffernan, K. S. Turner, J. Arrillaga, and C. P. Arnold, "Compu-tation of A.C.-D.C. System Disturbances - Part I, II and III," *IEEE Transactions on Power Apparatus and Systems*, vol. PAS-100, pp. 4341-4348, 1981.
- [7] U. Annakkage, N. K. Nair, Y. Liang, A. Gole, V. Dinavahi, B. Gustavsen, T. Noda, H. Ghasemi, A. Monti, M. Matar, R. Iravani, and J. Martinez, "Dynamic system equivalents: A survey of available techniques," *IEEE Trans. on Power Delivery*, vol. 27, no. 1, pp. 411-420, 2012.
- [8] P. Kundur, *Power System Stability and Control*, New York, 1994.
- [9] M. Heffernan, K. Turner, J. Arrillaga, and C. Arnold, "Computation of AC-DC system disturbances - Part I, II and III. interactive coordination of generator and converter transient models," *IEEE Trans. on Power Apparatus and Systems*, vol. 100, no. 11, pp. 4341 - 4363, 1981.
- [10] X. Wang, P. Wilson, and D. Woodford, "Interfacing transient stability program to EMTDC program," in *Proc. 2002 International Conference on Power System Technology, 2002*. pp. 1264-1269 vol.2.
- [11] M. Sultan, J. Reeve, R. Adapa, "Combined transient and dynamic anal-ysis of HVDC and FACTS systems," *IEEE Transactions on Power De-livery*, vol.13, no.4, pp.1271-1277,1998
- [12] F.Plumier. C.Geuzaine, and T. Van Cutsem, "A multirate approach to combine electromagnetic transients and fundamental-frequency simulations," in Proc. of Int. Conference on Power System Transients, 2013.
- [13] P.W.Sauer and M. A. Pai, "Power System Dynamics and Stability", 1st ed. Prentice Hall, 1997.
- [14] Turhan Hilmi Demiray, "Simulation of Power System Dynamics using Dynamic Phasor Models", Ph.D. dissertation, Swiss Federal Institute of Technology, 2008
- [15] F.Plumier. C.Geuzaine, and T. Van Cutsem, "A multirate approach to combine electromagnetic transients and fundamental-frequency simulations," in Proc. of Int. Conference on Power System Transients, 2013.
- [16] S.C.Gupta, "Phase-locked loops," *Proceedings of the IEEE*, vol. 63, no.2, pp. 291-306, Feb 1975.
- [17] H. W. Dommel, "Digital Computer Solution of Electromagnetic Transients in Single-and Multiphase Networks," *IEEE Transactions on Power Apparatus and Systems*, vol. PAS-88, pp. 388-399, Apr. 1969.
- [18] Cigré Working Group B4.57, "Guide for the Development of Models for HVDC Converters in a HVDC Grid," Cigré, 2014

Coupling Low Voltage Grids as Cost-Efficient Solution for Higher Share of Electric Vehicles

Christoph Baumann

Technische Universität Kaiserslautern

Lehrstuhl für Energiesysteme und

Energiemanagement Gottlieb-Daimler-Straße, 67663

_Kaiserslautern

Abstract—The share of private electric vehicle will increase in the next few years. Relatively high simultaneity is expected for the charging of private electric vehicles. In addition, a significant increase in peak load is assumed. This results in a need for investment, especially in low voltage (LV) grids. Coupling of LV grids can be a cost-efficient solution through a better distribution of the load flow. The potential for cost savings is huge as only few LV grids are coupled. However, there are barely any studies about mass coupling of LV grids, especially with special focus on high electromobility integration. This Paper provides an investigation to this topic. It deals with two tasks, the generating of worst case scenarios with achieved electromobility targets for 2030 and with the investigation of the impact of coupling to grids. In the scenarios, many different variants of charging points and charging power are considered, with simultaneous charging of all electric vehicle for taking the worst case into account. Based on this, load flow simulations for the coupled and uncoupled grid were performed and the results were evaluated by developed evaluation criteria. The results show that the coupling can not achieve significant improvements in stable grid operation. As a next step, the methodology will be applied to several real grids.

Index Terms—Charging stations, Power grid, Load modeling, Load flow.

I. INTRODUCTION

Electric vehicles (EV) will play a significant role in the near future, not only because of their greater efficiency, but also because of other positive aspects, such as reducing particulate matter emissions, NO_x, CO₂, ozone levels. The higher penetration of EVs, the stronger impact on the electricity grid. The transmission grid is relatively little affected by electromobility (e-mobility). With about 530 TWh of consumption per year and a peak load of 82 GW, the additional energy for three million EVs with 3 TWh per year is small with only about 0.5 % of the whole energy consumption [1]. The LV grid can be stressed by local accumulation of EVs. It is expected that with a higher use of private e-mobility due to high simultaneous charge of the private EVs, the peak load in LV grids will increase significantly. This requires investments in LV grid, e.g. grid reinforcements. Earthworks measures are associated with high costs, especially in the LV grid. It should be noted that the earthworks are particularly expensive when laying electrical cables. Experience shows that the earthworks when laying electrical cables is 5 times higher than for the

cable. Therefore, the cost and effort for laying new cables should be kept as low as possible.

In urban grids with dense population and high, homogenous power density, the coupling of LV grids is applied. Coupling of rural LV grids, which are normally planned as radial grids, does not take place yet. LV grids coupling can provide higher supply reliability, lower grid losses and higher uptake potential for generating plants or new loads. Moreover, a coupling can often be achieved without cost-intensive measures, for instance coupling by closing a disconnecting point or by connecting two cable distribution cabinets with a short cable. However, in these topologies, the power flow is completely unregulated, making protection design and grid operation difficult.

In some variants, coupling of LV grids can be a cost efficient solution for the challenge of a higher share of EVs. The questions are:

- Is it possible to achieve an improvement in grid operation through grid coupling?
- Are there any negative effects on grid operation due to coupling?

This paper provides a contribution to answer these questions. Since there was no need in the past, coupling of LV grids were barely subjects of researches. In [2] three variants for the coupling of two LV grids are compared, the use of a switch (direct coupling), the use of a full converter and the use of a power electronic power factor correction device STATCOM (Static Synchronous Compensator), but without a special focus on higher load due to private e-mobility. This paper will study the coupling of grids in consideration of e-mobility.

The paper is structured as follows: First, there is an introduction about the methodology and the simulation framework in section II. The evaluation criteria and the simulation results are presented in section III. In Section IV the paper gets summarized and outlook is given.

II. METHODOLOGY AND SIMULATION FRAMEWORK

A. Simulation Grid

In [3], synthetic grid models which represent typical LV grids are presented. Two S2b grids presented in [3] were arranged to the simulation grid as shown in Fig. 1, two feeders of each grid can be coupled by disconnectors. Simulations were done in a first step with open-switches state and in a

TABLE I
GRID DATA

Grid structure	Number of power feeders	Number of buildings	Number of transformers	Power of each transformer
S2b	4	100	1	250 kV A
simulation grid	8	200	2	250 kV A

second step the switches were closed. The synthetic grid has the grid data shown in Table I.

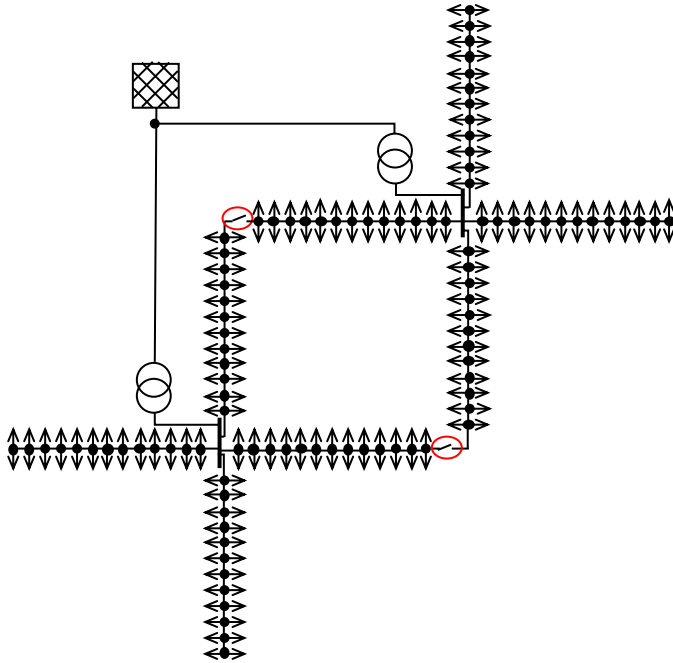


Fig. 1. Simulation grid

In the considered scenario for the year 2030, an EV volume of 6 million vehicles is assumed. The first step was to calculate the number of EVs in a village with 200 households. The statistical data of the Statistische Landesamt Rheinland-Pfalz were used [4] [5] to determine the number of vehicles in the grid. Rheinland-Pfalz has a population of 4.057 million people and the number of households is about 1.947 million. This gives an average of 2.08 people per household. In order to this the synthetic grid have 416 inhabitants. The number of inhabitants in Germany (82 million) and the number of EVs in 2030 (6 million) gives the number of EVs per inhabitant of about 0.073 vehicle per inhabitant. In case of this there will be 29 EVs in the simulation grid.

B. Load Situation

1) *Vehicles Amount:* In order to determine the maximum load for a worst case consideration, a load modeling was performed. Initially, the average mileage was determined. This results from the number of registered vehicles (45.8 million) and the number of kilometers (626.5 billion) traveled in

Germany [6]. An average mileage of about 37 km per vehicle is obtained. The vehicles were divided into three classes based on the assignment of the Kraftfahrtbundesamt (KBA) [7]:

- small
- medium
- big

TABLE II
CAR CLASSES [6]

Vehicle-classification (KBA)	Vehicle class	stock of vehicle 2017		Fit percentage
		Number of cars	Percentage	
minis small car	small	3.109.239	6,8 %	27,5 %
	total small	8.916.824	19,5 %	
compact class middle class vans/mini-vans	medium	12.002.528	26,2 %	46,8 %
	total medium	6.925.175	15,1 %	
		2.030.937	4,4 %	
upper middle class upper class SUVs vans utilities sports car	big	2.031.653	4,4 %	25,7 %
		275.750	0,6 %	
		4.224.728	9,3 %	
		2.093.798	4,6 %	
		1.702.737	3,7 %	
		860.861	1,9 %	
		11.189.527	24,5 %	
camper other	other	450.167	1,0 %	0 %
		1.179.163	2,6 %	
	total other	1.629.330	3,6 %	
	total	45.803.560	100 %	100 %

The number of classified vehicles in the synthetic grid with 29 EVs is 8 small, 14 medium, 7 big EVs.

2) *Settings of the Slack Node:* Depending on the grid operator and substation, the voltage distribution may vary. Fig. 2 shows the voltage distribution used here. The defaults are defined by [8] and according to VDE-AR-N 4105. Generating units can already disconnect from the grid at a voltage of 109 % U_n , which had been taking into account. According to applied planning criteria, the allowed voltage drop for the middle voltage (MV) grid and LV grid is set to 5 % U_n . To consider a worst case situation, the voltage of the MV level is set to 96.5 % U_n according to Fig. 2.

3) *Household Loads:* The household loads were generated with a tool for load time series [9]. This tool was released in 2017. It can be used to create load profiles for single buildings right through to entire grids. The compilation of the loads is based on the standard load profile by the Bundesverband der Energie- und Wasserwirtschaft as well as statistics from household devices. The time series are created in 15 minutes steps.

4) *Additional load through Electric Vehicles:* In the worst case scenario it is assumed that all vehicles are loaded at

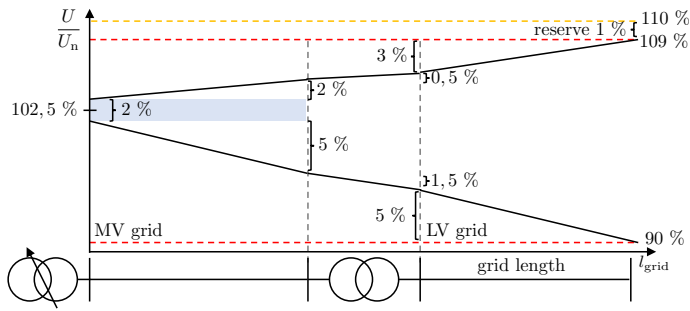


Fig. 2. Voltage distribution over the voltage levels

the same time. In order to determine this point in time of the maximum load, a loading curve was created by means of the study "Mobilität in Deutschland 2008" [10] from the year 2010. The charge curve obtained was superimposed with other charging curves of various studies and the mean value was formed. This is shown in Fig. 3.

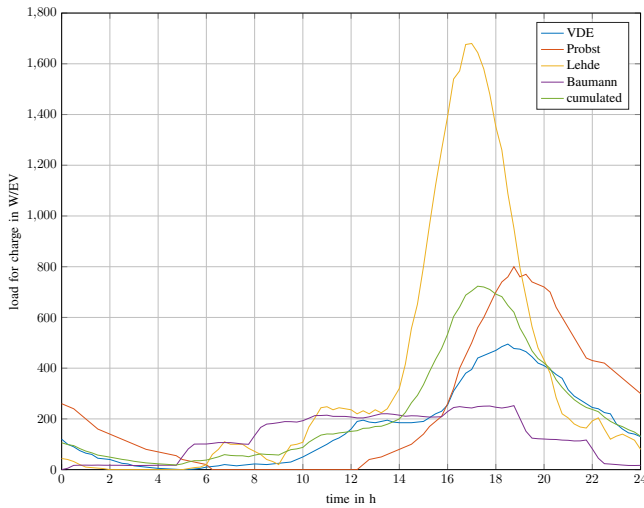


Fig. 3. Different load curves for charging electric vehicle

This load curve was then applied to the household load of the grid to determine the time when the vehicles were charged as shown in Fig. 4. The time with the highest load is marked in the diagram with a green line.

After the determination of the time, the vehicles were randomly distributed in the grid and the households acted with the corresponding charging power.

C. Simulation Variants

The simulation of the grid is performed for two states of the scenario for the year 2030. Once in the uncoupled state and once in the coupled state, each with 40,000 variants. The different vehicle classes were assumed with various charging power. Table III shows the load of the EVs for four different cases. Each case with 10,000 variants and the additional load in the grid per variant.

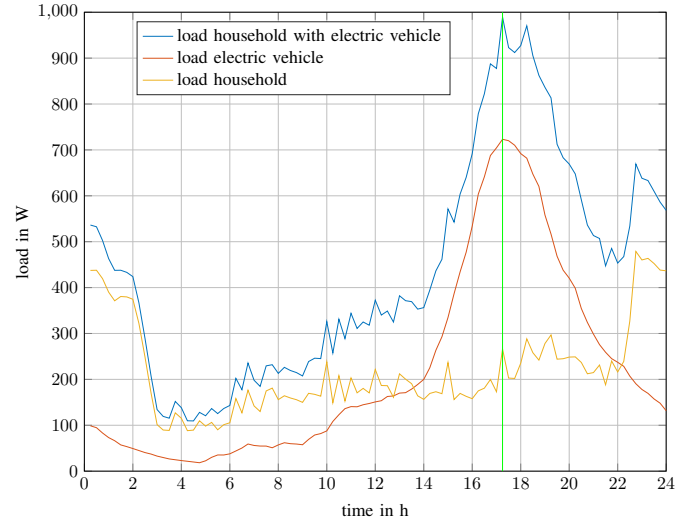


Fig. 4. Resulting household load with additional load from electric vehicle

TABLE III
CASES OF ADDITIONAL LOAD DUE TO ELECTRIC VEHICLES

Cases	Variants	Small	Medium	Big	Additional load
1	1 - 10,000	11.0 kW	11.0 kW	22.0 kW	385.0 kW
2	10,001 - 20,000	3.7 kW	11.0 kW	22.0 kW	326.6 kW
3	20,001 - 30,000	3.7 kW	3.7 kW	22.0 kW	231.7 kW
4	30,001 - 40,000	3.7 kW	3.7 kW	11.0 kW	154.7 kW

D. Simulation Process

The flow chart in Fig. 5 shows the process for the simulation. In the first step, the statistical data are evaluated, resulting in the number of EVs and their classification into classes. The further procedure envisages the determination of the grid load with the additional load of the EVs. From this the determination of the time for the worst case situation, which is to be examined, takes place. At the predetermined time, the vehicle loads are now randomly distributed in the grid and fed on the households. Then the grid is simulated with the additional load, firstly in the closed switch state and then in the open switch state.

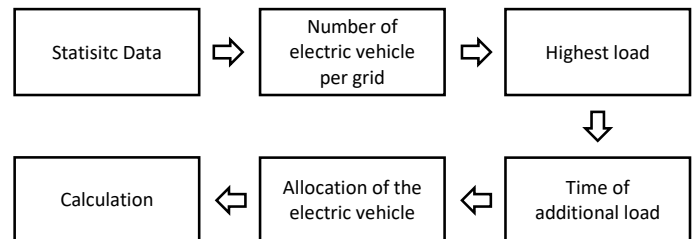


Fig. 5. Flow chart of the simulation process

III. SIMULATION RESULTS

A. Evaluation Criteria

In order to determine the changes which occur due to the additional load and the coupling in the network, different parameters have been defined. These are explained in more details below.

The evaluation criteria are the following:

- the voltage U
- the current I
- the voltage unbalancing factor b_u

The voltage band of $\pm 10\%$ according EN 50160 must be observed. Therefore, the voltage limit $U_{lim} = 0.9 \cdot U_n$. The rated short-time thermal current of the cable $4 \times 150 \text{ mm}^2$ NYY is 275 A according to [3]. b_u is limited to 2% according to the standard EN 50160. By using the equation 1, the unbalancing factor b_u can be calculated as follows. First the value for the negative-sequence system and the value of the positive-sequence system have to be calculated.

$$\underline{u}_{012} = \underline{T} \cdot \underline{u}_{L1L2L3} \quad (1)$$

with the system vector \underline{u}_{012} in equation 2,

$$\underline{u}_{012} = \begin{bmatrix} U_0 \\ U_1 \\ U_2 \end{bmatrix} \quad (2)$$

the transformation matrix \underline{T} with the complex phasor rotation operator \underline{a} in 3,

$$\underline{T} = \begin{bmatrix} 1 & 1 & 1 \\ 1 & \underline{a} & \underline{a}^2 \\ 1 & \underline{a}^2 & \underline{a} \end{bmatrix} \quad (3)$$

and the vector of the unsymmetric voltage of each line \underline{u}_{L1L2L3} in 4.

$$\underline{u}_{L1L2L3} = \begin{bmatrix} U_{L1} \\ U_{L2} \\ U_{L3} \end{bmatrix} \quad (4)$$

The b_u is calculated using the previously determined system sizes with equation 5.

$$b_u = \frac{u_2}{u_1} \cdot 100\% \quad (5)$$

- \underline{u}_{012} : system vector
- \underline{u}_{L1L2L3} : line vector
- b_u : voltage unbalanced factor
- u_2 : negative-sequence system
- u_1 : positive-sequence system
- \underline{T} : transformation matrix
- \underline{a} : complex phasor rotation operator

In order to indicate the improvement of the evaluation criteria from uncoupled to a coupled grid, the factors r_U in 6, r_I in 7 and r_b in 8 are introduced as well as the total factor r in 9. These indicates the improvements in the ratio of the coupled to the uncoupled grid.

Always the highest occurred value of a simulation variant in the coupled (\hat{U}_c , \hat{I}_c and \hat{b}_c) and uncoupled grid (\hat{U}_o , \hat{I}_o and \hat{b}_o) are considered. Please note that the improvement can be negative too.

$$r_U = \frac{\hat{U}_o - \hat{U}_c}{\hat{U}_o} \quad (6)$$

$$r_I = \frac{\hat{I}_o - \hat{I}_c}{\hat{I}_o} \quad (7)$$

$$r_b = \frac{\hat{b}_o - \hat{b}_c}{\hat{b}_o} \quad (8)$$

$$r = \frac{1}{3} \cdot (r_U + r_I + r_b) \quad (9)$$

- r_U : improvement ratio of U
- r_I : improvement ratio of I
- r_b : improvement ratio of b_u
- r : improvement ratio of the grid
- \hat{U}_o : peak value of U in the open switch state
- \hat{U}_c : peak value of U in the closed switch state
- \hat{I}_o : peak value of I in the open switch state
- \hat{I}_c : peak value of I in the closed switch state
- \hat{b}_o : peak value of b_u in the open switch state
- \hat{b}_c : peak value of b_u in the closed switch state

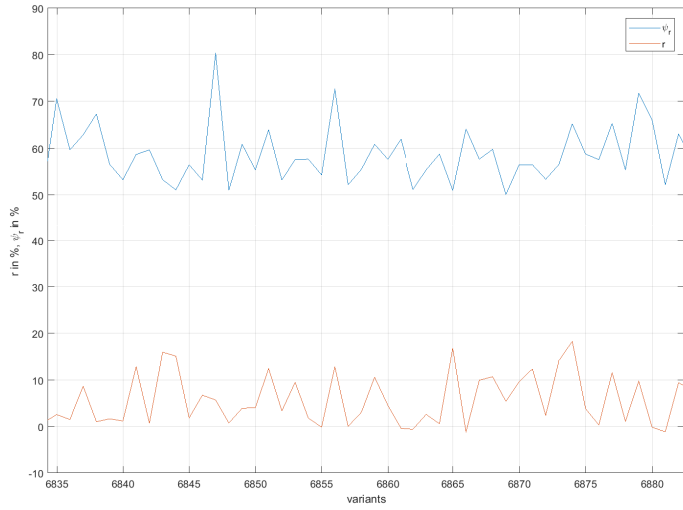
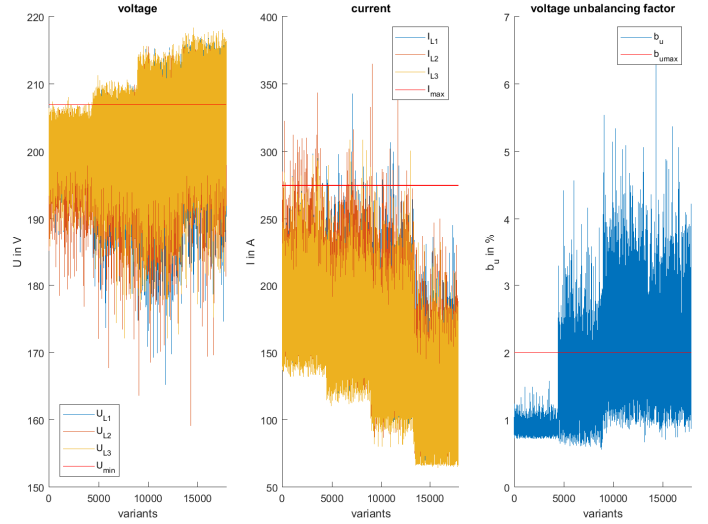
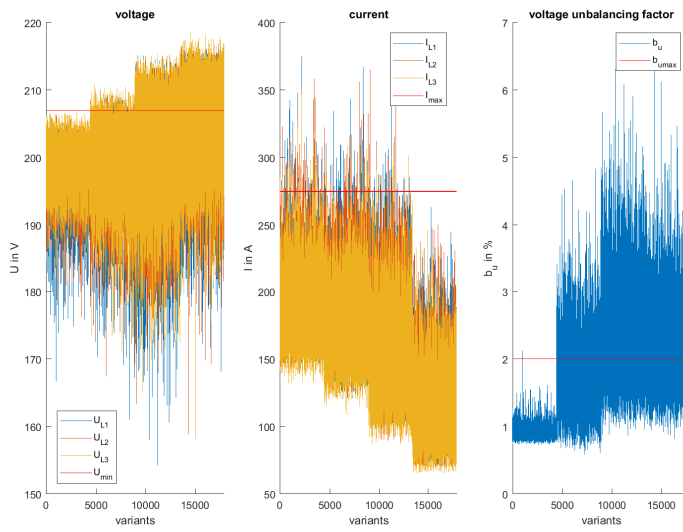
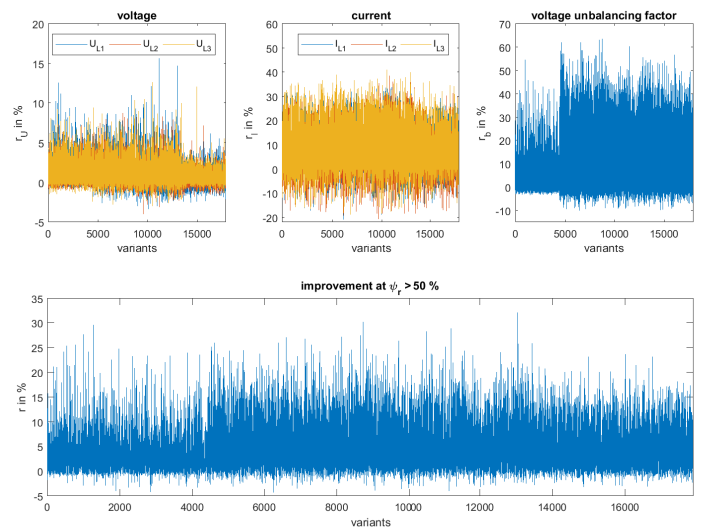
Due to identify the relevant variants as suitable use-case for the coupling of the grids, the penetration ratio is introduced. This is necessary to identify the variants with high additional load in the not coupable feeders. Since coupling the grids will have no significant effect to the feeders, limit values would always be exceeded. For this reason, variants with a penetration ratio lower than a defined value are not included in the evaluation. In this paper, two limits are considered, under which variants are excluded from the evaluation: $\psi_r > 50\%$ and $\psi_r > 30\%$. Thereby, the evaluated variants are reduced from 40,000 to 17,880 and 38,511.

The penetration ratio ψ_r is the additional load of EVs in the considered couplable feeders P_a divided to the additional load of all EVs in the grid P_t (10).

$$\psi_r = \frac{P_a}{P_t} \quad (10)$$

- ψ_r : penetration ratio
- P_a : additional load in the considered coupled part
- P_t : total additional load

Fig. 6 shows the relationship between ψ_r and r . The improvements and the ψ_r have a positive correlation. The bigger ψ_r the bigger the improvements. For low ψ_r , coupling the grids have no effect.

Fig. 6. Correlation between ψ_T and r Fig. 8. Maximum values in all variants in the coupled grid with $\psi_T > 50\%$ Fig. 7. Maximum values in all variants in the uncoupled grid with $\psi_T > 50\%$ Fig. 9. Visualization of the improvement with $\psi_T > 50\%$

B. Results

In the uncoupled grid with a penetration ratio of $\psi_T > 50\%$, Fig. 7 shows that in 3 out of 4 cases the charging loads of EVs are significantly lower than the voltage as well as excess current and unbalance. It can be seen that in the first case, the imbalance is not caused by the additionally applied vehicle loads, since in this case they are only charged symmetrically. In case of a lower additional load in the last 10,000 variants (4th case) the rated short-time thermal current is not reached.

The results by uncoupled grid are contrasted with the results by coupled grid shown in Fig. 8. Here, an improvement in the characteristic values can be seen in comparison with Fig. 7. Especially in the case of asymmetry, improvements are gained. But the marginal flow is less often achieved. On the other hand, compliance with the voltage can not be greatly improved by the coupling.

In the preceding graphics the compliance with the limit was

verify. Fig. 9 shows the improvements in the characteristic values in relative sizes. It can be seen that for all parameters an improvement can be observed. The biggest improvements can be achieved with b_{u1} . The current is also waiting for major improvements, but the biggest signs of deterioration can be seen here as well. In many variants, the coupling leads also to worse results for all three parameters. Over all its shown that the change in grid coupling is in the majority of variants (14,567) positive. Improvements of more than 30 % can be achieved. Despite these notable improvements in grid criteria, stable operating points can not be achieved through the coupling.

In table IV the improvements and deterioration of the characteristic values are compared. r is in about 4 out of 5 variants positive. In 1 out of 5 variants, there is a deterioration in the values. This shows that coupling in the investigated scenario does not always improve the grid situation.

TABLE IV
IMPROVEMENT RATIO WHERE $\psi_r > 50\%$

Improvement ratio	r_U	r_I	r_b	r
positive	15,328	13,858	14,516	14,567
negative	2,552	4,022	3,364	3,313

Fig. 10 shows r at $\psi_r > 30\%$. Similar to the investigation with $\psi_r > 50\%$, the majority of r are positive. Table V shows that about in 3 out of 4 variants the characteristic values are positive and in 1 out of 4 variants negative.

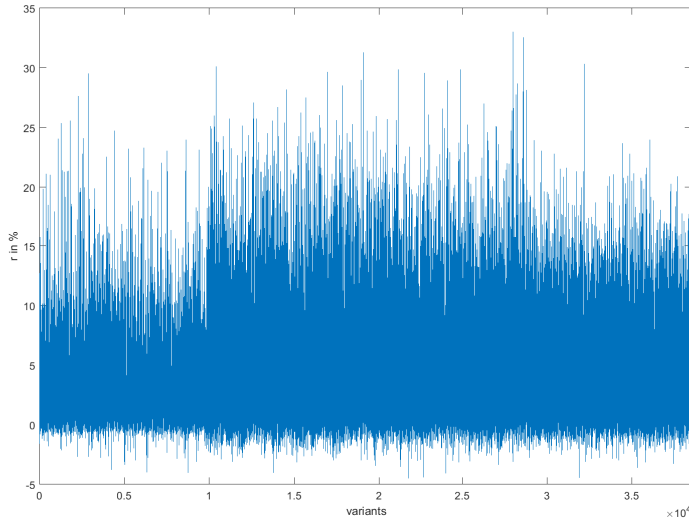


Fig. 10. Improvement over all variants with $\psi_r > 30\%$

TABLE V
IMPROVEMENT RATIO WHERE $\psi_r > 30\%$

Improvement ratio	r_U	r_I	r_b	r
positive	31,230	27,711	31,406	30,116
negative	7,281	10,800	7,105	8,395

IV. SUMMARY AND OUTLOOK

This paper presents an investigation on coupling of two LV grids to master the challenges posed by e-mobility. Based on synthetic grid models first insights were gained, which are used in the further work. The results of this paper show that an improvement of the characteristics can achieve by coupling the grids. The investigated scenario 2030, however, does not lead to the desired result of a stable grid operation, since coupling of two LV grids is not sufficient to handle such a high additional load. In the medium term, coupling of rural grids can be a sensible and cost-effective alternative for grid expansion. However, the grids can still operate with less inconvenient expansion measures and a smaller number of vehicles. In the future, further investigations on real grid models will be carried out with the presented methodology. It makes sense to show on the medium-term penetration of vehicles and the associated additional burden on the LV grids.

A sensible parameter is certainly the amount of vehicles in which a safe grid operation without larger expansion measures is possible. Further investigations on the arrangement of the vehicles in the grid can provide information on the variants in which coupling deteriorate the characteristics. It turns out that e-mobility represents a considerable additional burden for the LV grids. By 2030, with a penetration in Germany of planned 6 million vehicles, the LV grids must be expanded and dimensioned accordingly.

REFERENCES

- [1] Probst, Alexander. *Auswirkungen von Elektromobilität auf Energieversorgungsnetze analysiert auf Basis probabilistischer Netzplanung*. Dissertation. Stuttgart, Deutschland: Universität Stuttgart, 2014
- [2] Shahnia, Farhad; Ghosh, Arindam. *Coupling of neighbouring low voltage residential distribution feeders for voltage profile improvement using power electronics converters*, IET Generation, Transmission & Distribution 10.2 (2016) 535-547.
- [3] Wellßow, Wolfram H.; Weisenstein, Marco; Ma, Haiyan; Röhrenbeck, Stephan; Rui, Han; Benzarti, Anes *Synthetische NS-Netzmodelle für wissenschaftliche Untersuchungen*. URL: <https://kluedo.ub.uni-kl.de/frontdoor/index/index/docId/5210>. (called on: 30. April 2018) Kaiserslautern, Deutschland: Prof. Dr.-Ing. Wolfram H. Wellßow, Lehrstuhl für Energiesysteme und Energiemanagement, Technische Universität Kaiserslautern, 2018.
- [4] Statistisches Landesamt Rheinland-Pfalz, *Haushalte und Familien: Basisdaten Land Bevölkerung in Privathaushalten 2016 nach Haushaltsgröße und Altersgruppe*, URL: <https://www.statistik.rlp.de/de/gesellschaft-staat/haushalte-und-familien/basisdaten-land/tabelle-2/>. (called on: 22. April 2018) Bad-Münster, Deutschland: Statistisches Landesamt Rheinland-Pfalz, 2016.
- [5] Statistisches Landesamt Rheinland-Pfalz, *Haushalte und Familien: Basisdaten Land Privathaushalte 2016 nach Haushaltsgröße, Familienstand und monatlichem Nettoeinkommen*, URL: <https://www.statistik.rlp.de/de/gesellschaft-staat/haushalte-und-familien/basisdaten-land/tabelle-3/>. (called on: 22. April 2018) Bad-Münster, Deutschland: Statistisches Landesamt Rheinland-Pfalz, 2016.
- [6] Kraftfahrtbundesamt, *Bestand an Personenkraftwagen nach Segmenten und Modellreihen am 1. Januar 2017 gegenüber 1. Januar 2016*, URL: https://www.kba.de/SharedDocs/Publikationen/DE/Statistik/Fahrzeuge/FZ/2017/fz12_2017_pdf.pdf?__blob=publicationFile&v=3. (called on: 08. January 2018) Flensburg, Deutschland: Kraftfahrtbundesamt, 2018.
- [7] Plütz, Patrick; Kühn, Andre; Gnann, Till; Wietschel, Martin. *Markthochlaufszszenarien für Elektrofahrzeuge*. URL: <http://www.isi.fraunhofer.de/isi-wAssets/docs/e/de/publikationen/Fraunhofer-ISI-Markthochlaufszszenarien-Elektrofahrzeuge-Langfassung.pdf>. (called on: 10. January 2018) Karlsruhe, Deutschland: Fraunhofer ISI, 2014.
- [8] BDEW Bundesverband der Energie- und Wasserwirtschaft e.V. *Technische Richtlinie Erzeugungsanlagen am Mittelspannungsnetz*. URL: http://www.tab-strom.de/PDF_ALLE/Technische_Richtlinie_Erzeugungsanlagen_Msp_2008_06.pdf. (called on: 27. April 2018) Berlin, Deutschland: BDEW, Berlin, 2008.
- [9] Nau, Nicolas. *Synthesis of domestic load curves for low voltage grid simulations*. http://www.ees.eei.uni-erlangen.de/down/PESS_Konferenz/Paper/PESS%202017_S%20P07_Nicolas%20Nau.pdf. (called on: 27. April 2018) Kaiserslautern, Deutschland: Power and Energy Student Summit (PESS), Nürnberg, 2017.
- [10] Bundesministerium für Verkehr, Bau und Stadtentwicklung (BMVBS). URL: http://www.mobilitaet-in-deutschland.de/pdf/MiD2008_Abschlussbericht_I.pdf. (called on: 02. February 2018) *MiD - Mobilität in Deutschland 2008*. Bonn and Berlin, Deutschland: BMVBS, Bonn and Berlin, 2010

Highly Renewable Energy Integrated Grid Stability by Microgrid

Vishal Undre, Alberto Dolara, Sonia Leva
 Department of Energy
 Politecnico di Milano
 Milan, Italy

Abstract— Nowadays, more and more renewable energy sources getting connected to national grid. Generation from renewable sources depends on climate. Energy security can be achieved by microgrid. Microgrid comprise of Battery Energy Storage system, Fuel Cells, rooftop PV system, small wind turbines, Micro-cogeneration etc. If generation from renewable sources is insufficient; microgrid can be used as a backup solution. This allows us to regulate voltage and frequency deviation. In this paper grid stability has been analyzed. Also microgrid's advantages over Battery Energy Storage System (BESS) in terms of reliability, continuity and scope has been discussed.

Keywords-Microgrid; Grid stability; BESS, Fuel cell

I. INTRODUCTION

In recent few years, Italy had an extensive addition of renewable energy into national grid which is 29 GW between 2000-2016 period, 19.5 GW of which came from solar and 9.5 GW from wind, and which together should increase to 50 GW [1], [2]. Also Germany has been installed 40 GW PV until 2016 and 40 GW wind power.

Generation of wind and solar energy varies and increases the need for additional reserves. For example in Italy, on weakened electricity demand fell by around 15 GW in the 2012-2016 period. In 2012 the conventional energy fleet was 77 GW, while currently it is 56 GW.

In conclusion, while the reserve margin improved in 2016, it is still well below historic levels as shown in fig. 1 and 2, which, however, benefited from a generation fleet that is not comparable to the current one. Therefore, the problem of adequacy is still present for the Italian electricity system. With more and more penetration of renewables will need more increase in reserve will be required. Currently, Germany and Italy are the two EU countries with the highest DG penetration [3]. In Italy, since 2010, a huge deployment of DG occurred, leading to an important change in the technical and regulatory framework, e.g. technical prescriptions for the connection to the HV, MV and LV grids have been completely redefined.

Currently, the main contributions to the system stability are assumed as mandatory services (primary frequency control, voltage regulation, etc.), while energy services (secondary frequency control, congestion management, etc.) are regulated in a specific ancillary services market. Recently, a new resolution of the Italian Energy Authority activated a new mechanism for the reimbursement of the primary frequency control provision on a voluntary basis [3].

Goal of this paper is to analyze effects of microgrid on voltage profile of LV and MV network. In section II concept of microgrid and its advantages are explained. In section III, information about real-time implementation of microgrid given. In Section IV and V results and future work has been discussed.

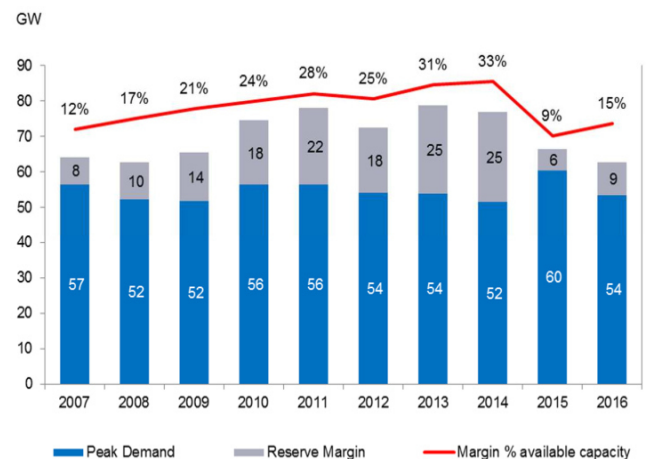


Figure 1. Reserve margin at summer peak demand

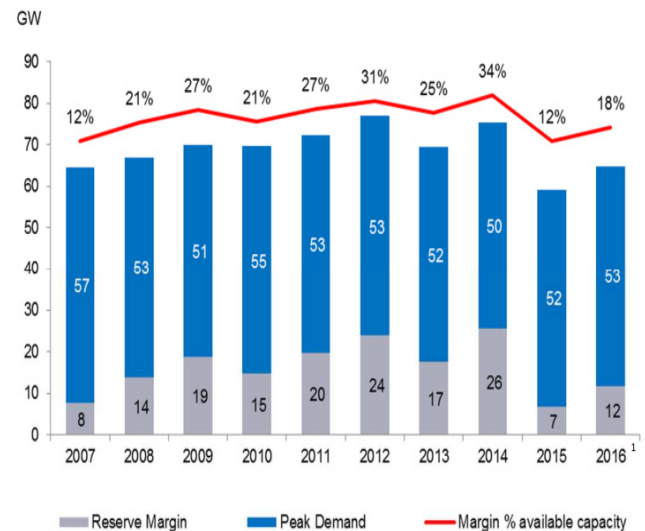


Figure 2. Reserve Margin at winter peak demand

II. ADVANTAGES OF MICROGRID

Concept of Microgrid

Microgrid has the potential to be the required solution for the above problems. Advantages of microgrid are

- Increase in system reliability and power quality
- Easy black start
- Expense of secondary backup power minimized
- Load shaving
- Win-win situation for consumers and distribution companies. Consumers will get electricity at lower prices and distributions companies will get reliability, improves grid stability and less penalties for interruptions.
- Reactive power compensation possible

Microgrid is a low-voltage distribution grid, which interconnects locally installed small, modular distributed energy resources, called DERs [4]. This grid can operate either in islanded mode or with macrogrid (i.e., utility grid). Microgrid system is gaining importance, to-day, because transmission and distribution systems are operating under extreme stress due to aging equipments as well as increasing growth of loads. Microgrids are, also, advantageous for CHP (combined heat and power) operation. This CHP operation enhances the system efficiency to 60% (approx.). This is a very high value compared to central power plant's overall fuel-to-electricity efficiency of 28%-32%. The scale of heat production from individual unit is small and therefore, it offers greater flexibility in matching to heat requirements. Overview of microgrid shown in fig. 3 [10]. Black start with microgrid is possible but problem of synchronization occurs.

Again, microgrid has a benign impact on environment. Emissions from fossil fuel based plants are very high and are creating cause of concern about global warming. Whereas emissions of natural gas based micro turbine, fuel cells have been reduced significantly through better design. Solar PV and wind fall under green technology [8].

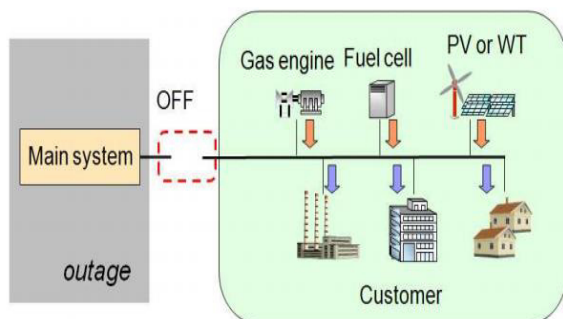


Figure 3. Overview of Microgrid

III. IMPLEMENTATION OF MICROGRID

Microgrid of capacity 100 kW will be implemented in Politecnico di Milano, Campus Bovisa, building BL25A as

shown in fig.4. microgrid will consist of 30 kW (combinely Fuel cell, Battery, Micro-cogenerator) and existing 70 kW roof PV plant. Simulation model was implemented in DigiSilent software. Simulation results will be useful for actual implementation of microgrid.

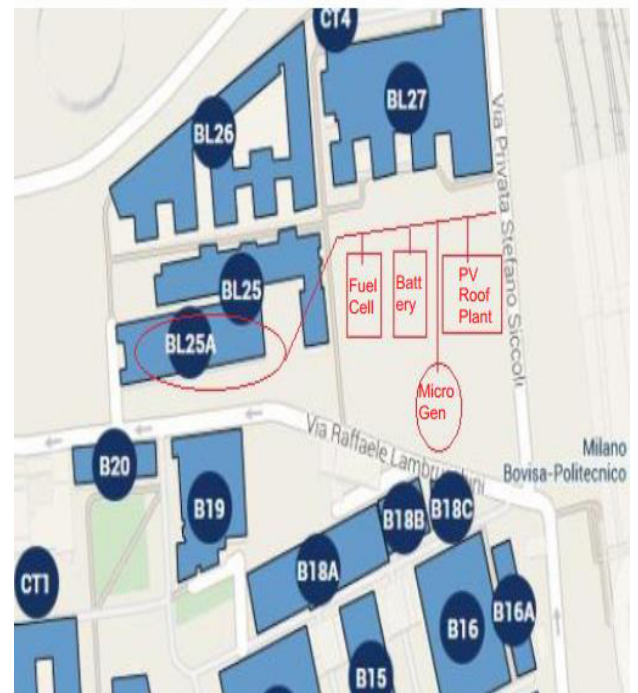


Figure 4. Microgrid implementation site

For understanding effect of microgrid on grid MV benchmark grid proposed by is CIGRE C6.04.02 is used [9]. MV grid supplies power to town and express feeder is connected to place where microgrid has to be connected. Microgrid can be connected to MV grid and grid stability can analyzed, but scope of this paper LV grid has been analyzed.

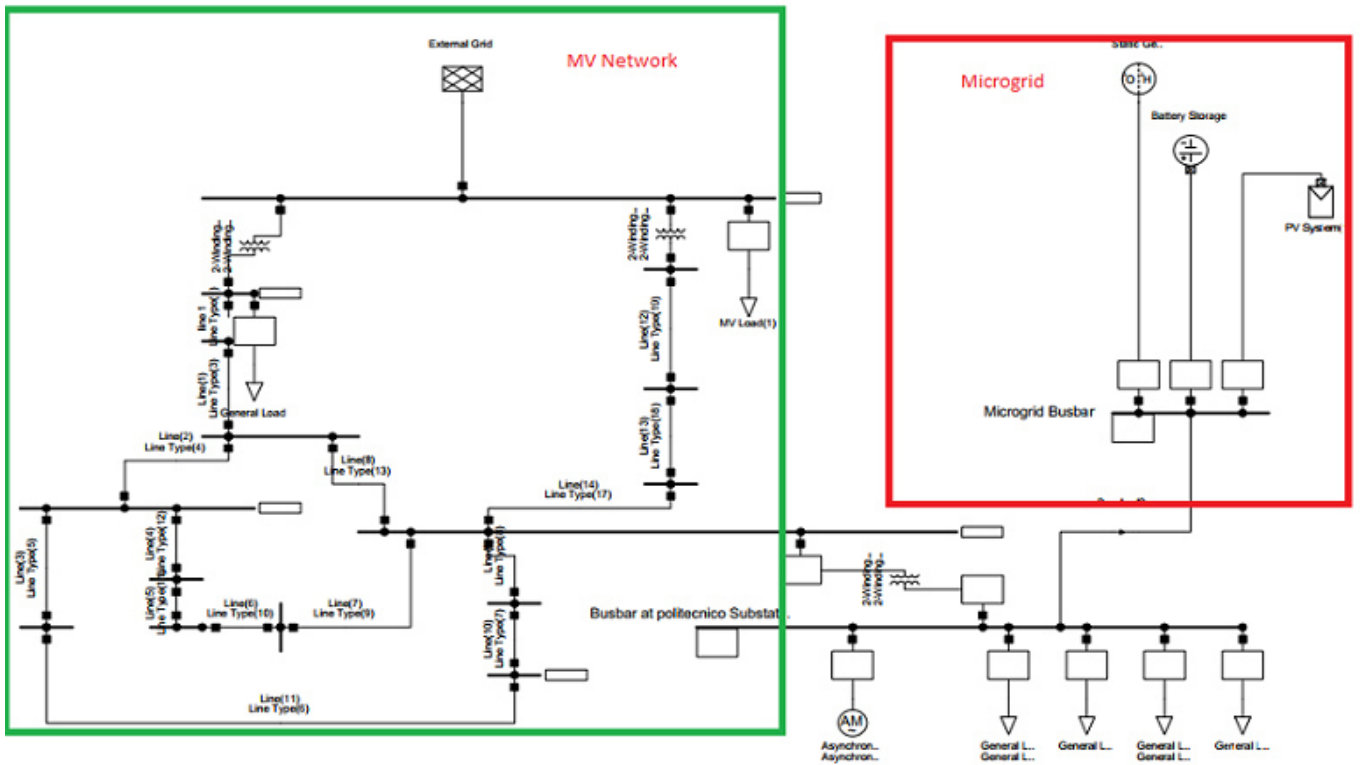


Figure 5. Benchmark MV Model and LV Network

IV. RESULT AND DISCUSSION

Network shown in fig. 5 simulated in DigiSilent software. Detailed list about types of loads, microgrid, and bus voltages describes below.

Table I describes about loads connected to 0.40 kV bus bar. Two pure resistive and complex loads are connected. Microgrid comprise of Fuel cell, Battery and PV roof plant. Other sources like micro-co-generation, diesel generator can be connected.

Table III and Table IV explain about voltage profiles of MV and LV grid with and without microgrid. With the help of microgrid voltage profile of not only LV grid has been improved but also of MV has been improved. There is also change in Deg column from negative to positive this explains that microgrid is feeding power into grid.

TABLE I. LIST OF LOAD CONNECTED TO LV GRID

Name Load	MW	Mvar
General Load 1	0.09	0
General Load 2	0.04	0
General Load 3	0.9	0.009
General Load 4	0.09	0.005
Induction Machine 1	0.09	0.035

TABLE II. COMPONENTS OF MICROGRID

Sr. No	Component of Microgrid	MW/ MWhr	Mvar
1	Fuel Cell	0.5	-
2	Battery	0.03	-
3	PV roof plant	0.9	-

TABLE III. BUS VOLTAGES WITH MICROGRID

Terminal	Rtd. V [kV]	Bus voltage		
		p.u.	kV	Deg
12	110	1.00	110	0
13	20	0.913	18.25	1.01
14	20	0.913	18.26	1.04
8	20	0.913	18.27	1.06
7	20	0.914	18.27	1.09
6	20	0.914	18.27	1.09
9	20	0.914	18.27	1.09
10	20	0.914	18.27	1.09
11	20	0.914	18.27	1.09
4	20	0.914	18.27	1.09
5	20	0.914	18.27	1.09
3	20	0.914	18.27	1.09
2	20	0.914	18.27	1.09
1	20	0.914	18.27	1.09
Bus bar at Politecnico (LV)	0.40	0.910	0.36	2.11
Microgrid bus bar	0.40	0.910	0.36	2.11

TABLE IV. BUS VOLTAGES WITHOUT MICROGRID

Terminal	Rtd. V [kV]	Bus voltage		
		p.u.	kV	Deg
12	110	1.00	110	0
13	20	0.910	18.25	-2.50
14	20	0.909	18.26	-2.57
8	20	0.908	18.27	-2.59
7	20	0.917	18.27	-2.65
6	20	0.907	18.27	-2.65
9	20	0.907	18.27	-2.65
10	20	0.907	18.27	-2.65
11	20	0.914	18.27	-2.65
4	20	0.907	18.27	-2.65
5	20	0.907	18.27	-2.65
3	20	0.907	18.27	-2.65
2	20	0.907	18.27	-2.65
1	20	0.903	18.27	-3.45
Bus bar at Politecnico (LV)	0.40	0.903	0.36	-5.19
Microgrid bus bar	0.40	0.000	0.000	0.00

From LV terminal (0.40 kV) it is concluded that voltage stability can be achieved with help of microgrid. This not only affects voltage profile of LV but also, MV grid voltage profile has been improved. If microgrid connected to MV network there will be more improvement in MV and LV grid. This analysis will be done in future work.

V. CONCLUSION AND FUTURE WORK

Presented work is initial part of my master thesis. In this paper voltage regulation of LV and MV grid has been analyzed. From results it can be concluded that, with the help of microgrid voltage profile of not only LV grid improved but also voltage profile of MV has been improved. Load connected to MV network will get some percent of power

from microgrid and because of this transmission losses will be minimized.

Applications of microgrid not limited to this. Future work of thesis will be power quality improvement by microgrid. Microgrid comprises of energy storage and generator therefore generation of electricity during peak hours will cut down price which is called load shaving.

REFERENCES

- [1] Terna group, "Monthly report on electricity system," May 2017.
- [2] NASA surface meteorology and solar energy: Global data set. Available: <https://eosweb.larc.nasa.gov/cgi-bin/sse/global.cgi>, Accessed on: April 26, 2018.
- [3] S. Nassuatoa, G. Magistrati, G. Marchegiani, C. Briviod, M. Delfantid, D. Falabrettid, M. Merlo, "Distributed storage for the provision of ancillary services to the main grid: project PRESTO," 10th International Renewable Energy Storage Conference, IRES 2016, 15-17 March 2016, Düsseldorf, Germany, pp. 182 – 193.
- [4] R. Lasseter, "Microgrids and Distributed Generation," Journal of Energy Engineering, American Society of Civil Engineers, Sept. 2007.
- [5] A. Dolara, F. Grimaccia, G. Magistrati, G. Marchegiani, "Optimization Models for Islanded Micro-Grids: A Comparative Analysis between Linear Programming and Mixed Integer Programming," Energies, vol. 10, no. 2, February 2017.
- [6] A. Dolara, E. Donadoni, S. Leva, G. Magistrati, "Performance Analysis of a hybrid micro-grid in Somalia," 2017 IEEE PowerTech, 2017.
- [7] A. Dolara, F. Grimaccia, G. Magistrati, G. Marchegiani, "Optimal Management Algorithm for Battery Energy Storage System Included in an Islanded Micro-Grid," 2016 IEEE 16th International Conference on Environment and Electrical Engineering (E3E), 2016.
- [8] A. Basu, S. Chowdhury, D. Ray, P. Crossley "Reliability Study of A Micro-Grid Power System," Universities Power Engineering Conference, 2008.
- [9] K. Rudion, A. Orths, Z. Styczynski, K. Strunz "Design of Benchmark of Medium Voltage Distribution Network for Investigation of DG," Power Engineering Society General Meeting IEEE, 2006, Montreal, Que., Canada.
- [10] T. Tsuji, K. Nakagawa, A. Ohmiya, T. Oyama "A Study on Power System Supply Reliability of Microgrid with Renewable Energy Considering switching Operation," 17th PowerSystem Computation Conference, August 22-26, Sweden, 2011.



Publisher

Prof. Dr.-Ing. Wolfram H. Wellßow
University of Kaiserslautern
Erwing-Schrödinger-Straße
67663 Kaiserslautern

ES+EM
*Energy Systems +
Energy Management*